Effects of ionizing radiation on cell-matrix interactions at the single molecule level

Effekte ionisierender Strahlung auf Zell-Matrix Wechselwirkungen auf Einzelmolekülebene
Zur Erlangung des Grades eines Doktors der Naturwissenschaften (Dr. rer. nat.)
genehmigte Dissertation von Dipl.-Phys. Florian Lauer aus Freudenstadt
Tag der Einreichung: 28.1.2015, Tag der Prüfung: 20.4.2015
Darmstadt 2015 — D 17

1. Gutachten: Prof. Marco Durante, PhD
2. Gutachten: PD Dr. Tobias Meckel

TECHNISCHE
UNIVERSITÄT
DARMSTADT

Fachbereich Physik
Institut für Festkörperphysik

Effects of ionizing radiation on cell-matrix interactions at the single molecule level
Effekte ionisierender Strahlung auf Zell-Matrix Wechselwirkungen auf Einzelmolekülebene

Genehmigte Dissertation von Dipl.-Phys. Florian Lauer aus Freudenstadt

1. Gutachten: Prof. Marco Durante, PhD
2. Gutachten: PD Dr. Tobias Meckel

Tag der Einreichung: 28.1.2015
Tag der Prüfung: 20.4.2015

Darmstadt 2015 — D 17

Bitte zitieren Sie dieses Dokument als:
URN: urn:nbn:de:tuda-tuprints-45336
URL: http://tuprints.ulb.tu-darmstadt.de/4533

Für Anny.

Abstract

Single molecule microscopy is a technology that allows for accurate assessment of the location and motion of single fluorescent molecules, even in the context of observations on living biological samples. In the present thesis, a flexible analysis tool for single molecule data as obtained in biological experiments was established. The development of a tool to faithfully detect and localize diffraction-limited images of individual fluorescent probes was necessary since data acquired under cell cultivation conditions that account for a three-dimensional microenvironment as experienced physiologically by cells in native tissue poses a challenge not faced ordinarily. After design, implementation, quantitative tests using simulations for comparisons and verification, and evaluation of the different steps of the analysis procedure including local background estimation, local noise estimation, de-noising approaches, detection, localization, and post-processing, analysis capabilities were utilized to evaluate the impact of x-ray irradiation on the plasma membrane architecture of U2OS human osteosarcoma cells as assessed by tracking individual fluorescent lipid-mimetic dye molecules diffusing in the outer membrane leaflet. It was shown that lateral diffusion in the plasma membrane is well described as two-phase anomalous subdiffusion and presence of 3D extracellular matrix leads to lower anomalous exponents of the fast fraction in comparison to monolayer cell culture. Interestingly, even high single-dose (25 Gy) treatments known to induce membrane-mediated apoptosis in tumor microvessel endothelium via membrane viscosity enhancing ceramide generation were not observed to alter membrane architecture in U2OS cells which can be related to amplifying, feedback-driven redox-signaling in the endothelium absent in U2OS. In summary, the sensitive and accurate framework developed in this thesis to assess minute changes of plasma membrane located dynamic processes did not uncover a marked influence of ionizing radiation on plasma membrane lipid dynamics *per se*. However, it lays the major foundation to allow for studies of receptor signalling pathways with the same accuracy in the context of physiologically meaningful 3D microenvironments.

Zusammenfassung

Einzelmolekülmikroskopie ist eine Technik, die das genaue Lokalisieren und Verfolgen der Bewegung einzelner fluoreszenter Moleküle – sogar bei der Betrachtung lebender biologischer Proben – erlaubt. In der vorliegenden Arbeit wurde ein flexibles Analysewerkzeug für Einzelmoleküldaten, wie sie Ziel von biologischen Experimenten sind, etabliert. Dies war notwendig, um unter Zellkulturbedingungen, die einer dreidimensionalen Mikroumgebung, wie Zellen physiologisch im nativen Gewebe erfahren, Rechnung tragen und dabei eine besondere Herausforderung darstellen, zuverlässig fluoreszente Sonden zu detektieren und zu lokalisieren. Nach Konzipierung, Implementierung, Testsimulationen für quantitativen Vergleich und zur Verifikation, sowie der Evaluierung der unterschiedlichen Schritte der Analyseprozedur inklusive der Bestimmung des lokalen Hintergrundes, des lokalen Bildrauschens, Entrauschung, Detektion, Lokalisierung and zuletzt Nachbearbeitung des Datensatzes wurden diese Analysefähigkeiten angewandt um durch das Verfolgen einzelner lipidähnlicher Farbstoffmoleküle im äußeren Blatt der Plasmamembran humaner U2OS Osteosarkomzellen den Einfluss von Röntgenbestrahlung auf die Architektur der Plasmamembran zu bestimmen. Es konnte gezeigt werden, dass die laterale Diffusion in der Plasmamembran durch zwei Phasen mit jeweils anomaler Diffusion gut beschrieben wird und dass bei Gegenwart einer 3D extrazellulären Matrix die anomalen Exponenten der schnellen Fraktion verringert werden im Vergleich zur gewöhnlichen 2D Zellkultur. Interessanterweise wurden auch nach hohen Einzeldosen (25 Gy), bei denen bekannt ist, dass sie über membranviskositäterhöhende Ceramiderzeugung membranvermittelte Apoptose im Tumor-Mikrogefäßendothel induzieren, keine Änderungen der U2OS-Plasmamembran beobachtet. Dies kann man beziehen auf die Abwesenheit von endotheliumtypischen, rückkoppelnd-verstärkenden Redox-Signalwegen in U2OS-Zellen. Zusammengefasst, konnte die empfindliche und präzise Analysestruktur, die in der vorliegenden Arbeit entwickelt wurde, um kleinste Veränderungen dynamischer Prozesse in der Plasmamembran aufzudecken, keine merklichen Einfluss ionisierender Strahlung auf die Lipiddynamik an sich in der Plasmamembran feststellen. Andererseits setzt sie das Fundament für Studien zu Rezeptorsignalwegen im Kontext physiologisch sinnvoller Mikroumgebungen mit der selben Genauigkeit.

Contents

1 Introduction

Cancer is one of the dominating causes of death. The number of patients is increasing and is expected to do so due to the demographics of aging societies. Cancer, i.e. malignant tumors, can be treated both curatively and palliatively using surgery, chemotherapy and radiation therapy. Common practise in clinics are adjuvant and neoadjuvant treatments, where patients are treated with combinations of operations, cytostatic infusions, and irradiations and additional antiangiogenic treatments. In general, treatment guidelines try to optimize the therapy based on a maximization of the tumor control probability (TCP) subject to constraints like tumor operability, or in the case of radiation oncology, normal tissue complication probability (NTCP), especially of organs-at-risk exhibiting high radiosensitivity. Thorough understanding of the mechanisms involved in influencing therapy outcome is needed to better predict patient to patient variability in treatment response (potentially leading to individual fractionation schemes as opposed to all-around guidelines). Another incentive for research in basic mechanisms is finding new ways of interference with cellular responses during radiation therapy in order to improve treatment outcome, such as reduced side effects like scarring and loss of organ functionality, reduced metastasizing, or better tumor growth delay or shrinkage.

While the central dogma of radiation biology states that the DNA, the carrier of genomic information, be the prime target of the irradiation, clinicians are faced with hard-to-predict treatment responses, and radiation resistance of poor responsive tumors or recidives.

Increasing amounts of data show that a crucial role in cellular response to ionizing radiation as used in radiation therapy is played by the environment of the cell. In order to contribute to understanding the cellular response to ionizing radiation, a system capable of subdiffractive single molecule detection and tracking of fluorescent labels was established and applied to probe the dynamics of plasma membranes of living cells embedded in a 3D matrix. Plasma membrane interaction with ionizing radiation is an emergent topic of interest since technological advancements in irradiation techniques allow for sharply localized dose deposition in oligofractionated stereotactic body radiotherapy (SBRT). Irradiation induced membrane signaling in the endothelium is recognized as a major pathway to programmed cell death or apoptosis, the ultimate goal against aberrant cancer cells.

In the following, the basic mechanisms and characteristics of ionizing radiation to achieve this goal are briefly summarized, making up the first section of the science background chapter. Characteristics and organization of the plasma membrane are reviewed in the second section. The rationale for cell culture in an *in vitro* 3D matrix is given in the third section. Then, a brief motivation based on the challenges faced introducing the microscopy technique applied is given. The last section covering the scientific background gives an introduction to diffusion theory.

The major topic of the present thesis – the development of an analysis procedure – is presented in the chapter following experimental materials and methods. Evaluations of the analysis procedure based on simulations are shown in the chapter thereafter, followed by an investigation of the membrane dynamics of an osteosarcoma cell line as probed by a fluorescent lipid analogue with cells growing on a flat 2D surface and embedded in a 3D matrix, unirradiated and after treatment with 1 Gy and 25 Gy.

After a discussion of the experimental findings and interpretatory *caveats*, the thesis closes with a short conclusion and an outlook.

2 Science background and Theory

2.1 Ionizing radiation

Radiation is the transport of energy where the transport is not bound to a medium. Ionizing radiation (IR) is a term applicable for any type of radiation that is capable of ionizing a medium traversed. IR is subcategorized into corpuscular radiation with massive carriers of energy and electromagnetic radiation i.e. photons. Photon radiation with energy range from 100 eV up to several MeV is called x-ray radiation although there are smooth transitions from extreme ultraviolet to x-rays and from x-rays to soft gamma radiation. The following section focuses on x-rays as no corpuscular radiation such as protons, neutrons, or ion radiation was used in this thesis.

2.1.1 Generation of x-rays

Typically, x-rays are produced as *bremsstrahlung* from accelerated electrons hitting a target and the subsequent *characteristic x-rays*. To this end, electrons from a heating filament are accelerated by an applied voltage in a x-ray tube or by microwaves in a linear accelerator. When the electrons reach the target, they interact with the electric field of the target material atomic nuclei and emit bremsstrahlung photons due to conservation of transversal momentum. While yield and bremsstrahlung spectrum are dependent on the target's atomic number Z, electron energy not turned into x-rays and also x-ray energy not leaving the target heats the target up. A typical material for x-ray tube anodes is therefore tungsten with high $Z = 74$ and high melting point. Electrons may also transfer energy to anode electrons and ionize the target material. If an electron of an inner shell is released, outer shell electrons fill the "hole" emitting either Auger-electrons or – and predominantly for high Z materials – photons of energy characteristic for the atomic structure therefore called characteristic x-rays.

2.1.2 Interaction with matter

X-rays may ionize atoms or molecules by *photoeffect* or *compton scattering*. The x-rays used in this thesis were produced by electrons accelerated by a voltage of 90 kV and thus no electron-positron pair production was occuring.

At photoeffect, the energy of the incoming photon is absorbed by a bound electron which by the process is released from the atom with a kinetic energy equal to the difference of the photon and the previous binding energy. At compton scattering, the photon is inelastically scattered at an electron, transfering energy to it and again releasing the electron from the atom with a residual kinetic energy equal to the difference of the transfered energy to the binding energy. Considering the kinematics of a scattering event of a photon with energy E_γ with a free electron at rest, one yields a transfered kinetic energy E_{kin} of the electron of

$$E_{\text{kin}} = E_\gamma \frac{a(1-\cos\theta)}{1+a(1-\cos\theta)} \tag{2.1}$$

where $a = \frac{E_\gamma}{m_e c^2}$, and θ is the scattering angle of the photon, m_e is the electron rest mass and c is the vacuum lightspeed. These released electrons deposit their kinetic energy until they stop. In principle, as they are massive, electrons deposit their energy similar to heavy charged particles, i.e. with a pronounced peak of local energy deposition right before they stop. Primary electrons released by the x-rays may in the process of slowing down ionize further atoms, releasing secondary electrons that may release terniary electrons and so forth. Neglecting generation of bremsstrahlung for slow electrons and nuclear recoil, loss of kinetic energy due to interaction with target electrons is described by a modified version of the Bethe-Bloch formula [Bethe, 1930, Bloch, 1933, Bohr, 1913]

$$-\frac{\mathrm{d}E_{\mathrm{kin}}}{\mathrm{d}x} = \frac{2\pi e^4}{m_e c^2 \beta^2} n_e \left[2\ln\frac{m_e c^2 \beta^2}{\langle I \rangle} - \ln[2\gamma^4(\gamma+1)] + \gamma^{-2} - \frac{2\gamma - 1}{\gamma^2}\ln 2 + \frac{1}{8}\left(\frac{\gamma-1}{\gamma}\right)^2 \right] \tag{2.2}$$

in atomic units, where $\beta = v/c$ is the incident electron's velocity v relative to the speed of light c, $\gamma = (1-\beta^2)^{-1/2}$ the Lorentz factor, $n_e = \frac{N_A Z \rho}{A M_u}$ the electron number density of the target, with Avogadro number N_A, the medium atomic and relative mass numbers Z and A, respectively, M_u the medium molar mass constant, the medium density ρ, $\langle I \rangle$ the mean excitation potential, and e the elementary charge (Note that e^2 in atomic units refers to $e^2/4\pi\epsilon_0$ in SI units, where ϵ_0 is the vacuum permittivity). The version [Kamaratos, 1984, see there for a concise account on stopping power theory] of equation 2.2 is derived from quantum mechanical perturbation calculation and includes relativistic terms. Most notably is the factor 0.5 in the argument of the first logarithm in comparison with the Bethe-Bloch equation for heavy charged particles which relates to the change in reduced mass. Notice that in contrast to other projectile particles, electrons are subject to quantum indistinguishability with medium electrons. Even more precise accounts of the collision stopping power include shell corrections, the density effect correction (which accounts for dielectric polarization of the medium), and higher order perturbation terms including the Barkas effect [ICRU, 1993].

Electrons released in ionization events transferring energy to other electrons in collisions may, of course, transfer enough energy for a further ionization. Effectively, (primary) electrons set free from atoms ionize further atoms, thereby potentially creating cascades of secondary electrons.

2.1.3 Dose

In contrast to the *kinetic energy released per unit mass* (KERMA) which is defined as $\frac{\mathrm{d}\bar{\epsilon}_{\mathrm{tr}}}{\mathrm{d}m}$ where $\mathrm{d}\bar{\epsilon}_{\mathrm{tr}}$ is the sum of the initial kinetic energies of all the charged particles liberated by the x-rays in a mass element dm, *absorbed dose* D is defined by the International Commission on Radiation Units and Measurements [ICRU, 1998] as

$$D = \frac{\mathrm{d}\bar{\epsilon}_{abs}}{\mathrm{d}m} \tag{2.3}$$

, where $\mathrm{d}\bar{\epsilon}_{abs}$ is the mean energy imparted to a mass dm. Absorbed dose is a deterministic quantity equivalent in the limit of a small domain to the mean $\bar{z}$ of the stochastic quantity *specific energy imparted* $z = \frac{\epsilon}{m}$ which is the quotient of the sum of the imparted energy in one or more energy deposition events $\epsilon = \sum \epsilon_i$ in a matter of mass m. Importantly, electrons released by ionization within dm may leave dm and deposit not all of their initial kinetic energy locally. On the other hand, electrons released in ionizations elsewhere may traverse or slow down to halt in dm and in doing so deposit energy, contributing to the absorbed dose. For the intricacies of microdosimetry, the interested reader is referred to Rossi and Zaider [1996].

Conventionally, doses in dosimetry, radiation oncology, and radiobiology are reported in dose to water which is done in this thesis as well. Thus, 1 Gy = 1 $\frac{\mathrm{J}}{\mathrm{kg}}$ of dose means 1 Gy of dose to water. Remind that 70 % of the volume of a cell is water.

When irradiating cells, non radiation equilibria with KERMA $\neq D$ have to be kept in mind. As photoionization cross sections are Z-dependent, silicon present in glass coverslips generates excess ionizations and electrons to scatter towards the cells, doubling dose for cells grown on glass coverslips as compared to cells grown on mylar foils [Kegel et al., 2007]. 90 kV tungsten target x-ray spectra filtered by a thin beryllium window and a 2 mm aluminum plate range from 30 keV to 90 keV with characteristic K-series peaks at 59.32, 57.99, 67.15, and 69.13 keV [Birch and Marshall, 1979]. The aluminum plate effecively filters out tungsten L-lines with energies below 12 keV. According to Berger et al. [2005], 30 keV, 60 keV, and 90 keV electrons have ranges in continuous slowing down approximation (CSDA) of 18 μm, 59μm, and 120 μm in water.

2.1.4 Radiation chemistry

Radiobiological damage of absorbed x-ray dose is primarily induced by *reactive oxygen species* (ROS) generated by water radiolysis and not by direct ionization. Dissociation and ionization of water molecules upon irradiation leads to decay products that may dimerize or recombine leading to ROS including radicals such as the hydroxyl radical $HO^{\bullet-}$ or the superoxide $O_2^{\bullet-}$, but also oxidants like hydrogen peroxide H_2O_2 and molecular oxygen O_2 [Spinks and Woods, 1990]. For sparsely ionizing radiation such as the x-rays used in this thesis, the H_2O_2 yield (after 10^{-7} s, i.e. the *primary* yield as opposed to the *initial* yield) is 0.073 μmol/J [Spotheim-Maurizot et al., 2008, chapter 1], for example. Generated ROS but also free, solvated electrons are highly reactive and may oxidize and thereby damage biomolecules including the DNA, proteins, and lipids.

2.2 Functions of the plasma membrane

To begin with, the plasma membrane is an essential part of any living cell insofar the membrane first and foremost separates the inside of the cell from the outside. Inextricably linked with this compartmentalization of the cell into the topologically inner part of the cell and the topologically outer – including, e.g., vesicles and the lumen of the endoplasmatic reticulum – is the selective “permeation” of information and mass through the membrane. A prime example of mass transport across the membrane is the movement of ions as facilitated by ion channels, transporters, and ion pumps providing homeostasis of the cellular milieu, or the osmotic passage of water molcules through the membrane as such or through aquaporins as integral part of cell growth. This section will start with an introduction covering the constituents of the plasma membrane with a focus on the components relevant for this thesis and will then go on with the structuring; then cover both lipid raft mediated transmembrane signal transduction as well as lipid signaling. The last part of this section will briefly introduce basic notions of cell adhesion with relevance to 3D cell culture.

2.2.1 Lipids and Receptors

Generally, cell membranes comprise of an approximately 5–10 nm thick lipid bilayer that incorporates peripheral and integral membrane proteins [Singer and Nicolson, 1972]. Animal, non-neural plasma membranes consist on average of 50% of protein [Alberts et al., 2005]. There is a plethora of different lipids present in biological membranes [Fahy et al., 2009], the main components being glycerophospholipids, sphingolipids, and sterols. At first, we will review the basic properties of these lipids.

2.2.1.1 Membranogeneous Lipids

Lipids are defined “as hydrophobic or amphipathic small molecules that may originate entirely or in part by carbanion-based condensations of thioesters (fatty acyls, glycerolipids, glycerophospholipids, sphingolipids, saccharolipids, and polyketides) and/or by carbocation-based condensations of isoprene units (prenol lipids and sterol lipids)" [Fahy et al., 2009]. *Sphingolipids* can be subclassified into ceramids, sphingomyelins, and glycosphingolipids. In general, sphingolipids [Pruett et al., 2008] are lipids with a sphingoid base such as sphingosin (2-amino-4-octadecene-1,3-diol) amide-linked to an acyl group such as fatty acids and O-linked to a residue group which may be a single hydrogen atom yielding a ceramide, phosphocholine/phosphoethanolamine group yielding a sphingomyelin, or carbohydrates yielding glycosphingolipids.

Glycerophospholipids are defined as "any derivative of glycerophosphoric acid that contains at least one O-acyl, or O-alkyl, or O-(1-alkenyl) group attached to the glycerol residue" [McNaught and Wilkinson, 1997]. Also known as phosphoglycerids, important subclasses are plasmalogens with vinyl ether linkage of, e.g., ethanolamine or choline to the first carbon atom of the glycerol, phosphatidates like phosphatidylethanoamines (PE), -cholines (PC), -serins (PS), -glycerol (PG), and -inositol (PI). Phosphorylated phosphoinositols are called phosphoinositides, including phosphatidylinositol phosphate (PI4P, or informally, PIP), phosphatidylinositol bisphosphate (PIP2) and phosphatidylinositol trisphosphate (PIP3). Glycerophospholipids and phosphosphingolipids are subclasses of the class of phospholipids. However, though being technically incorrect by neglecting phosphosphingolipids, the more general term "phospholipid" is often used synonymous to "glycerophospholipid" and contrasted to or used in conjunction with "sphingolipid".

Typical phospholipid molecules consist of a hydrophilic/polar head and two hydrophobic/non-polar tails. Saturated C-C bonds result in straight tails, whereas unsaturated bonds yield a bending of the tail which affects the geometry and thus the packing of lipids, altering density and mobility of lipids.

Sterols are a subgroup of steroids with a polar hydroxyl group at the 3-position of the A-ring of the otherwise nonpolar tetracyclic structure. Ubiquitous in animal cells is *cholesterol* which by virtue of its rigid and bulky nature modulates phospholipid and sphingolipid motion.

2.2.1.2 Properties of membrane lipids

Phospholipids form bilayers [Singer and Nicolson, 1971] by autoassembly as explained by thermodynamics derived from the Gouy-Chapman theory [Marsh, 2012, Träuble et al., 1976, Tristram-Nagle and Nagle, 2004].

Membrane lipids are synthesized in the endoplasmatic reticulum (ER) and possibly modified in the Golgi apparatus. While the distribution of lipid species on the inner and the outer leaflet of the bilayer is equal in the ER, later on a polarity or transbilayer asymmetry [Bretscher, 1972] arises as phospholipids are "sorted" by flippases (adenosine triphosphate (ATP) dependent, cytofacially directed), floppases (ATP-dependent, exofacially directed), and scramblases (ATP-independent, bidirectional) [Daleke, 2003, Pomorski and Menon, 2006] while spontaneous flipping/flopping of phospholipids is rare (flip/flop half life ranging from several hours to days, dependent on acyl chain length and degree of unsaturation).

In addition to asymmetry, lipid compositions differ from organelle to organelle [van Meer and de Kroon, 2011]. Local membrane composition differences result in variations in membrane thickness, lateral mobility, charge surface density, and curvature. Stimulated, localized lipid metabolism for instance is involved in phagocytosis [Yeung and Grinstein, 2007]. On a higher level of abstraction, changes in physical properties may transfer information: During programmed cell death, or apoptosis, usually cytofacial phospholipids are flipped und thus presented to phagocytes so that dead cells get phagocytosed and constituents get recycled.

2.2.2 Signaling, Lipids, and Rafts

An important task of molecular biology is to identify and decipher signaling cascades on this informational level in order to intervene at pathologies. While foremost attention has been paid by the scientific community to protein interactions on the basis of conformational changes exposing or hiding enzymatic i.e. catalytic centers of enzymes such as kinases and phosphatases, it is in the last decade increasingly becoming clear that lipids also play an important role in signaling, especially at the start of signaling cascades. In general, signal cascades feature different transduction levels with branching (multiple targets), interference (modulation of encymatic activity by other signals), positive and negative feedback loops (downstream self-(de-)activation), and amplification by second messengers like cyclic nucleotides, inositol triphosphate (IP3) or diacylglycerol (DAG) [Berridge and Irvine, 1984]. On a regular basis, signaling cascades start with receptor clustering upon ligand binding or foremost establishing therewith sensitivity to ligands.
Transmembrane protein clustering seems to involve sphingolipid- and cholesterol-rich dynamic microdomains called *lipid rafts* [Simons and Ikonen, 1997, Simons and Toomre, 2000, Mugler et al., 2012]. Controversially disputed [Munro, 2003], increasing evidence amounts [Lingwood and Simons, 2010].

Briefly, physical differences in lipids such as chain length, chain geometry, and head group cause different membrane components not to be homogeneously distributed on the cell surface but rather differentially aggregated in domains. Specifically, sphingolipids and cholesterol aggregate in microdomains termed *lipid rafts* that function as platforms for membrane protein clustering, depending, e.g., on transmembrane domain length and exposed charges interacting with the lipid's head moieties. Increased local surface density of specific proteins not only reduces the average monomer to monomer distance enhancing the probability of direct interaction but more importantly makes the linkage of monomers to oligomers and large cluster formation by means of binding of adaptor proteins and subsequent stabilization by scaffold proteins possible in the first place.

A prime example is the formation and maturation of focal adhesions, sites where thousands of integrin transmembrane adhesion molecules, receptors like receptor-tyrosine-kinases (RTKs) cluster, establishing rigid links between extracelluar environment and the actin cytoskeleton.
While it is known that sphingolipids but not glycerophospholipids display both acceptors and donors of hydrogen bonds, characterizations based on artificial membranes including separation into a liquid-disordered and a liquid-ordered phase has been disadvised to transfer to living cells [Lingwood and Simons, 2010]. It should also be noted that lipid rafts have been associated with membranes resistant to non-ionic detergents (DRM, detergent resistant membrane) [Brown and London, 2000].
Lipid rafts in the strict sense are distiguished from caveolae which are also rich in cholesterol, sphingolipids and proteins. Caveolae are pits formed and maintained by caveolin taking part in clathrin-independent caveolar endocytosis and can serve as mechanosensors [Parton and Simons, 2007].

2.2.2.1 Lipid signaling

Distinct from raft mediated signaling is lipid signaling, where lipids take part in reactions rather than orchestrate other messengers' activations. Since diacylglycerol (DAG) and inositol-1,4,5-triphosphophate have been demonstrated to specifically regulate second messengers of the protein kinase C (PKC) family and the release of calcium, respectively, the idea of lipid signaling is established [Berridge and Irvine, 1984, Nishizuka, 1984, 1992, 1995, Hannun and Obeid, 2008]. While in general PKC signaling is key, ubiquitous [Newton, 2010] and of high interest in molecular oncology, this introduction into lipid signaling will focus on signaling of ceramide, a sphingolipid metabolite. The sphingolipid metabolism network has a unique entry point, the *de novo* synthesis by serine palmitoyl transferase (SPT). 3-ketodihydrosphingosine is then reduced to dihydrosphingosine, acetylated by a dihydro-ceramide synthase; ceramide is subsequentially formed by desaturation of dihydro-ceramide [Hannun and Obeid, 2008].

2.2.2.2 Ceramide pathways

Ceramide is the hub of the sphingolipid metabolism network. Actually, ceramide is a family of >50 molecular species. There are six individual ceramide synthases known which favor different fatty acyl-Coenzyme A substrates leading to generation of distinct ceramides that may localize in distinct subcellular compartments. Also, ceramide may be generated by removal of the phosphorylcholine head group of sphingomyelin, catalysed by a sphingomyelinase (SMase). Five different SMases are known to be located at different subcellular compartments and on different sides of the membrane, showing distinct optimal pH values. In particular, activation of acid SMase (ASMase) translocated from lysosomes to the outer leaflet of the plasma membrane as a response to cellular stress mediates stress-induced apoptosis after exposure to stressors including but not limited to Fas/CD95, ischemia, TNF-α, chemotherapy, and ionizing radiation [Smith and Schuchman, 2008]. Ceramide is known to activate Ceramide-acivated protein phosphatase (CAPP), which interacts with the product of the Retinoblastoma gene (Rb) inducing G0/G1 cell cycle arrest. On another pathway, CAPP activates proteases responsible for cleavage of poly-(adenosine diphosphate ribose) polymerase (PARP) [Hannun, 1996], thus inducing pro-apoptotic signals [Obeid et al., 1993, Verheij et al., 1996]. Also, ceramide signals apoptosis via a pathway involving RAS, kinase suppressor of RAS (KRS), c-RAF-1, and MEK-1 leading to Akt/protein kinase B inactivation and BAD-triggered apoptosis [Kolesnick and Fuks, 2003].

2.2.2.3 Ionizing radiation induced plasma membrane signaling

Although ionizing radiation can damage lipids directly, a larger contribution to lipid damage is indicated to originate from water radiolysis products [Reisz et al., 2014, see there for a review of lipid radiation chemistry]. While in general, oxidative stress induced by ionizing irradiation triggers ASMase translocation, activation, and ceramide signaling [Haimovitz-Friedman et al., 1994, Santana et al., 1996, Corre et al., 2010], there are new radiation therapy modalities emerging that make use of membrane-mediated apoptotic signaling of the tumor microvasculature endothelium by means of fractionation regimes where membrane signaling becomes a major pathway. In contrast to conventional irradiation schemes or regular hypofractionation [Marcu, 2010], oligofractionation or single high dose (18–24 Gy) treatments [Garcia-Barros et al., 2003, Yamada et al., 2008] induce ceramide-mediated damage to the microvasculature and epithelial stem cells in the tumor stroma [Hellevik and Martinez-Zubiaurre, 2014]. It is believed that ASMase is regulated by redox mechanisms and activated by reactive oxygen species (ROS) generated in water radiolysis [Corre et al., 2013]. This additional apoptotic signaling seems to be important as endothelial and endothelial projenitor cells in the intratumor microenvironment are supposedly exposed to antiapoptotic signaling while tumor stroma fibroblasts are known to enter senescence after lethal radiation damage, yet secreting inflammatory cytokines such as the vascular endothelial growth factor (VEGF) that lead to angiogenesis. Consequently, treatments <10 Gy/fraction of human xenograft of rodent tumors are reported to show mild while >10 Gy/fraction treatments cause severe vasculature damages [Park et al., 2012].

2.2.3 Adhesion

While multicellular lifeforms are hardly imaginable without the phenomenon of cell adhesion, i.e. the binding of cells to substrata or other cells, adhesion is of essential importance on cell level beyond structure maintenance. Carried out by transmembrane cell adhesion molecules which connect extracellular structures with intracellular structures, cell adesion propagates mechanical stress on tissue level from cell to cell by elastic deformation of intermediary filaments [Alberts et al., 2005]. In the case of the actin cytoskeleton, the intracellular structure responsible for cellular integrity and morphology, transmembrane binding to substrata is essential for attachment, mechanosensing, durotaxis, and most importantly motility and migration. In addition to theses “mechanical” traits, cell adhesion transduces signals outside-in but is also susceptible to inside-out signals [Hynes, 1992]. Basically, mere presence of a certain extracellular structure may be a signal in its own right. On a regular basis, extracellular structures provide support, and cell adhesion causes antiapoptotic signaling, proliferation, and differentiation [Meredith et al., 1993].

Unsurprisingly, there are several classes of cell adhesion molecules; the major classes being cadherins, selectins, the immunoglobin (Ig) superfamily, and integrins. While cell-cell adhesion – including immune cell/inflammatory signaling – is predominantly accredited to the former three classes, the latter play a key role in adhesion to the extracellular matrix (ECM). In the following subsections, we will focus on integrin mediated cell adhesion to the ECM.

2.2.3.1 ECM and integrins

The extracellular space is filled with secreted molecules that provide a supporting scaffold for cells called the extracellular matrix (ECM) [Hynes and Naba, 2012]. Naturally, different cell types in different contexts behave differently and therefore ECM varies dynamically in composition, ligand exposure, density, anisotropy, elasticity tensor (including Young’s modulus, Poisson number, shear modulus), permeability, porosity, hydrophilicity/-phobicity from tissue to tissue through aging plus developemental, wound- or tumor-related matrix remodeling.

Main components are proteoglycans and fibrous proteins [Frantz et al., 2010]. A central role is taken by the arginine-glycine-aspartic acid (RGD) cell adhesion sequence present in fibronectin, vitronectin, fibrinogen, von Willebrand factor, thrombospondin, laminin, entactin, tenascin, osteopontin, bone sialoprotein, and under some conditions collagens [Ruoslahti, 1996].

Correspondingly, of the 24 known glycoprotein heterodimer integrins, 8 have been identified as recognizing the RDG sequence and another 4 have been identified as collagen receptors [Hynes, 2002]. Integrins in general consist of an alpha and a beta subunit that are non-covalently bound. Both subunits have a single transmembrane domain, large extracellular domains with binding sites, and up to exceptions small cytoplasmic domains. Beta subunits require divalent cations such as extracellular Ca^{2+} for proper functionality. While integrins do not possess catalytic domains, they provide cytoplasmic binding domains for other proteins that may expose catalytic domains after conformational changes upon binding. In fact, binding to specific cytoplasmic domains is mandatory for foremost exposure of the extracellular binding sites of the integrins. This instance of inside-out signaling carried out e.g. by talin has been termed “priming” to distiguish it from integrin “activation”, the conformational changes upon extracellular ligand binding transduced to the cytoplasmic domains enabling intracellular binding [Legate et al., 2006, Shattil et al., 2010].

2.2.3.2 Focal adhesion formation and maturation

Most eucaryotic cell adhere to substrata by means of cell matrix adhesion complexes (CMACs) principally composed of integrins. Upon activation by ligand binding to integrin, a sucessively large variety of proteins is recruited to the adhesion site, categorized into (i) integrin binding proteins such as mentioned talin, (ii) adaptor and/or scaffold proteins lacking enzymatic activity like vinculin, paxilin, α-actinin and (iii) enzymes [Berrier and Yamada, 2007]. Recruited proteins contribute to integrin clustering, binding to and aggregating receptors such as RTKs, providing kinase activity for adhesion-related signal transduction and linkage to the actin cytoskeleton. Dependent on size, actin-linkage and maturation of the CMAC, Lock et al. [2008] differentiates between

- focal points or nascent adhesions, small, newly formed CMACS linked to the actin meshwork
- focal complexes, mid-size CMACs linked to cortical actin or actin meshwork in lamellopodia
- focal adhesions, large CMACs elongated along the axis of force application by actin stress fibers
- fibrillar adhesions
- podosomes

There is a large body of research on actin linkage to adhesion sites [Kanchanawong et al., 2010], as well as actin cytoskeleton reorganization including induction of actin polymerization, depolymerization, crosslinking, and implications on motility and chemotaxis [Pellegrin and Mellor, 2007, Ridley and Hall, 1992]. While restricting ourselves to core ideas, we will have a first look on focal adhesion signaling.

2.2.3.3 Focal adhesion signaling

Signaling involving focal adhesions includes growth, survival, proliferation, differentiation, endothelial-mesenchymal transition, tissue morphogenesis, angiogenesis, and invasion [Giancotti, 1999, Legate et al., 2006]. Obviously, integrin mediated signaling plays a major role in tumorigenesis, cancer progression, metastasis, and responses to anti-cancer treatments [Rathinam and Alahari, 2010]. In focal adhesions, integrins associate to and modulate activity of various growth factor receptors. Activated FAK (focal adhesion kinase) forms stable complexes with Src that increase FAK activity and activate Src, which in turn activate for example the JNK (c-Jun N-terminal kinase) pathway, Rho GTPases (guanosine triphosphatases), and phosphatidylinositol-3 kinase (PI3K) which activates Akt/protein kinase B [Kim et al., 2011, Heß, 2006] that is a pro-survival signal. For an overview of the integrin adhesome the reader is referred to Zamir and Geiger [2001], Zaidel-Bar et al. [2007], Zaidel-Bar [2009], Zaidel-Bar and Geiger [2010], Geiger and Zaidel-Bar [2012].

2.3 Rationale for 3D cell culture

Fundamental research is by method reductionist, trying to gain insight in details and idealized systems. On the opposite, translational biomedical science is interested only in applicable research of clinical relevance in the real world. As science makes progress it outgrows its understanding of simplistic models and continues to use more realistic, complex models of reality. In the last decade, there is growing discomfort about the investigation of biomolecular mechanisms in cells grown on a surface such as petri dishes, glass slides or well bottoms. While without doubt animal models including nude mice and tumor xenograft models provide unmatched insight into investigated processes, especially the efficacy of treatments before stage I trials on humans are carried out, large scale screening of substances, investigations concerning new mechanisms, targets, and treatment approaches call for cheap and easy-to-handle model organisms. Along with tumor spheroids, 3D cell culture is seen as a possibility to bridge the gap between fundamental research and application by mimicking physiological growth conditions more realistically than 2D cell culturing [Yamada and Cukierman, 2007, Kimlin et al., 2013]. In particular, cells grown in 3D, for example Matrigel™, gelatin methacrylat (GelMA) [Nichol et al., 2010, Kaemmerer et al., 2014], or collagen I hydrogels [Szot et al., 2011] show different gene expression patterns, activity of expressed proteins, cytoskeleton organization, morphology, proliferation rate and resistance to anticancer treatments including chemotherapeutics and ionizing radiation in comparison to 2D-cultured cells. While this is expected due to the importance of adhesion mediated signaling pointed out above, the cellular reaction is indeed more physiological [Pampaloni et al., 2007].
In the following, the role of plasma membrane organization is investigated in order to elucidate its role in 3D cell culture conveyed resistance to ionizing radiation.

2.3.1 Cell adhesion mediated radioresistance

The idea behind radiation therapy (RT) is to kill the cancer cells utilizing ionizing radiation while sparing the healthy normal tissue. This is achieved be precise dose deposition and by exploitation of the fact that most cancer cells have an impaired DNA repair efficacy which is acquired in the developemental steps towards malignancy, e.g. a mutation in the p53 tumor suppressor gene [Levine et al., 1991]. However, there are several cancer types that are radioresistant including chordoma, chondrosarcoma, head-and-neck cancer and brain tumors that exhibit poor tumor control probability (TCP) at reasonable normal tissue complication probability (NTCP). In addition, especially high-grade tumors may acquire radiation resistance during the course of a RT treatment, giving rise to poor prognosis. This acquisition of radioresistance may be due to a radioresistant tumor subpopulation [Baumann et al., 2008] or a radioadaptive response [Ahmed and Li, 2008].

2.3.1.1 Cell adhesion mediated anti-radiogenic apoptosis and cell cycle arrest signals

Cell adhesion has been attributed to contribute to radioresistance [Fuks et al., 1992]. Anchorage dependent pro-survival signaling via the FAK/Src complex suppresses p53 by PI3K activation [Mitra and Schlaepfer, 2006, Kasahara et al., 2002], p53 being famously known as the “guardian of the genome“ that induces apoptosis when functional in increased concentrations [Sun, 2006]. PI3K is also activated by the epidermal growth factor receptor (EGFR), one of the RTKs that cluster in adhesion sites [Cordes et al., 2012]. EGFR in particular binds to PINCH1 (particularly interesting new cystein-histidine rich protein 1) that itself binds to ILK (integrin linked kinase). c-Jun amino-terminal kinase 1 (JNK 1), a known stress-induced kinase [Liu and Lin, 2005], is suppressed by integrin β_1 [Goel et al., 2013]. And interestingly, adhesion to ECM molecules increases the percentage of cells accumulating in G1 and G2 cell cycle phases upon irradiation. This is presumably via ILK mediated glycogen synthase kinase 3-β (GSK-3β) inhibition that blocks cyclin D1 proteolysis [Hannigan et al., 2005, Cordes and van Beuningen, 2003, Sandfort et al., 2007], providing a longer period of time for the cell to repair before DNA replication and cell division, respectively.

2.3.1.2 Cell morphology mediated chromatin organization

Morphology of cells is different in tissue or 3D cell culture as compared to 2D cell culture. 2D grown adherent cells exhibit typical actin stress fibers that are linked to focal adhesions as pointed out in the section on focal adhesion maturation. However, cells grown under more physiological conditions do not feature actin stress fibers. While mechanosensing at focal adhesions is well established [Geiger et al., 2009], mechanotransduction by stress propagation along actin fibers is a rather new idea. Although constantly remodeling at the molecular level – *panta rhei* –, the overall cytoskeletal tensegrity is a hardwired, interconnected structure that can transduce forces on cellular-level long distances. Filamentous actin is bundeled by α-actinin and linked by actin crosslinking factor 7 (ACF7) and plectin 1 to microtubules and intermediate filaments, respectively. Plectin 1 also connects intermediate filaments and microtubules. Most importantly, cytoskeletal actin filaments are connecting adhesion sites at the plasma membrane with the inner nuclear membrane protein SUN1 via nesprin 1 and 2, and nesprin 3 connects plectin 1 to SUN1 and SUN2 [Wang et al., 2009]. The SUN proteins are themselves connected to the lamins of the nuclear lamina.
Several mechanisms of tension-to-gene regulation are proposed [Wang et al., 2009]:

1. chromatin recombination: nuclear scaffold deformations and strain on chromatin might alter DNA accessibility and selfassembly of regulatory complexes like transcription factors or complexes involved in chromatin modification

2. nuclear matrix distortions: forces exerted to chromatin regions tethered to the internal nuclear scaffold might modulate activity of associated transcription factors
3. nuclear transport: forces transduced to the nuclear membrane might influence nuclear pore complex kinetics affecting nuclear transport (cytosole to nucleus) while possibly also changing mRNA transport from the nucleus to the cytosole
4. DNA melting: stretching of certain tethered DNA regions might lead to opening of the DNA double helix at adenine/thymine-rich sites and induce binding of transcriptional regulators.

As the cell shape is a phenomenon of cytoskeleton organization, implications for morphology mediated changes in radiation response are at hand. Indeed, cells grown *in vivo* (xenograft) or in 3D *in vitro* environments, showed the same shifted distribution of euchromatin (EC) to heterochromatin (HC) associated residual (post 24 h) DNA double strand breaks as indicated by γH2AX/53BP1 (histone 2AX phosphorylated on serine 139/p53 binding protein 1) foci (EC:HC 1:1) in relation to 2D environment (2:1) [Storch et al., 2010, Eke and Cordes, 2011, Storch and Cordes, 2012].

2.3.2 Adhesion sites in 3D: archipelago

The different morphology of cells in 3D environments in comparison to 2D cell culture is not only characterized by the different cytoskeletal organization, but also in a different organization of adhesion complexes. While mechanotransduction relies on pre-stress on the cytoskeleton tensegrity applied by myosin II, absence of thick stress fibers leads to a reduction of force applied to the adhesion site which modifies adhesion complex formation. In fact, controversy arose whether cells in 3D environments feature focal adhesions at all [Harunaga and Yamada, 2011]. In a response to Kubow and Horwitz [2011], Fraley et al. [2011] point out that focal adhesions become smaller as the distance to hard surfaces (i.e. the glass/plastic bottom) surrounding the 3D cell culture hydrogel increases until non-detectability using a confocal laser scanning microscope. There is, however, consensus that discrete adhesion sites exist [Harunaga and Yamada, 2011] with a distinct maturation lifecycle [Cukierman et al., 2002]. Not only does 3D motility differ remarkably from 2D in that morphology features pseudopodia instead of filopodia and lamellopodia [Fraley et al., 2010], but also adhesion protein phosphorylation states are altered [Cukierman et al., 2001] and adhesion complex composition can vary with ECM elasticity [Harunaga and Yamada, 2011].

While hierarchical composition and organization of 2D focal adhesions is investigated, see section 2.2.3.2 on focal adhesion formation and especially Kanchanawong et al. [2010], there are also investigations on the lateral organization. In particular, the dynamic cycling between slow free diffusion and immobilization of integrins β_1 and β_3 inside of focal adhesions and fast free diffusion outside of focal adhesions strongly support an archipelago model of focal adhesion organization [Shibata et al., 2012, Ivaska, 2012, Rossier et al., 2012].

In the archelago model of focal adhesions, (almost) free lateral diffusion in the fluid membrane of membrane proteins like Rac-1 [Shibata et al., 2013] takes place inside of focal adhesions, facilitating rapid formation, turnover, and disintegration poorly explained by the theories seeing focal adhesions as rigid assembly or as aggregation of rigid islands (venetian channel model). These findings were only possible through single particle tracking methods that inherently overcome the restrictions of ensemble methods. However, to date, investigations of lateral adhesion complex architecture have been limited to 2D systems. We think that 3D adhesions also are nanoscale archipelago like structures, probably even more dynamic due to smaller size.

2.3.3 Hypothesis

Independent of the exact mechanism of cell adesion mediated radiation resistance – i.e. no matter whether the crucial interaction is related to signaling (section 2.3.1.1) or to mechanical cytoskeleton-chromatin tension (section 2.3.1.2), or a mixture of both – this transfer of information from the cellular exterior to the cellular interior has to cross the plasma membrane. This transfer of information is realized by some carrier of information. Both cytoskeletal and adhesion site organization as well as adhesion site distribution are different in presence of a 3D ECM compared to 2D cell culture, affecting the plasma membrane organization. The hypothesis of this thesis is that the motion within the plasma membrane on the molecular level reflects the organization of the membrane and thus shows the effects of different cell culture conditions. Of further interest is the possible radiation response of the membrane organization as an instance of inside-out communication as opposed to the outside-in communication of the cell adhesion.

In order to investigate these phenomena, first of all appropriate tools had to be developed. Single molecule microscopy has been improved to cope with challenges faced in 3D cell culture conditions (see section 4); devoid of ensemble averaging artifacts, first measurements of the diffusion of a fluorescent lipid analogue (see section 3.5) are presented in section 5.2. Probing the impact on lipid-level membrane organization, these investigations build the foundations for future research on adhesion molecule dynamics in 3D, hopefully elucidating phenomena like ECM-mediated radiation resistance, possibly by changes in adhesion site archipelago architecture. The following section will introduce the technique of single molecule microscopy, the section thereafter will broach the topic of diffusion in a membrane.

2.4 Single molecule microscopy

2.4.1 Principle and image formation

Single molecule microscopy is based on the imaging of highly diluted fluorescent molecules [Schmidt et al., 1996]. In essence, fluorophores, i.e. fluorescent dye or protein molecules, are widefield imaged through a microscope and individual diffraction limited images of molecules are localized. The precision of the localizations primarily depend on the detected number of photons. To this end, fluorophores have to be separate enough to allow localization. Single molecule microscopy gained popularity with the advent of localization microscopy, the idea to form „super-resolution“ images by combining subdiffractive localization data. Slightly different approaches are photoactivation localization microscopy (PALM [Betzig et al., 2006]), fluorescence photoactivation localization microscopy (fPALM [Hess et al., 2006]), stochastic optical reconstaction microscopy (STORM [Rust et al., 2006]), and direct stochastic optical reconstaction microscopy (dSTORM [Heilemann et al., 2008]). Usually, photoactivatable fluorophores are used where low intensity ultraviolet light stochastically brings a small subpopulation from a dark state to a fluorescing one. Most applications fix 2D grown cells [van de Linde et al., 2011] and image fluorescently labeled antibodies as this methodology provides reasonable imaging conditions in terms of signal to noise ratio. Unfortunately, fixation does not allow for investigation of dynamic processes and in general introduces artifacts by the finite time for complete fixation. Consequently, where processes sensitive to realism with regard to physiology are studied, imaging of live cells is preferred. Localization microscopy is primarily used for imaging subcellular structures and molecular aggregates such as complexes or clusters – however, *single particle tracking* techniques can be applied if excitation light intensity is chosen so that fluorophores do not undergo photobleaching (long-lived dark state) until several frames were acquired. Note that this practice is in contrast to localization microscopy imaging, where excitation light intensity is rather tuned to yield as many fluorescence photons per frame and fluorophore as possible in order to achieve maximum localization accuracy.

Sensitive measurements should also take into account that fluorophore-fluorophore interaction in crowded systems might distort kinetic properties, both by molecular attraction and by posing as mutual obstacles.

2.4.2 Fluorescence detection

Fluorescence is an instance of photoluminescence where a material emits light after having been excited optically. More specifically, bound electrons are raised from ground state to an excited state upon excitation light photon absorption. In molecules, the excited state undergoes non-radiative decays, dissipating energy in vibro-rotational molecular motion until the electron returns to the ground state in a radiative decay by spontanous emission of a photon. Typical fluorescence lifetimes are in the order of ten nanoseconds due to the fact that the final radiative decay is dipole-allowed, meaning that no so-called intersystem crossing happens where the electron spin is flipped into a long-lived triplet state whose transition to the ground state is dipole-forbidden. Fluorophores used in life sciences feature extended π-electron systems that allow excitation and emission in the visible range of wavelengths, also leading to continuous excitation and emission spectra.

In general, emission anisotropy due to electric dipole orientation is neglected because of fluorophore rotation during integration time. For high numerical aperture ($>$1.2) objectives, fluorescence anisotropy limits the positional accuracy to 10 nm [Enderlein et al., 2006, Wöll et al., 2013] – well below the accuracies obtained in tracking experiments with limited photon buget per fluorophore per frame. Thus, fluorophores are regarded as isotropic point emitters. Of the fluorescence emitted by a point emitter in the focus, a fraction η is collected by the microscope objective, where η can be calculated using geometrical optics, yielding

$$\eta = \frac{\int_0^{2\pi}\int_0^{\arcsin\frac{\mathrm{NA}}{n}} \sin\theta \mathrm{d}\theta \mathrm{d}\phi}{4\pi} = \frac{1}{2}\left(1 - \cos\arcsin\frac{\mathrm{NA}}{n}\right) \tag{2.4}$$

with NA being the numerical aperture and n the refractive index of the immersion. For the used 100× NA1.49 objective with a refractive index of the immersion oil $n = 1.51$, η amounts to 42%. Minor corrections can be applied for point emitters that reside in the focal plane but not on the optical axis, but are small for emitters in the field of view. Modern microscopes use infinity-corrected optical systems so rays from point sources in the focal plane are parallel behind the objective. In this “infinity space” of parallel rays, filters are placed that reflect excitation light including reflected and backscattered light but pass the fluorescence with a larger wavelength than the excitation light corresponding to the energy dissipation in the radiationless vibro-rotational decays. Filtered fluorescence is then focused again by a tube lense forming the image which is either directly projected on the sensor or via a pair of relay lenses that provide an extra “infinity space”.

The sensor used is an electron multiplying charge coupled device (EMCCD). Alternative detector technologies are discussed in Michalet et al. [2007], where the authors acknowledge a preference for EMCCD technology in the single molecule microscopy community. Briefly, incident photons generate photoelectrons by internal photoeffect; photoelectrons are separated from the electron hole by a voltage and accumulated in a potential well for each pixel. These charges from the active region are shifted to a second, covered region of the sensor chip where pixel row by pixel row is read out into a register. Peculiar for EMCCDs, a gain register is following, where the signal is amplified by collision ionization using a distributed application of voltage. In the end, the signal is amplified once more and stored in a file after it is turned into digital data by a digital analog converter.

In the greater picture, the imaging device including microscope and sensor is well described as a so-called *linear time-invariant* (LTI) *system*. LTI systems feature general, well known characteristics: for field of view inputs i_1 and i_2 generating outputs $f(i_1) = o_1$ and $f(i_2) = o_2$, respectively, and real numbers λ and μ, the following equation holds valid:

$$f(\lambda i_1 + \mu i_2) = \lambda o_1 + \mu o_2 \tag{2.5}$$

Let input $i = i(x, y)$ be the field of view input as a function of the spatial coordinates and $\delta(x, y) = \delta(x)\delta(y)$ the 2D Dirac delta functional defined by $\int_{-\infty}^{\infty} f(x)\delta(x)\mathrm{d}x = f(0)$ for any function f on the real numbers. Then obviously: $i(x,y) = \int i(\hat{x},\hat{y})\delta(x-\hat{x},y-\hat{y})\mathrm{d}\hat{x}\mathrm{d}\hat{y}$. Note that the integration is over the field of view. It follows directly that $f(i(x,y)) = \int i(\hat{x},\hat{y}) f(\delta(x-\hat{x},y-\hat{y}))\mathrm{d}\hat{x}\mathrm{d}\hat{y}$. Therefore, the output of any input is known if $f(\delta(x,y))$ is known, which we from here on call the *point spread function* PSF. Essentially: $o(x,y) = i(x,y) * PSF(x,y)$, where $*$ means convolution. On a note it should be said that this is an idealization, as pixelation, numerical discretization, out-of-focus scattering and fluorescence cause deviations from perfect LTI theory.

The PSF of a isotropic point emitter in the focal plane can be calculated in Fraunhofer approximation from Fourier optics as the focal plane is in the far field. Derivations can be found in Saleh and Teich [2008], Hecht [2001] and are based on diffraction after round apertures; here the result is presented:

$$\mathrm{PSF}(r) = N\left(\frac{J_1(2\pi \mathrm{NA} r/\lambda M)}{\pi r \mathrm{NA}/\lambda M}\right)^2 \tag{2.6}$$

where $r = \sqrt{x^2+y^2}$, M, λ are the radial coordinate in the image plane, magnification, and wavelength, respectively. J_1 is the Bessel function of the first kind of order one. This diffraction pattern is called the Airy disk. The first root is located at $2\pi \mathrm{NA}\hat{r} = 3.8317...$, where $\hat{r} = rM$ is the radial coordinate in the object plane, which can be rearranged to the definition of the Airy disk radius, the distance from the central maximum to the first minimum:

$$r_{\mathrm{Airy}} = 0.61\frac{\lambda}{\mathrm{NA}} \tag{2.7}$$

A somewhat arbitrary, yet ubiquitous definition of resolution was proposed by Lord Rayleigh (1842–1919) and is that two point-like objects can be resolved if the distance between their Airy disks is at least so that the central maximum of the one object lies at the first intensity minimum of the other object's Airy disk. In the field of localization microscopy, the Airy disk is commonly approximated by a 2D Gaussian distribution:

$$I(x,y) = N\frac{1}{2\pi\sigma_x\sigma_y}\exp\left(-\frac{(x-x_0)^2}{2\sigma_x^2} - \frac{(y-y_0)^2}{2\sigma_y^2}\right) \tag{2.8}$$

with expected integral photon number per frame $N = \int I(x,y)\,\mathrm{d}x\mathrm{d}y$ and emitter position at x_0, y_0. In fact, the Gaussian approximation is even better for a freely rotating dipole emitter [Stallinga and Rieger, 2010]. The photons arriving at the detector can be interpreted as random samples of the distribution $I(x,y)/N$, allowing estimation of the true position. Different estimation approaches will be presented in a later section.
Let

$$\mu_k = \int_K I(x,y)\,\mathrm{d}x\mathrm{d}y \tag{2.9}$$

be the integral of $I(x,y)$ over a pixel K. Then μ_k is the expectation value on the number of fluorescence photons incident on pixel K in the integration time T, where

$$I(x,y) = \int_T \hat{I}(x,y,t)\,\mathrm{d}t \tag{2.10}$$

is the fluence, i.e. the flux at position x, y on timepoint t, $\hat{I}(x,y,t)$ integrated over the time interval T. In general, T will be constant during a measurement. Be aware that up to the factor T, fluence is equivalent to the average flux during the frame acquisition while time-average flux is equivalent to time-average intensity up to a constant factor of the average photon energy. In the style of astronomical photometry, flux is used in the following to denote the brightness of a fluorescent particle, tacitly averaged over single frame acquisition time.

To be precise, single fluorophores are single photon sources and subject to photon antibunching and subpoissonian photon statistics. However, excitation light intensities and detector integration times render fluorophore “dead time” negligible. Photon incidence over the course of the integration time can be seen as a stochastic process. Given there arrive on average g photons per unit interval, Δt is a *sufficienty small* time intervall, and granted the following assumptions valid:

1. rarity: there is maximally one event (speak: photon) in the interval $[t, t + \Delta t]$
2. the probability to have an event in the interval is proportial to the length of Δt. For g =constant it is thus independent of t
3. ignorance of past: the occurrence of a event in the interval Δt is not influenced by previous events

– with the acknowledgement that events/photons are discrete, these *Poissonian assumptions* yield the conclusion that the number n of incident photons on some area in an interval T is a random number of the Poisson distribution with expectation value μ

$$P_\mu(n) = \frac{\mu^n}{n!} \exp(-\mu) \tag{2.11}$$

which is sometimes called “the law of small numbers” or “the law of rare events”. In particular, both the photon numbers of each single pixel are Poisson distributed, but also the integral number of detected photons. However, fluorophores in an excited state may undergo intersystem crossing (IC) where the electron makes a spin flip so that the electronic state is a triplet one rather than a singlet one. Because the lowest triplet state is dipole forbidden to decay into the singlet ground state due to angular momentum conservation, triplet states are long lived. Even worse, triplet states are elevatedly reactive, probable to undergo reversible as well as irreversible reactions – processes colloquially known as blinking and photobleaching, respectively. And although it seems fair to say that pH levels vary neglegibly across the cytosole, surface charge density variations may be of relevance for pH level dependent fluorescence quantum yields of membrane anchored fluorophores. So, in principle, fluorescence is rather a *compound Poisson process* with a variable expected emission $g(t)$. Fortunately, triplet state lifetimes are short compared to integration times (microseconds) – however oxygenation-based dark state lifetimes are much longer (comparable to the integration time [van de Linde et al., 2011]), and correspond to the bespoken blinking. Therefore it is justified to assume a mean emission during integration with $\overline{g(t)}T = \mu$.

While electron multiplication in EMCCD cameras renders readout noise neglegible, it introduces multiplicative “excess noise” such that Poisson distribution’s property of the equality of the mean and the variance no longer holds valid. Rather, the variance is increased by a factor of

$$F^2 = 2(\tilde{G} - 1)\tilde{G}^{\frac{\tilde{N}+1}{\tilde{N}}} + \frac{1}{\tilde{G}} \tag{2.12}$$

where $\tilde{G}$ is the electron multiplying gain and $\tilde{N}$ is the number of electron multiplication registers [Robbins et al., 2003]. As one can see, F^2 tends to 2 for large $\tilde{G}$ and $\tilde{N}$. Investigations in the excess noise distribution are rare and statistical analysis and modelling are in the beginning, for instance Hirsch et al. [2013]. This is primarily because of two reasons: (i) often, non-Poissonity is neglected in the course of calibration where the gain is determined from the variance to mean relationship of camera counts (leading to photon number underestimation) and (ii) the finding of Mortensen et al. [2010], that excess noise merely translates into an increase in the accuracy (variance) of estimated parameters by a factor of 2 in comparison with analysis based on photon statistics. In this thesis, simulations in section 5.1 are done using photon statistics and camera count to photon conversion was done as described by the camera manufacturer (i.e. not using variance vs. mean plots).

2.4.3 Background signals

Cells do emit fluorescence in the absence of exogeneous fluorophores, a phenomenon called autofluorescence. Autofluorescence is mainly due to nicotinamide adenine dinucleotide (NADH), riboflavin and flavin coenzymes [Aubin, 1979, Benson et al., 1979]. In addition to the scattering of light in bulk collagen, collagen also exhibits fluorophores making things even worse in 3D [Monici, 2005]. Because autofluorescence in general has broad spectral distribution, filtering is mandatory in single molecule microscopy. Small, freely in three dimensions fast moving dim fluorophores are responsible for continuous background fluorescence on the 5 μm lengthscale; different cell organelles exhibit different autofluorescence, of special note are vesicles, endosomes, and lysosomes of dimensions similar to the diffraction limit.

2.4.4 HILO and TIRF illumination

More than other imaging technologies, localization microscopy is dependend on automation, since the large amounts of data have to be processed in a unique fashion for sharp super resolution images or accurate diffusion constant determinations, not handleable efficiently for human beings. Generally, automated image procession tends to yield better results if provided with image data of higher contrast $\frac{I_{\max}-I_{\min}}{I_{\max}+I_{\min}}$. Besides appropriate filtering, camera technology and fluorophore improvements (quantum yield, photobleaching resistance, pH (in)dependence, ...), a simple means to improve contrast is to reduce the illuminated volume.
Frequently applied is the *highly inclined laminated optical sheet* (HILO) illumination scheme [Tokunaga et al., 2008], where excitation laser light is focused off the optical axis into the back focal plane of the objective, exiting the objective on the sample side as an inclined parallel beam. In contrast to epifluorescence illumination scheme, not the whole volume along the optical axis is illuminated and thus excited to fluoresce, but only in the section of the sample illuminated by the inclined beam whose thickness is variable with the inclination angle. Being an intermediate illumination scheme between *total internal reflection fluorescence* (TIRF) microscopy [Axelrod, 1981] and epifluorescence microscopy, HILO combines small excitation volumes with the ability to image relatively deep in the sample (essentially limited by the objective working distance, $<100\ \mu$m) which is crucial for imaging of cells in 3D environments. Regularly, HILO illumination provides the necessary contrast to recognize image features in the first place.
For cells grown in 2D environments, TIRF is providing an even better contrast. In TIRF illumination, the excitation light is focused so far off the optical axis into the back focal plane of the objective, that an incident angle θ greater than the critical angle for internal reflection at the glass substrate (refractive index $n_1 = 1.51$) to sample (e.g. cytosol with a refractive index of $n_2 \approx 1.33$) surface, $\theta_C = \arcsin \frac{n_2}{n_1}$ is reached. However, since an abrupt discontinuity in the electromagnetic field of the illumination is at odds with the wave equation which can be derived from the Maxwell equations of classical electromagnetism, an exponentially decaying evanescent wave $E = E_0 \exp(-z/d_p)$ forms, penetrating

$$d_p = \frac{\lambda}{2\pi}\left[\frac{\sqrt{\left(n_1^2 \sin^2\theta - n_2^2 + \kappa_2^2\right)^2 + (2n_2\kappa_2)^2} + n_1^2 \sin^2\theta - n_2^2 + \kappa_2^2}{2}\right]^{-1/2} \tag{2.13}$$

into the sample where κ_2 is the extinction coefficient of the sample. For transparent samples with $\kappa_2 = 0$, equation 2.13 reduces to

$$d_p(\kappa_2 = 0) = \frac{\lambda}{2\pi}\left[n_1^2 \sin^2\theta - n_2^2\right]^{-1/2} \tag{2.14}$$

which yields a penetration depth for the light intensity $I \propto E^2$ equal to

$$d = \frac{\lambda}{4\pi}\left[n_1^2 \sin^2\theta - n_2^2\right]^{-1/2} \tag{2.15}$$

In order to reduce motion blur, illumination was done in a stroboscope-like manner, with excitation light flashes of 5 ms duration.

2.5 Diffusion

Diffusion is the net transport of particles from a region of higher concentration to a region of lower concentration. A derivation for Fick's law of diffusion (Adolf Fick, 1829–1901) of the net particle flux j can be found in Demtröder [2006, p. 214ff.].

For one-dimensional diffusion in x-direction of particles with number density ρ, mean velocity $\bar{v}$, and mean free path Λ, Fick's law states

$$j_x = -\frac{\Lambda \bar{v}}{3}\frac{\mathrm{d}\rho}{\mathrm{d}x} = -D\frac{\mathrm{d}\rho}{\mathrm{d}x} \tag{2.16}$$

which can be written in vectorial notation for the general case

$$\vec{j} = -D\nabla\rho \tag{2.17}$$

using the Nabla symbol $\nabla = (\frac{\partial}{\partial x}, \frac{\partial}{\partial y}, \frac{\partial}{\partial z})$. In combination with the continuity equation

$$\nabla\vec{j} = -\frac{\partial}{\partial t}\rho \tag{2.18}$$

one gets for $\nabla D = 0$ the *diffusion equation*

$$\frac{\partial}{\partial t}\rho = D\Delta\rho \tag{2.19}$$

with the Laplace operator $\Delta = \frac{\partial^2}{\partial x^2} + \frac{\partial^2}{\partial y^2} + \frac{\partial^2}{\partial z^2}$. One solution of the one dimensional diffusion equation is

$$\rho(x,t) = \frac{\tilde{\rho}}{\sqrt{\pi 4Dt}} \exp\left(\frac{-(x-x_0)^2}{4Dt}\right) \tag{2.20}$$

where the boundary condition is $\rho(x,0) = \tilde{\rho}\delta(x)$, with $\tilde{\rho} \in \mathbb{R}^+$ and Diracs's $\delta(x)$ functional defined by $\int f(x)\delta(x)\mathrm{d}x = f(0)$ for any function $f : \mathbb{R} \to \mathbb{R}$, including constant $f(x) = 1$.

2.5.1 Brownian motion

While the diffusion equation is usually interpreted as an equation about concentrations, it can also be interpreted as an equation on single particle probability distributions for $\tilde{\rho} = 1$ (then, equation 2.20 is called the *propagator* or the *van Hove self-correlation function*). Single particle diffusion was first observed at pollen grains suspended in water by botanist Brown [1828]. In this interpretation, the diffusion equation is essentially identical to the *Fokker-Planck equation* (also known as *Komolgorov-Forward equation*)

$$\frac{\partial}{\partial t}P(x,t) = -\frac{\partial}{\partial x}[A(x,t)P(x,t)] + \frac{1}{2}\frac{\partial^2}{\partial x^2}[B(x,t)P(x,t)] \tag{2.21}$$

sans drift ($A(x,t) = 0$) and with constant diffusion ($B(x,t) = 2D$). The Fokker-Planck equation is the Kramers-Moyal expansion of the Master equation for Markov processes (transforming a integro-differential equation into an infinite order partial differential equation) stopped at the second term [Paul and Baschnagel, 2013, p. 47]. The macroscopic Fokker-Planck partial differential equation is equivalent to the microscopic *Langevin* stochastic partial differential equation [Lemons and Gythiel, 1997, Langevin, 1908] of the movement of a particle of mass m and velocity v in a fluid subject to external force $F(x,t)$ and a fluctuating force $L(t)$ due to collision with the molecules of the fluid:

$$m\dot{v}(t) = -f\,v(t) + F(x,t) + L(t) \tag{2.22}$$

In absence of an external force and $L(t)$ being white Gaussian noise, i.e. $L(t)$ has a Gaussian probability distribution, the expectation value of $L(t)$ is zero and there is no correlation over time ($\langle L(t)L(t')\rangle = B\delta(t-t')$), one yields for $m \to 0$ the Brownian motion of a particle in a (low Reynolds number, i.e. non-turbulent) fluid with inverse mobility $f = 1/\mu$ (which is defined as $\mu = v_{\text{drift}}/F$ by the asymptotic drift velocity v_{drift} under application of a constant force F) subject to Newtonian friction ($F_{\text{friction}} \propto v$) according to Stokes' law

$$f = 6\pi\eta r \tag{2.23}$$

for spherical particles of radius r in a fluid of dynamic viscosity η with $B = \frac{2}{f}k_{\text{B}}T$ from the Einstein-Smoluchowski relation

$$D = \mu k_{\text{B}}T \tag{2.24}$$

where k_{B} is Boltzmann's constant and T is absolute temperature. The Gaussian propagator of free diffusion is essentially a consequence of the central limit theorem applied to the fluctuating momentum transfers $L(t)$ in the Langevin equation 2.22 [Höfling and Franosch, 2013]. Mathematically, Brownian motion is a continuous-time stochastic process [for a thorough introduction to stochastic calculus, see Øksendal, 2003]. Informally, a stochastic or random process is a sequence of random variables that represent the progression of a system over time where the evolution is random rather than deterministic. Formally, stochastic processes are defined as follows: Let $(\Omega, \mathscr{F}, P)$ be a probability space with sample space Ω of possible outcomes, a set of events $\mathscr{F}$ associated with probabilites, i.e. a function P from the events to probabilities. Even more precisely, $\mathscr{F}$ is a σ-algebra and P is a probability measure. Let furthermore be (S, Σ) a measureable space with S a set and Σ a σ-algebra over S, where a σ-algebra over X is a subset Σ of the power set of X that satisfies:

1. Σ is non-empty. There is at least one $A \subset X$ in Σ
2. Σ is closed under complementation: If $A \in \Sigma$, then so is its complement, $X \setminus A$
3. Σ is closed under countable unions: If $A_1, A_2, A_3, \ldots \in \Sigma$, then so is $A = A_1 \cup A_2 \cup A_3 \cup \ldots$

In addition, let T be an totally ordered index set ("time"), usually $T \in \{\mathbb{N}_0, \mathbb{R}^+\}$. A stochastic process X is then a family of random variables $X_t : \Omega \to S, t \in T$ meaning a function

$$\begin{aligned} X : \Omega \times T &\to S \\ (\omega, t) &\mapsto X_t(\omega) \end{aligned} \tag{2.25}$$

such that $X_t : \omega \mapsto X_t(\omega)$ is for all $t \in T$ a $\mathscr{F}$-Σ measurable function. For every $\omega \in \Omega$ one yields a function $X(\cdot, \omega) : T \to S, t \mapsto X(t,\omega) = X_t(\omega)$. These functions are either called the *paths*, *trajectories*, or the *realizations* of the stochastic process. Now, (1-dimensional standard) Brownian motion refers to the Wiener process W_t (after Norbert Wiener, 1894–1964), which is a stochastic process where

1. almost surely $W_0 = 0$
2. for time points $0 \leq t_1 < t_2 < t_3 < \ldots < t_m$, the increments $W_{t_1} - W_{t_0}, W_{t_2} - W_{t_1}, \ldots, W_{t_m} - W_{t_{m-1}}$ are stochastically independent
3. for all $0 \leq t_1 < t_2$: $W_{t_2} - W_{t_1} \sim \mathcal{N}(0, t_2 - t_1)$ meaning that the increments are stationary and normally distributed with expectation value zero and variance $t_2 - t_1$.

Be aware that mathematical continuous-time Brownian motion does not exhibit a ballistic time scale regime [Huang et al., 2011b, Einstein, 1906] associated with time scales beneath the typical times it takes a real particle to travel the mean free path (picoseconds). However, this time scale regime is well below the experimental time scales (milliseconds). Importantly, owing to the properties of Wiener processes, sampling a continuous-time Brownian motion (such as in a measurement of a time lapse sequence) is equivalent to a discrete time Brownian motion (which can be simulated in random walks).

2.5.2 Diffusion in 2D

Interestingly, if the acceleration convective terms in the Navier-Stokes equation [e.g. Demtröder, 2006, p. 238] are disregarded and an attempt is started to solve the steady-state two-dimensional motion of a hydrodynamic creeping-flow of a contiuum, viscous, incompressible fluid past a cylinder at rest, one will reach the conclusion that it is not possible to satisfy all boundary conditions (constant fluid velocity at infinite distance from the cylinder and zero velocity on the cylinder surface) [Almeida and Vaz, 1995], a conclusion that became famous as Stoke's paradox. A solution of the creeping-flow equations would allow to derive a (constant) friction coefficient f (cf. equations 2.22, 2.23) to be used in the Einstein-Smoluchowski relation (equation 2.24). To avoid Stokes' paradox, firstly either the acceleration convective terms can be reintroduced, arriving approximately at the boundary conditions, with a velocity-dependent friction coefficient, or, secondly, the system is considered finite, now with a friction coefficient which depends on the system size. The third solution for the definition of a diffusion coefficient in two dimensions [Saffman and Delbrück, 1975] was, to consider the two-dimensional, viscous fluid as embedded in a three-dimensional medium of low, yet finite viscosity (such as water). Effectively, this geometry allows for dissipation of shear forces into the surrounding medium. For a cylinder of radius R and height h diffusing in a membrane of viscosity η, bounded by fluids with viscosity $\eta_1 = \eta_2 = \eta'$, Saffman and Delbrück [1975] derived

$$f = 4\pi\eta h \left(\ln \frac{\eta h}{\eta' R} - \gamma \right)^{-1} \tag{2.26}$$

where $\gamma = \lim_{n\to\infty} \left(\sum_{k=1}^{n} \frac{1}{k} - \ln(n) \right) \approx 0.577$ is the Euler-Mascheroni constant. Note that this is valid for low viscosity bounding fluids only, where $\epsilon = (R/h)[(\eta_1 + \eta_2)/\eta] \leq 0.1$. For larger values of ϵ, other formulae for f were derived [Almeida and Vaz, 1995]. To summarize, despite initial objections, diffusion and in particular diffusion coefficients in 2D are well-defined.

2.5.3 Analysis of Brownian motion

Analysis of Brownian motion is based on the fact that the time-average mean square displacement

$$\mathrm{MSD}(t) = \langle (\vec{r}(t+\tau) - \vec{r}(\tau))^2 \rangle_\tau \tag{2.27}$$

of a particle trajectory $\vec{r}(t)$ is expected to be equal to $2Dt + 2Dt = 4Dt$ for two dimensional diffusion, i.e. lateral diffusion within a plane such as a membrane, with a $2Dt$ term for both x and y direction.

$$\mathrm{MSD}(t) = 4Dt \tag{2.28}$$

This expectation is theoretically achieved for a infinitely long trajectory, which, however is not attainable in reality due to finite fluorophore photostability, detection rate, tracking success and field of view. For optimal imaging conditions, the classical approach is to estimate a $\hat{D}$ value from the slope of the $\mathrm{MSD}(t)$ curve for every trajectory tracked and then to calculate a (ensemble) mean value from these values. Only the slope is used in this approach because a finite localization accuracy σ_0 introduces an

offset σ_0^2 to the expected MSD curve. Fitting is done to a number of MSD values (e.g. time laspes 2–4 [Kusumi et al., 1993, Murase et al., 2004], 2–5 [Ernst and Köhler, 2013], 1–3 [Crane and Verkman, 2008], 1–8 [Biermann et al., 2014]) with a weighted least square minimization [Saxton, 1997], where the MSD is calculated from all possible displacements of the trajectory (in contrast to only independent, nonoverlapping displacements) [Kusumi et al., 1993]. The idea to use only independent, nonoverlapping displacements was initially introduced because of the severe autocorrelation [Michalet, 2010, equation 29] of the empirical MSD(t) curves of finite trajectories [Qian et al., 1991, see there for weights of the least squares fit]. Proponents of this analysis method argue that the ensemble mean of the slopes of the individual MSD curves yields an up to a factor of 4 an accurate estimate of the diffusion coefficient.
However, for a diffusion coefficient spatially varying on scales below the typical track length, diffusion coefficient histograms will not show the distinct two populations since within every track the diffusion is averaged out in the MSD curve. Therefore, this approach to analysis is not feasible to gain information on membrane structures smaller than the area covered by the whole trajectory. To overcome this, the alternative is to investigate the distribution of the square displacements in time lapse t for all times and the whole ensemble. This is ususally done in terms of the cumulative distribution function (cdf) [Schütz et al., 1997]. The cumulative distribution is used instead of the direct histogram in order to handle the problem of the choice of the bin size; also, noise in the histogram is integrated out [Weigel et al., 2012]. The model commonly used to describe the diffusional behavior of live cell single molecule tracking experiments assumes two populations, a fast diffusing one and a slow one [Lommerse et al., 2005, Schaaf et al., 2009, Schütz et al., 1997, Ohsugi et al., 2006, Crane and Verkman, 2008, Semrau and Schmidt, 2007, Eggeling et al., 2009]. Hence, the model exhibits three degrees of freedom: D_1, D_2, and the relative population size α.

2.5.4 Confined diffusion

Diffusion within confined compartments has been reported for the slow fraction of diffusing membrane-bound guanosine triphosphatase H-Ras anchored in the cytoplasmic leaflet of mouse fibroblasts [Lommerse et al., 2005] and zebrafish embryos [Schaaf et al., 2009]. Confined diffusion yields

$$\mathrm{MSD}(t) = \frac{L^2}{3} - \frac{32L^2}{\pi^4} \sum_{k=1(\mathrm{odd})}^{\infty} \frac{1}{k^4} \exp\left[-\left(\frac{k\pi}{L}\right) D t\right] \tag{2.29}$$

for diffusion in an impermeable square [Wieser and Schütz, 2008], which has been approximated by Schaaf et al. [2009], Lommerse et al. [2005] to

$$\mathrm{MSD}(t) = \frac{L^2}{3}\left(1 - \exp\left(-\frac{12Dt}{L^2}\right)\right) \tag{2.30}$$

It has been argued that this might be caused by lipid microdomains or by steric hindrance by the filamentous actin meshwork associated with the cytoplasmic surface of the plasma membrane. While Schaaf et al. [2009] themselves draw the lipid raft explanation into question, the second model, first known as the “membrane skeleton” fences model [Tsuji et al., 1988, Kusumi et al., 1993] was soon expanded to the picket and fences model [Kusumi et al., 2010], where membrane skeleton anchored transmembrane proteins pose as barriers (pickets) for both diffusing membrane proteins as well as lipids even of the outer membrane leaflet. The barrier effect is explained to be both due to steric hindrance and circumferential slowing, which is a collective term for hydrodynamic friction (in term of hydrodynamic theory) and increased packing (in terms of free-volume theory) [Umemura et al., 2008]. In consequence, a finite probability to hop to the neighbouring membrane compartment has been reported [Murase et al., 2004, Ritchie et al., 2005] and the concept of hop diffusion was proposed and is most prominently advocated for by the Kusumi group [e.g. Kusumi et al., 2012, 2010]. The small compartments and their confinement time are not accessible with fluorescent single molecule microscopy, but require a temporal resolution around 25 μs attainable with gold nanoparticle (diameter 40 nm) tracking. Using gold-tagged unsaturated phospholipids, hop diffusion was observed [Fujiwara et al., 2002], yet gold tags were shown to interact with the membrane skeleton including receptor crosslinking [Ritchie et al., 2005]. On the other hand, Nishimura et al. [2006] argue that ceramide and other high-melting-temperature lipids are believed to form solidlike phases presenting obstacles to diffusion.

2.5.5 Anomalous subdiffusion

Anomalous subdiffusion in 2 dimension characterized by MSD(t) development according to a power law

$$\mathrm{MSD}(t) = 4K_a t^a \tag{2.31}$$

with anomalous parameter $0 < a < 1$ is a phenomenon facing increasing interest despite its exotic appearance due to its ubiquitous presence in complex heterogeneous materials including polymeric networks and porous materials (think not only high tech; e.g. contaminants in ground water), colloids, but also amorphous semiconductors, and, most relevant to this thesis, in biophysical systems of macromolecular crowding. This section draws from the excellent review of Höfling and Franosch [2013]; for a deeper discussion, the interested reader is referred to there.

There are a number of roads that arrive at the power law of the MSD. Category one are Gaussian models with a Gaussian propagator. Deeming long-term anomalies associated with so-called hydrodynamic memory of diffusing vortices for non-steady motion during the derivation of the coefficient of friction f irrelevant, I rate microscopic approaches more convincing. *Fractional Brownian Motion* (FBM) is attained if the fluctuating force in the Langevin equation 2.22 representing the momentum transfer in collisions with fluid molecules is temporally correlated. Although the noise term is still Gaussian, it is not white noise. The statistics of the displacements, the propagator is again Gaussian, but the MSD is a function of time according to equation 2.31. An alternative approach is to consider the medium as visco-elastic with frequency-dependent viscosity $\eta(\omega)$ and shear modulus $G(\omega)$. Power law behavior $G(\omega) \propto \omega^a$ has been observed for the cytoplasma [Wilhelm, 2008] and whole cells [Alcaraz et al., 2003] and leads to long term subdiffusion.

The second category is the *continuous-time random walk* (CTRW), where particles “jump” displacements after some random waiting time has passed. Waiting times are easily interpreted in biological contexts as trapping due to chemical attachment. Anomaluos diffusion is obtained if the jump rate distribution (i.e. the Fourier transformed of the time-dependent jump-distribution) is not “appropriately well-behaved”, i.e. is non-analytic at zero frequency

$$\psi(\omega) = 1 - (-\mathrm{i}\omega\tau)^a + \text{higher order terms} \qquad \omega \to 0 \tag{2.32}$$

with non-integer exponent $0 < a < 1$, imaginary unit $\mathrm{i} = \sqrt{-1}$, some time scale τ and neglecting the higher order terms. Under certain conditions (generalized hydrodynamic approximation and the Cole-Cole jump-rate distribution), the corresponding propagator a then a solution of the so-called fractional Fokker-Planck equation, a variant of equation 2.21 involving fractional time derivatives [Metzler and Klafter, 2000] whose discussion is beyond the scope of this section.

The third category are Lorentz models of *obstructed motion*. Originally discussed as elastic scattering of ballistic particles on randomly placed hard spheres as a microscopic model for Drude’s electric conductivity, Saxton [1993] first recognized the relevance of obstacles such as membrane proteins to diffusion in membranes, coining the phrase “diffusion in an archipelago”. While for low obstacle densities the motion of a Brownian particle does look like free, though reduced, diffusion at long time scales, short term diffusion is anomalous. Correlations are induced by the static disorder of immobile obstacles and the self-avoidance of possibly moving, non-overlapping obstacles. When macroscopic transport is possible, the medium of diffusion is said to percolate; for high obstacle densities this might not be the case (for an introduction to percolation theory which is beyond this section on anomalous diffusion, see Stauffer [1979]). In the 2D continuum, for instance, macroscopic transport across a 2D-medium with randomly placed disc voids ceases at a critical 2D-medium coverage ≈ 0.323 [Quintanilla et al., 2000] with the emergence of a percolating void extending to infinity, marking a percolation threshold (note that voids are different from obstacles in that they may overlap). For comparison, the protein surface area fraction has been estimated to be ca. 0.3 [Saxton, 1993]. On the other hand, detergent-resistant lipids believed to represent lipid rafts account for 50 % of the membrane surface area [Pike, 2003] and percolating lipids rafts are found e.g. in the apical surface of epithelial cells [Meder et al., 2006, Danielsen and Hansen, 2008]. While obstacle presence thus causes anomalous diffusion at spatial and temporal regimes where the heterogeneity is “visible” to the diffusing particle ensemble, at the percolation threshold, anomalous diffusion extends over all regimes (i.e. heterogeneity prevails on all scales). Note that even for small obstacle densities it is possible that particles are confined and at high obstacle densities may render particles virtually immobile. The bottom line is, hop-diffusion’s membrane skeleton parcell grid with finite escape probabilities is very similiar to randomly distributed, moving obstacles. Consequently, hop-diffusion, which exhibits a transition regime between short-term (microseconds) confinement and long-term (seconds) free diffusion will present itself at the intermediate time lapse scale of tens of milliseconds as anomalous subdiffusion.

To make it even more complicated, different origins of anomalous diffusion do not exclude each other and may be combined. For instance, Weigel et al. [2011] reported to have observed CTRW on an fractal by tracking $K_V2.1$ potassium ion channels in live human embryonic kidney cells. Importantly, all categories of anomalous diffusion discussed can be interpreted in terms of a time-dependent diffusion coefficient (remind that time t refers to “internal time” and not time in the lab frame) so that the right hand side of equation 2.31 reads in 2 dimensions

$$4K_a t^a = 4D(t)t \tag{2.33}$$

$$D(t) = K_a t^{a-1} \tag{2.34}$$

The analysis conducted in this thesis assumes a Gaussian propagator which is investigated for different time lapses. For a lipid analogue, binding events with long-term attachment as modeled in the CTRW scenario are not anticipated. Deviations from Gaussianity to identify different mechanisms of anomalous diffusion are beyond the scope of this thesis focusing on single molecule detection in 3D microenvironments. However, two populations of diffusive motion corresponding to tracer localization in lipid raft and non-raft plasma membrane regions are expected.

On a note, it has also been proposed to interpret anomalous diffusion not only in a botton-up way but to appreciate that anomalous subdiffusion has been suggested as a search strategy superior to free Brownian motion in the context of binding partners which can be seen from an evolutionary point of view.

3 Materials & Methods

3.1 Coverslip cleaning procedure

Cleanliness is of great importance in single molecule microscopy. In order to achieve supreme cleanliness, a custom protocol was carried out. Round coverslips (Ø25 mm, #1.5, Glaswarenfabrik Karl Hecht KG, Sondheim, Germany) were separately hold in an upright position in a custom made Teflon holding device, and completely covered in technical grade acetone (Applichem, Darmstadt, Germany) for 15 min. Retrieved coverslips are afterwards dried in clean bench air circulation. Early flaming of ethanol soaked coverslips turned out not to contribute to surface cleanliness due to burn residues. Acetone-based cleaning is a pre-cleaning step to minimize contaminations of the plasma cleaner.

Plasma cleaning was performed utilizing a Zepto (Diener electronic GmbH + Co. KG, Ebhausen, Germany) plasma cleaner using water saturated ambient air as the processing gas to yield hydrophilic glass surfaces. A pressure of 0.6 mbar and a driving frequency of 40 kHz at a power of 50 W for plasma treatment of 100 seconds achieved good cleaning results.

3.2 Cell line

The U2OS cell line (ATCC–HTB-96) was derived in 1964 from a 15 year old caucasian girl, from a moderately differentiated sarcoma of her tibia [Niforou et al., 2008]. Osteosarcoma cell lines were shown to exhibit meaningful osteoblastic phenotypes [Wang et al., 2014, Clover and Gowen, 1994] which plays a central role in tissue engineering. Due to the reciprocal knowledge transfer between tissue engineering and 3D cell culturing, widely used U2OS were used in this thesis for maximal 3D cell culture know how. *In vitro*, U2OS secrete non-mineralized ECM and do not form spheroids.

U2OS form tumors in nude mice with invasion and weak angiogenesis [Mohseny et al., 2011]. The tumor suppressor genes p53 and pRb are functional in U2OS, while transcription factor c-Myc levels are increased fivefold [Niforou et al., 2008]. c-Myc is involved in cell growth and proliferation, regulated by PI3K signaling in pancreatic cancer [Schild et al., 2009] and GSK3 [Gregory et al., 2003]. U2OS show high level of integrin β_1 (which is part of all collagen-binding integrin dimers), moderate level of α_3, α_V and low levels of α_4,α_5 and α_6 expression [de Ruijter et al., 2001].

U2OS cells are known to enter cell cycle arrest rather than go into apoptosis, with 1.2 % apoptotic cells 48 h post 12 Gy x-irradiation as assayed by TUNEL (Terminal deoxynucleotidyl transferase deoxyUridine-triphosphate Nick End Labeling) and flow cytometry [Allan and Fried, 1999].

Cells were cultured in 25 cm^2 flasks using Dulbecco's modified Eagle's minimal essential medium (DMEM) with 10 % fetal calf serum, 1 % penicillin/streptavidin, 1 % non-essential amino acids at 37 °C in humidified atmosphere containing 5 % CO_2 by volume. Passaging was done twice a week using Accutase on 70–80 % confluence.

3.3 2D cell culture

Cells were seeded on cleaned coverslips (see section Coverslips cleaning procedure above) and provided with medium. U2OS adhere relatively fast (1/2–1 h).

3.4 3D cell culture

For 3D cell culture, microscopy sets demanding constraints. On the other hand, *in vitro* 3D cell culture is everything but standardized. Collagen I hydrogels were used based on clinical relevance and previous work in tissue engineering (see section 2.3). Since U2OS cells do not form spheroids, hydrogels in the form of drops on coverslips proved appropriate [Kämmerer, 2014], a cell culture design inspired by the “hanging drop” approach [Pampaloni et al., 2007]. Prior to gel application, plasma cleaned coverslips were spin coated with 40 μl of freshly prepared 2 % vol (3-Aminopropyl)trimethoxysilane (Sigma-Aldrich, St. Louis, MO, USA) solution in acetone utilizing a SPIN150 (SPS Europe Spincoating, Putten, The Netherlands) spin coater at 500 revolutions per minute (rpm) for 30 s and then 3000 rpm for another 30 s. Coating was performed in order to prevent easy disattachment of the gel from the glass substrate. After coating, coverslips were again separately placed in the Teflon holding device and two times washed in distilled water for 5 min. Coverslips were dried overnight at room temperature and stored in a dust-free place until gel application.

For ten gels á 20 μl, 133.3 μl of 3 mg/ml rat tail collagen I (Sigma-Aldrich, St. Louis, MO, USA), 7.4 μl of 7.5 % $NaHCO_3$ solution (Sigma-Aldrich, St. Louis, MO, USA), and 20 μl of 10× phosphate buffered saline were cooled by placing the reaction tubes in ice and then mixed with 39.3 μl of cell suspension (cells of a 70 % confluent T25 flask pelleted and resuspended in 1 ml). Resultant gels have a density of 2 mg/ml, located in the medium range of the published density spectrum (0.65 mg/ml – 3 mg/ml) [Harunaga and Yamada, 2011], also used by [Fraley et al., 2010, 2011, Kubow and Horwitz, 2011]. Upon combining the collagen with $NaHCO_3$, polymerization starts off. The prior cooling of the ingredients renders polymerization slow enough for proper mixing and preparation of several gels before polymerization is too progressed. Yet, cells predominantly do not sink on the glass surface due to the viscosity. Mixing and subsequent application of polymerizing gels on the center of prepared coverslips is done with care not to produce bubbles. After application, gels incubate for 1/2 hour at 37 °C for complete polymerization. Polymerized gels are then covered with medium and kept at 37 °C in humidified atmosphere containing 5% CO_2.

3.5 Fluorophores

As probe for measurements in membrane dynamics, the plasma membrane stain CellMask™Orange (Thermo Fisher Scientific, Waltham, MA, USA) was used. CellMask™Orange (CMO) stain is amphiphilic, featuring a lipophilic moiety and a hydrophilic negatively charged dye, which anchors the molecule in the membrane so that it does not permeate to the inner leaflet or intercalates across the lipid layers. In agreement with the free area model of diffusion, diffusion coefficients of lipids in fluid lipid bilayers are essentially independent of the lipid probe used, and diffusion of a tracer is almost independent of its acyl chain length [Almeida and Vaz, 1995]. In comparison to traditional membrane stains like DiI, CMO is advertised to provide slow internalization [life Technologies, 2014]. As mentioned in the section on fluorescence detection, internalized dye-laden vesicles on the lengthscale of the diffraction limit are detrimental for investigations in single molecule dynamics in the plasma membrane. CMO’s excitation and emission maxima are at 554 nm and 567 nm, respectively. Specifically, the possibility for future experimental expansion towards concurrent assessment of membrane dynamics and green fluorescent protein (GFP) labeled membrane bound receptor dynamics is ensured. Note that CMO is not activated stochastically using ultraviolet light or reducing agents in order to minimize labeling perturbations by the large portion of dark state fluorophores.

3.6 Microscope setup

The microscope setup was designed for multispectral 3D live cell single molecule imaging in mind. A Lumen 220 Pro metal-halide lamp (Prior Scientific, Cambridge, UK) is accompanied by 75 mW diode pumped solid state lasers with wavelengths 640 nm (OBIS; coherent, Santa Clara, CA, USA), 561 nm (sapphire; coherent, Santa Clara, CA, USA), 488 nm (sapphire; coherent, Santa Clara, CA, USA), and 408 nm (OBIS; coherent, Santa Clara, CA, USA) for illumination.

Laser beams (0.7 mm $1/e^2$ diameter) are combined using dichroic filters. An AOTFnC-400.650 non-collinear TeO_2 acousto optical tunable filter (AA optoelectronics, Orsay, France) [Chang, 1974] is used for frequency selection and stroboscope-like illumination. For details in acousto optical tunable filters (AOTFs) and acousto optics in general, the reader is referred to Saleh and Teich [2008, chapter 19]. Briefly, radio frequency (RF) signals drive a piezoelectric transducer coupled to a birefringent crystal, inducing sound waves. Sound waves like these are longitudinal acoustic oscillation modes manifesting themselves as periodic density fluctuations, giving rise to grating-like diffraction on the basis of photon-phonon interaction, where phonons are the quasi-particles associated with oscillations.

For RF generation an 8 channel multi digital synthesizer (MDS8C; AA optoelectronics, Orsay, France) was used via a USB remote control (RC03; AA optoelectronics, Orsay, France). The RF corresponding to the 561 nm laser was 93.268 MHz which was driven at maximal intensity for the deflected beam as measured by a powermeter (PM100D; Thorlabs Inc., Newton, NJ, USA) linked to a S130C photodiode power sensor (Thorlabs Inc., Newton, NJ, USA). RF power was accordingly set to 19.7 dBm equivalent to a power of $P = 1\text{ mW}\ 10^{\frac{19.7}{10}} = 93.3\text{ mW}$ at operation voltage of 5 V.

While the zeroth order beams are directed at a beam dump, a single mode fiber [Saleh and Teich, 2008, chapter 9] is aligned with the diffracted beams for mode cleaning. The end of the fiber is mounted to an opical axis, facing a Keplerian telescope 15× beam expander consisting of a lens pair with focal lengths $f_1 = 10$ mm, $f_2 = 150$ mm at a distance of $d = f_1 + f_2 = 160$ mm. Further mode cleaning by means of a spatial filter in the beam expander proved unnecessary and the use of a spatial filter albeit without use of the fiber was less efficient than otherwise. A circular variable aperture was avaliable for custom *ad hoc* beam narrowing. Finally, the expanded beam was deflected at a 90° angle to a motorized (PI M-126.DG1; Physik Instrumente GmbH & Co. KG, Karlsruhe, Germany) stage (PI 17338; Physik Instrumente GmbH & Co. KG, Karlsruhe, Germany) where the beam was deflected again and focused into the back focal plane of the microscope objective. Stage movements allowed for precise off-axis excitation beam light paths as required for HILO and TIRF illumation. The microscope used was a Nikon TI eclipse (Nikon, Chiyoda, Tokio, Japan) because of its unique dual filter wheel design allowing for flexible switching between single molecule microscopy mode with laser excitation and orientation mode with the metal halid lamp in different incoming light ports.

As camera for widefield imaging, an iXon EM+ DU-897D-C00-#BV (Andor Technology, Belfast, UK) [Andor Technology, 2011] back-illuminated electron multiplying charge coupled device (EMCCD) camera was used in frame transfer mode with an active region of 512×512 pixels, pixel size 16 μm. Quantum efficiency (QE) of DU-897 chips is >90% for the wavelengths relevant in fluorescence microscopy. Digitization rate was 10 MHz. The camera's dynamic range is 14 bit, so acquired images were stored as 16 bit unsigned integer valued tiff files. The time between subsequent exposures in frame transfer mode was 1.75 ms regardless of field of view dimensions as determined from inspection of trigger signals using a digital oscilloscope. Minimal exposure possible in frame transfer mode depends on region of interest dimensions with 10 ms exposure attainable for ≤ 128 pixels in direction of readout. Electron multiplication gain renders the readout noise negligible at readout rate like this, readout noise being the main drawback in sufficiently cooled scientific CCDs [Smith et al., 2004]. iXon EM+ cameras are cooled with a peltier element to ≈ -68 °C in order to minimize thermal noise. At exposure times < 50 ms, dark image correction was not necessary. Flatfield correction is important for photometry, was however not performed in this thesis. Keep in mind that in contrast to astronomy, where EMCCDs are used as well, fluorescence microscopy makes use of excitation light that is typically inhomogeneous and not only laterally, but especially in localization microscopy vertically.

Stroboscope-like illumination was realized by camera triggered AOTF gating with graphical user interface (GUI) and subroutines implemented [Tchani, 2013] in 64 bit LabVIEW™2013 (National Instruments, Austin, TX, USA). Camera controls and acquisition settings were executed using micromangager software [Edelstein et al., 2010] on a Windows™7 personal computer.

3.7 Irradiation

Irradiation was carried out using an Isovolt Titan E (GE Sensing & Inspection Technologies, Ahrensburg, Germany) x-ray source. Presence of glass coverslips was accounted for by a weighting factor as indicated in section 2.1.3. The weighting factor as suggested by Kegel et al. [2007] for cell culture using glass coverslips was used for both cells grown directly on glass and cells cultured in collagen I hydrogels on top of glass coverslips. Doses were delivered at 30 cm source to surface distance with cell cultures placed on the 2 mm aluminum filtering plate. For 1 Gy irradiation, the delivery time was set to 10 s at a current of 19.0 mA and for 25 Gy to 2 min 24 s at 33.7 mA.

3.8 Measurement

Immediately after irradiation, medium covering adherent cells or hydrogels was removed and phosphate buffered saline (PBS) solution containing 1 ng/ml CMO (section 3.5) was applied. Permeation of CMO through collagen I hydrogels was fast ($\approx$ 1 min), sufficient accumulation in plasma membranes however took about 15 min. Data were acquired from living cells up to 90 min post application of CMO. Measurements were performed under room temperature leading to slightly reduced rate of endocytosis and thus less fluorophore-laden vesicles which distort the assessment of lateral diffusion in the plasma membrane in comparison to 37 °C. Illumination intensity for fluorophore excitation was tuned to balance the fluorescence photon budget per fluorophore per frame for detection versus long track lengths for better displacement statistics. Typically, the 561 nm excitation laser was operated at 40 mW, yielding 11 mW exit power at the objective as determined with a PM100D (Thorlabs Inc., Newton, NJ, USA) powermeter linked to a S130C photodiode power sensor (Thorlabs Inc., Newton, NJ, USA). Excitation beam dimensions were assessed in epifluorescence mode using fluorescent dye solution, fitting a Gaussian beam profile to an image with integration time 50–200 ms. While at the same time verifying proper beam and sensor alignment, the area encircled by the $1/e^2$ radius was used to derive an intensity of about 1.2 kW/cm^2. Typical off-optical axis distance in HILO mode (see section 2.4.4) was 2.6 mm equivalent [Tokunaga et al., 2008] to an angle

$$\theta = \arcsin\left(\frac{2.6\text{ mm}}{f_{\text{obj}} n}\right) \tag{3.1}$$

of 59° for the HILO beam from the optical axis for a refractive index $n = 1.51$ and objective focal length $f_{\text{obj}} = 2$ mm. At this angle, the increase in intensity due to the inclination is by a factor of $1/\sin\theta \approx 1.16$.

4 Localization analysis procedure

Most single molecule detection microscopy operates at TIRF conditions [Ohsugi et al., 2006], with bright dyes such as from the ATTO (ATTO-TEC GmbH, Siegen, Germany) or Alexa Fluor (Thermo Fisher Scientific, Waltham, MA, USA) series [Wieser et al., 2007, Xu et al., 2012, Löschberger et al., 2012, Heilemann et al., 2009, 2008][see also Dempsey et al., 2011], gold nanoparticles [Kusumi et al., 1993], fluorescent beads or at high illumination laser intensities that drive fluorophores into a dark state within a single frame [Lee et al., 2011]. For the demanding challenges faced in 3D environmental live cell imaging, sophisticated image procession and analysis routines were established. The particularities of single molecule tracking in noisy high background data call for an analysis approach differing somewhat from other localization microscopy challenges (for a general discussion of the interdisciplinarity of computer vision in cell biology, see Danuser [2011]). In fact, single molecule tracking has to cope with the image noise under the constraint of limited photon budget per frame and low tracer density.

For data extraction, particle candidate positions in image stacks of acquired fluorescence data are *detected* and subpixel *localization* data is retrieved from subregions centered at candidate positions along with the flux and, depending on the imaging modality, ellipticity. More precisely, candidate positions are detected on background substracted data; then, emitter position is localized to subpixel accuracy and model dependent shape parameters including the flux are estimated. From these parameters, localized emitter signals are modeled and substracted from the data – a processing step called *deflation*. Deflated data is then iteratively searched for further candidate positions until a user-defined number of iteration steps was reached. Detection method and parameter specification may vary from iteration to iteration e.g. when using a sucessively lowered detection threshold. The merged dataset of the iterations is then open for selective postprocessing before localization data is handed over to further analysis. In an academic setting, flexibility and the possibilty to quickly integrate new published algorithms or mathematical approaches is crucial. From experiment to experiment, fluorophore intensity, density, mobility, integration time, background, and noise may vary depending on various factors including, but not limited to the used fluorophore's quantum yield, wavelength, ECM composition, ECM density, expression level, cell number density within the ECM, and size and cell compartment of the tagged protein. Therefore, a one-fits-all analysis will not allow for the needed flexibility. Rather, a modular design is needed with freedom for different analysis modules under different experimental circumstances. Also, modular design of the analysis procedure will allow easy extension by adding new, optional modules that implement ideas that continue to be published.

Analysis routines were written in Matlab™(The MathWorks, Natick, MA, USA) and carried out by a function call with the data image stack path and a parameter set specifying and adressing modules as input, yielding a data structure containing arrays of localization data. Shown below is a simplified flowchart of the localization procedure.

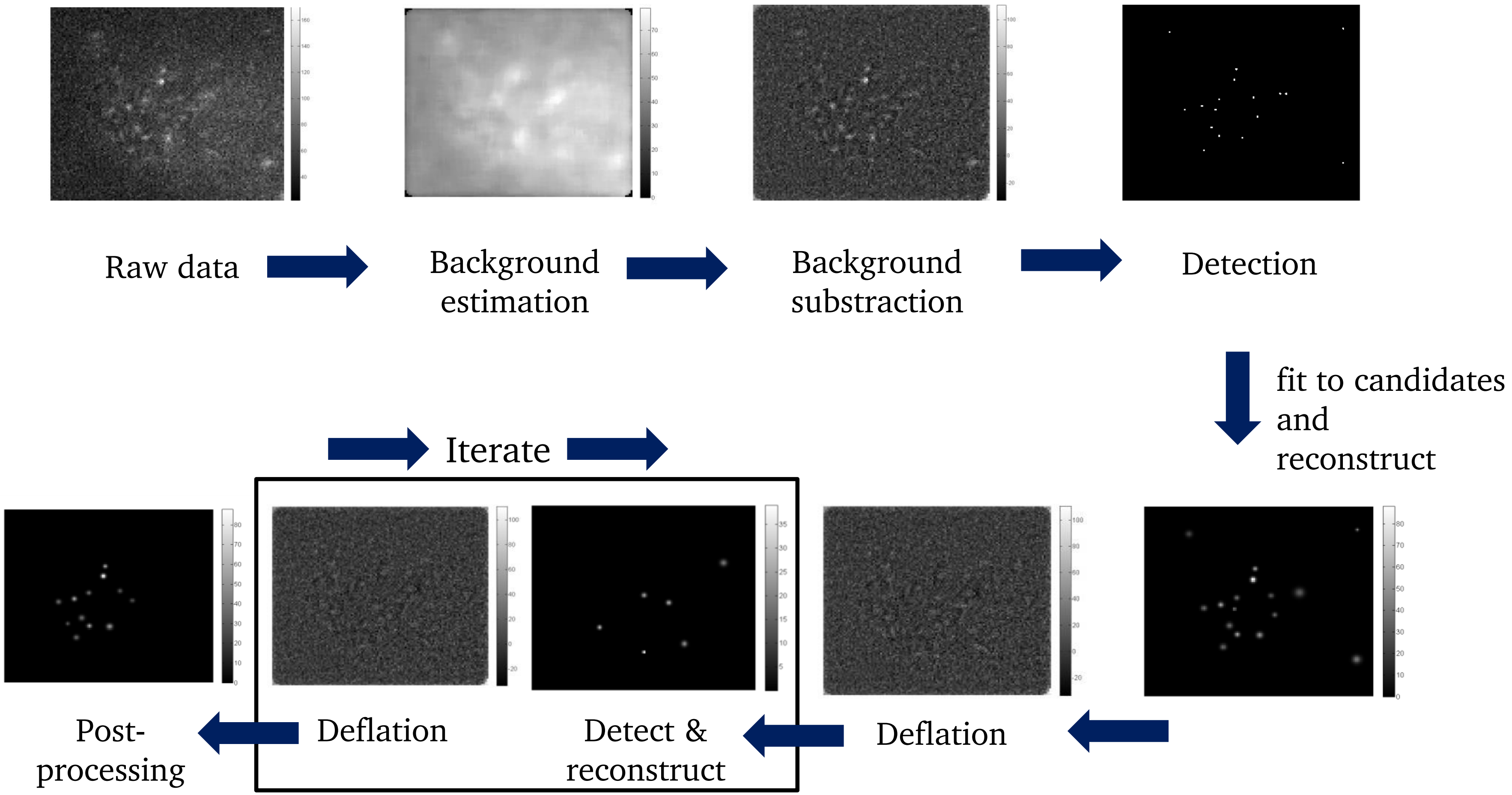

Figure 4.1.: Outline of the localization procedure.

4.1 Background correction

As explained above, hydrogel cell cultures come with challenging imaging conditions. Spatially heterogeneous, temporally non-constant background on noisy data calls for special care in background estimation/substraction techniques. Traditional approaches like time-averaged images of the whole image stack or temporally moving window weighted means were not suitable due to the time-dependence of the background fluorescence and the disadvantages for slow moving molecules, respectively (keep in mind that free diffusion/Wiener process is a martingale, that means the most probable position of the diffusion particle in the next frame is the present position). For the impact of the background on localization accuracy, see also Stallinga and Rieger [2012].

4.1.1 Temporally stable background

Temporally stable background is estimated most accurately on a pixel by pixel basis as mean value over time. Based on the considerations just mentioned, background estimation based on temporal averaging is included for completeness only since temporal stability is a claim generally not valid in single molecule microscopy. Note that a temporally sliding window of background estimation will exacerbate detection of fluorophores with small displacements, potentially missing evidence of temporary binding or complexation events and biasing towards larger diffusion constants.

4.1.2 Spatially constant background

Under the assumption of a spatially constant, yet temporally varying background signal, and the further assumption that there are more pixels representing background than fluorophores of interest, background estimation can be done robustly by histogramming each frame and taking the maximum of the histogramm as frame-wise background estimate. This *naive* approach might be suitable for TIRF imaging conditions but is anticipated to reflect the invalidity of the assuptions at heterogenenous background as faced with cells in 3D microenvironments.

A variant of this approach is to denoise prior to the estimation (see section 4.2).

4.1.3 Moving average

In the moving average background estimation technique, for each pixel in the input data a subregion is taken and a weighted average of the pixel values is calculated according to a specified mask. The simplest case is a uniform weighted square mask centered at the corresponding pixel in question. Mathematically this amounts to a convolution of the input image with the mask. Convolutions like this can be calculated very efficiently by the fast Fourier transform (FFT) and use of the convolution theorem

$$f * g(x) = \mathscr{F}^{-1}[\mathscr{F}[f](k) \cdot \mathscr{F}[g](k)] \tag{4.1}$$

where $\mathscr{F}[f]$, $\mathscr{F}^{-1}[F]$ are the Fourier and the inverse Fourier transform, respectively. Averaging is based on the fact that the mean value is the maximum likelihood estimator for Gaussian or Poisson noise corrupted values while the “moving” is based on the diagnosis of spatially varying background that can be approximated as locally homogeneous if the spatial dimensions of background variation are large compared to the mask/moving average window edgelength.

However, at emitter presence, i.e. significant photon counts originating from a fluorophore of interest in the pixels of the averaging window, pixel values represent not a locally flat background only and background estimation based on averaging will overestimate linearly due to the linearity of the mean. Though in principle, mask dimensions can be chosen to render the contribution of emitter signals negligible, this is not a practicable option as correspondingly, the resolution of the background estimation will diminish and furthermore emitter density will set a limit to reasonable mask dimensions.

4.1.4 Moving median

The median value m of a set of real numbers is defined as $\frac{1}{2} = \mathrm{cdf}(m)$ where cdf is the cumulative density function of the set. For a finite, discrete set with even cardinality, Matlab™interpolates linearly. In contrast to the mean value, the median is non-linear and thus more robust at emitter presence because low numbers of outlier pixel values do not lead to overestimation.

4.1.4.1 Square mask

For emitter signals of full width at half maximum (FWHM) of 250 nm, in the 2D Gaussian approximation with FWHM= $2\sqrt{2\ln 2}\sigma$, the 2.5σ (3σ) disk has an area of ≈ 20 (30) pixels á 107× 107 nm^2 respectively. While the moving window size is a user defined parameter, this consideration suggests a window edge length of minimum 7 pixels corresponding to a median value of a set of 49 values. Mostly, 9×9 masks were used for superior robustness.

4.1.4.2 Border of a square

An alternative to the square mask moving median approach of background estimation is to exclude the central pixels and only use the border pixels of a square mask for estimating the background, effectively nihilating the impact of the central emitter on the background estimation at that position. However, "border median" estimation is anticipated to be less smooth than square mask moving median estimation owing to the reduced statistics, i.e. the number of contributing pixels. Also, neighbouring emitters with a spacing equivalent to the mask dimensions may yield considerable background overestimation.

4.2 Denoising

Low signal to noise ratio scenarios faced in fluorescent protein detection under 3D cell culture conditions call for elaborated attempts at noise reduction postprocession. Two different categories are imaginable:

1. denoising the data in order to improve candidate position detection and at the same time the model parameter estimation
2. denoising the data in order to improve candidate position detection yet estimate model parameters on raw (true) data.

In this thesis, denoising refers to the former concept while intermediary denoising is considered as part of different candidate detection methods dealt with in section 4.3.

Prima facie, a simple small moving average such as the 3×3 used in Shuang et al. [2014], Ritter et al. [2010a] seems to be a good idea. Local noise in absence of emitters in terms of standard deviation is reduced by a factor of $\frac{1}{\sqrt{3\times 3}} = \frac{1}{3}$. However, emitter signals are smeared out, and the square 3×3 mask introduces anisotropies. As pointed out in the section on moving average based background estimation, moving average is a classical filtering technique being essentially a long pass filter that cuts off components of small spatial frequency. Despite its mediocre efficacy due to the inherent linearity, averaging filters are still used, even consecutively or in form of difference of box filters.

Be aware that the following optional denoising modules were included in the analysis software but are not used later on in the analyis of simulated or measured data. Denoising is not compatible with Poisson likelihood methods of parameter estimation. Furthermore, especially nonlinear denoising techniques may preserve or enhance background discontinuities, and depending on the noise realization, smear fluorophores of interest into the background, in particular under low signal to noise ratio conditions [Smal et al., 2010]. A thorough discussion and investigation of denoising approaches encompassing nonlinear interferences between denoising approaches, denoising parameters, detection schemes, detection thresholds, and localization accuracy dependent on the signal to noise ratio is beyond the scope of this thesis.

Nevertheless, feature conserving denoising techniques may be of future benefit, and therefore this section is included, presenting the adaptive Wiener filter, the matched filter, non-local means denoising and a technique specifically aimed at Poissonian noise.

4.2.1 Wiener filter

The Wiener filter is the linear filter which is optimal in terms of mean square error. Currently, Wiener filters are e.g. used in speech recognition [Chen et al., 2006]. In the narrow sense, Wiener filters have the assumption of additive white noise that is a stationary process [Lee, 1980]. Under this condition, Wiener filters outperform nonlinear median filters [Kumar et al., 2010]. As noise in fluorescence images is non-stationary, Wiener filters in the broad sense apply local *adaptive Wiener filter* on moving windows [Kuan et al., 1985, Jin et al., 2003]. Adaptive Wiener filters are called *local linear minimum mean square error* (LLMMSE) filters. Note that these filters are only locally linear but globally nonlinear. The window size determining the local subregion is related to the minimum feature size of interest and is therefore set to a 7×7 square. Adaptive Wiener filtering is readily implemented in the Matlab™image processing toolbox.

4.2.2 Matched filter

Since the PSF is known, it can be used as a *matched filter*. Matched filtering is essentially cross-correlation with the PSF that is performed by convolution [Smith, 1997a]. By use of the convolution theorem, the computationally efficient FFT algorithm, and the identity

$$\begin{aligned}
\mathrm{cor}(f(x), g(x)) &= \int f(x)g(x+y)\mathrm{d}x \\
&= \int f(\xi - y)g(\xi)\mathrm{d}\xi \\
&= \int f(-(-\xi + y))g(\xi)\mathrm{d}\xi \\
&= f(-\xi) * g(\xi) \\
&= \mathrm{conv}(f(-\xi), g(\xi)) \\
&= \mathrm{conv}(f(\xi), g(-\xi))
\end{aligned}$$

with square integrable real valued functions f,g on the real numbers, correlation can be calculated easily – especially since for symmetric PSFs $g(x) = g(-x)$.

Matched filters are optimal in the sense that peak signal values are farther above the noise than with any other linear filter [Smith, 1997b]. Specifically, for a Gaussian shaped signal with integral I and FWHM= $2\sqrt{2\ln 2}w$ subject to additive white Gaussian noise σ_N, matched filtering raises the signal to noise ratio (SNR$_{\mathrm{im}}$, see equation 5.6) from $I/2\pi w^2\sigma_N$ to $I/2\sqrt{\pi}w\sigma_N$ [Meckel et al., 2011] (note the improvement factor is $\sqrt{\pi}w$ with w in pixels [Wu, 1992]).

4.2.3 Nonlocal means

Nonlocal (NL) means denoising [Buades et al., 2005b,a] was developed as a denoising scheme that keeps image features such as edges preserved. Briefly, for every noisy n_k, a search window of size $s \times s$

around site k is searched by comparing $u \times u$ patches $\mathscr{B}_l$ with the $u \times u$ patch $\mathscr{B}_k$ centered at k. For every l, a weight w_{kl} is calculated from the similarity d_{kl} expressed as weighted euclidean distance $d_{kl} = \|(\mathscr{B}_l - \mathscr{B}_k) * K\|_2^2$ with weighting by a normalized $u \times u$ kernel K, so that

$$w_{kl} = \exp\left(-\frac{d_{kl}}{h}\right) \tag{4.2}$$

where h is a parameter specifying the degree of denoising. Then the NL-means estimate is

$$\hat{n}_k = \frac{\sum_l w_{kl} n_l}{\sum_l w_{kl}} \tag{4.3}$$

4.2.4 PURE-LET

In the literature of signal processing as well as image restoration, additive white Gaussian noise is a ubiquitous model. To account for the Poisson noise encountered in low photon count images, traditional approaches seek homoscedaticity by means of variance-stabilizing transforms (VSTs, e.g. the seminal Anscombe transform [Anscombe, 1948]). More recent developments are aimed at minimizing not straightforwardly the risk as expressed as mean square error (which is not straightforwardly calculated) but rather an unbiased estimate of the risk known as Stein's unbiased risk estimate (SURE [Stein, 1981]). The similar approaches of Luisier et al. [2010] and Hirakawa et al. [2012] both make use of the Haar discrete wavelet transform. The approach of Luisier et al. [2010] called Poisson unbiased risk estimator - linear expansion of thresholds (PURE-LET) was integrated. Basically, they exploit the fact that Haar wavelet coefficients are differences of Poisson random variables to derive the Poisson unbiased risk estimator (PURE) for each of the orthogonal wavelet scales and optimize estimates of wavelet coefficients based on the criterion of a minimized PURE using a soft thresholding function with two linear parameters (linear expansion of thresholds LET_0). Further improvement is gained by an additional linear parameter that controls the impact of the interscale predictor of the wavelet coefficient on the estimate (LET_1). The final step uses a Gaussian-smoothed version of the interscale predictor to apply smooth thresholding between two different LET_1 estimates (LET_2). In short, PURE-LET denoises framewise by optimizing 2 (LET_0), 3 (LET_1), and 6 (LET_2) linear parameters per frame, respectively. In order to reduce artifacts stemming from a lack of translational invariance of the wavelet basis, "cycle spinning" cyclically shifts the data, unshifts the denoised data, and thus effectively "averages out" translational invariance [Coifman and Donoho, 1995].

4.3 Detection of candidate positions

A major task of emitter fitting techniques – as opposed to emitter density estimation techniques such as compressed sensing (CSSTORM) [Zhu et al., 2012], Bayesian bleaching and blinking (3B) [Cox et al., 2011], and deconSTORM [Mukamel et al., 2012] – is to find the supposed positions of emitters. Because there is a substantial pointillistic superresolution community interested in fast imaging in dense emitter conditions, most recent contributions and effords from the field aim to tackle these issues. For instance, Daostorm [Holden et al., 2011], Huang et al. [2011a], and PALMER [Wang et al., 2012, Quan et al., 2011] apply simultanous subregion multiemitter fitting using MLE (Daostorm is cited to use least square minimization [Small and Stahlheber, 2014, Min et al., 2014], however, Holden et al. [2011] actually refer to DAOPHOT code inspections revealing MLE code with several penalties and modifications), where the criterion for Holden et al. [2011] is to find none further emitter, Huang et al. [2011a] looks at F-tests and likelihood ratios, and PALMER decides the emitter number to fit based on the Bayesian information criterion (BIC), as does Manzo et al. [2014]. Although Manzo et al. [2014] apply their algorithm to stimulated emission depletion (STED) microscopy movies, their appoach is transferable to widefield single molecule data. They deflate images by sucessively eroding patches of overlapping PSFs. Earlier implementations of deflation approaches include MTT [Sergé et al., 2008], Quickpalm [Henriques et al., 2011], Michel et al. [2007], and 3D-Daostorm [Babcock et al., 2012], where overlapping PSFs are not fitted simultanously but rather successively. Babcock et al. [2012] argue that simultanous fitting is computationally inefficient as it requires calculation of the inverse of a large matrix which scales badly. FALCON [Min et al., 2014] deconvolves first with a sparsity promoting prior (weighted l_1 norm) and then again on the spatial support with least squares, where maxima are used for initial localization. Babcock et al. [2013] increased speed of the compressed sensing method by use of l_1 homotopy compared to the previous convex optimization used in Zhu et al. [2012]. Importantly, Min et al. [2014] point out the severe biasedness in grid oversampling methods like compressed sensing as used in Zhu et al. [2012] and Kim et al. [2013].

4.3.1 Threshold

The most simple methods to identify supposed emitter positions is to find local maxima exceeding a certain threshold [Thompson et al., 2002]. Absolute values are of limited sense in the presence of variable background, therefore commonly the threshold is given in terms of standard deviations above zero or better the estimated background; equivalent formulations use p-values, constant false positive rates or peak signal to noise ratios. One example using such an approach is QuickPALM [Henriques et al., 2011]. One adaption of this is not to define an overall or framewise noise, but rather a local noise.

4.3.2 Laplacian of Gaussian

Local maxima can be found by inspection of the second derivative. For 2D image data, this is the Laplace operator

$$\Delta = \frac{\partial^2}{\partial x^2} + \frac{\partial^2}{\partial y^2} \tag{4.4}$$

which is in discretized form a convolution with the kernel

$$\Delta = \begin{bmatrix} 0 & 1 & 0 \\ 1 & -4 & 1 \\ 0 & 1 & 0 \end{bmatrix} \tag{4.5}$$

Due to the discretization, however, pure application of Laplace filters yield significant aberrant extrema even in only slightly noisy data. Therefore, either prior or after the Laplace filter, smoothing is commonly applied. Since convolution is a commutative algebra ($f * g = g * f$), the order does not play a role. Even more, as convolution is also associative ($f * (g * h) = (f * g) * h$), the Laplace and the blurring filter can be combined so that effectively only one convolution has to be computed. In blob detection, Gaussian blurring – i.e. convolution with a suitably sized Gaussian – is preferred since Gaussian convolution is reproductive (sequential convolution with Gaussians of variances σ_i^2 is equal to a single convolution of a Gaussian with variance $\sum_i \sigma_i^2$), which is exploited in computer vision task of arbitrary size "blob"-feature detection by searching for maxima in "scale-space", i.e. the original image blurred with Gaussians of different width. In single molecule detection, blob sizes are known (at least for in-focus emitters) and consequently full scale space inspection is not necessary. Rather, Gaussian blur with a width corresponding to the PSF dimensions is performed only. The combined Laplacian-of-Gaussian (LoG) filter [Huertas and Medioni, 1986] is colloquially also known as the mexican hat filter and has in the past often been approximated by Difference of Gaussian (DoG) filters. However, classical blob detection techniques like the DoG or the LoG filters are designed with greatly oversampled blobs in mind, where discretization is neglegible and pixel dimensions are small compared to the blob diameter.

4.3.3 Correlation

As mentioned in the matched filter subsection on denoising (section 4.2.2), PSF knowledge can be exploited in emitter detection by enhancing the peak signal to noise ratio. While empirical PSFs could be used, in this thesis a theoretical PSF approximated by a 2D Gaussian was used to avoid the spread in an empirical average PSF due to localization inaccuracy and pixelation. Matched filters combined with the criterion whether the peak signal exceeds the background level by a given factor of standard deviations of noise is a Neyman-Pearson test [Turin, 1960] which has been subject of research for radar data during the cold war. For the locally variable noise faced in microscopy, local noise levels are more suitable than global noise, yielding locally optimal detectors [Capon, 1961]. Instead of using the post-convolution noise as criterion, an estimate of the raw data noise was used. Doing this can be interpreted as focusing not on the peak signal to noise ratio as done in Meckel et al. [2011], but rather the integral signal to noise ratio. Since a) peak signal and integral signal only differ by a PSF width dependent factor, and b) pre convolution/raw noise level and post-convolution noise level differ by a PSF width dependent factor, both methods are essentially equivalent after adjustment of the applied threshold. On the other side, a raw data noise estimation map is created nevertheless (handled in section 5.1.2) and dual computational efford is avoided.

4.3.4 Wavelets

In Fourier analysis, signals or functions are decomposed into sinusoids. Wavelets are another decomposition where the components are not only localized in spatial domain, but also in frequency domain. Because of this property, wavelet transforms are of interest in signal procession. Olivo-Marin [2002] proposed the á trous wavelet for pattern recognition in biological samples, and was e.g. implemented in the spot detection routine accompanied with the u-track implementation of Jaqaman et al. [2008] by a former Olivo-Marin lab PhD student and is also used in Izeddin et al. [2012], Kechkar et al. [2013], Ovesny et al. [2014].

4.3.5 Bayesian Information Criterion

Sergé et al. [2008] used a generalized likelihood ratio criterion for emitter detection, i.e a criterion expressed in constant false alarm rate on the ratio of likelihoods of emitter presence/absence as estimated. However, for both presence and absence of an emitter, their likelihood models assumed Gaussian noise which is not valid for low photon counts.

For each pixel, an estimate for the likelihood of hypothesis H_1 (an emitter is present, centered on the pixel in question) and hypothesis H_0 (no emitter is present) is computed: First, given H_0, the local expectation value is estimated by a local average. Specifically, the pixel value is question is estimated by the average of the pixel values of the border of the square 7×7 neighbourhood, efficiently computed as convolution of the raw data n:

$$\mu = n * \frac{1}{24} \begin{bmatrix} 1 & 1 & 1 & 1 & 1 & 1 & 1 \\ 1 & 0 & 0 & 0 & 0 & 0 & 1 \\ 1 & 0 & 0 & 0 & 0 & 0 & 1 \\ 1 & 0 & 0 & 0 & 0 & 0 & 1 \\ 1 & 0 & 0 & 0 & 0 & 0 & 1 \\ 1 & 0 & 0 & 0 & 0 & 0 & 1 \\ 1 & 1 & 1 & 1 & 1 & 1 & 1 \end{bmatrix} \tag{4.6}$$

Let μ_k be the expected number of photons in pixel k. Then the Poisson likelihood to observe n_k photons is

$$P(n_k|\mu_k) = e^{-\mu_k} \frac{\mu_k^{n_k}}{n_k!} \tag{4.7}$$

The loglikelihood $L(H_0) = \ln P(n_k|\mu_k)$ is thus

$$L_0 = -\mu_k + n_k \ln \mu_k - \ln n_k! \tag{4.8}$$

where μ_k is estimated by convolution. On the other hand, the loglikelihood $L_1 = L(H_1)$ for a emitter with a PSF g, where g is normalized ($\sum g_{ij} = 1$), has to be evaluated at the most likely emitter intensity. Assuming emitter presence central of the pixel, the flux can be estimated pixelwise by calculating

$$\hat{I}_k = \frac{n_k - \mu_k}{g_{rr}} \tag{4.9}$$

where $g_{rr} = \max\{g_{ij}|1 \leq i \leq 2r+1, 1 \leq j \leq 2r+1\}$ is the peak value of the normalized PSF. Note that $\hat{I}_k$ may be negative. All values of this map $\hat{I}_k$ less then a threshold of t are set to 0.

$$\tilde{I}_k = \begin{cases} \hat{I}_k & \text{if } \hat{I}_k = \max\{(\hat{I}_k, t\} \\ 0 & \text{otherwise} \end{cases} \tag{4.10}$$

Then, $\tilde{I}_k$ is convolved with the PSF and background is added:

$$s_k = \tilde{I}_k * g_{ij} + \mu_k \tag{4.11}$$

The corresponding loglikelihood is

$$L_1 = -s_k + n_k \ln s_k - \ln n_k! \tag{4.12}$$

Since the logarithm is strictly monotonically increasing, likelihood ratios are equivalent to loglikelihood differences and the model independent factorial $\ln n_k!$ can be omitted.

The Bayesian Information Criterion (BIC) is the difference $\Delta\text{BIC} = \text{BIC}(H_0) - \text{BIC}(H_1)$, with

$$\text{BIC}(H_i) = -2L_i + K_i \ln \nu \tag{4.13}$$

where K_i is the number of parameters of hypothesis H_i, $i \in \{0,1\}$, and ν is the number of samples. Here, $\nu = 1$ (pixelwise evaluation), $K_0 = 1$ (background parameter), and $K_1 = 2$ (background and flux). The BIC penalizes excess number of model parameters – however, since $\ln 1 = 0$, ΔBIC is up to a constant factor equal to the logarithm of the likelihood ratio. Finally, local maxima in the ΔBIC map exceeding a threshold b are identified.

The BIC may be used in post localization procession of data exhibiting several pixels of a region of interest and hypotheses/models with several parameters such as PSF width, emitter position, etc. A more thorough explanation of BIC is given there, in section 5.1.9.

4.3.6 Kullback-Leibler Divergence

The Kullback-Leibler (KL) divergence $D_{\text{KL}}(P||Q)$ of Q to P is an information theoretical measure how much information is lost if P is approximated by Q. It was discovered by Solomon Kullback and Richard Leibler [Kullback and Leibler, 1951] while working for the National Security Agency [NSA, 1999, 2002]. Note that the KL divergence is not a metric as it is for example not symmetric. The KL divergence of Q to P for discrete distributions P, Q is defined as

$$D_{\text{KL}}(P||Q) = \sum_i P(i) \log \frac{P(i)}{Q(i)} \tag{4.14}$$

For candidate detection, $D_{\text{KL}}(n_k||\mu_k)$ and $D_{\text{KL}}(n_k||s_k)$ is calculated for every pixel. Then, local maxima in the $D_{\text{KL}}(n_k||\mu_k) - D_{\text{KL}}(n_k||s_k)$ map are identified after convolution with a negative Laplacian of Gaussian.

4.4 Parameter inference

Parameter estimation lies at the heart of single molecule microscopy. Essentially, the best fitting parameters of a PSF model are seeked. As discussed in section 2.4.2, the classical model gives

$$G(x_0, y_0, I, W, B) = I\frac{4\ln 2}{\pi W^2}\exp\left(-\frac{4\ln 2(x-x_0)^2}{W^2} - \frac{4\ln 2(y-y_0)^2}{W^2}\right) + B \tag{4.15}$$

for pixel position $x \in \{1, 2, ..., x_{\max}\}, y \in \{1, 2, ..., y_{\max}\}$ within a region of interest (ROI) of dimension $y_{\max} \times x_{\max}$. I is the flux in photons, and $W = 2\sqrt{2\ln 2}\sigma$ is the full width at half maximum of a Gaussian of standard deviation σ. Single emitter fitting methods continue to improve while multiemitter fitting methods break ground. As pointed out above, multiemitter fitting methods like Holden et al. [2011], Huang et al. [2011a], and PALMER [Wang et al., 2012, Quan et al., 2011] try to fit the parameters (often at fixed width W) of several emitters in a ROI simultanously. Of course, high emitter densities calling for multiemitter fit methods are favourable for superresolution imaging since the number of localizations per frame increases, leading to a higher imaging speed translating into a higher framerate of PALM/STORM movies of reconstructed data. Of note, reported localization precisions of arbitrary emitter density lose their intended meaning if the emitter density corresponds to a nearest neighbor distance smaller than the inherent single emitter localization accuracy because emitter localization then basically can as reliable done by random guessing. In general, simultanous multiemitter fitting is regarded as not as reliable and thoroughly understood [Small and Stahlheber, 2014] and therefore not as popular as single emitter methods. For single particle tracking applied to single molecule microscopy, emitter density has to be kept so that particles can be unambiguously assigned. A proposed criterion for reasonable tracking has been stated [Jaqaman et al., 2008] as

$$\frac{\text{NND}}{\sqrt{\text{MSD(1 frame)}}} \ll 0.5 \tag{4.16}$$

, where NND is nearest neighbor distance and MSD is mean square displacement (see section 2.5.3). Non-quantitative or tracking unsuitable methods like Bayesian bleaching and blinking (3B) microscopy [Cox et al., 2011] or deconvolution based deconSTORM [Mukamel et al., 2012] were not considered.

More complicated models are:

$$G(x_0, y_0, I, W, B, \epsilon) = I\frac{4\ln 2}{\pi W^2}\exp\left(-\frac{(x-x_0)^2 4\ln 2}{W^2/\epsilon^2} - \frac{(y-y_0)^2 4\ln 2}{W^2\epsilon^2}\right) + B \tag{4.17}$$

introducing the ellipticity $\epsilon = \sqrt{\frac{W_y}{W_x}}$ with FWHMs W_x and W_y along the $x$and y axis, respectively. Accordingly, the generalized width $W = \sqrt{W_x W_y}$ is the geometric mean.

Pixelation of the detector can be accounted for in the estimation of positional accuracy [Thompson et al., 2002]. Even better, the model itself can be pixelated [Smith et al., 2010, Rolfe et al., 2011], both symmetric and elliptical:

$$G(x_0, y_0, I, W, B, \epsilon) = I\frac{1}{4}\Delta E_x \Delta E_y + B \tag{4.18}$$

$$\Delta E_x = \text{erf}\left(\frac{(x-x_0+0.5)}{W/\epsilon 2\sqrt{2\ln 2}}\right) - \text{erf}\left(\frac{(x-x_0-0.5)}{W\epsilon/2\sqrt{2\ln 2}}\right) \tag{4.19}$$

$$\Delta E_y = \text{erf}\left(\frac{(y-y_0+0.5)}{W/\epsilon 2\sqrt{2\ln 2}}\right) - \text{erf}\left(\frac{(y-y_0-0.5)}{W\epsilon/2\sqrt{2\ln 2}}\right) \tag{4.20}$$

With $\epsilon = 1$ for the symmetric case.

With the exception of the classical center of mass, position estimates primarily optimized for speed were not considered, including Parthasarathy [2012] and Fluorobancroft [Andersson, 2008].

4.4.1 Center of mass

The most simple method to yield subpixel localizations of to calculate the center of mass position (e.g. used in the classic Gelles et al. [1988]), here without loss of generality given for the x axis:

$$\hat{x}_{CM} = \frac{\sum\limits_k \tilde{n}_k x_k}{\sum\limits_k \tilde{n}_k} \tag{4.21}$$

with $\tilde{n}_k = n_k - \min_k\{n_k\}$ offset substracted photon counts of ROI pixel k. Note that offset may be negative due to prior background correction. Proper background correction is crucical for center of mass estimation. On a related note, center of mass of a binarized (thresholded) ROI is called the centroid and has been shown to be inferior to the regular center of mass [Cheezum et al., 2001].

The center of mass estimator is a fast method because it involves no iteration. Its motivation lies in the fact that the center of mass is the maximum likelihood estimator of the position under the assumption that the PSF is a smooth, i.e. unpixelated, Gaussian distribution.

Center of mass is positional only and e.g. used in Quickpalm [Henriques et al., 2011]. In thinking along the line of the initial motivation, widthes can be estimated.

$$\hat{W}_x = 2\sqrt{2\ln 2}\sqrt{\frac{\sum\limits_k \tilde{n}_k (x_k^2 - \hat{x}_{CM}^2)}{\sum\limits_k \tilde{n}_k}} \tag{4.22}$$

based on the maximum likelihood estimator for the variance under the same assumptions. As the ML estimator is biased, Bessel's correction $\frac{\sum_k 1}{(\sum_k 1)-1}$ is applied under the square root. Do note that the square root is nonlinear and introduces some bias meaning the corrected estimator of the variance is unbiased but the square root of the unbiased estimator of the variance is not an unbiased estimator of the standard deviation. However, the corrected estimator is less biased than the uncorrected and in the end, errors due to model unappropriateness (pixelation, Gaussian approximation) and lack of robustness both in terms of noise and sample size, i.e. ROI dimensions, render the error introduced by using this specific estimator neglegible.

The straightforward approach to estimate the number of detected photons without a fit is realized by simple counting:

$$N = \sum_k \tilde{n}_k \tag{4.23}$$

While in principle calculation of an estimate $\hat{\epsilon} = \sqrt{\frac{\hat{W}_y}{\hat{W}_x}}$ was possible, this was very unreliable and as a result, nonfitting approach was done with a fixed ellipticity $\hat{\epsilon} = 1$ and a width $\hat{W} = \sqrt{2\ln 2}(\hat{W}_x + \hat{W}_y)$. Note that while in the elliptical case the generalized width W is the geometric mean, for the symmetric case both $\hat{W}_x$ and $\hat{W}_y$ are inpedendent samples of the same random number, estimated by the arithmetic mean.

4.4.2 Nonlinear least squares

Parameters can be estimated by searching for the set of parameters for which the sum of squared errors, i.e. the difference between model and data, is minimized. For nonlinear models/functions, this must be done iteratively and is commonly known as the method of least squares (LS). For heteroscedastic data, i.e. of non-uniform variance, corrupted by white Gaussian noise, Gauss showed that minimization for the sum of squared errors where each error is weighted according to its datapoint's reliability, in particular the inverse of the variance of the respective data point, is the maximum likelihood estimator of this noise model (additive white Gaussian noise) [Rieger and Stallinga, 2014, Press et al., 1997, Box et al., 2005]. In common parlance, this method is called weighted least squares or χ^2 optimization with

$$\chi^2 = \sum_k \frac{(n_k - f(\vartheta_k))^2}{\sigma_k^2} \tag{4.24}$$

where the sum goes over all datapoints n_k, and ϑ_k encompasses the independent variables both of pixel position and model. $\sigma_k = \sigma$ reduces the formula to the unweighted least squares.

χ^2 optimization has been applied in e.g. Kubitscheck et al. [2000]. In 2001, Cheezum et al. [2001] showed superior performance of least squares methods against alternatives including center of mass, crosscorrelation and sum of absolute differences minimization, a method used in medical imaging. Unweighted least squares were used in e.g. Sergé et al. [2008], Abraham et al. [2009] and also in Thompson et al. [2002] under the name of Gaussian mask estimator [Mortensen et al., 2010, Rieger and Stallinga, 2014]. Usually, least squares are minimized using the Levenberg-Marquardt algorithm [Levenberg, 1944, Marquardt, 1963].

In this thesis however, the trust-region-reflective algorithm was used, a trust region approach based on Newton's interior-reflective method [Coleman and Li, 1994, 1996] because Levenberg-Marquardt does not comply with boundary specification for the parameters, a feature of the former greatly enhancing fitting performance.

Based on considerations of χ^2 fitting of signal above threshold subject to Gaussian or Poissonian noise, Bobroff [1986] recommends thresholds near the convergence limit of optimal parameter estimation ($t \gtrapprox 2, t \gtrapprox 3$ to 4 for Gaussian and Poissonian case, respectively; t in Bobroff's notation is half width at PSF=threshold in units of PSF standard deviation). While in-ROI fit is done to all pixels, ROI dimensions do represent a threshold in Bobroff's sense. Bobroff does not take into acount limited photon budget, thus tighter sampling is benefitial. At Nyquist sampling of pixel size ≈ PSF standard deviation, this translates into optimal ROI dimensions of 7×7 to 9×9 pixel dimensions ($2 \cdot 3 + 1 = 7, 2 \cdot 4 + 1 = 9$).

Calculations concerning the accuracy were done by Thompson et al. [2002], publishing the thereafter widely used formula

$$\langle (\Delta x_{LS})^2 \rangle = \frac{s^2 + a^2/12}{N} + \frac{8\pi s^4 b^2}{a^2 N^2} \tag{4.25}$$

and

$$\langle (\Delta N)^2 \rangle = N + \frac{4\pi s^2 b^2}{a^2} \tag{4.26}$$

where N, s, b^2 are the total number of detected photons, the PSF standard deviation width, and mean number of background photons per pixel, respectively (note that Thompson et al. [2002] use the noise standard deviation b but Stallinga and Rieger [2012] denote the mean number of background photons using the same letter). $\frac{a^2}{12}$ is the variance of a top hat function with width a. Intriguingly, localization accuracy $\langle (\Delta x)^2 \rangle$ is about optimal for $s = a$, i.e. the Nyquist criterion (actually, the optimal pixel size in terms of localization accuracy is signal to noise dependent, but $1 \leq a/s \leq 2$ for a wide range of SNR [Winick, 1986]). For years, empirical least square fits where infamous for their 30 % excess uncertainty in position, already recognized by Thompson et al. [2002]. Mortensen et al. [2010] presented the more correct

$$\langle (\Delta x_{LS})^2 \rangle = \frac{s^2 + a^2/12}{N} \left(\frac{16}{9} + \tau \right) \tag{4.27}$$

$$\tau = \frac{2\pi b (s^2 + a^2/12)}{N a^2} \tag{4.28}$$

formula by taking into account higher order terms.

Weighted least squares may encounter pixel of negative or zero value. As pixel numbers occur in the denominator, under low photon conditions or background correction, weighted least squares are substantially less precise than unweighted least squares [Mortensen et al., 2010].

4.4.3 Maximum likelihood

Given a model G that predicts $\mu_k = G(x_k, y_k, x_0, y_0, I, \ldots)$ photons for pixel $k \in \{1, \ldots, x_{\max} y_{\max}\}$ at x_k,y_k, the Poisson likelihood of the actually measured n_k photons in the pixels of the ROI is

$$\mathscr{L}(x_0, y_0, I, \ldots) = P(\{n_k\}|\mu_k) = \prod_k e^{-\mu_k} \frac{\mu_k^{n_k}}{n_k!} \tag{4.29}$$

Since the logarithm is strictly monotonically increasing, seeking the model parameters that maximize the likelihood is equivalent to looking for the maximum of the easier to calculate log-likelihood

$$L(x_0, y_0, I, \ldots) = \ln \mathscr{L} = \sum_k -\mu_k + n_k \ln \mu_k - \ln n_k! \tag{4.30}$$

Since the last term $\ln n_k!$ is independent of model parameters, it can be discarded for the iterative minimization, in particular as calculation of the factorial is slow. Note also that the factorial is rapidly increasing: 170! equals about $7.25 \cdot 10^{306}$ and 171! already exceeds the largest number that can be encoded in IEEE 754 double precision floating point numbers.

Abraham et al. [2009] compared MLE fits with unweighted least square fits with position being the only fit parameter, signal amplitude and background level fixed to known values, that is. They conclude MLE to be a little more robust against model misspecification, tested with misspecified fixed width values and Gaussian models fit to Airy patterns. *Nota bene*: Though consistently speaking of “pixelated Gaussian”, their appendix makes clear that they do not use pixelwise integrated model functions. MLE with pixelated Gaussians was introduced by Smith et al. [2010].

4.4.3.1 CRLB

The Cramér Rao inequality relates under mild regularity conditions the variance-covariance matrix cov($\hat{\theta}$)= σ_{ij}^2 of any unbiased estimator $\hat{\theta} = [\hat{\theta}_x, \hat{\theta}_y, \hat{\theta}_I, \ldots]$ of quantity θ to the inverse of the Fisher information matrix:

$$\langle \sigma_{ij}^2 \rangle \geq I_{ij}^{-1}(\theta) \tag{4.31}$$

with

$$I_{ij}(\theta) = \left\langle \frac{\partial L(\theta)}{\partial \theta_i} \frac{\partial L(\theta)}{\partial \theta_j} \right\rangle \tag{4.32}$$

where $\langle \cdot \rangle$ means the expectation value over different realizations, i.e. here photon detections. Simultanous fitting of parameters leads to off-diagonal elements; the Cramér Rao lower bounds (CRLBs) for the variance of the estimator of the parameter θ is equal to the diagonal elements of the matrix inversion of $I(\theta)$: $\text{var}(\theta_i) = (I^{-1})_{ii}$. ML estimators are known to attain this lower bound asymptotically. The CRLB for the localization accuracy was calculated for Gaussians [Winick, 1986] and Airy patterns [Ober et al., 2004]. A broader framework to include width and flux was published subsequently [Ram et al., 2006]. Ram et al. [2006, 2010] reassured that typical scalar diffraction theory PSFs including Airy and Gaussian patterns lead to diagonal Fisher information matrices allowing for easy inversion of the diagonal elements. Typically, detector area is assumed to be much larger than the diffraction limited spot, which is well fulfilled.

Mortensen et al. [2010] gives the localization CRLB

$$(\Delta x_{\mathrm{CRLB}})^2 = \frac{s^2 + a^2/12}{N} \left(1 - \tau \int_0^\infty \mathrm{d}t \frac{t}{1 + \tau e^t}\right)^{-1} \tag{4.33}$$

which can be well approximated [Rieger and Stallinga, 2014] by

$$(\Delta x_{\mathrm{CRLB}})^2 = \frac{s^2 + a^2/12}{N} \left(1 + 4\tau + \sqrt{\frac{2\tau}{1 + 4\tau}}\right). \tag{4.34}$$

Similar equations have been derived for width and photon number [Rieger and Stallinga, 2014]:

$$\Delta s^2_{\mathrm{CRLB}} = \frac{s^2}{4N} \left(1 + 8\tau \sqrt{\frac{8\tau}{1 + 2\tau}}\right) \tag{4.35}$$

$$\Delta N^2_{\mathrm{CRLB}} = N \left(1 + 4\tau \sqrt{\frac{\tau}{14(1 + 2\tau)}}\right) \tag{4.36}$$

For pixelated models, the $\frac{a^2}{12}$ factors in the formulae and the definition of τ have to be omitted as they mitigate non-pixelation of the Gaussian model to first order. This mitigation is not necessary for inherently pixelated models.

4.4.4 Bayesian inference

An alternative to the frequentist paradigm of statistical inference is the Bayesian approach [Sivia and Skilling, 2012]. Each approach has its pros and cons which renders one more suitable than the other for a specific problem. To make it more complicated, there are even philosophical differences about the nature of parameters. This dispute is far from over and going on for almost a century [Bayarri and Berger, 2004], when Bayesian ideas reemerged with computer technology capable of carrying out the calculations. First, differences between frequentist and Bayesian points of view will be explained. Based on the differences, preference of one method over the other will be motivated. Then, the problem at hand of single molecule parameter estimation will be classified accordingly.

4.4.4.1 Frequentist vs. Bayesian point of view

Let $(y_i)_{i \in I}$ be data and θ a parameter of a function f corresponding to a model M of the data. In reality, independent measurements may not yield the exact same data but rather, data are stochastic. Mathematically, this means that data are random variables whose distribution is modeled as f according to the model M. For example, y_i may be detected photon numbers. Model M now includes our whole knowledge about this photon detection process, including what we implicitly know about electromagnetic radiation, quantum electrodynamics, general relativity, etc., and on the other hand the fact that photons detected are not created by design or by a lightning-wielding Zeus. In consequence, model M is encapsulated in function $f(\theta)$.

In frequentist statistics, there is one single, fixed, true value θ_T. As a consequence, the y_i are random numbers drawn from a probability $P(y_i|\theta_T)$. The joint probability of all y_i is thus

$$\prod_i P(y_i|\theta_T, M) \tag{4.37}$$

The task of statistical inference is to estimate the true, unknown value θ from the realizations y_i. Let for example be $G(x_0, y_0, I, W)_k = \mu_k$ a model of a diffraction limited spot in a image ROI under consideration for each pixel k, Poissonian photon statistics are anticipated:

$$n_k \sim \text{Poisson}(\mu_k) = e^{-\mu} \frac{\mu_k^{n_k}}{n_k!} \tag{4.38}$$

Accordingly, the joint probability to measure the actual realizations $\{n_k\}$ is

$$P(\{n_k\}|\{\mu_k\}) = \prod_k e^{-\mu_k} \frac{\mu_k^{n_k}}{n_k!} \tag{4.39}$$

Now, the dependence of the $\mu_k = G(\theta)$ is taken into account with $\theta = (\theta_1, \theta_2, ...) = (x_0, y_0, I, W)$ the parameters of model G:

$$P(\{n_k\}|\theta, G) = (P(\{n_k\}|\{\mu_k = G(\theta)_k\}) \tag{4.40}$$

As a function of the parameter, this is called the likelihood:

$$\mathscr{L}(\theta) = P(\{n_k\}|\theta, G) \tag{4.41}$$

Frequentists state that the best estimate of θ_T is the value of θ_{ML} which maximizes its likelihood, i.e. the probability that the actually realized data do realize. For many realizations r , they argue, $\theta_{ML,r}$ converges in probability towards the true value and hence the name “frequentist”: For all $\epsilon > 0$:

$$\lim_{r\to\infty} P(|\theta_{ML,r} - \theta_T|) \geq \epsilon) = 0 \tag{4.42}$$

As a remark, the concept of confidence intervals is often misinterpreted: Since from a frequentist point of view the true value θ_T is fixed, i.e. not a random variable, it has no associated probability density. Therefore, e.g. 95 % confidence intervals (a, b) cannot mean that the true value is with a probability of 95 % between a and b. Rather, θ_T is in (a, b) or not. In particular, a and b are the random variables and (a, b) being a 95 % confidence interval means that the true value is 95 % of the time (frequency!) in the confidence interval of the different realizations.

Bayesian statistics [Bayes, 1763] argues, that one is not really interested in the parameter that maximizes the likelihood of the data’s occurence or equivalently, the probability of the data given the parameter $P(n_k|\theta)$ - but in fact the most probable parameter in the light of the data: $P(\theta|n_k)$.

This quantity is in relation to the likelihood via Bayes’ rule:

$$P(B|A) = \frac{P(A|B)P(B)}{P(A)} \tag{4.43}$$

which is easily derived from the definition of the conditional probability

$$P(A|B) := \frac{P(A,B)}{P(B)} \tag{4.44}$$

where $P(A,B)$ is the joint probability of events A and B. Accordingly, not only the data, the n_ks, are random numbers but also the parameter θ. Applying Bayes’ rule we yield:

$$P(\theta|n_k) = \frac{P(n_k|\theta)P(\theta)}{P(n_k)} \tag{4.45}$$

The first factor in the numerator is the familiar likelihood. Since θ is a random number, a probability distribution can be assigned to it. In particluar, $P(\theta)$ is the distribution of the parameter irrespective of or prior to any measurement or glance at the data. Hence, $P(\theta)$ is called the prior distribution or simply the *prior*. The left hand side of the equation $P(\theta|n_k)$ the conditional distribution of the parameter given the data, i.e. in the light of data. In contrast to the prior, this quantity takes into account the measurement, is evaluated post measurement and thus called the a posteriori probability or simply the *posterior*.

Naturally, parameter distributions are interpreted as manifestations of knowledge: Narrow distributions correspond to precise knowledge as to where in parameter space the parameter is located and conversely, broader distributions correspond to less precise knowledge and ignorance.

$P(n_k)$ is parameter independent and is thus basically a normalization constant with $P(n_k) = \int P(n_k|\theta)P(\theta)\,\mathrm{d}\theta$ called the *evidence*. Evidence is an important tool in Bayesian model selection but not so relevant in parameter estimation.

The parameter value for which the posterior is maximal is called the maximum a posteriori (MAP) estimate.

$$\hat{\theta}_{\mathrm{MAP}} = \arg\max P(\theta|n_k) \tag{4.46}$$

In this sense, the prior is a penalty to the likelihood for parameter space regions considered improbable. Also, frequentists may apply a penalty to the likelihood as a means of regularization, yielding a parameter estimate based on quasi-likelihood optimization. In contrast, proper Bayesian methodology makes use of the full posterior distribution and uses the mean posterior parameter value:

$$\hat{\theta}_{\mathrm{MMSE}} = \int \theta P(\theta|n_k)\,\mathrm{d}\theta \tag{4.47}$$

The subscript MMSE indicates that this estimator is optimal in the sense that of all estimators $\hat{\theta}$ it minimizes the mean square error

$$\mathrm{MSE}(\hat{\theta}) = \langle(\hat{\theta} - \theta)^2\rangle \tag{4.48}$$

$$\hat{\theta}_{\mathrm{MMSE}} = \arg\min \mathrm{MSE}(\hat{\theta}) \tag{4.49}$$

where the mean is taken over all possible θ and data n_k realizations..

However, the integral in the definition of $\hat{\theta}_{\mathrm{MMSE}}$ is hardly tractable with trapezoidal numerical evaluation by sampling the parameter space: For 9 × 9 pixels, spatial parameter sampling with 5 nm steps within the 9 × 9 ROI, sampling of 100 steps for the flux, the width and the offset parameter, $9 \cdot 9 \cdot 900/5 \cdot 900/5 \cdot 100 \cdot 100 \cdot 100 \approx 2.610^{12}$ evaluations would have to be done. The solution to this is integration by *Markov chain Monte Carlo* (MCMC).

4.4.4.2 The Monte Carlo method

Instead of the trapezoidal approximation of the definite integral $\int_\Omega f(x)\,\mathrm{d}x$ of a function $f : \mathbb{R}^n \supset \Omega \to \mathbb{R}$ to be computed deterministically, the Monte Carlo method [Metropolis and Ulam, 1949] of integration is to draw random samples from the parameter space and average the values of the function to integrate at these points. For $V = \int_\Omega \mathrm{d}x$ and N uniform samples $x_1, x_2, ..., x_N$, the integral can be approximated:

$$\hat{\mu}_N := V\frac{1}{N}\sum_{i=1}^{N} f(x_i) \approx \int_\Omega f(x)\,\mathrm{d}x$$

In fact, under “nice” conditions [Geyer, 1992], $\hat{\mu}_N \to \int_\Omega f(x)\,\mathrm{d}x$ almost surely by virtue of the law of large numbers and $\lim\limits_{N\to\infty} \hat{\mu}_N - \int_\Omega f(x)\,\mathrm{d}x \sim \mathcal{N}(0,\sigma^2)$ by virtue of the central limit theorem. For a more detailed discussion of the various differently strong formulations and their asymptotic behavior of both the law of large numbers and the central limit theorem with regard to MCMC, which is beyond the scope of this thesis, see Tierney [1994].

Markov chain Monte Carlo methods overcome the drawbacks of rejection sampling Monte Carlo methods: The latter produces random samples of a specified distribution by drawing random numbers of a simple majorant distribution and rejects according to the discrepancy between majorant and the distribution of interest. This strategy is, however, subject to the “curse of dimension” illustrated by the exponential decay in acceptance of the sampling of a n-dimensional unit sphere from a unit n-hypercube majorant for increasing n.

Markov chain Monte Carlo (MCMC) makes use of the eponymous Markov chains to overcome those inefficient rejection rates. Marcov chains are (discrete time) stochastic processes with the Markov property, i.e. the state of the system in the next timestep is only dependent on the present state, which is also known as memorylessness. Formally, a Markov chain is a sequence of random variables $X_1, X_2, X_3, \ldots, X_t, \ldots$ with

$$P(X_{t+1} = x | X_1 = x_1, X_2 = x_2, \ldots, X_t = x_t) = P(X_{t+1} = x | X_t = x_t) \tag{4.50}$$

if both probabilities are well defined, i.e. $P(X_1 = x_1, X_2 = x_2, \ldots, X_t = x_t) > 0$. In our context, the X_t of course refer to positions in parameter space which is explored by the Markov chain, the x_t are called the states of the Markov chain. Different designs of transition probabilities $P(X_{t+1} = x | X_t = x_t)$ refer to different updating algorithms. Markov chains with time-independent transition probabilities $\pi_{ij} = \pi_{ij}(t) = P(X_t + 1 = x_j | X_t = x_i)$ are called *homogeneous*. A homogeneous Markov chain is called *irreducible* if and only if it is possible to get from any state to any state in finite time. A state x_t is called periodic, if a return to state x_t can only occur in regular time steps. On the other hand, a state x_t is called aperiodic if there exists a $n \in \mathbb{N}^0$ such that for all $\grave{n} \geq n : P(X_{\grave{n}} = x_t | X_0 = x_t) > 0$. Aperiodic Markov chains are Markov chains were all states are aperiodic. A homogeneous Markov chain – or more colloquially the distribution of $\pi(x_i) = \pi_i$ is the states – is said to be stationary, if and only if for all x_i

$$0 \leq \pi_i \leq 1 \tag{4.51}$$

$$\sum_i \pi_i = 1 \tag{4.52}$$

$$\pi_i = \pi_j \pi_{ji} \tag{4.53}$$

Even more, a Markov chain not necessarily has to be time-homogeneous to have an equilibrium distribution. The property of detailed balance

$$\pi(x_i) P(X_{t+1} = x_j | X_t = x_i) = \pi(x_j) P(X_{t+1} = x_i | X_t = x_j) \tag{4.54}$$

of reversible Markov chains is sufficient for the existence of an equilibrium distribution. Now in MCMC, transition probabilities are designed so that the stationary distribution is the distribution of interest, i.e. in our case the posterior. Different designs are possible, one very general design [Hastings, 1970] decomposes the transition probability π_{ij} into a new state proposal probability $q(x_i, x_j)$ and an acceptance probability $\alpha(x_i, x_j)$:

$$\pi_{ij} = \begin{cases} q(x_i, x_j)\alpha(x_i, x_j) & \text{if } i \neq j \\ 1 - \sum_k q(x_i, x_k)\alpha(x_i, x_k) & \text{if } i = j \end{cases} \tag{4.55}$$

$$\alpha(x_i, x_j) = \begin{cases} \min\left(\frac{\pi(x_j) q(x_j, x_i)}{\pi(x_i) q(x_i, x_j)}, 1\right) & \text{if } \pi(x_i) q(x_i, x_j) > 0 \\ 1 & \text{if } \pi(x_i) q(x_i, x_j) = 0 \end{cases} \tag{4.56}$$

For $q(x_i, x_j) = q(x_j, x_i)$, we have we have $\alpha(x_i, x_j) = \min(\pi(x_j)/\pi(x_i), 1)$, which is the Metropolis algorithm [Metropolis et al., 1953].

In the case of multidimensional $X_t = (x_{t,1}, x_{t,2}, ..., x_{t,k}, ..., x_{t,K})$, one basic strategy to explore the parameter space is to successively sample from the conditional distributions $\pi(x_j|x_{-j})$, where $x_{t,-j} := (x_{t,1}, x_{t,2}, ..., x_{t,j-1}, x_{t,j+1}, ...x_{t,K})$ as follows [Smith and Roberts, 1993]:

$$x_{t+1,1} \text{ from } \pi(x_1|x_{t,-1}) \tag{4.57}$$

$$x_{t+1,2} \text{ from } \pi(x_2|x_{t+1,1}, x_{t,2}, x_{t,3}, ..., x_{t,K}) \tag{4.58}$$

$$x_{t+1,3} \text{ from } \pi(x_2|x_{t+1,1}, x_{t+1,2}, x_{t,3}, ..., x_{t,K}) \tag{4.59}$$

$$... \tag{4.60}$$

$$x_{t+1,K} \text{ from } \pi(x_K|x_{t+1,-K}) \tag{4.61}$$

This scheme is called Gibbs sampling, a special kind of Metropolis-Hastings. It should be mentioned that although „Markov chain“ terminologically refers to the stochastic process, the *realizations* of a run are occasionally refered to as a specific "chain" as well, or interchangably, as a run. This technically non-correct usage should be interpreted as a metonymy, a figure of speech, and should not lead to any misunderstandings.

4.4.4.3 OpenBUGS and MCMC

The open source software openBUGS [Lunn et al., 2009], a decendant of WinBUGS [Lunn et al., 2000], was used in this thesis. WinBUGS itself uses the BUGS (Bayesian inference Using Gibbs Sampling) language [Spiegelhalter et al., 1996], which allows to specify hierarchical models by means of directed acyclic graphs (DAG) [Lauritzen et al., 1990]. Basically, hierarchical models consist of deterministic and stochastic nodes containing constants or random numbers; values from declared nodes can themselves be used as input for deterministic nodes such as for a arithmetic operation or for a stochastic one, i.e. as input parameterizing the distribution a random number is drawn from. In the end, "final" nodes are compared to data supplied, and during the so called burn-in phase, a Markov chain explores the parameter space of the initial nodes and eventually equilibrates at values that "reproduce" the data downstream the directed acyclic graph of the model. Of course, the initial stochastic nodes correspond to the parameter to infer and their distribution is the respective prior. Occasionally, parameters of a prior distribution are not fix in their own right, but themselves modeled as random numbers, acknowledging ignorance on a higher level. The distributions, and by analogy their parameters, of prior parameters are called hyper-priors.

Gibbs sampling is predestined for hierarchical models, as only conditional probabilities are needed for computation which are at the same time the natural inputs of model design and prior parameters.

4.5 Tracking

In order to retrieve information on dynamics from localizations, localizations from different time points have to be related to each other. This can either be done by assessment of the correlation between a localization r at time t and localizations r' at timepoints $t' > t$ [Semrau and Schmidt, 2007, particle image correlation spectroscopy (PICS)] or by tracking. Essentially, PICS is based on estimation of the propagator (see section 2.5.1). While PICS offers some serious advantages including robustness against high localization densities and in principle the direct estimation of the immediate (un-mediated, motion model independent) propagator, the current implementation requires extensive manual parameter adjustment. The alternative, multi target tracking is a difficult task in computer vision. Especially in single molecule tracking, gaps occur in particle traces due to finite detection probability, sub-rayleigh distance overlapping, and temporary non-fluorescent states ("blinking"), in particular under the noisy imaging conditions that come with 3D cell cultures. The optimal approach to join localizations to tracks is *multiple hypothesis testing* [Reid, 1979, there in the cold war context of missile defense, air defense, ocean and battlefield surveillance], where all possible tracks in a particle ensemble image sequence are explored and the globally optimal set of non-conflicting tracks is returned. However, even for tens of particles imaged for tens of consecutive frames, this is computationally prohibitive. Simpler algorithms called "greedy" join subsequent localizations based on proximity to the last known position and stop tracks on the criterion of threshold distances. Greedy tracking is known to perform poor on traces with gaps and high tracer density [Chenouard et al., 2014]. A list of available implementations of different tracking algorithms is given in Meijering et al. [2012]. Most promising are approaches that combine the computational efficiency of nearest neighbour linking and global optimization, as was done by Jaqaman et al. [2008], where a first step links localizations to track segments based on Kalman filter application in time and in reverse time (exploiting symmetry with regard to the direction of time), and then, in a second step, optimizes the joining of track segments (also across gaps) globally, i.e. considering the set of all segments within the framework of the linear assignment problem (LAP, [Burkard and Cela, 1999, Jonker and Volgenant, 1987]). The much cited alternative Sergé et al. [2008] goes from frame to frame, linking localizations based on likelihoods on the assumption of free diffusion. However, the global optimization step of Jaqaman et al. [2008] seems to contribute greatly to its success [Rolfe et al., 2011, Sibarita, 2014]. Therefore, the implementation of Jaqaman et al. [2008] was used in this thesis after its reliability was tested (section 5.1.10).

5 Measurements

5.1 Simulations

5.1.1 Background estimation

In order to evaluate the estimation of background signals, simulations were performed. Simplified models, e.g. flat background, do not reflect the complex signals sufficiently. Accordingly, a more realistic background which takes into account actual spatial signal variations encountered when imaging cells in 3D hydrogels due to heterogeneous scattering in the presence of out of focus fluorescence was modeled as a average frame of a typical real measurement. The specimen was U2OS cells embedded in collagen hydrogel marked with membrane marker CellMask™Orange (Thermo Fisher Scientific, Waltham, MA, USA; see section 3.5), imaging depth was 20 μm. The obtained average frame was subsequently scaled by a factor $0.1 \leq s \leq 10$ to quantify the performance dependency on signal height. Scaling rather than addition of different offsets was done on the basis of considerations of signal scaling dependency on integration time per frame or illumination intensity. The original average frame background model M is displayed in figure 5.1, pixel values correspond to photon numbers. The mean photon count was 10.53 ± 0.85 (standard deviation).

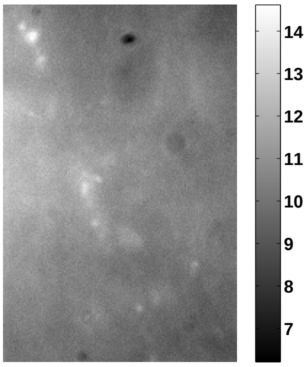

Figure 5.1.: original background model based on measurement average, pixel values in photon numbers

For each scaling factor, 200 frames were generated and subsequently subjected to Poisson noise, i.e. each pixel value was used as the expectation value of a Poisson pseudo-random number generator. These data $M \cdot s$ were used to quantify the performance of different techniques to accurately estimate the background ($\hat{B}$) in terms of the root mean square (RMS) deviation $\sqrt{\langle (\mathrm{Poisson}(Ms) - \hat{B})^2 \rangle}$, where the mean $\langle \cdot \rangle$ is taken over all pixels of all frames (figure 5.2). For comparison, the RMS deviation of the true background to the noisy variant $\sqrt{\langle (\mathrm{Poisson}(Ms) - Ms)^2 \rangle}$ was included as item "no" estimation. "naive" refers to the method of section 4.1.2, "average" to spatially moving average (section 4.1.3), "time" to pixel-wise time average (section 4.1.1), "median" to moving median (section 4.1.4.1), "wiener" to the "naive" method with prior denoising using the adaptive Wiener filtering technique (section 4.2.1), and "bordermedian" to the method of background estimation by a moving median using the border of a square mask only.

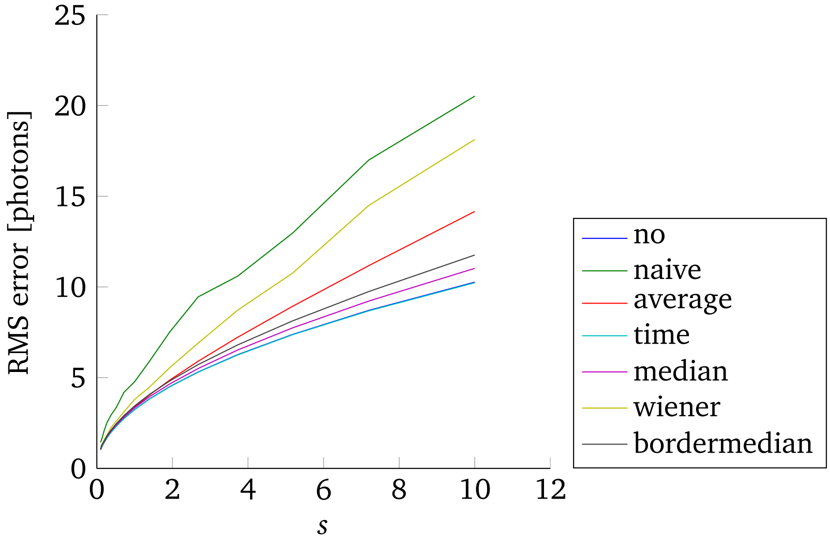

Figure 5.2.: root mean square error of background estimation techniques at the Poisson corrupted image of figure 5.1, scaled by a factor of s before corruption.

By design, this background model is simplistic as it e.g. does not include *moving* out-of-focus fluorophores, cell organelles, etc. Obviously, temporal averaging is destined to converge to the true background. On the other side, this can be seen as an indicator, that 200 frames are sufficient to cancel out variance in the performance due to the randomness from simulation to simulation.

In order to account for bleaching effects, scaled pixels ($sM(x,y,t)$) were weighted with an exponential, mimicking first-order bleaching kinetics. The decay time constant was chosen so that in the final frame the signal height was half the initial value in the first frame: $sM(x,y,t) \cdot \exp(-\frac{t}{199 \ln 2}), t = 0, \ldots, 199$. The results of this simulation are shown in figure 5.3.

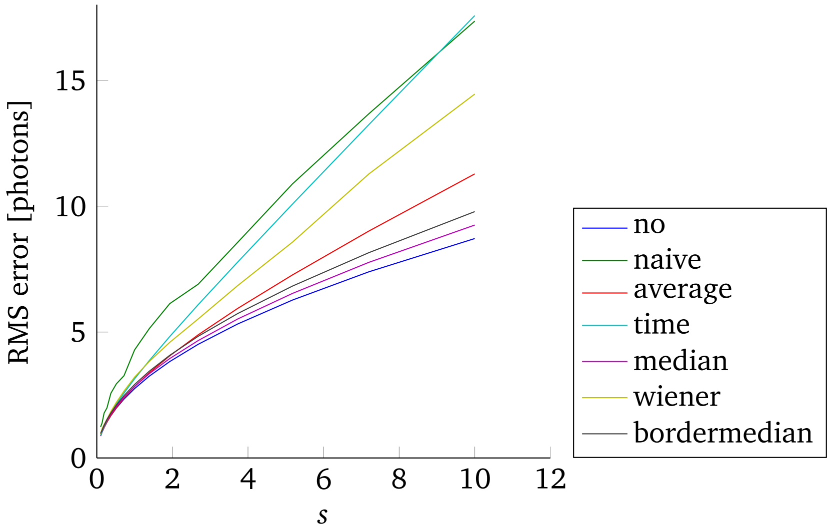

Figure 5.3.: root mean square error of background estimation techniques at the Poisson corrupted image of figure 5.1, scaled by a factor of s and time-dependent exponential bleaching before corruption.

Under these conditions, temporal average performs considerably less well. This should be kept in mind, when turning to the further investigation how performances are in the presence of in-focus fluorophores. To this end, 20 emitter were placed at random on each frame, with the PSF approximated by a pixelated Gaussian with FWHM 2.35 pixels and 100 photons per frame. Corruption by Poisson noise was performed after emitter placement to properly account for flux stochasticity. RMS deviations were calculated from background without emitters. For a proper comparison, emitter-free background was Poisson corrupted as well. With $E = E(x, y, t)$ the expected emitter photon counts: $\mathrm{RMS} = \sqrt{\langle(\mathrm{Poisson}(Ms) - \hat{B}(\mathrm{Poisson}(Ms + E)))^2\rangle}$, where now the underlying data $Ms+E$ of the estimate $\hat{B}$ is explicated for clarity. Bleaching was not modeled to allow for straightforward signalheight to performance relation. The "no" item in figure 5.4 corresponds to the quantity $\sqrt{\langle(\mathrm{Poisson}(Ms) - \mathrm{Poisson}(Ms + E))^2\rangle}$, which is included for comparison of magnitude.

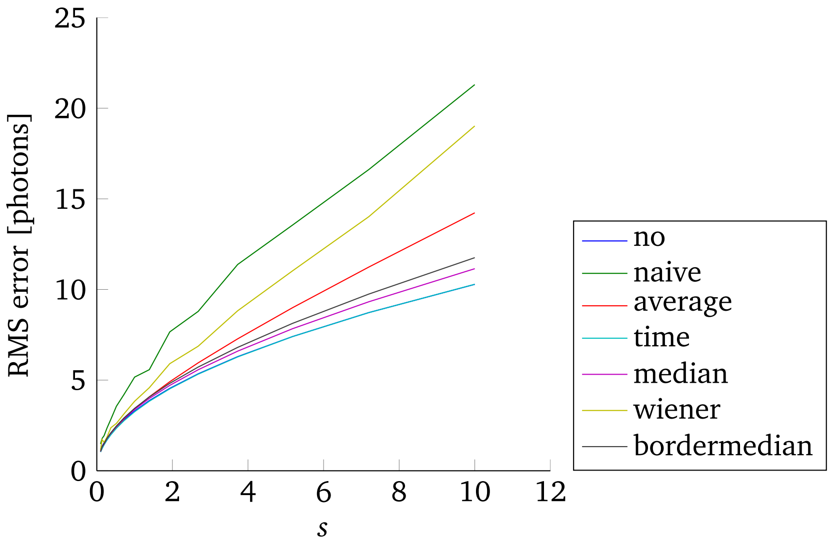

Figure 5.4.: root mean square error of background estimation techniques at Poisson corrupted data of figure 5.1 scaled by a factor of s and presence of randomly placed emitters.

As can be concluded from figures 5.2, 5.3, and 5.4, median filtering is most effective under realistic conditions. Of note, the Wiener filtering and naive estimation combination is superior to moving average filtering in the case of unscaled background plus high offsets (>100 photons per pixel, not shown). The different approaches of background estimation investigated were carried out with different kernel/sliding window sizes. For instance, the moving average window size was set to a larger size than the moving median method in order to mitigate the lower robustness due to linearity. Kernel sizes used are listed in table 5.1.

method	kernel dimension
moving average	10×10
moving median	9×9
Wiener filter	4×4
border median	9×9

Table 5.1.: kernel dimensions of background estimation techniques investigated

Note that the border median method calculates its statistic from $9 \times 9 - 7 \times 7 = 32$ pixels and not 81. A larger window of the Wiener filter method would take into account more non-local values and albeit more robust, is expected to perform even poorer. To investigate the tradeoff between robustness and locality, median filtering was done with different kernel sizes. Obviously, at emitter absence, a filter kernel of size one yields the identity map where input equals output. As evident, performance tests have to include emitters. It should be noted that emitter density is a major impact on background estimation performance when there is considerable overlap of diffractively blurred spots. At higher densities, smaller kernels might lead to background estimation at a fluorophore location just not influenced by nearby fluorophores, increasing robustness. Too small kernels however, as pointed out, are prone to misconceive emitter signals as background, meaning adverse background overestimation at fluorophore presence that makes candidate position identification unnecessarily hard.

Another thing to keep in mind is that the degree of heterogeneity in the background signal which of course varies from measurement to measurement has an influence of the optimal kernel dimensions: In homogeneous background scenarios, larger kernels are favorable. In contrast, heterogeneous backgrounds call for appreciation of the locality of the signals by employment of smaller kernels that not overly neglect medium lengthscale variations.

That said, to provide a grasp of the order of magnitude on the background estimation performance, median filtering was investigated at different kernel sizes. Similar to before, 20 emitters with a expectation value of 100 detected photons were placed on each frame and the RMS deviation $\mathrm{RMS} = \sqrt{\langle(\mathrm{Poisson}(M) - \hat{B}_d(\mathrm{Poisson}(M+E)))^2\rangle}$ was calculated for each kernel size $d \times d$. As can be seen in figure 5.5, the moving average approach is robust against sliding window misspecifications. The Wiener filter approach of applying a Wiener filter before carrying out the “naive” estimation as layed out above shows improving behavior for larger sliding window sizes, yet alway poorer than the alternatives in the range of window sizes under investigation. Median filtering shows a distict minimum in RMS error, located at $7 \leq d \leq 11$ pixels kernel edgelength. Note that kernel edgelengths have to be odd in order to prevent spatial shifts of the estimated background signal.

In consequence, median filtering with a sliding window size of 9×9 pixels will be used henceforth in this thesis.

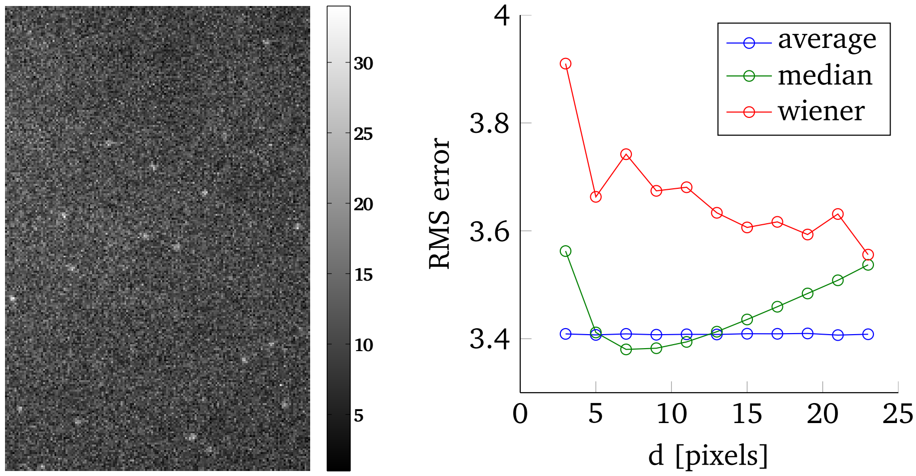

(a) typical frame with 20 emitters

(b)

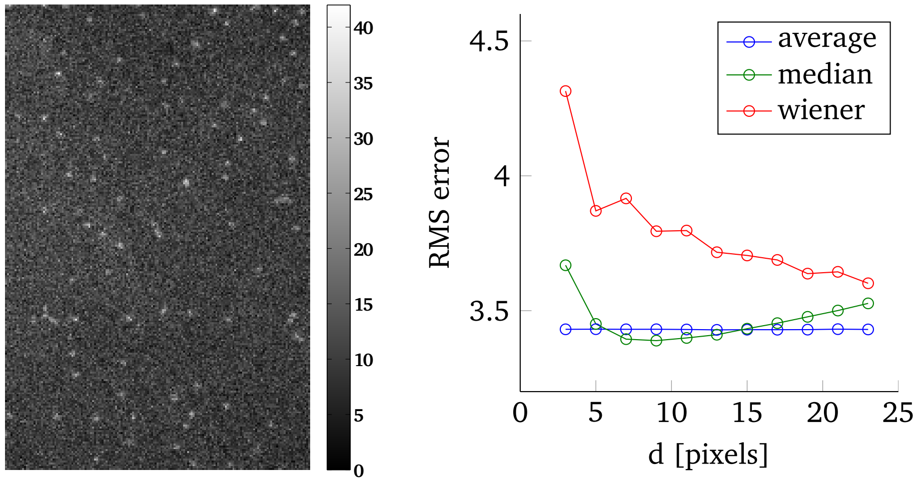

(c) typical frame with 100 emitters

(d)

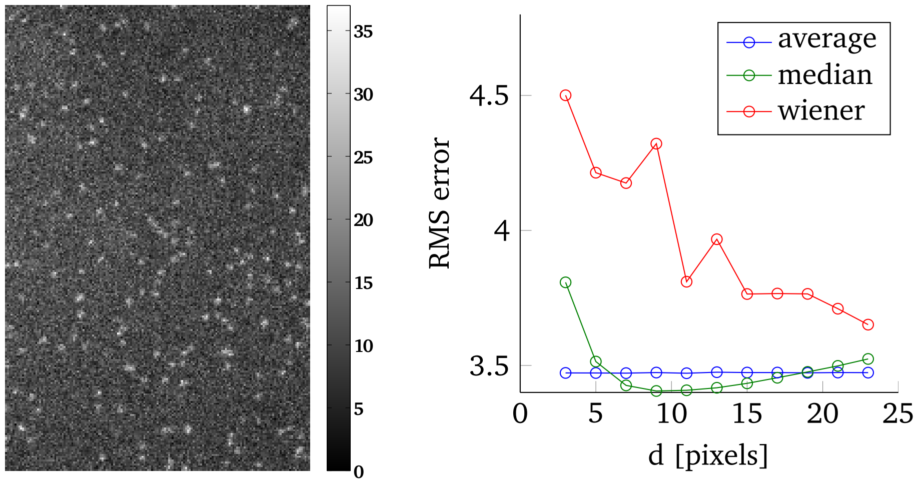

(e) typical frame with 200 emitters

(f)

Figure 5.5.: (b,d,f) RMS deviation in photons for moving average, moving median and Wiener filter background estimation at $d \times d$ pixels sliding window size. **(a,c,e)** Typical frames of simulated data with 20, 100, and 200 emitters per frame.

5.1.2 Noise estimation

The estimation of present noise is an important task in the challenge of candidate position identification. As opposed to the theoretical approach of simply using the previously estimated background at hand and exploiting equality of the expectation value and the variance for any Poisson distributed random number X, the "empirical" approach takes into account the local variation in the background, i.e. explicitly including deviation from the "locally flat" hypothesis. Note that this takes into account deviations from Poisson noise including multiplicative noise and readout noise contributions.

A classic robust estimator for statistical dispersion, used e.g. in [Olivo-Marin, 2002], is the median absolute deviation from the median (MAD):

$$\mathrm{MAD} = \mathrm{median}_i(|X_i - \mathrm{median}_j(X_j)|) \tag{5.1}$$

For Gaussian distributed X, the relation between the MAD and the estimate for the standard deviation $\hat{\sigma}$ is $K\mathrm{MAD} = \hat{\sigma}$ with $K = 1/\Phi(\frac{3}{4})^{-1} \approx 1.4826$, Φ is the standard normal cumulative distribution function and Φ^{-1} is its inverse also known as its quantile function. However, there is no "standard Poisson distribution" that could be scaled and shifted to any Poissonian distribution. Also, the Poissonian distribution is nonsymmetric while symmetry $\Phi(-x) = 1 - \Phi(x)$ is used in the derivation of $K = 1/\Phi(\frac{3}{4})^{-1}$. In order to assess the strategy of noise estimation by means of MAD, figure 5.6 shows the obtained $\hat{K} = \frac{\sqrt{\lambda}}{\mathrm{MAD}(\mathrm{Poisson}(\lambda))}$ of 5000 random numbers Poisson(λ) per datapoint. Obviously the nested nonlinearity of the median in the MAD estimate yields complex, nonmonotonic behavior. For the sake of simplicity, in order to test the capabilites of MAD for empirical noise estimation, the K factor was chosen according to the Gaussian model, $K = 1.4826$. Performance was evaluated with simulated Poissonian noise: A 220×220 array with a constant slope from 0 on the left to 30 on the right side was corrupted by Poisson noise with 500 realizations. To assess the reliability of the noise estimation, root mean square (RMS) deviations were calculated of the estimated noise standard deviation from the theoretical noise standard deviation according to Poisson statistics. With default zero padding, i.e. virtual pixels with zeros at the array borders that ensure that the filtered image is of the same dimensions as the unfiltered original, artifacts appear in the borders of the noise estimation map. To circumvent these artifacts which saturate any colormaps that provide relevant information about the actual accuracy of the noise estimation, 10 pixel margins of all borders with artifacts were cropped from the RMS map in figure 5.7. What can be seen is that the MAD applied to Poissonian noise is of rather poor performance and unexpectedly, is subject to interference of the inner and outer median's nonlinearity. Since local gradients in signal intensity, and thus photon shot noise may be encountered for instance due to uneven excitation light illumination, another approach to noise estimation is advised.

To tackle this issue, square deviations from the 3×3 moving average filtered image were calculated, subsequently 15×15 averaged and taken the square root from. In figure 5.8, the root mean square error of the estimated noise standard deviation to the theoretical value is depicted, again the mean being taken from 500 realizations:

$$\hat{\sigma}(x,y) = \sqrt{\left\langle \left(n(\dot{x},\dot{y}) - \langle n(\xi,\phi) \rangle_{(\xi,\phi)\in[\dot{x}-1,\dot{x}+1]\times[\dot{y}-1,\dot{y}+1]} \right)^2 \right\rangle_{(\dot{x},\dot{y})\in[x-7,x+7]\times[y-7,y+7]}} \tag{5.2}$$

$$\mathrm{RMS}_{\hat{\sigma}} = \sqrt{\left\langle \left(\hat{\sigma}_i - \sqrt{\mu(x,y)} \right)^2 \right\rangle_{i\in 1,\ldots,500}} \tag{5.3}$$

This definition of a noise estimator was designed so that the inner averaging of the local signal is taken over a region smaller than the PSF's dimensions and the outer averaging of the square deviation considerably larger than the PSF's dimensions. Noise estimation at emitter presence as simulated in figure 5.9a, Poisson corrupted version in figure 5.9b, is shown in figure 5.9c. Artifacts at the border are

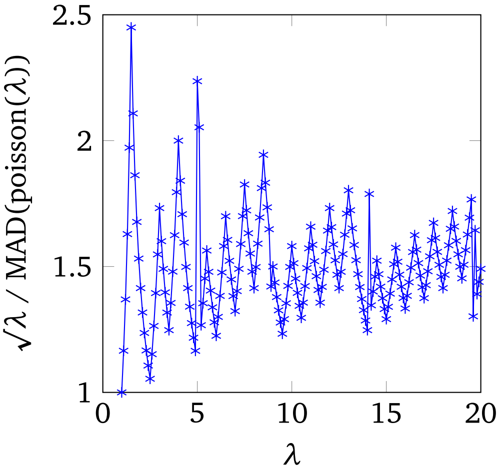

Figure 5.6.: Median absolute deviation from the median to standard deviation calibration curve. 5000 Poissonian random numbers per datapoint. Median's nonlinearity leads to complex, non-monotonic behavior.

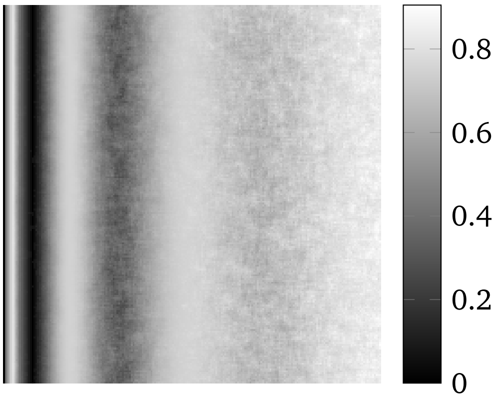

Figure 5.7.: RMS accuracy in noise standard deviation estimation by means of MAD. Average taken from 500 realizations. Ground truth Poisson variance ranges from 0 (left) to 30 (right), 10 pixel cropping margin. Nested nonlinearities interfere with each other.

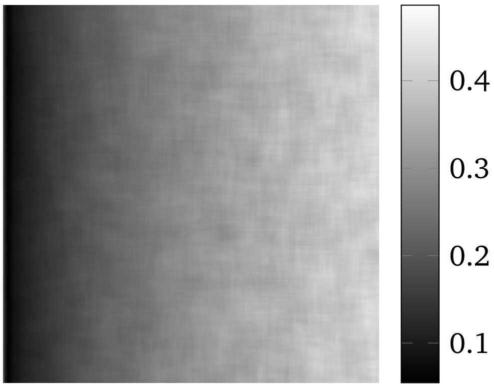

Figure 5.8.: RMS accuracy in noise standard deviation estimation by means of local RMS signal deviation according to equation 5.3. Average taken from 500 realizations. Ground truth Poisson variance ranges from 0 (left) to 30 (right), 10 pixel cropping margin. Monotonic decrease in accuracy for larger noise.

not cropped. Keep in mind that in real data analysis, fluorophore candidate positions are only considered if a “safety margin” is kept related to the size of the localization ROI.

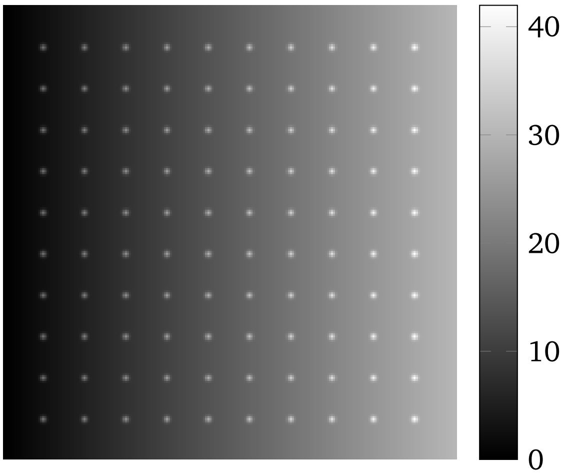

(a) Simulation expectation values, gradient plus emitters á 100 photons.

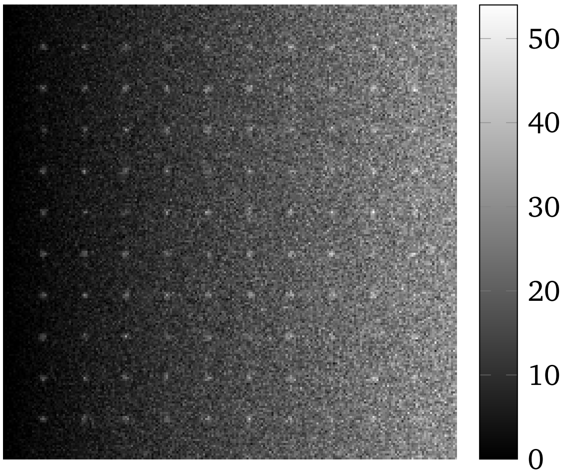

(b) Poisson corruption.

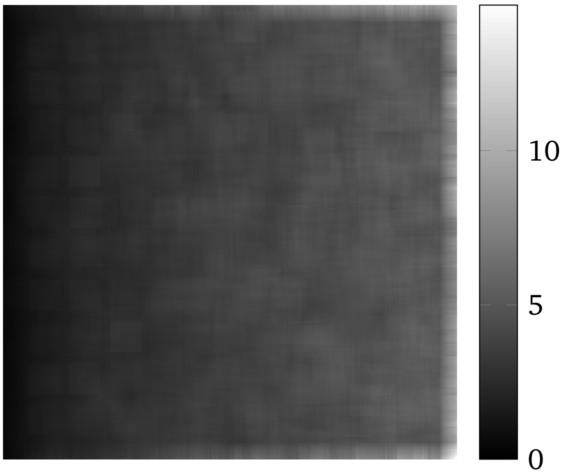

(c) Noise standard deviation estimation from Poisson corrupted data.

Figure 5.9.: Noise estimation at emitter presence.

5.1.3 Denoising

In order to investigate the capabilities of the denoising approaches of section 4.2, emitters were simulated on flat background at different signal to noise ratios (SNRs). In these simulations, the detected fluorophore photon number per frame was chosen to be 100 as this is a realistic, typical value. Different SNRs were realized by adjusting the background level before corrupting the data by Poisson noise.

There is quite a jungle of definitions of the SNR, varying from discipline to discipline. Electrical engineering and signal processing tend to use ratios of squared signals and noise standard deviations as they are ordinarily interested in the power of a transmitted signal while measuring voltages ($P = UI = U^2/R$), given in dB. Single molecule microscopists with these influences such as [Sergé et al., 2008] tend to report their SNR values as

$$\mathrm{SNR}_{\mathrm{EE}} = 10\log_{10}\left(\frac{\hat{I}^2}{\sigma_N^2}\right)[\mathrm{dB}] = 20\log_{10}\left(\frac{\hat{I}}{\sigma_N}\right)[\mathrm{dB}] \tag{5.4}$$

Where $\hat{I}$ is the signal above background at the peak and σ_N the background signal noise standard deviation. Denoising literature, e.g. Luisier et al. [2010], Deledalle and Tupin [2010], uses the peak signal and gives SNR in dB.

$$\mathrm{SNR}_{\mathrm{denoise}} = \mathrm{PSNR} = 20\log_{10}\left(\frac{I_{\max}}{\sigma_N}\right)[\mathrm{dB}] \tag{5.5}$$

where $I_{\max}$ is the peak signal including background.

Image processing influenced single molecule microscopists [Jaqaman et al., 2008, Larkin and Cook, 2012], but also Yoon et al. [2008], Robin et al. [2014], Meckel et al. [2011] use the rather straightforward

$$\mathrm{SNR}_{\mathrm{im}} = \frac{\hat{I}}{\sigma_N} \tag{5.6}$$

Also, there is the variant

$$\mathrm{SNR}_{\mathrm{im2}} = \frac{\hat{I}^2}{\sigma_N^2}. \tag{5.7}$$

Note that due to the nature of the photons, optical power is proportional to the intensity which means SNR $\propto \hat{I}$ seems more logical than SNR $\propto \hat{I}^2$or $\propto \log_{10}\hat{I}^2$. However, even the classical photonics textbook Saleh and Teich [2008] uses the squared version $\mathrm{SNR}_{\mathrm{im2}}$. Furthermore, versions are in use (e.g. in Schmidt et al. [1996]) where instead of the peak signal above background, the integral signal above background I is used:

$$\mathrm{SNR}_{\mathrm{im3}} = \frac{I}{\sigma_N} \tag{5.8}$$

A SNR definition peculiar to single molecule microscopy is accounting for the increased signal noise at the location of interest due to the Poisson distribution, eg. used by Kubitscheck et al. [2000], Cheezum et al. [2001], Izeddin et al. [2012], Chenouard et al. [2014], Andersson [2008]:

$$\mathrm{SNR}_{\mathrm{SM}} = \frac{\hat{I}}{\sqrt{\sigma_N^2 + \sigma_S^2}} \tag{5.9}$$

with $\sigma_S^2 = I$.

In the following discussion of detection efficiency, SNR refers to the straightforward definition of $\mathrm{SNR}_{\mathrm{im}}$. For the practicioner, this definition furthermore has the advantage that the SNR can be easily *ad hoc* calculated during a measurement, prior to more rigorous analysis, because the camera count to photon number conversion factor cancels out and peak values can be obtained effordless in contrast to integral fluxes which are available post analysis only. In postprocession, however, $\mathrm{SNR}_{\mathrm{im3}}$ is more advantageous since it is not as susceptible to single pixel outliers as $\mathrm{SNR}_{\mathrm{im}}$.

SNR values were logarithmically evenly spaced from 1 to 10. Within a 39 × 39 square an emitter is placed at random within the central pixel in order to account for subpixel location effects on the PSF, which was approximated by a pixelated Gaussian with 2.35 pixels FWHM equivalent to 235 nm at a pixelsize of 100 nm. Background was flat and calculated from the corresponding SNR value of a centrally located PSF, assuming Poisson noise. The randomly placed fluorophore plus the additive background were then corrupted by Poisson noise. Typical realizations can be seen in figure 5.10. For each SNR value, 500 emitters were simulated.

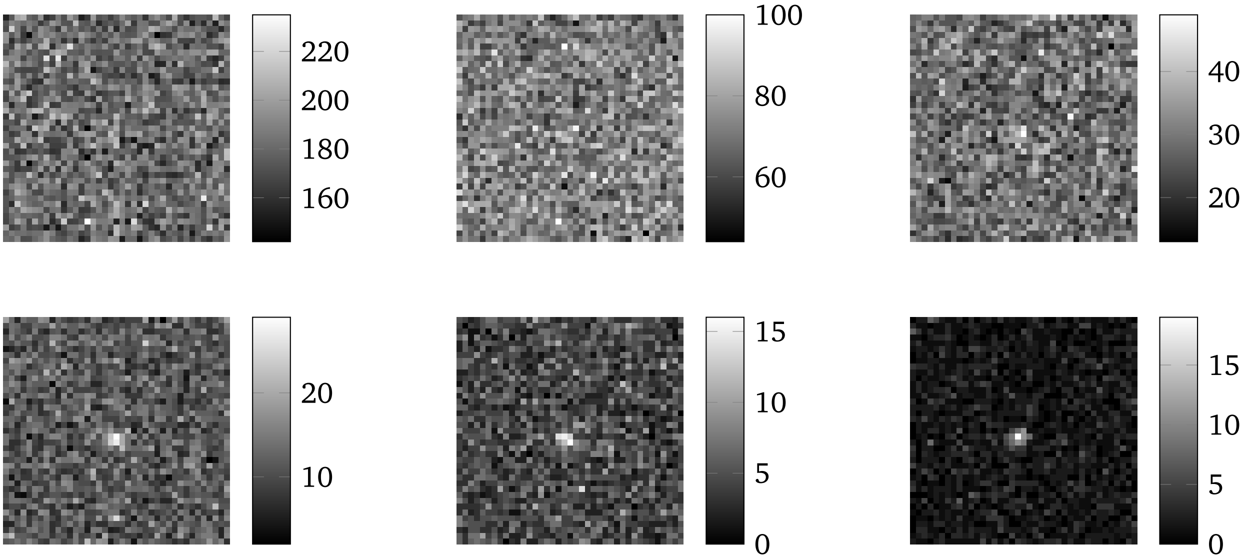

Figure 5.10.: Samples of simulated data. SNR equal to 1, $10^{0.2} \approx 1.6$, and $10^{0.4} \approx 2.5$ from left to right in the upper row and $10^{0.6} \approx 4.0$, $10^{0.8} \approx 6.3$, and 10 in the lower row

Figure 5.11 displays the improvement in SNR by convolution of Gaussian kernels of different widths. The improvement is given as the ratio of the SNR after and before the denoising procedure. These two SNR values are determined as the ratio of the mean central pixel value minus the applied background level to the root mean square deviation of the whole dataset from the uncorrupted data.

One can see that for severely corrupted data, signals of interest are potentially blurred away as indicated by the < 1 factor of improvement. Interestingly, kernel widths smaller than the signal width perform better than the matched filter of width 2.35 pixels which is anticipated to be optimal in presence of additive white Gaussian noise.

The performance of median filtering is shown is figure 5.12. While median filters are robust in the absence of emitters, emitter signals of interest may be nonlinearly spread out or diminished dependent on the relation of PSF and filter dimensions. In particular, median filters with edge dimensions > 3 pixels effectively filter the emitter away. However, filters with edge dimensions of a even number of pixels introduce an anisotropy which is detrimental for localization and explains the better performance of the 3 × 3 filter against the 2 × 2 filter.

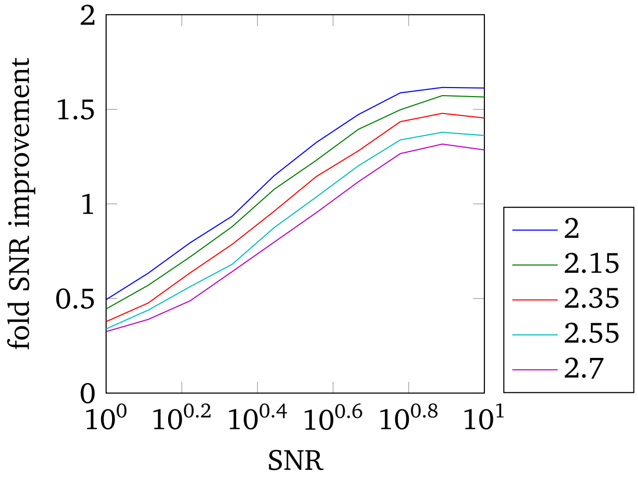

Figure 5.11.: Performance of Gaussian blur denoising for different kernel FWHMs in pixels: SNR improvement vs. SNR

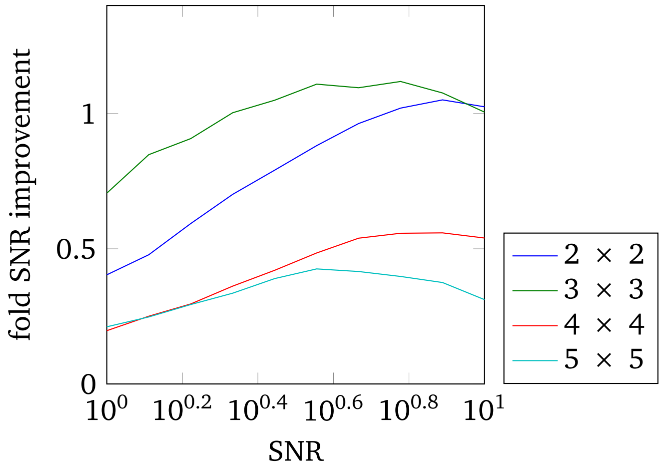

Figure 5.12.: Performance of median filtering denoising for different filter dimensions in pixels: SNR improvement vs. SNR

As can be seen in figure 5.13, adaptive Wiener filtering also filters away emitters under low SNR conditions at filter dimensions larger than 3 × 3. While not as performing in the high SNR regime as the larger filters, 2 × 2 and 3 × 3 sized filters do improve the SNR also in the low SNR regime.

In figure 5.14, non local means denoising was assessed using a 3 × 3 search window and a 5 × 5 similarity window at different filtering parameters h (see equation 4.2). The curves for $h = 2$, $h = 5$, and $h = 8$ nicely show that optimal h values correspond to the noise level (in terms of noise variance).

Figure 5.15 shows the performance of PURE-LET denoising (see section 4.2.4) for LET_1 and LET_2 using different numbers of spin cycles. Greater numbers of cycles have a positive effect but scale with computation time. It seems that taking into account higher (i.e. coarser) levels of wavelet analysis does not improve but rather deteriorates the denoising. The maximum number of wavelet levels is determined by the data dimensions and the degree of expansion of the thresholds. The behavior of the denoising at low wavelet levels encourages further expansion of thresholds which is shown in figure 5.16. One can see the additional benefit in comparison to figure 5.15. Moreover, one can see that first level wavelet consideration seems to perform well regardless of the SNR while second level wavelet consideration seems to give extra benefit in the higher SNR regime but poorer performance than the single wavelet denoising in the low SNR regime.

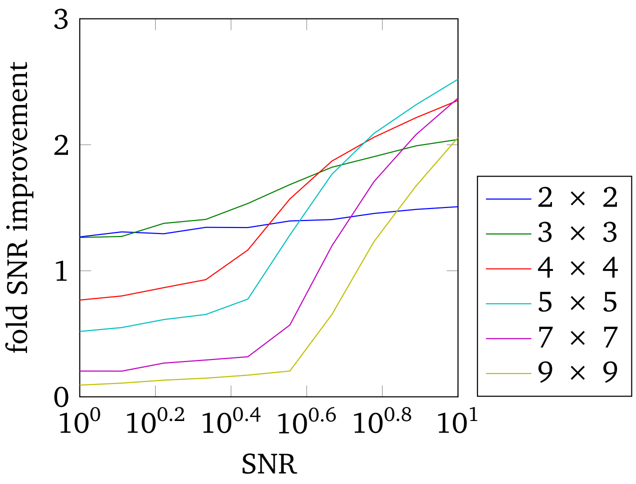

Figure 5.13.: Performance of adaptive Wiener filtering denoising for different filter dimensions: SNR improvement vs. SNR

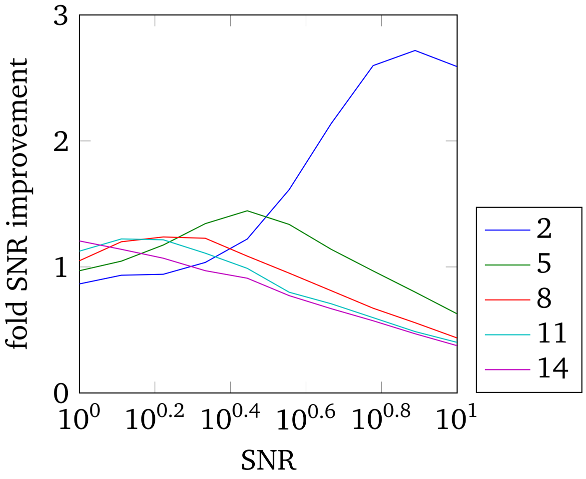

Figure 5.14.: Performance of non local means denoising for different h parameters: SNR improvement vs. SNR

5.1.4 Detection of candidate positions

In order to evaluate the different techniques for fluorophore detection introduced in section 4.3, detection efficiency and false positive rates were determined. More specifically, each technique was applied using a range of method parameters such as thresholds to simulated data at different SNRs. For each SNR value and detection technique, 5000 emitters were simulated so that emitter position and noise realizations were averaged out for reliable detection quantification. Emitter parameters were the same as used in section 4.2.

Since detection always takes place after background estimation – and depending on the method, background substraction – all detection approaches under investigation were carried out with background estimation. To ensure comparability, all detection approaches were accompanied by the same background estimation technique. Because moving median was shown to be most useful, it was chosen; filter dimensions were set to 9 × 9.

Two different, distinct notions are of interest: The detection efficiency and the rate of failure. The detection efficiency is the chance of retrieving an accurate candidate position for an emitter. A detection was considered successful, if the candidate position was less than 1 pixel width away from the true

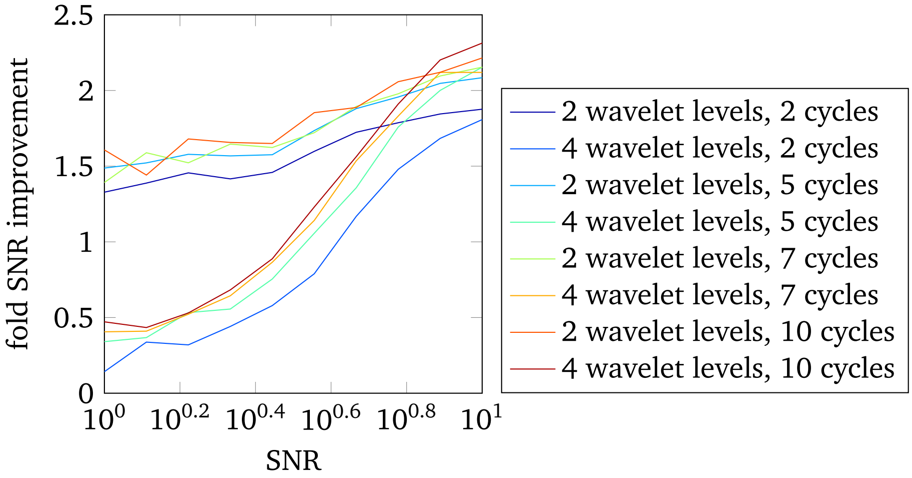

Figure 5.15.: Performance of PURE-LET denoising using LET_1 for different cycles and number of wavelet levels, SNR improvement vs. SNR

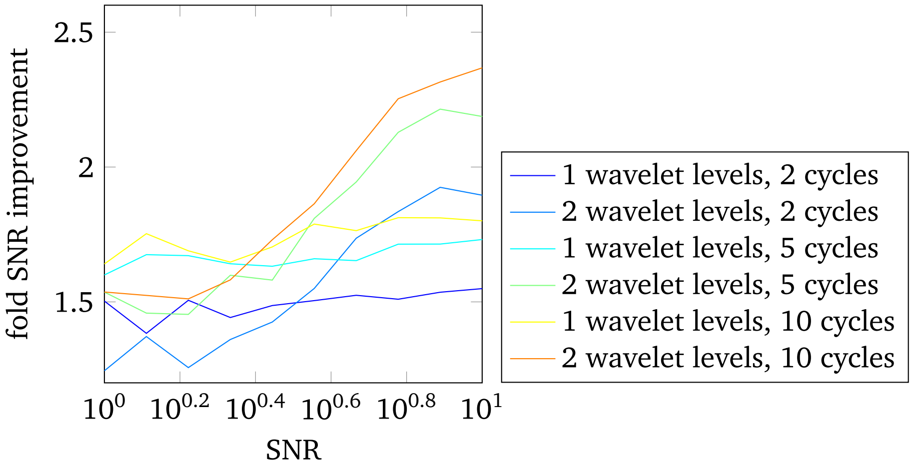

Figure 5.16.: Performance of PURE-LET denoising using LET_2 for different cycles and number of wavelet levels, SNR improvement vs. SNR

position along both the x- and y-direction. More explicitly, considering without loss of generality only the x axis, the criterion was $\lfloor x_{\text{true}} - 1 \rfloor < x_{\text{cand}}$ and $\lceil x_{\text{true}} + 1 \rceil > x_{\text{cand}}$ with true position $x_{\text{true}} \in [18.5, 19.5)$ where $x = 19.0$ is the center of the central pixel, candidate position x_{cand} and floor $\lfloor x \rfloor$ is rounding down whereas ceiling $\lceil x \rceil$ is rounding up. As a consequence, for a true position $x_{\text{true}} = 18.51$ candidate x-positions 18 and 19 were accepted. This reflects that candidate positions are given in integer pixels only. The rationale of accepting different candidate positions rather than only the central pixel is evident for a true position close to the pixel border so that stochastics determine in which pixel the most emitter-related signal accumulates rather than the PSF shape and the expectation values.

The ratio η is defined as the ratio of the number of successful detections and the total number of emitters to detect, i.e. 5000. A low η corresponds to poor detection efficiency, $\eta = 1$ is 100 percent detection probability.

The rate of false positives, i.e. alleged candidate positions that do not correspond to an emitter, is trickier to quantify as it not only depends on noise level, but also on emitter density and number of available pixels. Although absolute false positive numbers will vary in analysis of real world data, the rate of falsely reported candidate positions on a 39 × 39 square with a 100 photon emitter in the center is a reasonable surrogate for the purpose of comparing different detection approaches. ϕ is defined as the ratio of the number of all candidate positions not meeting the above mentioned success citerion and the total number of actual emitters. Thus, ϕ can be interpreted as false detection per true emitter at low emitter density.

In general, false positives and false negatives equally distort quantitative analysis of the data obtained from tracking single molecules. Thus, good detection efficiency has to be balanced with false alleged detections. Most detection techniques have a parameter to tune and the optimal parameter value may depend on the quality of the data. Since false positive candidate positions are expected to yield poor single molecule data estimations, well recognizable by low flux estimates, untypical spot widths etc., while false negatives are lost and cannot be dealt with in post-localization processing as is possible for the erronous candidates, first priority in the detection step is a high efficiency and then secondly at a low false positive rate.

In figure 5.17a, η is shown for the simple thresholding technique explained in section 4.3.1. Thresholds were given in in terms of local noise standard deviations, estimated using the local RMS deviation technique (section 5.1.2). For large SNR, efficiency η converges to ≈ 0.85 with unsurprisingly larger η values at low SNR for smaller thresholds. Bad data quality scenarios exhibit a SNR of about $3 = 10^{0.477\ldots} \approx 10^{0.5}$. At this SNR, η is below 0.8 for all thresholds investigated. The false positive rate ϕ depicted in figure 5.17b is almost independent of the noise which nicely reflects the fact that the threshold is given in terms of the noise. In fact, a quick estimate of the expected rate of false detections at threshold of 1 yields

$$\frac{(1-0.68)}{2}\left(21^2-4\right) = 69.92 \approx 70 \tag{5.10}$$

using $P(|X| < \sigma) \approx 0.68$ for $X \sim \mathcal{N}(0,\sigma^2)$, a margin of 9 (39-9-9=21) pixels corresponding to the background estimation filtering window edge length and a $2 \times 2 = 4$ true positive area. This value matches nicely with the simulation result. Deviations from ideal SNR independance of ϕ are due to noise misestimations. The stochastics of the emitter photons on low background levels, i.e. high SNR, can be seen in the high SNR regime of the ϕ curves.

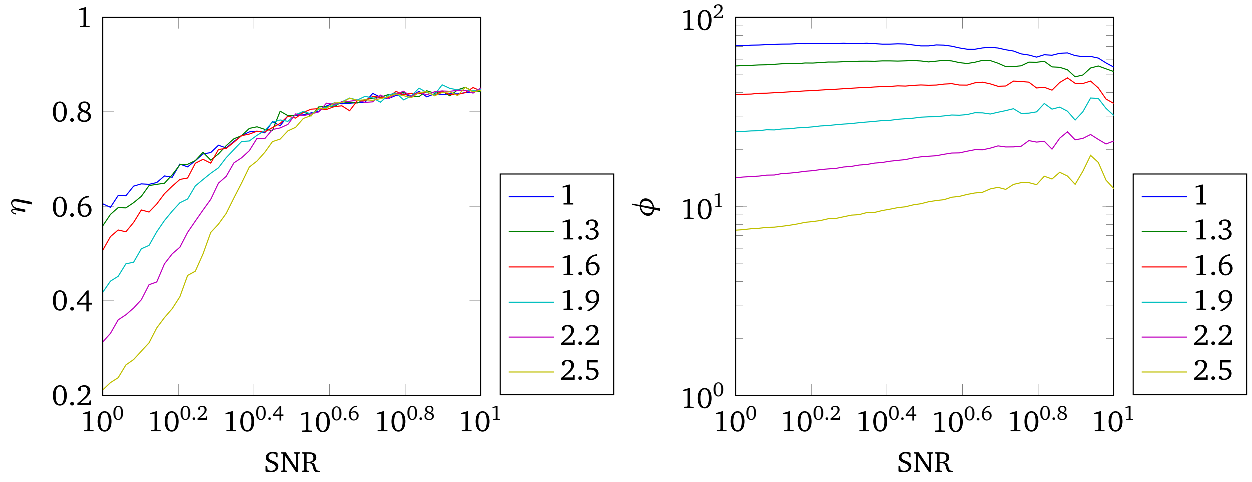

(a) Threshold method efficiency for different thresholds

(b) False positives

Figure 5.17.: Threshold method

Figure 5.18a shows η for the matched filter/correlation method (section 4.3.3, featuring convergence to $\eta = 1$ and a sharper increase in efficiency with increasing SNR. For threshold values at least 1.3, raising the threshold simply amounts to a shift of the η(SNR) curve to the right which alows for easy tuning of the threshold value. At the same time, the false posive rate is several orders of magnitude below the simple thresholding technique.

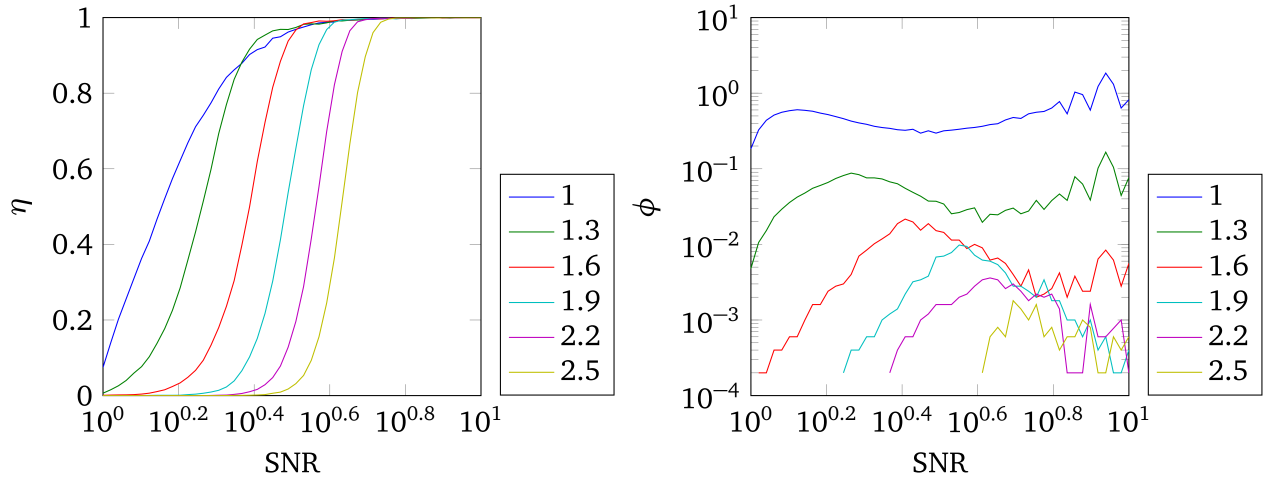

(a) Correlation method efficiency for different thresholds

(b) False positives

Figure 5.18.: Correlation method

The η of the Laplacian of Gaussian (LoG) method (section 4.3.2) as depicted in figure 5.19a converges to 0.8 for large SNR and in general performs poorer than the matched filter technique. The false posive rate of the higher thresholds increases for large SNR values, a feature not seen in the matched filter method.

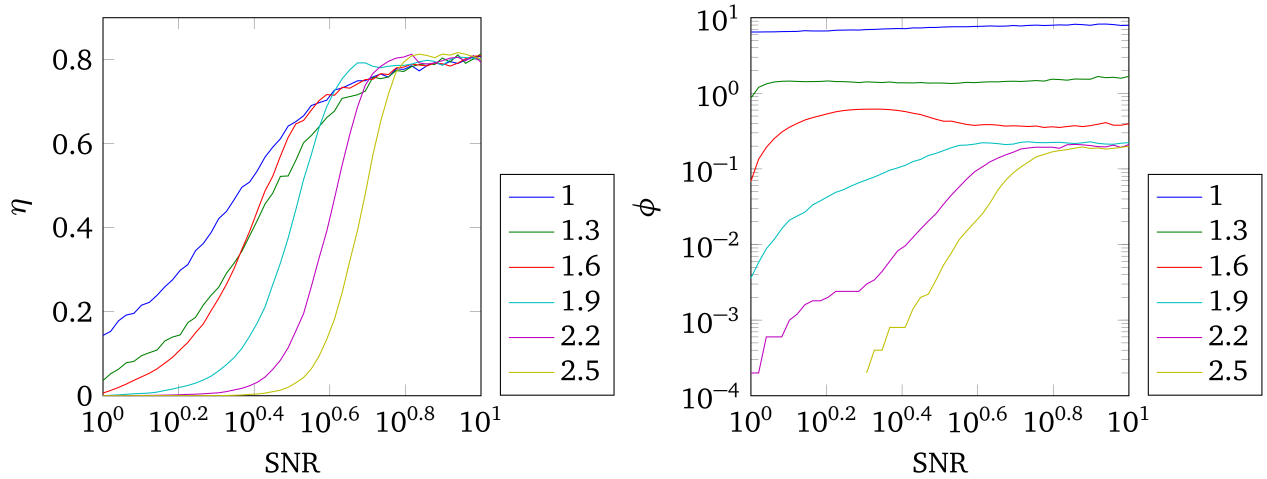

(a) LoG method efficiency for different thresholds

(b) False positives

Figure 5.19.: Laplacian of Gaussian method

The wavelet method (section 4.3.4) is not designed for low SNR scenarios, features a steep increase in η between SNR $= 10^{0.4} \approx 2.5$ and $10^{0.6} \approx 4$, and reaches $\eta = 0.9$ (figure 5.20a). Similar to the Laplacian of Gaussian method, the wavelet method shows a plateau of around $\phi = 10^{-1}$ i.e. 500 false positive candidate positions per the 5000 simulated emitters for SNR $> 10^{0.6} \approx 4$.

The detection by means of the likelihood ratio method (section 4.3.5 was evaluated at a cutoff level of 30 photons for different likelihood ratio thresholds. Generally, the exact value of the likelihood ratio threshold does not seem to play a crucial role both in efficiency (figure 5.21a) and false positives (figure 5.21b). Note that the threshold values refer to the loglikelihood difference, which means that a threshold

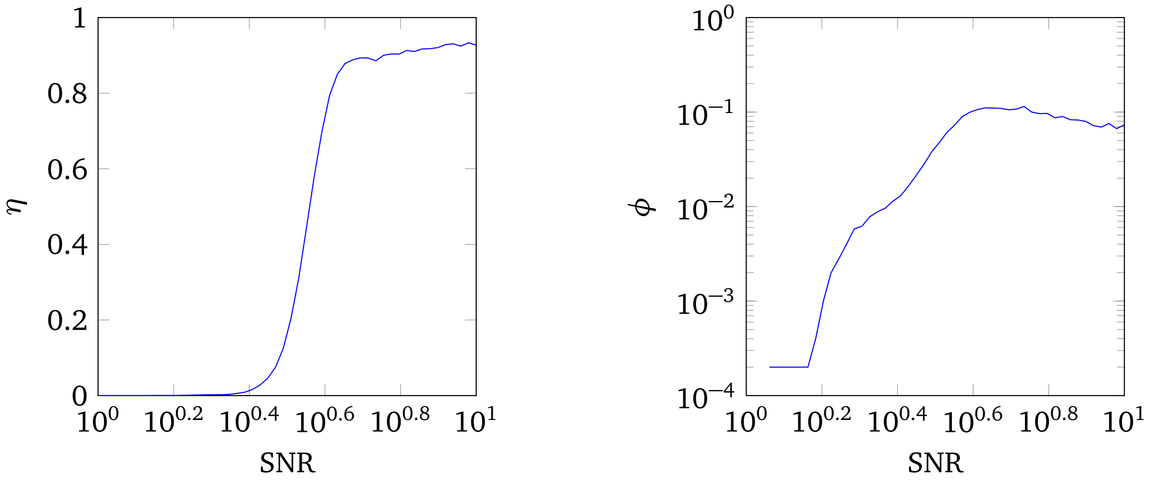

(a) Wavelet method efficiency for different thresholds

(b) False positives

Figure 5.20.: Wavelet method

of 1.7 corresponds to a likelihood ratio of $\exp(1.7) \approx 5.5$. For high SNR, all tested threshold values yield η around 0.95 with saturation not achieved. Noteworthy, ϕ is decreasing for large SNR. Yet, ϕ values are relatively large.

In order to investigate the influence of the cutoff value, it was varied while the threshold was kept fixed at 1. Interestingly, as the cutoff increases, a dip in the efficiency around SNR$=10^{0.3} \approx 2$ appears for cutoffs larger than 30, getting more pronounciation for larger values (figure 5.22a). For large SNR, η converges to values close to with the exepction of the cutoff value 60. It seems that cutoff values too close to the true flux, i.e. closer to the true value (100) than the false positive value (0), severly intervene in the detection process. The dramatic change in η from > 0.95 for cutoff of 50 down to < 0.7 for cutoff of 60 goes along with a qualitative change in the shape of the ϕ curves in figure 5.22b and an order of magnitude more false negatives at SNR$=10$ and cutoff values 40 and 50. Interstingly, zero cutoff seems to yield a noise independent false positive rate ϕ, even apparently more robust than the simple thresholding technique from figure 5.17b. Anyways, false positive rates are well above the ϕ values of the matched filter correlation method (figure 5.18a), especially in the low SNR regime. Note that the cutoff value of 30 used in the investigation of the BIC threshold values is a critical one as the η curve in figure 5.22a is on the verge to show the “dip” shape as opposed by the cutoff values 0 and 15 which basically conincide.

The detecton method based on the Kullback-Leibler divergence as explained in section 4.3.6 is investigated in the same manner as the likelihood ratio approach: First, for a single cutoff value, different treshold values are tested. Then secondly, different cutoff values are tested at a fixed threshold level. In figure 5.23a, η is shown for different threshold values at a cutroff value of 40. One can see that raising the threshold is paid by with loss in efficiency, at first in the low SNR regime (threshold = 10), then disastrously on the whole SNR range under investigation (threshold = 20). As a brief reminder, threshold values correspond to Laplacian of Gaussian filtered maps of the difference of information loss if the local window region is approximated by flat background or a diffraction limited spot. The information loss is given in nats, a measure of information that is based on the natural logarithm as opposed by the bit based on the binary logarithm, with 1 nat $= \frac{1}{\ln 2}$ bit.

In figure 5.23b, one can see that raising the threshold leads to a decrease in false positives in the lower SNR regime, but at the same time an increase for the upper SNR regime. While in the upper SNR regime reasonable ϕ values are achievable, in the lower regime ϕ is comparably large.

For the case of the fixed threshold of 1 at varying cutoff values in figure 5.24a, the convergence value of $\eta = 1$ is reached by all but the cutoffs at 0 and 60. Interstingly, the cutoff at 60 is less severe than

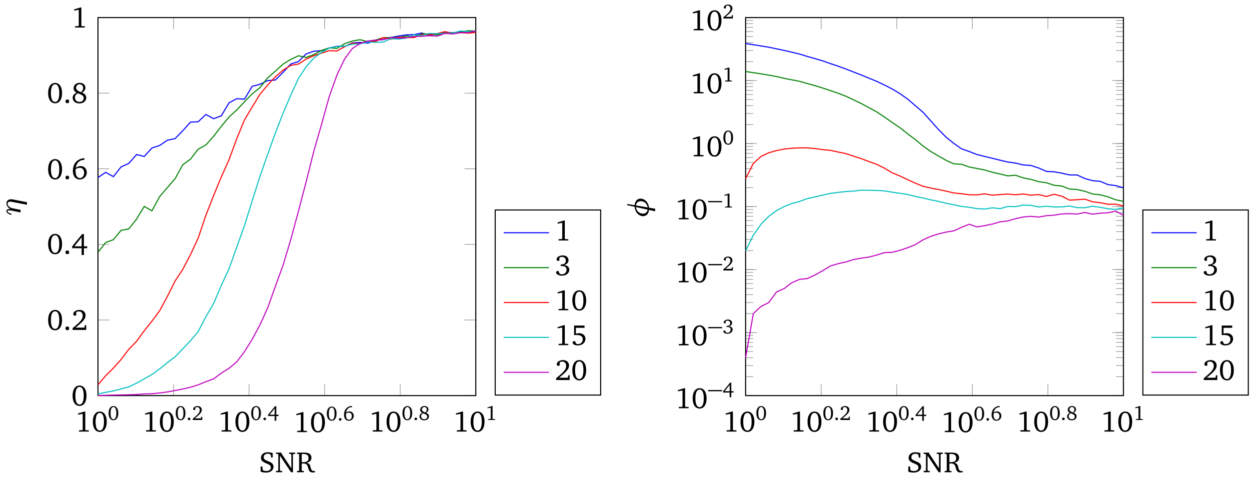

(a) BIC method efficiency for different thresholds

(b) False positives

Figure 5.21.: BIC method, 30 photons cutoff

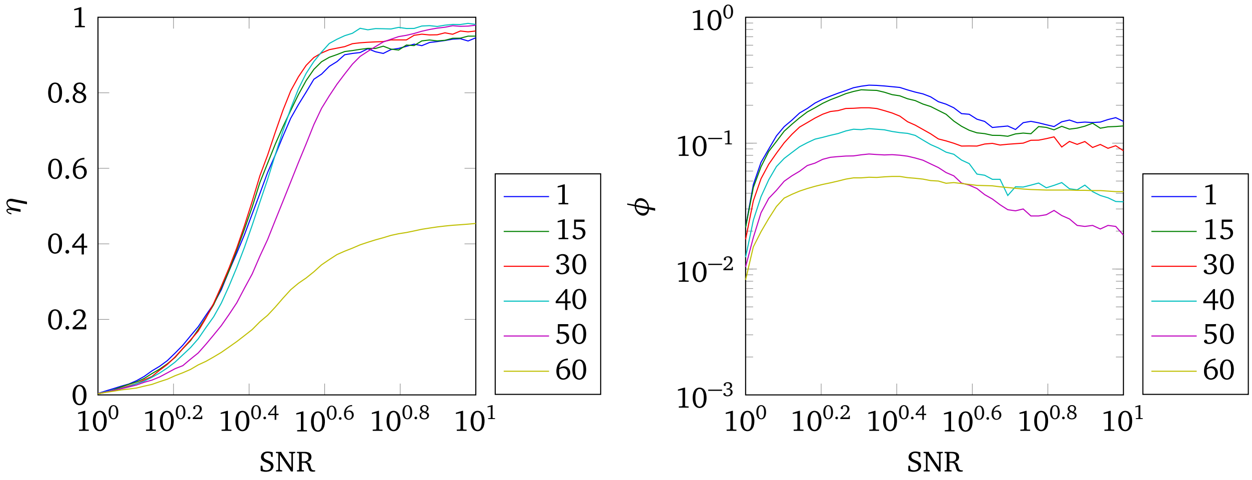

(a) BIC method efficiency for different cutoffs

(b) False positives

Figure 5.22.: BIC method, threshold=15

in the case of the likelihood ratio approach in figure 5.22a with a plateau of $\eta > 0.9$ still. On the other hand, zero cutoff yields a drastic, unexpected decrease at large SNR, probably because the flanks of the diffraction limited spot yield higher values in the Kullback-Leibler divergence difference map than the peak centers and the subsequent Laplacian of Gaussian peak finding sheers out. Accordingly, one can see in figure 5.24b that ϕ at large SNR for the cutoff at 0 is almost two orders of magnitude larger than for the cutoff at 15. The cutoff value of 40 used in figure 5.23 can be seen to reach $\eta = 1$ and show reasonable low values false positive rates ϕ, at least in the high SNR regime.

5.1.4.1 Summary

All approaches to retrieve candidate positions converge to some stable detection efficiency plateau for large SNR values. While simple thresholding and Laplacian of Gaussian do not reach $\eta = 0.9$, matched filtering and the Kullback-Leibler divergence based approach reach η of 100 % even for a SNR of 4.

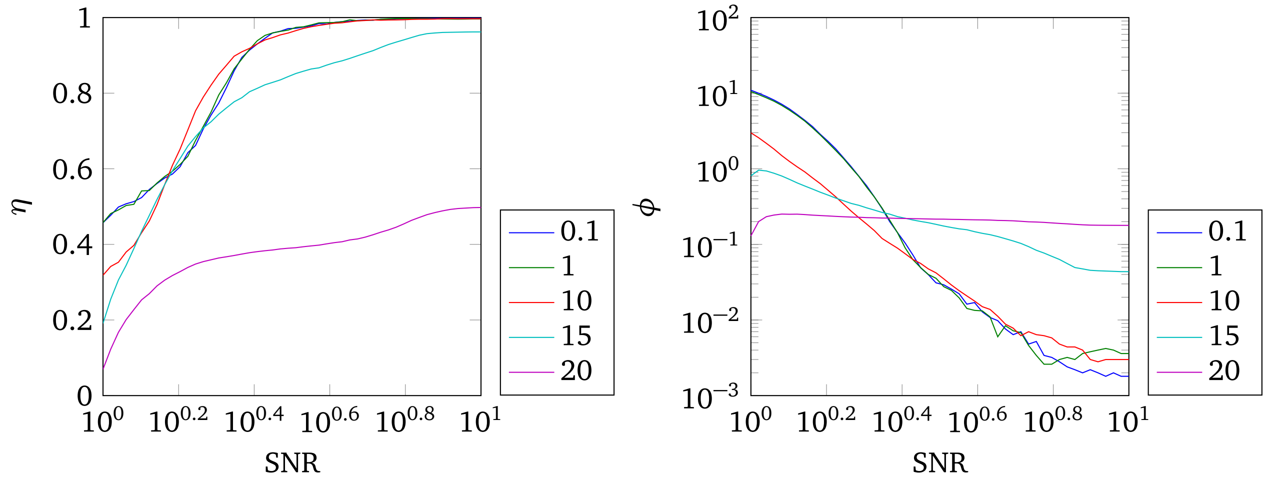

(a) Kullback-Leibler method efficiency for different thresholds

(b) False positives

Figure 5.23.: Kullback-Leibler method, 40 photons cutoff

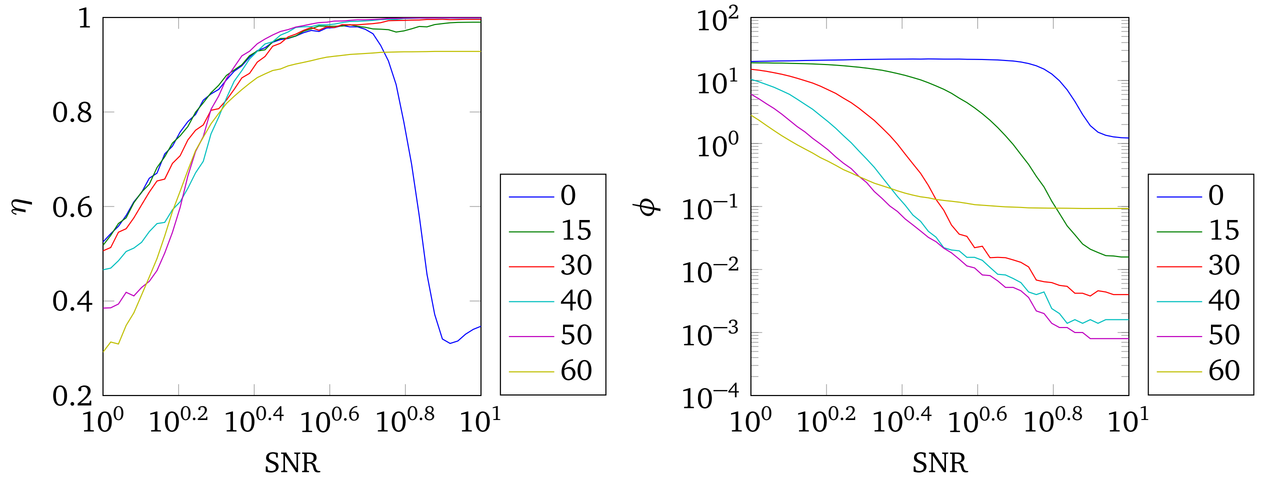

(a) Kullback-Leibler method efficiency for different cutoffs

(b) False positives

Figure 5.24.: Kullback-Leibler method, threshold=1

Interestingly, different approaches to retrieve candidate positions behave differently concerning their false positive rates in response to varying SNR values: The Laplacian of Gaussian method as well as the wavelet method feature higher ϕ values at high SNR rather than low SNR, a behavior contrasted by the likelihood ratio and the Kullback-Leibler method.

Obviously, the optimal approach to detection may be different from experiment to experiment, depending on fluorophore quantum yield, dichroits used, fluorophore abundance, amount of data acquired, and experimental design which may render an experiment more or less sensitive to incomplete detection (think PALM imaging vs. tracking) or false positives (tracking und dense conditions vs. tracking under sparse conditions, possibility of efficient postprocession). In conclusion, the matched filter is considered a good all-around method for typical single molecule microscopy data. Although of poorer performance than the Kullback-Leibler approach in the extreme low SNR regime, matched filtering is overall superior thanks to its very low false positive rate.

5.1.5 Localization

In the next step, the localization accuracy was quantified for different estimation techniques. To this end, each approach was performed on datasets of 2000 simulated emitters at different SNR. This time, FWHM was chosen to be 2.2 pixels, amounting to 235 nm for a pixelsize of 107 nm. Photon flux was again chosen to be 100 per emitter and frame, and the position was also random within the central pixel.

In order to account for realistic conditions, candidate positions were not provided to the localization routines as simulated, but rather retrieved by detection. For all localization methods, the same detection approach of matched filtering was taken, an approach evaluated in section 5.1.4 to be the all-purpose method of choice. Again, 9×9 median filtering was conducted to estimate the background signal. The ROI size around candidate positions used for localization was chosen to be 9×9 as well. To get rid of contributions to the localization error originating from false positives, localizations were the refined location was more than 2 pixels away from the true position were discarded. This cleaning is mandatory for the quantification of the localization accuracy, because random position false positives contribute non-constructively to the assessment of localization accuracy by means of root mean square deviation.

In figure 5.25, the accuracy is shown in terms of the root mean square deviation from the true position. Consistently, all methods show a clear improvement in terms of localization accuracy for increasing SNR values. Distinctly, the center of mass (CoM) method is far off worse then the other methods. As predicted by theory, least square (LS) fitting yields worse results than maximum likelihood estimation (MLE). For the location prior used, the Bayesian (Bayes) posterior estimate by means of MCMC conincides with the MLE. Remarkably, it plays little role for the accuracy of the localization whether the width of the PSF was provided (fixW) or part of the fitting parameters (varW). In accordance with theory, MLE's accuracy converges against the Cramér-Rao lower bound (CRLB), which was calculated on the basis of the approximation of the PSF by a Gaussian, taking into account pixelation. Since the single emitter CRLB depends on the exact position of the emitter, but essentially the mean accuracy is of interest, the CRLB for the comparison was calculated for a emitter positioned at the expectation value of the absolute distance from the center of the central pixel to the pixel border, i.e. in the center of a pixel quadrant. Specifically, the position used for the mean CRLB was shifted a quarter of a pixellength to the right and down (in positive x- and y-direction in Matlab coordinates). PSF symmetry ensures a correct value.

Both least square optimization and MLE were done using Matlab's trust-region reflective algorithm, which allows for specification of constraints for the fitting parameters. A full list of the constraints imposed is given in table 5.2.

parameter	lower boundary	upper boundary
x,y	-4	+4
I	0	$10\lvert\sum(n_k - \hat{B})\rvert$
W	0.1	5
B	$\min_k\{n_k\}$	$\max_k\{n_k\}$
E	0.1	10

Table 5.2.: constraints for parameters in iterative fitting, both least squares and maximum likelihood. n_k: photon number in pixel k, $\hat{B}$: background estimate according to section 4.1, x, y: spatial coordinates, I: number of photons, W: FWHM in pixels, B: local flat background estimate, E ellipticity

The location prior takes explicitely into account that we extract a fitting region around a candidate position for subpixel localization refinement. By design, the method assumes that given there is a emitter in the region, the true position is probably around the center. Of course, a too informative, i.e. sharply localized, location prior would yield poor results for instances of non-optimal candidates for example in the PSF flank under noisy circumstances, that means in cases where the pior information "more or less precisely the center" is not valid. To stay on the conservative side, location priors for x- and y-position was chosen to be a Gaussian centered at the center of the ROI, with a single axis standard deviation of 2.5 pixels, around 2.68 times the single axis standard deviation of the PSF and the $\pm 2\sigma$ area fully covering the ROI. Localization outside the ROI was negated by truncating the prior Gaussian at the ROI borders. A full list of the prior distributions for the parameters is given in table 5.3.

parameter	distribution	truncation
x,y	$\mathcal{N}(0, 2.5^2)$	$-4 < x, y < 4$
I	$\mathcal{N}(100, 30^2)$	-
σ	$\mathcal{N}(0.9343, 0.2^2)$	-
B	$\mathcal{N}(\hat{B}, 50^2)$	-
E	$\mathcal{LN}(1, 0.25^2)$	0.1<E<10

Table 5.3.: prior distributions of parameters for Bayesian inference. $\mathcal{N}(m, s^2)$ refers to the normal distribution with expectation value m and variance s^2, $\mathcal{LN}(\mu, s^2)$ to the log-normal distribution with probability density $\frac{1}{\sqrt{2\pi}sx}\exp\left(-\frac{(\ln(x)-\mu)^2}{2s^2}\right)$ for $x > 0$ and 0 otherwise.

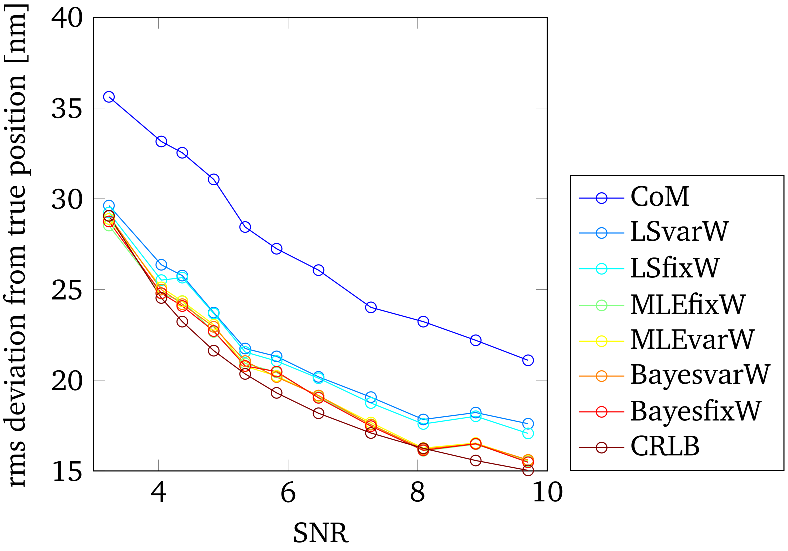

Figure 5.25.: Localization accuracy in x-direction, lines included to guide the eye

In addition, the impact of the fitting region on the accuracy was tested for dimensions 7 × 7 and 9 × 9. As shown in figure 5.26, the size of the fitting region makes only a minor impact. This is plausible since the most relevant part of the data, where the emitter contribution is maximal, is localized in the center of the region of interest. However, extra pixels allow for more accurate estimation of the local background at the emitter signal. On the other hand, too large fitting regions may contain neighbouring emitters.

5.1.6 Photon number/flux

The quality of flux estimation using the different techniques was evaluated in the same simulation runs as the localization accuracy. Again, accuracy was quantified in terms of root mean square deviation. As there enters the photon number of 100 only as an expectation value into the simulation, a minimal accuracy of $\sqrt{100} = 10$ rather than 0 is established by virtue of the Poisson distribution even at zero background level corresponding to SNR= ∞. As one can see in figure 5.27, the "center of mass" method, i.e. equation 4.23, performs poorest with an relative advantage on the non-discarded data

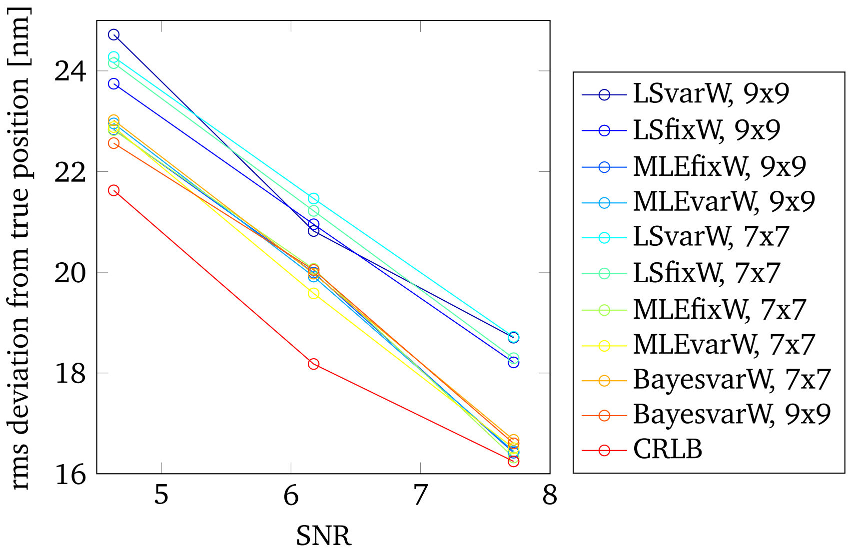

Figure 5.26.: Localization accuracy in x-direction for 7×7 and 9×9 regions

only in the extreme low SNR regime. Interestingly, least square optimizations outperform maximum likelihood methods. This can be explained by the fact that the pixels contributing most to the total number of photons have more relative weight in unweighted least squares than in maximum likelihood. Clearly one can see from the least square methods how knowledge of the PSF width can be exploited by fixing the width instead of using it as optimization parameter. At MLE, the difference of using a fixed or a variable width is not so pronounced. The difference between these models can also be seen at the Bayesian MCMC optimization. Bayesian methods not only dominate the frequentist methods but also surpass the CRLB. Moreover, Bayesian MCMC estimation is much less affected by noise than the other methods. Note that the Bayesian accuracy converges against the mentioned inherent minimal accuracy for large SNR. The dependency on the ROI dimensions is displayed in figure 5.28.

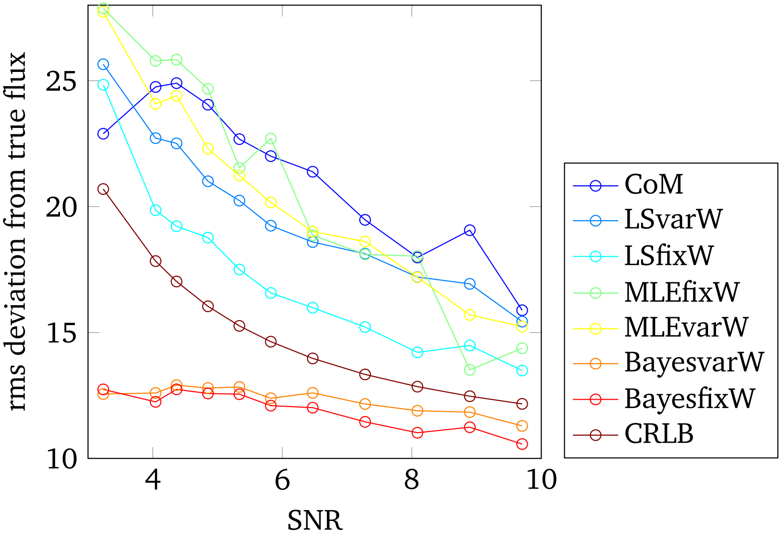

Figure 5.27.: Flux estimation accuracy in terms of root mean square deviation from true value in photons

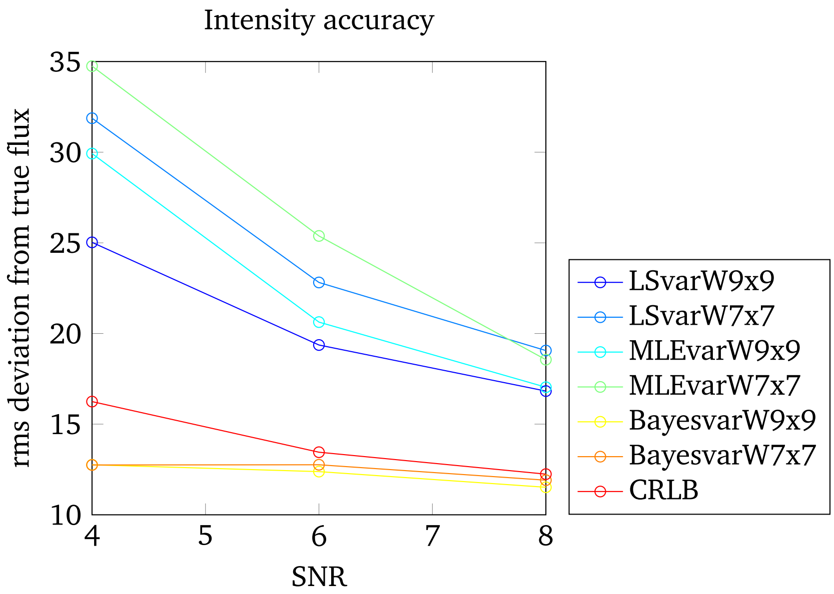

Figure 5.28.: Flux estimation accuracy in terms of root mean square deviation from true value in photons for 7×7 and 9×9 regions

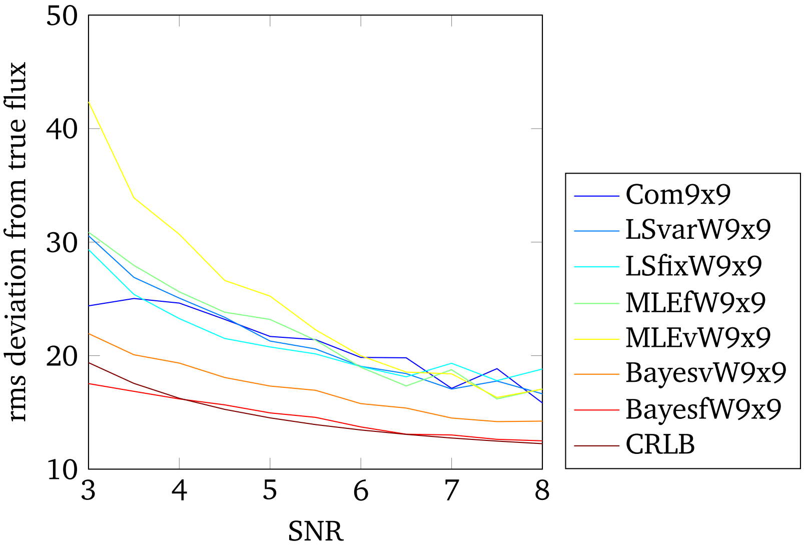

Figure 5.29.: Flux estimation accuracy in terms of root mean square deviation from true value in photons with a vague flux prior

5.1.7 Ellipticity

The ellipticity parameter is used for retrieval of the z-position from astigmatic imaging [Kao and Verkman, 1994, Holtzer et al., 2007]. For a comparison of different approaches to z-estimation using astigmatism, see Spille [2014]; alternatives are a helix-shaped PSF [Pavani et al., 2009] or biplane imaging [Juette et al., 2008, Mlodzianoski et al., 2009]. 3D position determination allows for investigations of diffusion in 3D such as of messenger ribonucleoprotein particles (mRNPs) [Ritter et al., 2010b, Spille et al., 2012, Thompson et al., 2010]. For accurate adjustment of astigmatism, a pair of obliquely crossed cylindrical lenses [Thompson, 1900] with a convex and a concave one with adjustable relative angle can be inserted into the detection light path, perferably – in order to reduce non-astigmatism aberrations – between two relay lenses where detection light originating from the focal plane in the sample is parallel.

The assessment of the accuracy of the ellipticity estimate is shown in figure 5.30. The algebraic method is far worse than the fitting approaches. Least squares are poorer than the maximum likelihood method while Bayesian inference is superior for all SNR values. Note that the prior probability for ellipticity is centered at $\epsilon = 1$, reflecting symmetry around the focal plane.

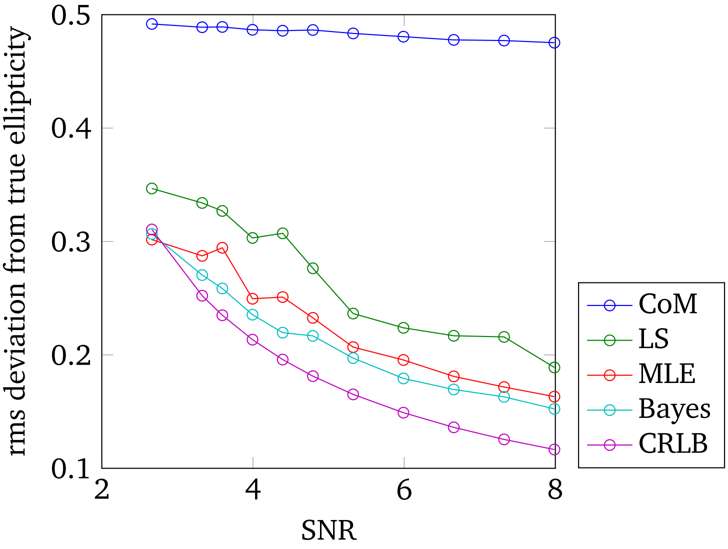

Figure 5.30.: Ellipticity estimation accuracy in terms of root means square deviation from true value of 1.5

However, in the experimental chapter of this thesis, diffusion in a membrane is investigated and astigmatism based-tracking in 3D is not applied.

5.1.8 MCMC diagnostics

The analysis by means of MCMC readily provides not only the minimum mean square error estimate of the parameters equivalent to the expectation value of the posterior distribution where the integration of taken the exectation value is approximated by random samples of the distribution, but also gives account of the accuracy of the estimates expressed in terms of the posterior standard deviation, which is approximated by the standard deviation of the set of the random samples. This, however, presumes that the samples drawn actually conform with the posterior distribution, which is the distribution the Markov chain is designed to converge against. Therefore, it is crucial for faithful parameter estimation that the target distribution is reached i.e. the Markov chain has converged. To this end, so-called burn-in samples are drawn which are steps *en route* to the target distribution that run not into the analysis. However, there is no established quantity that discloses without doubt that a Markov chain has converged. Still, heuristics exist which try to quantify the “goodness of convergence”. The most famous converge diagnostic is the Gelman-Rubin *estimated potential scale reduction factor* $\hat{R}$ [Gelman and Rubin, 1992, Brooks and Gelman, 1998, Gelman et al., 2013], which uses multiple chain realizations converging to the same distribution to calculate the square root of the ratio of the estimated true variance to the mean within-chain variance:

$$W = \frac{1}{m}\sum_{j=1}^{m} s_j^2 s_j^2 = \frac{1}{n-1}\sum_{i=1}^{n}(\theta_i j - \bar{\theta}_j)^2 \tag{5.11}$$

where W is the mean *w*ithin chain variance, and s_j^2 is just the formula for the jth chain. For non-converged chains, W underestimates the true variance of the stationary distribution.

$$\frac{B}{n} = \frac{1}{m-1}\sum_{j=1}^{m}(\bar{\theta}_j - \bar{\bar{\theta}})^2 \bar{\bar{\theta}} = \frac{1}{m}\sum_{j=1}^{m}\bar{\theta}_j \tag{5.12}$$

$\frac{B}{n}$ is the *b*etween chain variance and each of the m chains comprises of n draws. The variance of the stationary, i.e. in our case the posterior distribution, is estimated as a weighted average of W and B:

$$\hat{\sigma}_{+}^{2} = \frac{n-1}{n} W + \frac{B}{n} \tag{5.13}$$

For overdispersed starting values of the chains, $\hat{\sigma}_{+}^{2}$ overestimates the true variance, but is unbiased if the chain start values are drawn from the stationary distribution. Accounting for the sampling variability of the estimate of the mean yields a pooled posterior variance of

$$\hat{V} = \hat{\sigma}_{+}^{2} + \frac{B}{mn} \tag{5.14}$$

The estimated potential scale reduction factor $\hat{R}$ is then defined as

$$\hat{R} = \sqrt{\frac{\hat{V}}{W}} = \sqrt{\frac{m+1}{m} \frac{\hat{\mathrm{Var}}(\theta)}{W} - \frac{n-1}{mn}} \tag{5.15}$$

which equals to 1 for convergence. For practical purposes, $\hat{R} < 1.05$ is used as indication that the burn-in sequence is long enough [Spiegelhalter et al., 1996, Brooks and Gelman, 1998] (note that sometimes $\hat{R}$ is defined as $\hat{V}/W$; the estimated potential scale reduction factor, however, always refers to the version with the square root). Each parameter estimated with the Markov chain corresponds to an own $\hat{R}_i$. Since sequences that have not converged in one dimension of the parameter space probably have not converged at all, only the maximum $\hat{R}_{\max} = \max_i \hat{R}_i$ is reported for each fluorophore candidate position.

parameter	start value
x,y	-4
I	0
W *symm*	2.3
W *ellipt*	$\sqrt{\hat{W}_x \hat{W}_y}$
B	$\hat{B}$
E	1

Table 5.4.: $\hat{W}_x$ as defined in 4.4.1, corrected for apparent increase due to pixelation

However, in order to promote fast convergence, starting values are not overdispersed but rather set to reasonable “guesstimates” (see table 5.4). To check whether the length of the burn-in sequence is sufficient, a typical low-SNR signal (SNR=3) is analysed with the variable width model using overdispersed starting values out of competition. For this check, 3 runs are made: One where all start values are one pior standard deviation below the prior peak, one where the start values lie on the prior peak and one where all values are one prior standard deviation above the prior peak. For the symmetric Gaussian PSF models, both with fixed and variable width, the burn-in sequence was 1000 samples long. The elliptic PSF model was burnt-in for 4000 samples. In all cases, 4000 samples were drawn in each chain after the burn-in phase which were thinned out by a factor of 2 to 2000 samples which form the basis for the parameter estimation. “Thinned out” means the rejection of a fraction of the drawn samples which is a means to reduce correlation between samples.

The decision concerning the amount of samples used to infer the parameters and also the degree of thinning was based on the criterion that the Monte Carlo error due to sampling is less than 5 % of the posterior standard deviation of any parameter as recommended in the openBUGS manual, where the Monte Carlo error is defined as

$$\epsilon_{\mathrm{MC}} = \sqrt{\frac{s^2}{nm}} \tag{5.16}$$

Where is s^2 is the estimated variance of the nm samples, taking into account correlation between the samples by means of the batch means method [Gilks et al., 1996, p. 50]. While $\hat{R}$ according to equation 5.15 is calculated by an openBUGS wrapper function, a version of the Gelman-Rubin statistic that relies not on variances, but on the pooled and within-chain width of the 80 % credible interval is reported openBUGS-internally. These so-called bgr-diagnostics of all monitored parameters are displayes in figure 5.33, and show not only a convergence of the ratio (red) to 1, but equally [Brooks and Gelman, 1998] important of the pooled (blue) and within-chain (green) statistics. For optimal sampling, normal priors are shifted and scaled so that sampling is effectively done for the standard normal distribution. The PSF width parameter is sampled as standard deviation and subsequently converted to FWHM. One can see that the local offset estimate actually converges rather at 1200 samples. This is due to the vagueness of the background prior with a standard devation of 50, which is more than ten times the standard deviation of the background at the expected offset for SNR=3, offset $= (13.64/3)^2 = 20.7$ photons, where 13.64 is the mean peak photon number of a pixelated Gaussian PSF with a flux of 100 photons and a FWHM of 2.2 pixels. The peak of the local offset prior is set to the local background estimate as conducted in section 4.1 which has been shown to be rather accurate. Therefore, it can be more or less savely concluded, that at more helpful start values, i.e. on the educated guesses and not dispersed around them, all chains have converged to the stationary distribution, especially at less severe noise levels and with a fixed PSF width parameter.

The mean $\hat{R}_{\max} = \max_i(\hat{R}_i)$ according to equation 5.15, where i goes over the set of parameters to infer, of the simulation runs conducted to evaluate the localization accuracy plus-minus the standard deviation is shown in figure 5.31 and in figure 5.32 for the case of the vague flux prior. Note that in theses runs, start values are not over-dispersed.

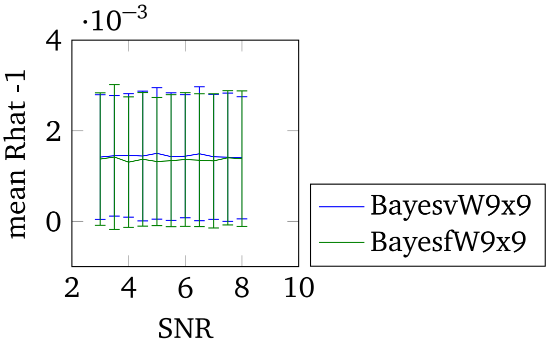

Figure 5.31.: mean max Rhat

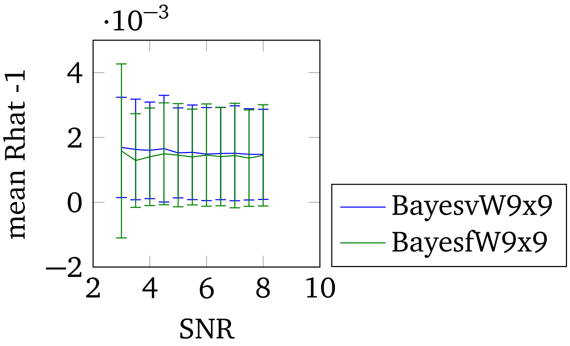

Figure 5.32.: mean max Rhat with vague flux prior

Typical autocorrelation plots in figure 5.34 show rapid decay after few samples. Note that perfect non-autocorrelation is unattainable in MCMC. On the other hand, under ergodic conditions such as after convergence to the stationary distribution, autocorrelation is not a problem as big as one may think since

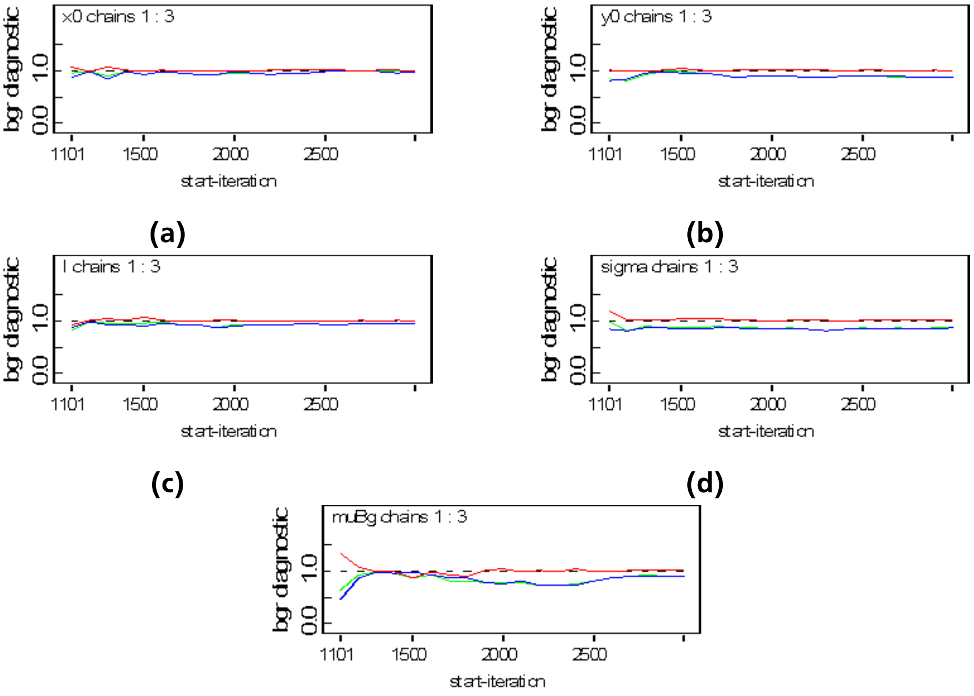

(a) **(b)** **(c)** **(d)** **(e)**

Figure 5.33.: Gelman-Rubin statistic of x,y,I,Bg, and width parameters based on the width of the 80 % interval of the pooled runs (blue), average width of the 80 % intervals within the individual runs (green) and the ratio of pooled / within (red).

ergodicity ensures validity of relevant convergence theorems [Gilks et al., 1996, Tierney, 1994, Geyer, 1992]. Yet, small autocorrelation leads to smaller Monte Carlo errors at the same amount of samples – or, conversely, allows to reduce the amount of samples needed for reliable inference because the posterior is explored faster.

Sample scatterplots are shown in figure 5.35 to show cross correlation. One can see that the spatial coordinates (figure 5.35a), one spatial coordinate (x_0) and the flux I (figure 5.35b), x_0 and the width (figure 5.35c), x_0 and the offset μ_{Bg} (figure 5.35d,) and the offset and the width (figure 5.35g) are uncorrelated. Width and flux (figure 5.35e) and offset and flux (figure 5.35f) are slightly correlated as expected from the model definition: a larger width "treats" more background photons as fluorophore signal or a smaller width "treats" fluorophore photons as background signal and likewise are the photons competitively "distributed" beween fluorophore signal and offset. "Treating" and "distributing" are deliberately put into quotes to indicate the terms as a figure of speech. Correlation coefficients r are provided in the figure captions. Be aware not to confuse r with the coefficient of determination of linear models with a single independent variable, r^2.

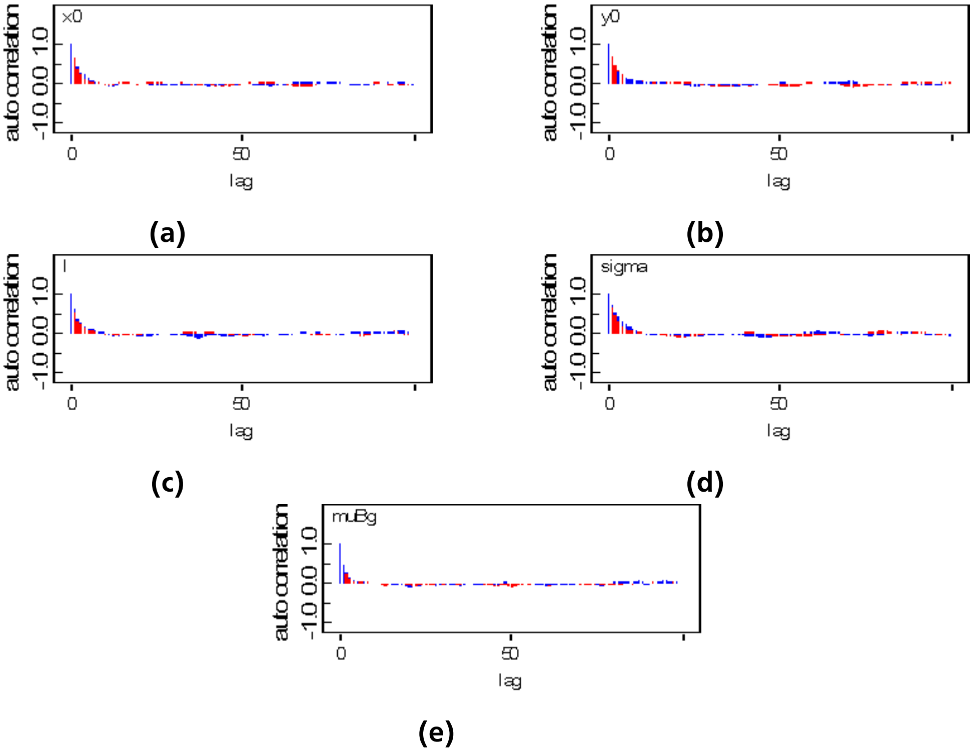

(a) (b) (c) (d) (e)

Figure 5.34.: Typical autocorrelation plots for SNR=3, for (a) X, (b) Y, (c) I, (d) width, (e) offset. Run 1 (red) and run 2 (blue) are overlayed. Autocorrelation rapidly drops exponentially.

5.1.9 Postprocession

In order to assign different localizations in sequences of frames to the corresponding underlying molecule trace, a process called tracking, high detection yields are necessary, which call for low thresholds in the candidate identification step. Since these low thresholds come with increased rates of false positives, post processing after localization is often required to sort out localizations that are based on false positive candidates or abberrant fitting.

Therefore, criteria were sought that allow to identify localizations not corresponding to actual fluorophore presence. The most basic and straightforward idea is to exclude datapoints based on fit parameters. Since the boundaries defining the constraints on the fitting parameters are rather generous, fits where one or several of the fitting parameters is implied to lie on one of the boundaries are likely to correspond to fits gone awry.

Low values of flux estimates may correspond to candidate positions of single pixel large outlier values as expected from the stochasticity. Also, if the width is known, unphysical width estimates can be identified if the width is used as a fitting parameter. For example, too small widthes are related to single pixel outliers while too large widthes may correspond to falsely detected background features such as vesicles. The distance between the candidate position and the final localization is expected to be small, typically < 1.5 pixels for reasonable candidates and fits not gone awry. An estimate for the quality of each localization is furthermore given by the integral SNR, which can be calculated from the total flux estimate and the local noise estimate. Note that the integral $\mathrm{SNR}_{\mathrm{im3}} = \frac{I}{\sigma_N}$ is more robust against single pixel outliers than peak $\mathrm{SNR}_{\mathrm{im}} = \frac{\hat{I}}{\sigma_N}$. Goodness-of-fit is readily assessed in terms of the reduced χ^2_{red}:

$$\chi^2_{\mathrm{red}} = \frac{\sum_k^N (\mu_k - n_k)^2}{n_k (N - \#\mathrm{dof})} \tag{5.17}$$

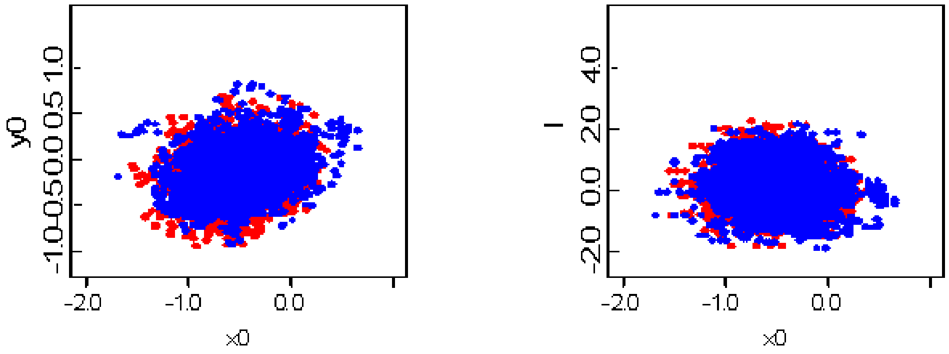

(a) $r = 0.23$ **(b)** $r = -0.07$

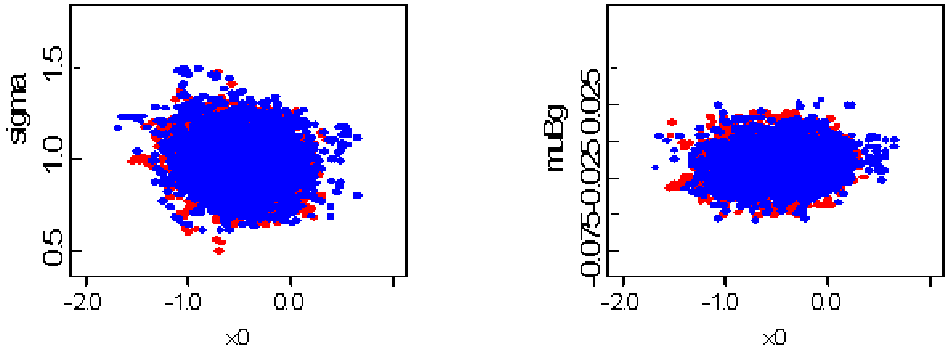

(c) $r = -0.14$ **(d)** $r = 0.06$

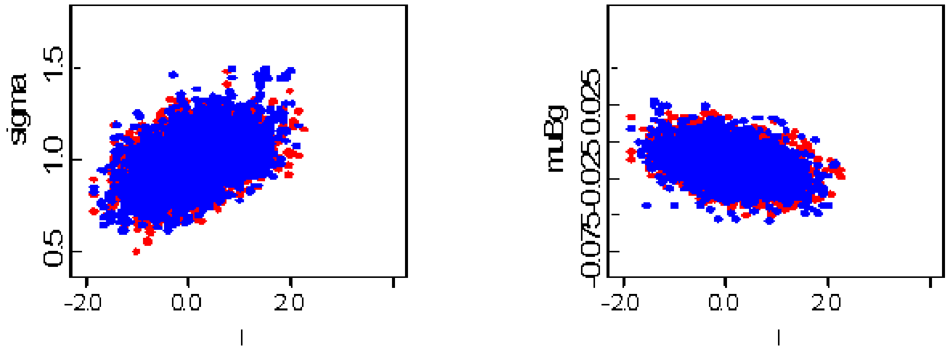

(e) $r = 0.44$ **(f)** $r = -0.36$

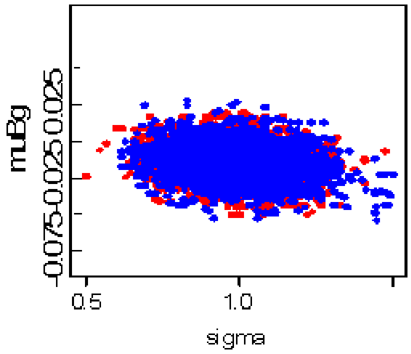

(g) $r = -0.20$

Figure 5.35.: Typical scatterplots for SNR=3, for (a) Y vs. X, (b) I vs. X, (c) width vs. X, (d) offset vs. X, (e) width vs. I, (f) offset vs. I, (g) offset vs. width. Run 1 (red) and run 2 (blue) are overlayed.

where n_k is the detected number of photons at pixel k, μ_k the expected number of photons at the same pixel according to the model in question, N the number of pixels in the fitting ROI and #dof the number of degrees of freedom of the model, for example #dof = 4 for a fit to the flux, the x and y position and the local offset. However, χ^2_{red} may be of little interest when it is not the quantity optimized, such as in MLE or even more, when Bayesian statistics reject the inherently frequentist χ^2_{red} altogether. Approaches that not declare one of the hypotheses the Null-hypothesis and only care about her rejection or acceptance and thereby, according to Bayesian statistics, treat hypotheses not equally but rather treat arbitrarily different. According to Bayesian theory better evaluation whether model/hypothesis one (there is indeed a fluorophore present in the ROI investigated) or model/hypothesis two (there is no fluorophore present in the ROI) is more appropriate.

Relating to the coefficient of determination R^2 of linear regression, a pseudo-R^2 can be defined for nonlinear models as one minus the ratio of variation of the residuals and the variation of the data. In other words, for n_k detected photons at pixel k and a model predicting μ_k photons at the same pixel, a pseudo-R^2 can be defined as

$$R^2 = 1 - \frac{\sum_k (n_k - \mu_k)^2}{\sum_k (n_k - \bar{n})^2} \tag{5.18}$$

where $\bar{n}$ is the mean of the n_k. Note that $\bar{n}$ is the maximum likelihood estimate given absence of fluorophores and flat background. Basically, $\bar{n}$ refers to the model "no fluorophore", while the set of μ_ks corresponds to a fit of a given PSF model. R^2 can be interpreted as a measure for the likelihood ratio, given additive white Gaussian noise.

Another means to compare different models is Akaike's Information Criterion (AIC) [Akaike, 1973, 1974]. Briefly, suppose that stochastic data x is generated by an unknown process $f(x|\theta)$, parameterized with the variable θ. For two estimates $\hat{\theta}_1$ and $\hat{\theta}_2$ that correspond to maximum likelihood estimates of the competing models $g_1(x|\theta)$ and $g_2(x|\theta)$, one would chose the one model which minimizes the information loss as specified by the Kullback-Leibler divergence $D_{\text{KL}}(g_i||f) = \int g_i(x|\hat{\theta}_i) \log g_i(x|\hat{\theta}_i)/f(x|\theta)\,\mathrm{d}x$, $i = 1,2$. However, the Kullback-Leibler divergence cannot be calculated since f is unknown. Now, Akaike could show that the negative loglikelihood of the maximum likelihood estimate $-\ln \mathscr{L}(\hat{\theta})$ is a biased estimate of $D_{\text{KL}}(g_i||f)$ and that the bias asymptotically converges (infinite number of samples) against the (negative) number of parameters K to estimate. Thus, the AIC is defined as

$$\text{AIC} = -2 \ln \mathscr{L}(\hat{\theta}) + 2K \tag{5.19}$$

where the factor of 2 is included for historical reasons. The model with the smallest AIC is chosen. Relative likelihoods can be assigned to competing models g_i:

$$l_i = \exp\left(\frac{\text{AIC}_{\text{min}} - \text{AIC}_i}{2}\right) \tag{5.20}$$

where $\text{AIC}_{\text{min}} = \min_i\{\text{AIC}_i\}$ is the minimal AIC. Equivalently, "Akaike weights"

$$w_i = \frac{l_i}{\sum_i l_i} \tag{5.21}$$

can be used. The version correcting for a finite number of samples ν (i.e. here the ROI size) is called the corrected AIC [Burnham and Anderson, 2004, reviewed in]:

$$\text{AICc} = \text{AIC} + \frac{2K(K+1)}{\nu - K - 1} \tag{5.22}$$

and should be generally preferred over the uncorrected AIC [Burnham and Anderson, 2004]. An alternative is the Bayesian Information Criterion (BIC) [Schwarz, 1978]

$$\text{BIC} = -2 \ln \mathscr{L}(\hat{\theta}) + K \ln \nu \tag{5.23}$$

There are subtle differences in the derivation of AIC and BIC, such as the AIC assumes an unknowable underlying truth and the best approximating model is to be picked while BIC seeks the true model underlying the data [Kuha, 2004]. However, the true model needs not to be among the models to be compared. In general, *ad hoc* outlier rejection is inherently "dirty" as what an outlier is has to be arbitrarily defined. In this spirit, absolute numbers of AIC and BIC should not be overinterpreted but pragmatically used. The meaning of BIC is that BIC differences of models approximate the logarithm of the evidence ratio, where the evidence of a model is defined in section 4.4.4 as the integral over the likelihood times the prior. The evidence ratio, also kown as "Bayes factor", is the Bayesian model selection criterion *par excellence*. BIC has been used in [Quan et al., 2011] and the follow-up publication [Wang et al., 2012]. Different model priors can be applied as factors to the numerator or the denominator if models are not *a priori* equally likely. Model weights calculated in the fashion of equation 5.21 but using BICs, can be interpreted as posterior model probabilities when assuming equal model priors. For certain model priors, Akaike weights can be retrieved as Bayesian model posterior probabilities as well [Burnham and Anderson, 2004]. For absolute numbers, model priors have to be taken into account: Obviously, if there are 100 fluorophores imaged on a 200 × 200 frame, the probabilities to find a fluorophore or none at a randomly selected pixel are not equal (1:1) but rather 100:39900 or 1:399. For identification of outliers, however, constants to all localizations are neglegible.

Figure 5.36 illustrates the merits of post procession based on the data of Figure 5.9b.

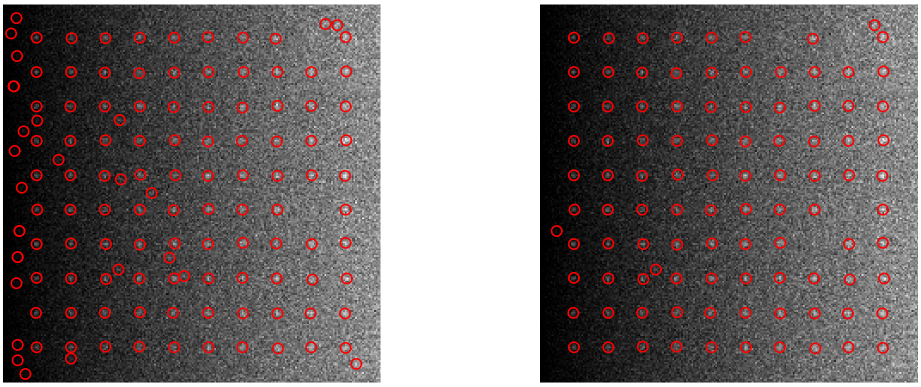

(a) Fixed width MLE localizations of Figure 5.9b with detection by matched filter with a threshold of 1. Note the over-sensitivity in the high-SNR regime.

(b) Exclusion of localizations with an estimated photon number of less than 20 or a ΔBIC value of less than 1 in favour of particle presence leads to reduction in false positives.

Figure 5.36.

In order to assess the capabilities to sort out bad data in post procession quantitatively, localizations of an analysis on simulated data with a SNR of 4 are displayed as scatterplots (figures 5.37 and 5.38) of one postprocession parameter versus the distance of the localization to the true position.

Here, 2000 emitters were simulated at a SNR of 4 and analysed with 9 × 9 median filter background estimate, matched filtering using a threshold of 1.5, and localization by means of MLE of a symmetric variable width Gaussian. One can clearly identify the 19 mis-localizations characterized by their large distance from the true position. Note that this number is consistent with figure 5.18b. These mis-localizations originate from false positive candidates as can be seen from their sub-pixel (107 nm) distance to the corresponding candidate (figure 5.37f). Against expectation, the mis-localization population is not distinct in terms of estimated flux (figure 5.37a), width (figure 5.37b), local background estimate (figure 5.37c), and local noise estimate (figure 5.37d). Appreciate that SNR=4 refers to a background expectation value of ≈ 11.6 for emitter signals with 100 detected photons, with a corresponding noise of $\sqrt{11.6} \approx 3.4$ which is nicely reproduced in accordance with sections 5.1.1 and 5.1.2. Consequently, mis-localizations are not distinct in terms of integral SNR (i.e. SNR_{im3}), that is calculated as the

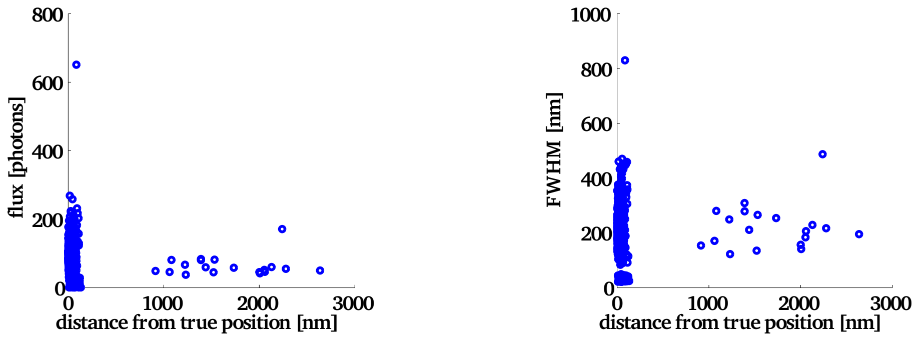

(a) flux vs. positional deviation

(b) FWHM vs. positional deviation

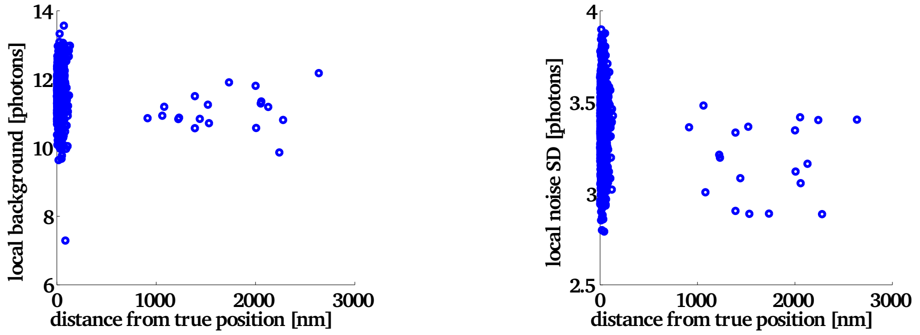

(c) local offset estimate vs. positional deviation

(d) noise estimate vs. positional deviation

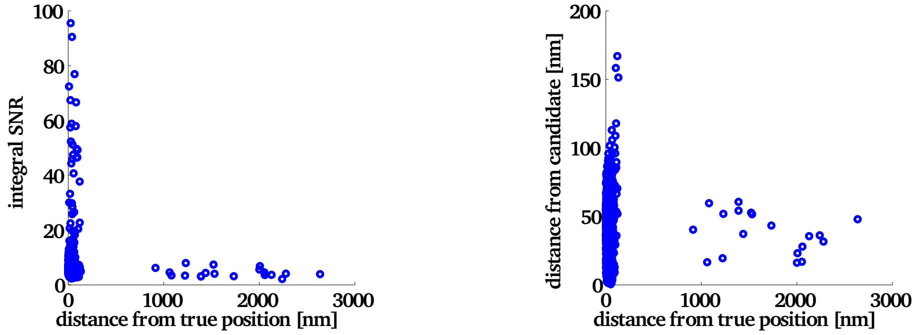

(e) integral SNR vs. positional deviation

(f) localization to candidate distance vs. positional deviation

Figure 5.37.: pixelated Gaussian, MLE, variable PSF width, SNR=4

ratio of the estimated flux and the estimated local noise standard deviation. Be aware that while SNR in terms of peak values above ground is advantageous for describing the quality of data as acquired (or simulated), integral SNR might still be useful in postprocession. While mislocalizations are not distinct from true positives, they yet feature – as expected – low integral SNR. Mislocalizations not necessarily are bad fits as witnessed by their reasonable χ^2_{red} as shown in figure 5.38a. The *prima facie* astonishing fact that the mislocalizations feature comparable fluxes, widthes and χ^2_{red}s can be explained by the candidate finding procedure which “ensures” that false positive candidates resemble the PSF matched filter to a certain degree as specified by the threshold applied. In other words, less optimal candidate detection schemes may more easily allow to identify their excess false positives. Still, superior detection with less false positives to begin with is generally favorable.

The Akaike weight of the “there is a emitter” model against the competing “there is flat background” model, both of which take into account the Poissonian nature of the photons, does not allow for identification of mislocalizations since they apparently also feature large Akaike weights close to one (figure 5.38c). Akaike weights were calculated from the corrected AICc. Remind that AICc is different from BIC

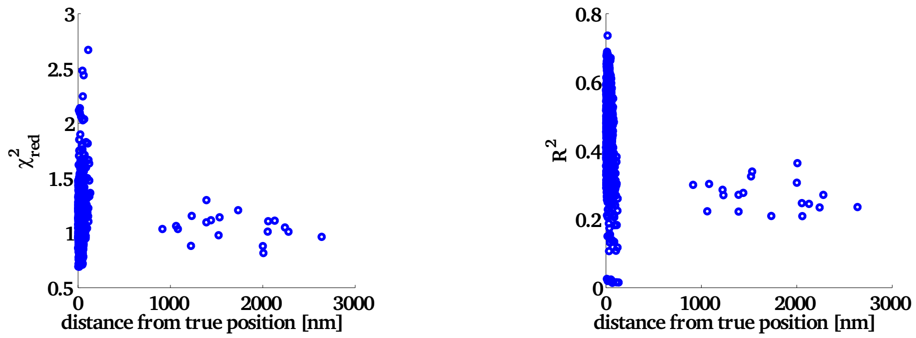

(a) χ^2_{red} vs. positional deviation **(b)** Pseudo-R^2 vs. positional deviation

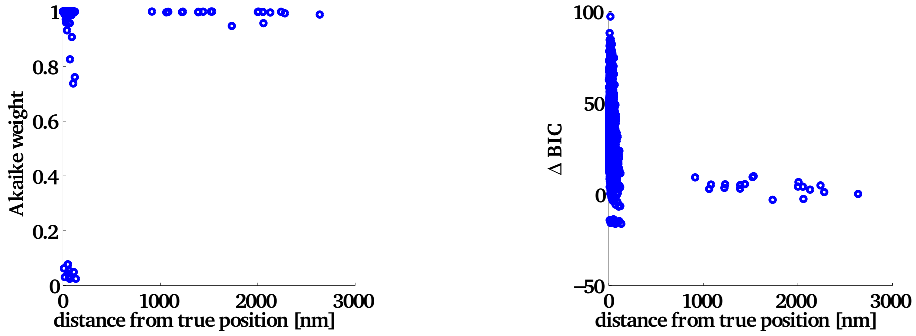

(c) Akaike weight vs. positional deviation **(d)** BIC difference vs. positional deviation

Figure 5.38.: pixelated Gaussian, MLE, variable PSF width, SNR=4

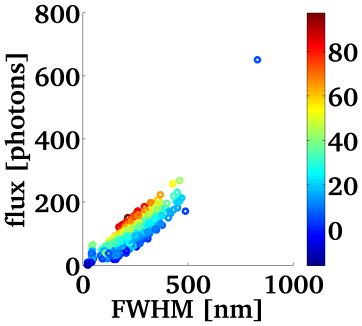

Figure 5.39.: flux vs. FWHM with color-coded BIC difference

only by a constant that depends on the number of model parameters and the sample size, i.e. the ROI dimensions. Thus, a ΔAICc scatterplot will look like a shifted and stretched version of figure 5.38d. The ΔBIC in figure 5.38d refers to the difference in BIC of the two models. It seems that the mislocalizations feature low ΔBIC (figure 5.38d) and pseudo-R^2 (figure 5.38b) values based on which rejection is possible since only small fractions of the total amount of localizations are below pseudo-R^2 of, say, 0.3 (figure 5.40a) or a ΔBIC below 15 (figure 5.40b).

Of course, parameter estimation may go awry not only in the spatial coordinates: For instance, take the estimate of 650 photons in figure 5.37a. It is the same datapoint featuring a FWHM of $>$ 800 nm (figure 5.37b) and a local background of 7.3 photons. Under conditions of spatially non-constant background and variable fluxes, grotesque width parameters most faithfully raise a flag on bad data. Note also the distinct subpopulation of subpixel FWHM also recurring at the lower end of the R^2 values and exhibiting low Akaike weights in figure 5.38c, and below zero BIC difference in figure 5.38d. Under imaging conditions further corrupted, these detections of fluorophores, where the model fit is indistinguishable from single noise-outlier pixels, will be buried under a population of false positive candidates and regularly will have to be sacrificed for the greater good. Keep in mind that a model prior ratio of $1 : 39^2 - 1$ as implied by the simulation would result in a further shift in BIC differences towards negative values by $\log(39^2 - 1) \approx 3.2$, even more clearly favoring the "no fluorophore" model (keeping in mind the suggestion above not to overestimate absolute numbers).

The usefulness of the BIC is probably most clearly demonstrated in the color-coded scatterplot of figure 5.39, where one can clearly see that localizations with large estimated fluxes at reasonable FWHMs exhibit the largest ΔBIC values and iso-ΔBIC lines indeed seem to represent comparable levels of data quality, especially the cutoff line originating from the detection scheme seems to be aligned with a low-ΔBIC isoline that by the way reproduces the flux $\propto$ FWHM^2 correlation on the level of a data population, confer the positive single localization correlation in figure 5.35e.

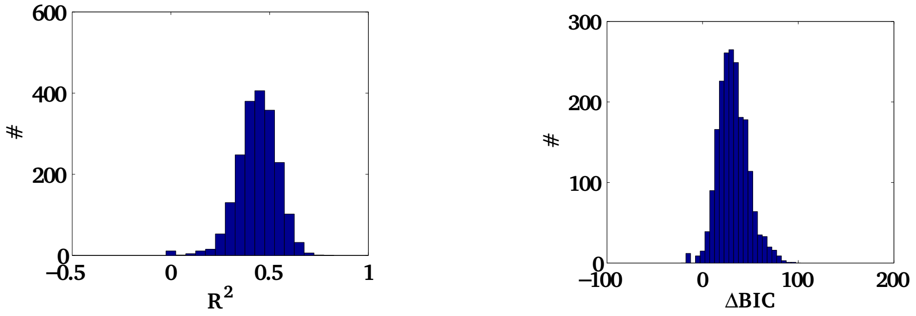

(a) histogram of pseudo-R^2 **(b)** histogram of ΔBIC

Figure 5.40.

5.1.10 Tracking

Tracking, i.e. the assignment of localizations to a trace of a fluorophore that is imaged through time, is done by the widely acknowledged [Martin-Fernandez and Clarke, 2012, Rolfe et al., 2011] tracking tool u-track [Jaqaman et al., 2008]. u-track's approach uses the mathematical framework of the linear assignment problem to link in a first step consecutive localizations in a temporally greedy, spatially globally optimal way and in a second step to simultanously close gaps and capture merge/split events of the tracked particles by joining track segments using temporal global optimization. While merging/splitting of tracks is of relevance under dense emitter conditions only where diffractive images of fluorophores may overlap, gaps due to fluorophore blinking, i.e. switching to a dark state for a limited number of frames, or poor detection owing to the high noise, are a major concern which is mitigated by u-track in the global optimization step.

5.1.10.1 Simulation of diffusing particles

In order to assess the reliablity of u-track under the conditions faced here, simulations were carried out. Starting with 10 randomly placed emitters on a 100×100 pixel grid, free diffusion was simulated for different diffusion coefficients. Sequences of 500 frames with a time lapse of 10 ms were created at a SNR of 4. To achieve realistic blinking behavior, a three state Markov model was implemented. With expontial probability distribution of a mean lifetime of 100 frames, simulated particles stay in the initial, fluorescing state. Otherwise, they turn into a dark, non-fluorescing state while still diffusing. The bright to dark state transition is reversible with a return time constant of 1 frame (10 ms). Both bright and dark states may non-reversibly "bleach" into a permanent dark state with a time constant of 10 frames (100 ms). In each frame, with a Poissonian distribution, 0.1 new particles are expected to appear at random positions, interpreted as stochastic return of (pre-acquisition or out of field of view) bleached fluorophores.

Bright states were again simulated with a flux of 100 photons per frame. However, the PSF FWHM was increased to 267 nm which amounts to 2.5 pixels á 107 nm. To introduce real-world deficiencies, the “matched” filter’s dimensions were set to 2.2 pixels FWHM. Analysis was carried out using 9 × 9 median filtering for background estimation and MLE localization with a pixelated variable width Gaussian. Post analysis, localizations with pseudo-R^2 less than 0.3 were discarded, possible introducing further gaps in the tracks to retrieve.

5.1.10.2 Tracking parameters

Actual tracking was performed with a maximum gap of particle absence of 2 frames, a minimum segment legth of 2 frames to be considered in the second step, disabled analysis specifically designed for the linear motion in Jaqaman et al. [2008], a search radius lower limit of 2 pixels and an upper limit of 5 pixels (more than 4 times the expected frame-to-frame diffusion distance at the largest diffusion coefficient simulated). Keep in mind that these search radii refer to frame-to-frame linking and that gaps between track segments exceding the maximum search radius may be closed (i.e. linking of track segments separated by frames with no localizations assigned to either segements) in the global optimization step. Compare the factor of 4 with the factor of 2.55 in Wieser and Schütz [2008] which is derived from the onset of the stable plateau of the diffusion coefficient estimate as a function of the search radius from a greedy tracking algorithm (i.e. without global optimization), which will result in severe underestimation of diffusion faster than anticipated.

As “Brownian motion standard deviation multiplication factor”, the default value of 3 was used and the usage of the local particle density for the search radius estimation was enabled. The power of the scaling of the Brownian search radius was set to 0.5 in accordance with free diffusion theory, but the scaling is reduced to 0.01 after a gap of three frames to penalize the linking of disparate localizations. Flux ratio limits are specified as 0.5 and 2 in order to prohibit linking of visibly distinct particles. The penalty factor for gap closing was set to a moderate 1.5, the resolution limit to 2.3 pixels equivalent to 246 nm.

An improper penalty in gap closing can be identified by inspection of the cumulative distribution function (cdf) of the square diplacements: A too high penalty accompanied with a too small maximum search radius yields a cdf curve that “directly” and “non-differentiably” reaches 1 rather than approaching it asymptotically (quotes are used to indicate that this statement is applied to binned empirical data and is true in a technical sense only for an infinite number of square displacements and infinitesimal bin sizes; yet, in empirical data non-asymptotic, non-exponential behavior still is easily recognized). The case of a too low penalty can be identified equally easy since overly ambitious gap closing yields a long tail in the cdf with slower than exponential asympotic behavior which stands out from the typical exponential regime in the low square displacements by a distinct “edge” or site of non-differentiability in the cdf that marks the poor track segement joining on top of the frame-to-frame tracking.

5.1.10.3 Evaluation

For diffusion coefficients of $D = 0.4$, 0.6, 0.8, 1.0, and 1.2 $\mu\text{m}^2/\text{s}$, three simulations each were run, analyzed, and tracked. From each set of tracking data, tracks with a length of 5 frames or less were discarded. For each simulation, the squared displacements for time lapses of 1, 2, 3 and 4 frames were pooled and an expontial was fit via least squares to the squared displacements’ cumulative distribution function. The cumulative distribution function was sampled at intervals of 11.4 nm^2 from 0 nm^2 up to 0.57 μm^2, where the upper boundary is equal to 50 pixels^2 and corresponds to ≈ five times the root mean square displacement expected from free diffusion of $D = 1\ \mu\text{m}^2/\text{s}$ within 10 ms. From the fit parameter, the diffusion coefficient is estimated and for each simulation the estimates from the different time lapses are averaged and a standard deviation is calculated. For each diffusion coefficient, these estimates from the simulation runs are averaged; errorbars represent the mean single run standard deviation (figure

5.41). On the basis of the limited number of simulated particles and the afterward rejection of data, the simulated diffusion coefficients were reproduced (2 σ level).

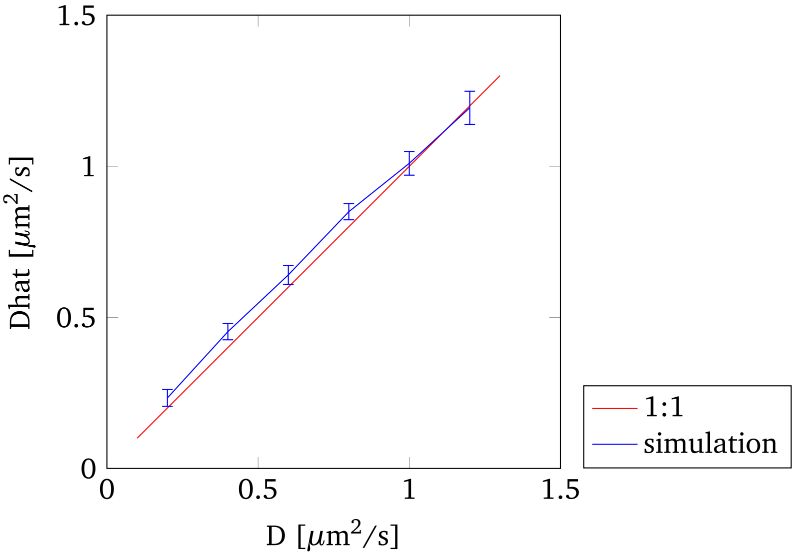

Figure 5.41.: Diffusion coefficient estimates. Errorbars represent the mean run standard deviation from three runs. Lines included to guide the eye; red line represents expectation value of simulated diffusion.

5.1.10.4 Two component model

Since the cell membrane is known to be non-homogeneous in composition (see section 2.2.2) and information is encoded in this heterogeneity that translates into differential local viscosity, regulating initialization of receptor clustering, cluster stability and disintegration, analysis based on a homogeneous population with a single diffusion coefficient is bound to miss the relevant features.

In order to check whether retrieval of diffusion is reliable, the simulated diffusion described above (section 5.1.10.3) was executed for the different fractions individually which were subsequently superpositioned in order to get simulated ensembles of particles. To account for the increased particle density due to the superposition of the fractions, the expected new number of particles per frame was reduced from 0.1 to 0.05. The numbers of simulated frames per run was raised to 3000 to account for the reduction of particles per frame and the increased demand for statistics due to the additional degrees of freedom in the fit to the cumulative distribution. *Nota bene*: In real world measurements, almost arbitrary pooling of individual data acquistions can be done to reach the needed statistics.

Two scenarios were played out:

1. $D_1 = 1.0\ \mu\text{m}^2/\text{s}$, $D_2 = 0.3\ \mu\text{m}^2/\text{s}$, $\alpha = 0.5$
2. $D_1 = 0.7\ \mu\text{m}^2/\text{s}$, $D_2 = 0.1\ \mu\text{m}^2/\text{s}$, $\alpha = 2/3$

As done in the single fraction case in section 5.1.10.3, three runs of each simulation were performed. This time, analysis was conducted for time lapses 1–10 to account for the extended model complexity. Mean values were calculated and mean standard deviations from the three runs were collected as in the single fraction case before. The empirical cumulative distribution of the squared displacements for a given time lapse t was fitted to using unweighted nonlinear least squares in the range from

$$\Delta r^2_{\text{min}} = 4t\langle\sigma_r\rangle^2 \tag{5.24}$$

to

$$\Delta r^2_{\text{max}} = 4t\ 6\ \mu\text{m}^2/\text{s} \tag{5.25}$$

where $\langle \sigma_r \rangle$ is the mean localization accuracy of the localizations underlying the tracks as estimated from equation 4.27 or directly estimated from the location posterior distribution standard deviation. Note that the angle brackets in equation 5.24 denote averaging over all localizations, while the angle brackets in equation 4.27 denote the individual localization expectation value. Δr^2_{max} is chosen to spread the investigated region to three times the mean square displacement of the by a factor of two overestimated diffusion coefficient of 1 $\mu\text{m}^2/\text{s}$. Although the localization accuracy is independent of the size of the time lapse t, scaling was included in order to keep the region of the fit in terms of squared displacements comparable in regard to the relation $\Delta r^2_{\text{max}}/\Delta r^2_{\text{min}}$ characterizing the region around the mean square displacement, where the two different diffusion coefficients are most distiguishable, up to the asymptotic behavior of the cumulative distribution towards 1. While a Δr^2_{min} of 0 does not alter the values of the estimates for the simulations conducted, a fit to the cumulative distribution for square displacements larger than Δr^2_{min} as defined in equation 5.24 only prevents the inclusion of immobile dyes (temporarily) attached to ECM components, which is important for accurate estimation of the relative population size. The strategy to fit the two fraction model

$$\text{cdf}_t(\Delta r^2) = \alpha \frac{1}{4D_1 t} \exp\left(\frac{-\Delta r^2}{4D_1 t}\right) + (1-\alpha)\frac{1}{4D_2 t} \exp\left(\frac{-\Delta r^2}{4D_2 t}\right) \tag{5.26}$$

was as follows: In a first step, the single parameter monoexponential model for the single diffusion coefficient was least square fit with the start value of the mean square displacement, which is the maximum likelihood estimator for perfectly (i.e. without noise), albeit random, exponential distributed data. The monoexponential estimate was then a tiny bit varied up and down and these two values were plugged into the biexponential fit as start values for the faster fraction and the slower fraction diffusion coefficients. Ordering of the two parameters within the function to fit is essential to prevent involuntary swapping of the parameters during optimization which would prevent the convergence of the fit. The start value of the relative fraction size α was 0.5. By design of these start values, where one knows that whatever the faster D_1 is, it is above the monoexponential estimate and likewise, as long as there is a slow fraction, is must be slower than the monoexponential estimate – by design of these start values, the algorithm was effectively prevented from getting stuck in local minima of the least squares.

Estimates of D_1, D_2, and α match simulated values within 2 average standard deviations for both scenario 1 (figure 5.42) and 2 (figure 5.43). In fact, with the exception of the estimate $\hat{D}_2$, all estimates match the simulated values to 1 average standard deviation accuracy (table 5.5).

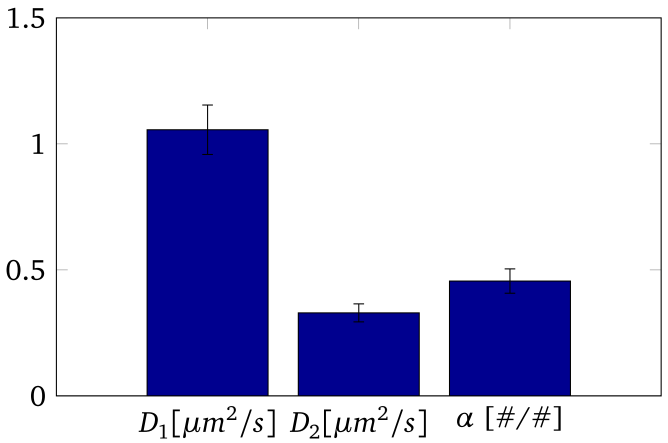

Figure 5.42.: Estimates of diffusion coefficients D_1, D_2 and relative population α

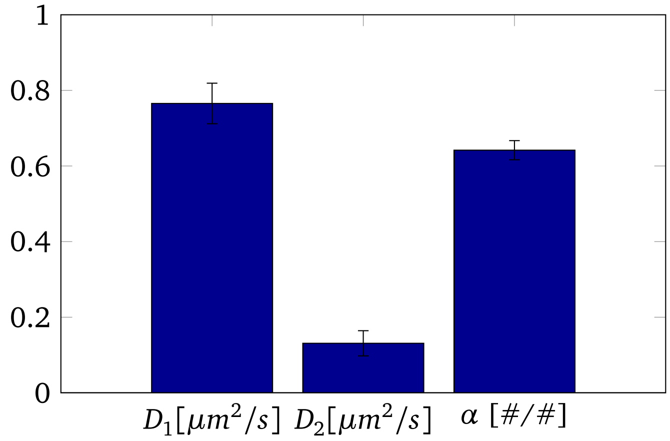

Figure 5.43.: Estimates of diffusion coefficients D_1, D_2 and relative population α

scenario 1		scenario 2	
$D_1 = 1\ \mu\text{m}^2/\text{s}$	$\hat{D}_1 = 1.056 \pm 0.098\ \mu\text{m}^2/\text{s}$	$D_1 = 0.7\ \mu\text{m}^2/\text{s}$	$\hat{D}_1 = 0.765 \pm 0.054\ \mu\text{m}^2/\text{s}$
$D_2 = 0.3\ \mu\text{m}^2/\text{s}$	$\hat{D}_2 = 0.330 \pm 0.036\ \mu\text{m}^2/\text{s}$	$D_2 = 0.1\ \mu\text{m}^2/\text{s}$	$\hat{D}_2 = 0.131 \pm 0.033\ \mu\text{m}^2/\text{s}$
$\alpha = 0.5$	$\hat{\alpha} = 0.456 \pm 0.048$	$\alpha = 0.666$	$\hat{\alpha} = 0.642 \pm 0.025$

Table 5.5.

This indicates that estimates are reproducible and accurate under different underlying free diffusion truths and in particular are neither erratic nor simply reproduce search radii or start values. To confirm further the choice of the $r_{\max}$ value, the localizations of scenario 2 were provided to the tracking algorithm using different maximum search radii. In figure 5.44, one can see that D_2 and α are largely independent of $r_{\max}$ while D_1 shows a little drift. For a higher emitter density, the impact of $r_{\max}$ is expected to be greater; however, the slope in the D_1 curve seems to be minimal around $r_{\max}$ = 4.5–5 pixels. For figure 5.44, localizations from all three simulation runs were used and cdf_t was fitted for $t = 1, \ldots, 10$, mean diffusion coefficients and fractions determined. Errorbars again represent mean standard deviations, with the standard deviations from the different time lapses t and the averaging over the three simulation runs.

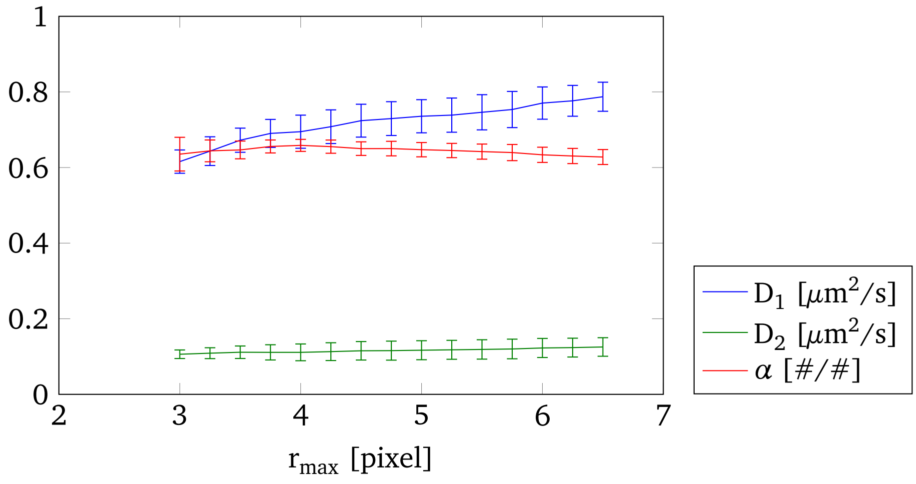

Figure 5.44.: Estimates of diffusion coefficients D_1, D_2 and relative population α for different maximal search radii. Y axis applies to D_1 and D_2 in μm^2/s and dimensionless α

For the situation as faced in biological samples, with potential non-free diffusion, the different estimates $\hat{D}_i(t) = \hat{D}_i(\mathrm{cdf}_t)$ based on the cdf of the square displacements at time lapse t are not averaged but rather a fit to the mean square displacement as estimated from the time-dependent diffusion coefficient approximation $\mathrm{MSD}(t) = 4\hat{D}(t)t$ is conducted for the fraction $i \in \{1,2\}$. In figure 5.45, showing a typical fit to the cdf of the square deviations of tracked single membrane marker dye molecules (CellMask™Orange, Thermo Fisher Scientific, Waltham, MA, USA; see section 3.5) in the plasma membrane of U2OS human osteosarcoma cells (see section 3.2) embedded in a collagen I hydrogel, one can see how the single component model is not able to appropriately capture the shape of the curve. Least square fits of the two-component model were carried out for 10 different time lapses, a compromise between the lower optimal number of fitting points (2, [Michalet, 2010]) for free diffusion and even larger numbers that try to follow the shape of the MSD curve to greater time lapses (which feature larger uncertainties due to statistics). The comparably large residuals (fit values minus data) at small displacements in figure 5.45c correspond to the order of magnitude of the localization accuracy: From the uniaxial lateral accuracies σ_x and σ_y, one gets the localizations accuracy σ_r which appears once for each the "departure" location and the "destination" in the accuracy Δd of every displacement

$$\sigma_x, \sigma_y \approx 25\mathrm{nm} \tag{5.27}$$

$$\sigma_r = \sqrt{\sigma_x^2 + \sigma_y^2} \tag{5.28}$$

$$\Delta d = \sqrt{\sigma_r^2 + \sigma_r^2} \approx 50\ \mathrm{nm} \tag{5.29}$$

The error of square displacements $SD = d^2$ is therefore

$$\Delta SD = \frac{\partial SD}{\partial d}\Delta d = 2d\Delta d \tag{5.30}$$

which yields for a displacement of $\sqrt{0.01\mu\mathrm{m}^2} = 0.1\mu\mathrm{m}$ (cf. figure 5.45c) $\Delta SD = 2 \cdot 0.1\mu\mathrm{m} \cdot 50\ \mathrm{nm} = 0.1\mu\mathrm{m}^2$ for immobile fluorophores such as temporarily attaching to collagen or the cover slip. These dysproportional amounts of small displacements are evitable only with probes even more specific since the expectation value of the displacement is zero in absence of drift and thus small displacements cannot be pinned down to originate from attachment rather than Brownian motion. Also, due to the temporariness and the stochasticity, the discard of whole tracks is not an option.

In figure 5.46, typical fits of the confined diffusion model (figure 5.46a, equation 2.30) and the anomalous diffusion model (figure 5.46b, equation2.31) to the mean square displacements $\mathrm{MSD}(t)$ of both fractions as suggested from the cumulative distribution at time lapses t are shown. One can nicely see the deviation from free diffusion. Inspection of the sum of squared residuals reveals the anomalous diffusion model to be describing the data distinctly better: Although both models feature the same number of degrees of freedom, the sum of squared residuals of the confined diffusion is a factor of 5 larger than of the anomalous diffusion model for the fast fraction and a factor of 3 larger for the slow fraction (figure 5.47).

Since analysis of the behavior of the individual fractions is based on the analysis of the cdfs, localization data is pooled in order to get as clean cumulative distributions as possible while keeping the ability to calculate error bars. Depths of the cells embedded in collagen I hydrogels ranged from 5 μm to 34 μm. Illumination was always for 5 ms, exposure was mostly 10 ms. Correction for finite illumination time [Savin and Doyle, 2005] is rarely done in the field, is more important for continuous illumination and few time lapses, and has been omitted. Field of views with $>$ 128 pixels in read-out direction of the

CCD take longer than 10 ms; in such circumstances, time lapse steps were set to 20 ms or a correction based on the field of view dimensions and a linear interpolation of frame transfer times of squares in the center of the sensor was added, typically around 2–3 ms. 9 × 9 median filtering was used as background estimation technique, localization was done using the correlation (cf. section 4.3.3) with a 2D Gaussian of 235.4 nm FWHM, and thresholding level of 1.5 noise standard deviations. Data points with a flux of less than 20 photons per frame, a FWHM less than 64.2 nm or greater than 642 nm or a pseudo R^2 as defined in equation 5.18 of lower than 0.2–0.3 were discarded. On occasion, BIC difference as calculated from equation 5.23 was required to be above 15–20. Specific criteria for data rejection were chosen based on inspection of reconstructed data set created from the localizations and comparison with the raw data. Remind that data quality varies with different imaging depths and tighter restriction may be needed for poor quality data while the same restrictions applied to data of better quality would unneccessarily reject valid data that might be more questionable under other circumstances.

On the remaining, reliable localizations, tracking was performed using the parameters given in section 5.1.10.2. Only tracks longer than 5 frames were included in the analysis of the cdfs. Datasets showing erratic behavior characterized by unsteady estimates of the population ratio α correlating with unreliable D_1 and D_2 estimates, were discarded. Also, outliers were removed. Remind that errors in detection, localization, tracking, square displacement cdf analysis – though effords are taken to minimize abberant data early in the line of data procession as layed out – propagate to the diffusion model fit. Especially the slow fraction is prone to errors since glass substrate or collagen attached fluorophores distort the square displacement distribution in the regime of small displacements.

In figures 5.48, 5.49, 5.50, 5.51, 5.52 model parameters $K_{a_1}, K_{a_2}, \alpha, a_1$ and a_2, respectively are shown for 2D (blue) and 3D (red) cell culture conditions, with measurements after x-ray irradiation of 0 Gy, 1 Gy, and 25 Gy. In addition to the bars displaying mean values plus/minus standard errors of the mean, the actual data points are added in order to make the scattering and the value distribution transparent. Data points typically represent an analysis based on 600 tracks with a mean length of 12 frames. Be aware that figures 5.48 and 5.49 display the numerical values of the K_{a_1} and K_{a_2} whose dimension is $\mu\mathrm{m}^2/\mathrm{s}^a$ involving the anomalous parameter, respectively. These numerical values correspond to $D(t = 1 \text{ second})$ in $\mu\mathrm{m}^2/\mathrm{s}$. For your interest, $0.5\mu\mathrm{m}^2/\mathrm{s}^{0.9} \cdot (10 \text{ ms})^{0.9-1}$ equals $0.79\ \mu\mathrm{m}^2/\mathrm{s}$, while $0.3\mu\mathrm{m}^2/\mathrm{s}^{0.7} \cdot (10 \text{ ms})^{0.7-1}$ equals $1.19\ \mu\mathrm{m}^2/\mathrm{s}$ and $0.01\mu\mathrm{m}^2/\mathrm{s}^{0.3} \cdot (10 \text{ ms})^{0.3-1}$ equals $0.25\ \mu\mathrm{m}^2/\mathrm{s}$. Note the interpretation of Robin et al. [2014], where D as obtained from $\mathrm{MSD}(t) = 4Dt^a$ is given in $\mu\mathrm{m}^2/\mathrm{s}$ and interchangably called “short term diffusivity” and “diffusion coefficient”.

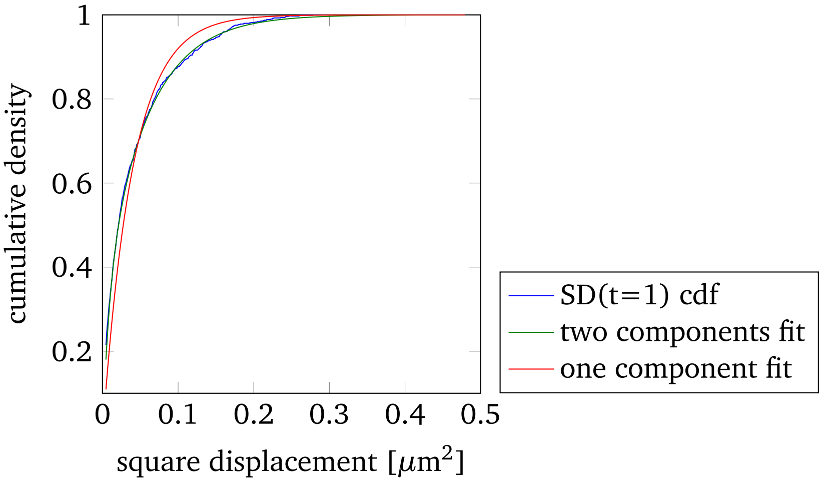

(a) typical fit of single component model (red) and two component model to cumulative distribution of square displacements (blue). Time lapse 1 frame equivalent to 10 ms.

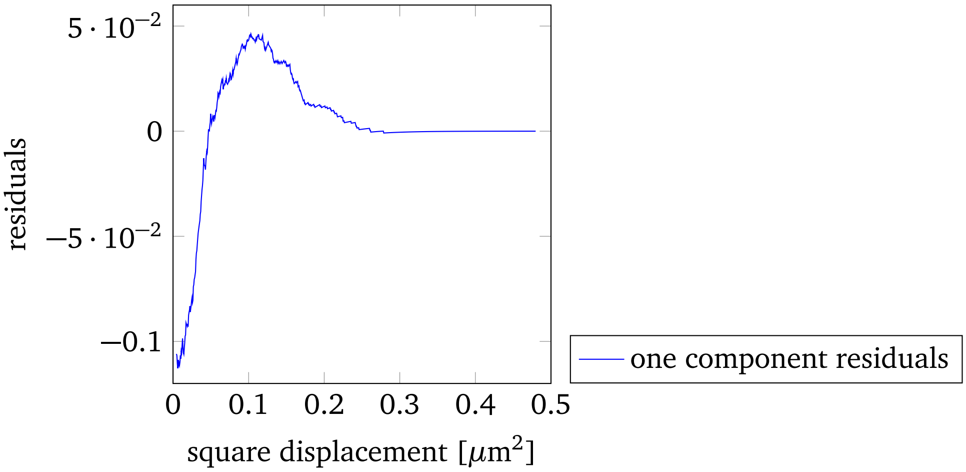

(b) residuals of single component model

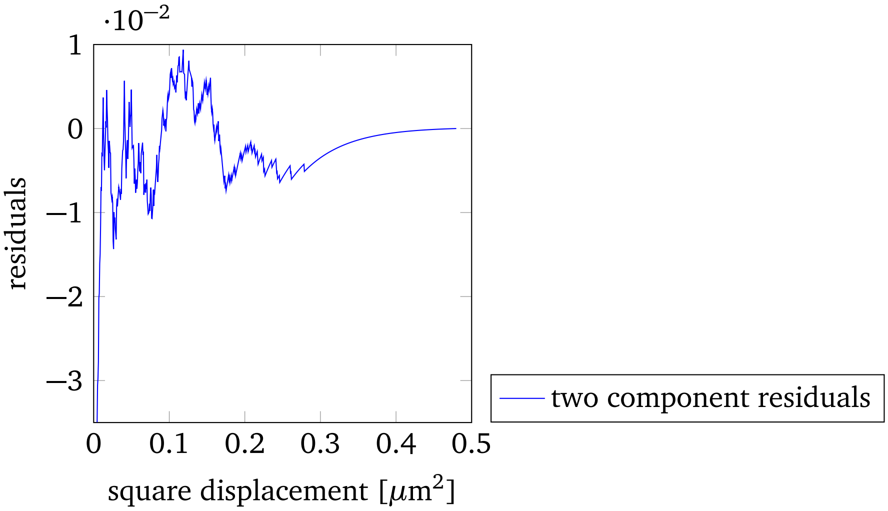

(c) residuals of two component model

Figure 5.45.: typical cdf fit, 1 Gy, 5–12 μm deep in collagen

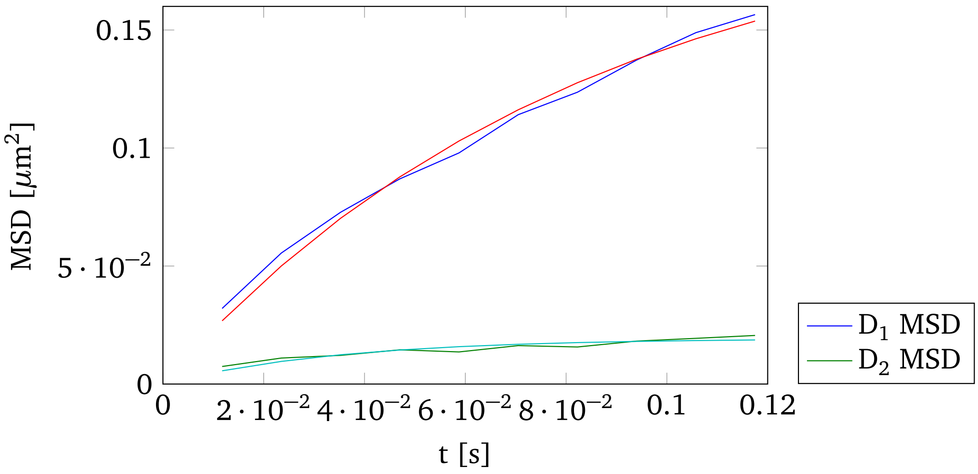

(a) confined diffusion model

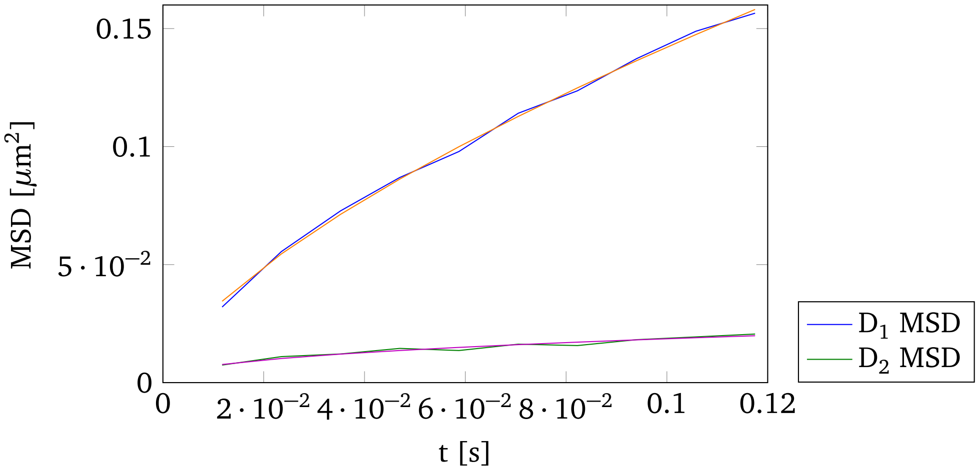

(b) anomalous diffusion model

Figure 5.46.: 25 Gy, 19 μm deep in collagen. **(a)** confined diffusion model fit, **(b)** anomalous diffusion model fit. Note both models feature the same number of degrees of freedom.

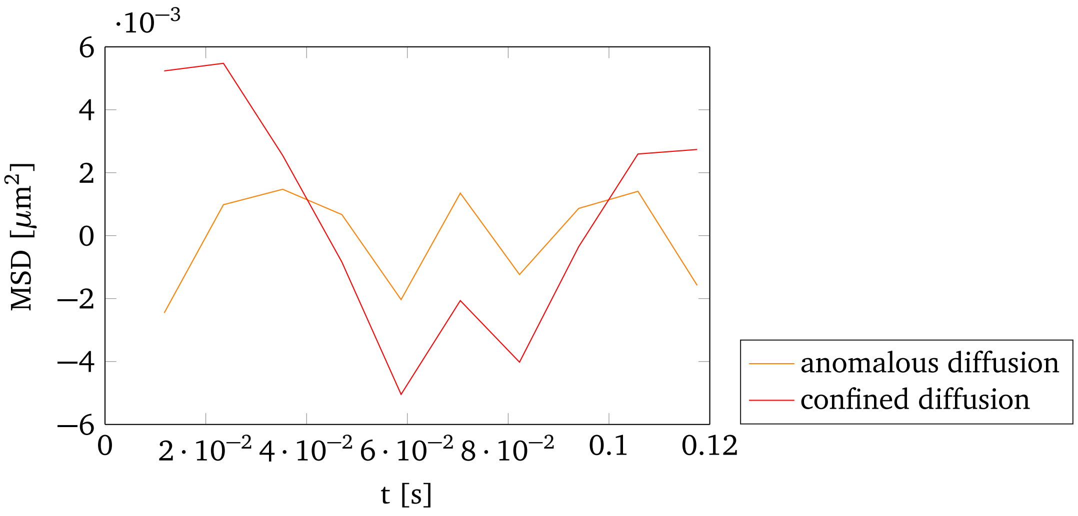

(a) Fast fraction residuals

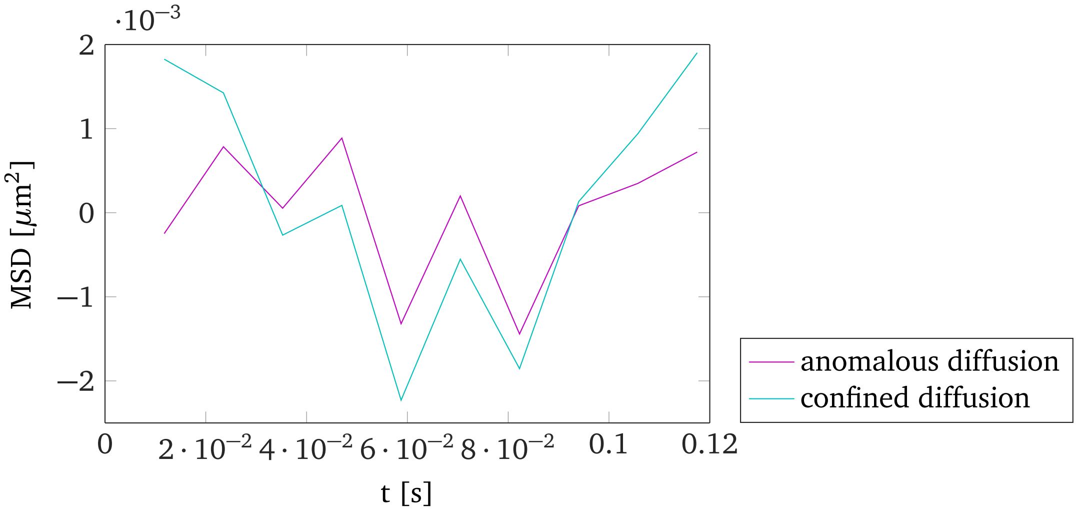

(b) Slow fraction residuals

Figure 5.47.: Residuals of the fits from Figure 5.46

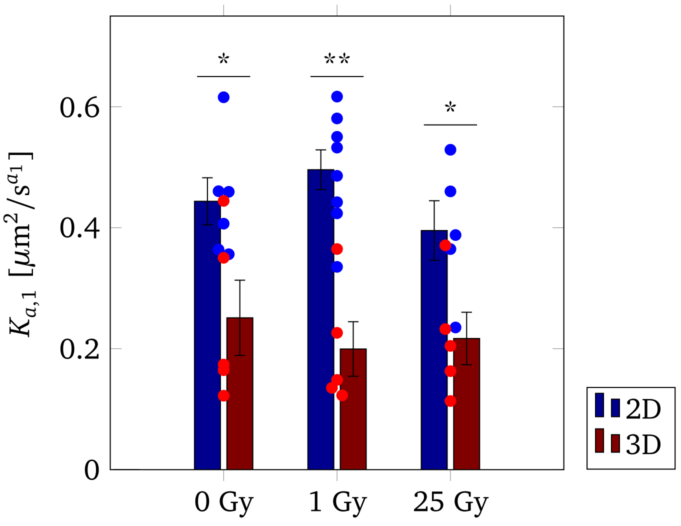

Figure 5.48.: generalized coefficient of diffusion K_{a_1} of the fast fraction; error bars represent standard errors of the mean; *,**: significant (p<0.05, p<0.01) as examined by Mann-Whitney U-test

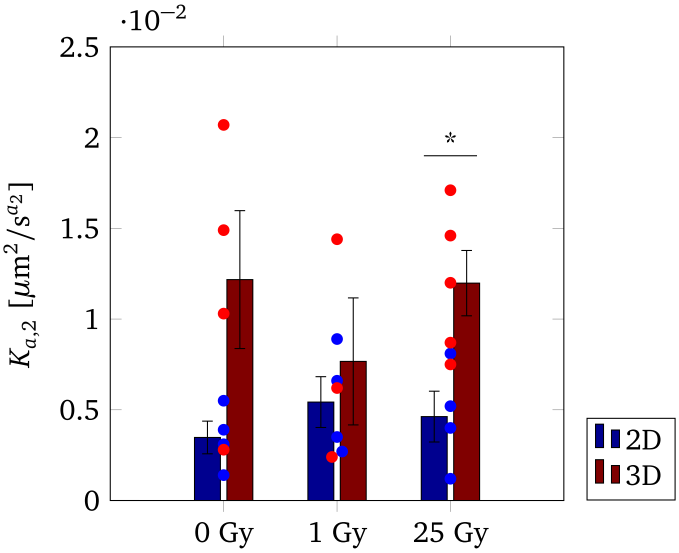

Figure 5.49.: generalized coefficient of diffusion K_{α_2} of the slow fraction; error bars represent standard errors of the mean; *: significant (p<0.05) as examined by Mann-Whitney U-test

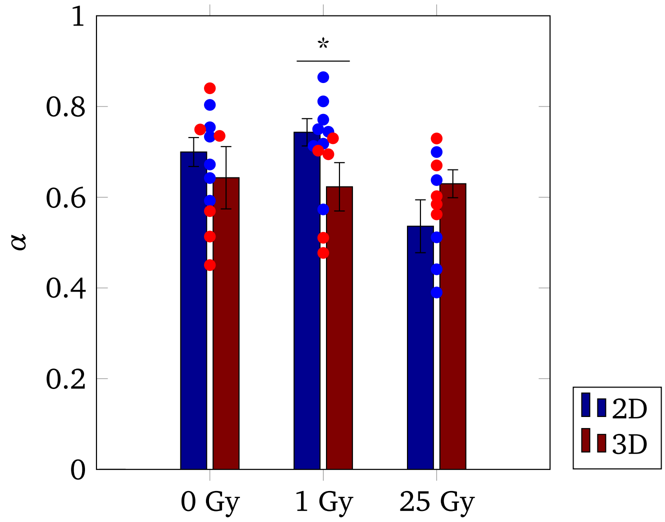

Figure 5.50.: relative fraction size α; error bars represent standard errors of the mean; *: significant (p<0.05) as examined by Mann-Whitney U-test

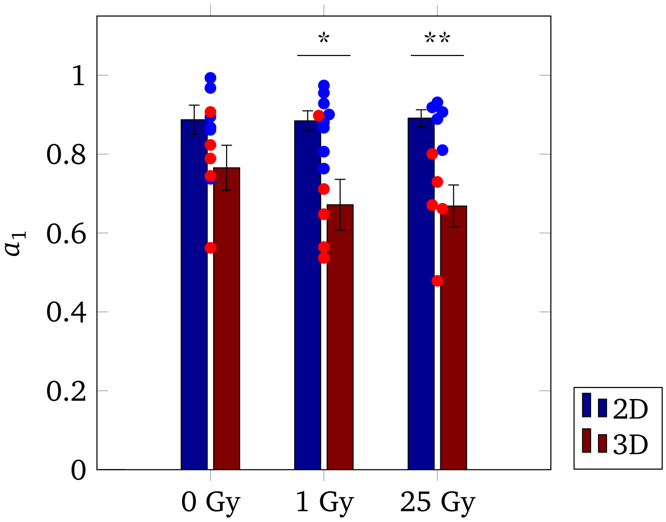

Figure 5.51.: anomalous exponent a_1 of the fast fraction; *,**: significant ($p<0.05$, $p<0.01$) as examined by Mann-Whitney U-test

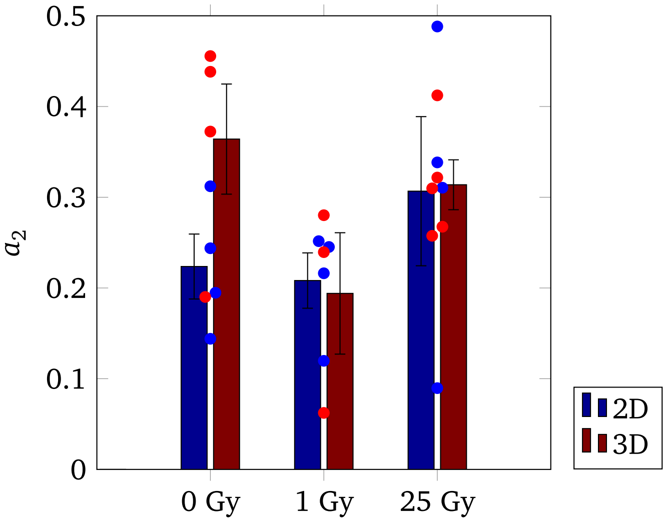

Figure 5.52.: anomalous exponent a_2 of the slow fraction

6 Discussion

6.1 Tracking of single molecules in the plasma membrane of cells in 3D ECM cell cultures

For the first time, single fluorescent molecules were detected and tracked in the context of 3D cell culture. Previously, single molecule detection in 3D cell cultures was limited to static assessment of molecule aggregates while tracking was limited to 2D cell cultures [Lauer et al., 2014]. This is because single molecule microscopy techniques popularly applied to achieve the necessary sensitivity including stochastic fluorophore activation at high illumination intensities, scanning approaches including STED (stimulated emission depletion) microscopy, and two-photon confocal microscopy are not feasible for assessment of dynamics on molecular level. However, the data analysis presented in this thesis allows for detection and tracking of formerly inaccessible, swift single fluorescent molecules in the plasma membrane of cells cultured in 3D ECMs. This was possible owing to design, and evaluation, and optimization of processing methods. Since the overall tone of this thesis is to emphasize the flexibility of the analysis tools, some guidelines following shall enable future end-users to adjust parameters to their experiment.

The degree of background signal heterogeneity is not expected to differ markedly from the conditions faced in this thesis even in future experiments on 3D cell culture not based on collagen I. Therefore, background estimation is recommended to be carried out using 9×9 median filtering (figure 5.3).

Correlation with a matched filter is a detection scheme with a good detection efficacy to false positive rate trade-off (figure 5.18). For extremely low SNR conditions, the approach based on the Kullback-Leibler divergence may be superior (figure 5.23). The detection threshold should be chosen to achieve 100 % on a conservatively estimated SNR value. The correlation kernel should be chosen with regard to the emission wavelength of the fluorophore in use. Preliminary kernel FWHM definitions can be obtained from visual inspection of the raw data. From preliminary analysis using a variable width model, inspection of the width histogram of localized fluorophores may yield a more accurate kernel width.

While localization in z-direction was not done in the present thesis, deflation may be done using elliptical kernels for successive detection of fluorophores below and above the focal plane. Another application of deflation using different detection schemes may be to combine matched filtering and the Kullback-Leibler divergence-based method under circumstances of large fluctuations of the SNR within the field of view.

Cell orientation relative to the focal plane may allow for localizations with fixed FWHM (i.e. FWHM is not a parameter to be fitted) although in general cell and plasma membrane orientation will be oblique to the focal plane so that more accurate localizations would be achieved using PSF models with a variable width.

The excess accuracy of parameter estimation using Bayesian inference by MCMC methods especially with regard to photon flux and ellipticity (figures 5.27 and 5.30) was not necessary for the investigations of the present thesis. Future research e.g. concerning the cluster status of membrane proteins by evaluation of the photon flux may benefit in form of more sensitive discrimination between different levels of oligomerization. Under experimental circumstances such as in the present thesis where flux estimation is not a primary concern, MLE is recommended as MCMC evaluation is a significant computational effort.

Facing an extremely low SNR, where reliable detection becomes problematic, denoising using PURE-LET with LET_2, 2 wavelet levels and 10 cycles (figure 5.16) or more may be appropriate.

Finally, post processing is advised to discard identifiable false positive detections or fits gone awry (figure 5.36). Depending on the detection threshold chosen in light of the SNR of the data, post processing has to be more or less rigorous. Inspection of data is most conveniently done using scatterplots such as figure 5.39. Besides atypical widths, especially the pseudo-R^2 as defined in equation 5.18 and the ΔBIC provide a means to identify questionable localizations (figure 5.40).

6.2 Two membrane phases

On first sight, one can see in figures 5.48 and 5.49 that the parameters K_{a1} and K_{a2} are an order of magnitude disparate for all cell culture conditions and all doses investigated. Note that for a single component ensemble the estimates $D_1(\mathrm{cdf}_t)$ and $D_2(\mathrm{cdf}_t)$ would coincide with arbitrary α, preferentially at the starting value $\alpha = 0.5$. It should be stated explicitly that the two-phase model of the membrane is a model that is phenomenological and rather a suitable description of the data than a microscopic theory. It implies that membrane lipids organize into homogeneous phases and that there are exactly two of these phases. While there have been conducted many studies on the phase diagramm of two-component lipids mixtures, several on three-component mixtures, and few on four-component (or three + cholesterol) lipid mixtures, biological membranes feature a plethora of lipids whose interplay and organization is scarcely understood. Although the assumption that the lipid composition of all lipid rafts is the same and independent of time or, say, membrane proteins seems simplistic, it is useful to group the cell membrane into two main phases, neglecting minor intra-phase raft-to-raft variations or non-raft heterogeneity. In addition to the widespread, established lipid raft/non-raft dichotomy, still simplistic multi-phase models require additional parameters with impending overfitting and numerical instability.

The relative weight α of the fast fraction indicates predominance of the fast fraction (figure 5.50), implying a percolating phase of fast diffusion and a non-percolating phase of slower diffusion.

6.3 Non-Brownian motion

Both fast and slow fraction show non-Brownian behavior. Transmembrane proteins anchored to the cytoskeleton are anticipated to pose as immobile obstacles while macromolecular crowding may give rise to viscoelastic effects with long-time correlations. Although the effect of molecular crowding is still controversial [Weigel et al., 2012], the effect of cytoskeletally tethered membrane proteins and lipids has frequently been shown in the dramatic increase (four- to fivefold [Crane and Verkman, 2008]) in diffusion in blebs, membrane protrusions virtually free of membrane-cytoskeleton attachments.

6.4 2D vs. 3D, and the fast fraction

Previously, the impact of 3D cell culture conditions on diffusion within a membrane has not been the subject of any characterization. In 2D, with tracking experiments using objective-type TIRF on the dorsum, experimenters face dorsal actin stress fibers potentially associated with membrane compartmentalization and distinct clustering of receptors and adhesion molecules into focal adhesions now rather understood as “archpelagos” (Saxton) than as “venice” (i.e. the obsolete venetian channel model of focal adhesions) meaning tracers in the membrane not only diffuse in and out of focal adhesions but are by and large unhindered between tethered membrane proteins. The focal adhesions encountered in 2D cell culture conditions are present only on at contact with the substrate (i.e. the cell bottom) and furthermore only at the outer “rim” (i.e. the transition between top and bottom). Hence, in accordance with the data and our hypothesis, tracer diffusion in the central area of the dorsal plasma membrane could display free or confined diffusion.

Cells in 3D microenvironments in contrast, are devoid of stress fibers and focal adhesions as known from the 2D scenario. Since this corresponds not or not primarily to a decrease in expression, it is rather a change in the distribution of both adhesion molecules and the cytoskeletal actin. Thus instead of isolated areas of high obstacle density in the 2D case, the 3D scenario of a more homogeneous distribution is expected to provide obstacles to membrane diffusion all around the membrane with a degree of tethering dependent on the extracellular density of ligand, i.e. matrix, molecules. Consequently, the anomalous coefficient of the fast fraction α_1 is reduced to ≈ 0.7 in 3D in comparison to ≈ 0.9 in 2D for all doses (figure 5.51). It is noteworthy that tissue-like microenvironments have been reported to induce significant changes in the lipid composition of the plasma membrane: More precisely, the sphingolipid content increases from 10 % to 15 % for heavily ECM secreting mouse fibroblasts in 3D matrix in comparison to monolayer conditions [Jordanova et al., 2009]. At this point it should also be mentioned that U2OS cells embedded in a collagen I hydrogel grow along collagen fibers and thus exhibit a distinct elongated morphology which poses a challenge to find membrane regions suitable for imaging.

Interestingly, an anomalous exponent of 0.7 corresponds to an obstacle density at the percolation threshold while 0.9 corresponds to an obstacle density of 0.8 relative to the density at the percolation threshold[Weigel et al., 2012]. This seems to reflect the concentration of membrane proteins in large focal adhesions under 2D cell culture conditions and the more even distribution – probably into small 3D adhesion complexes – of membrane proteins under 3D cell culture conditions.

6.5 Slow fraction

The slow fractions feature anomalous exponents below 0.5 (≈ 0.27, figure 5.52). This corresponds to non-percolating membrane regions, i.e. confined diffusion. Note that rudimentary confined diffusion models such as diffusion confined to a circle or a square are hard to distiguish on the basis of limited time points of the MSD curve (cf. figure 5.46a and 5.46b). Yet, data support the anomalous diffusion model corresponding to the probably more realistic model of a labyrinth of obstacles. As discussed in section 2.5.5, anomalous subdiffusion may also be due to hop-diffusion being observed at intermediate time scales. The more pronounced scattering of the α_2 values may be explained in the light of the confinement by insufficient averaging over different sizes of confinement regions. Remind that only a fraction of $\alpha - 1$ relates to confined diffusion. Anomalous subdiffusion was also proposed as an alternative model to the immobile/free dichotomy in fluorescence recovery after photobleaching (FRAP) [Feder et al., 1996].

6.6 Comparison with cell-level anomalous exponents

For a rough idea of crowdedness, one can compare the anomalous exponents of 2D-diffusion within the membrane with anomalous exponents obtained from intracellular microrheology studies, where $\alpha = 0.5 - 0.6$ was found for investigations on the frequency-dependent shear modulus within cells using magnetic beads [Wilhelm, 2008] and $\alpha = 0.5$ by measuring the response of intracellular granules trapped and displaced with optical tweezers [Yanai et al., 2004]. An alternative, yet less convincing interpretation for the low anomalous exponents α_2 refers to terms of viscoelasticity rather than labyrinth-like, i.e. fractal, regions of confinement. Specifically, Wilhelm [2008] interprets α to range from solidlike ($\alpha = 0$) to liquidlike ($\alpha = 1$) and cites values of anomalous exponents obtained from cells stretched between microplates ($\alpha = 0.2 - 0.3$ [Desprat et al., 2005]) , cell deformed by local torque ($\alpha = 0.2 - 0.25$ [Fabry et al., 2001]) or force exerted on membrane-bound microbeads ($\alpha = 0.18 - 0.21$ [Balland et al., 2006]) or by poking with a microtip ($\alpha = 0.22$ [Alcaraz et al., 2003]). Naturally, care should be taken when relating anomalous exponents from diffusion experiments with anomalous exponents obtained from shear modulus experiments since the latter only relates to viscoelasticity while the former is at least partially due to presence of obstacles.

6.7 Reported anomalous exponents of lipid diffusion in 2D-grown cell membranes

Using STED (stimulated emission depletion) microscopy FCS (fluorescence correlation spectroscopy), Eggeling et al. [2009] report almost free ($a \approx 1$) diffusion of Atto647N-labeled phosphatidylethanolamine (PE) at $D = 0.5\ \mu\mathrm{m}^2/s$, but anomalous diffusion with $a < 0.7$ for sphingomyelin (SM), gangliosin GM1 and the GPI (glycosylphosphatidylinositol) anchor in PtK2 rat-kangaroo epithelial cells grown on glass. Referring in 2009 to trapping times and temporary binding in the article and to anomalous diffusion in the supplement only, anomalous diffusion and anomalous exponents are more prominent in Mueller et al. [2011, where C. Eggeling is last author]. There, they refine their finding to $a < 0.9$ for glycerophospholipids including saturated PE (DPPE, 1,2-dipalmitoyl-*sn*-glycero-3-phosphoethanolamine), unsaturated PE (DOPE, 1,2-dioleoyl-*sn*-glycero-3-phosphoethanolamine) and PC (phosphatidylcholine), and $a < 0.66$ for SM and GM1. Using confocal mode, they assess a diffusion coeffient of 0.4–0.6 $\mu\mathrm{m}^2$/s for most lipids, while ceramide and DOPE attain 0.9 $\mu\mathrm{m}^2$/s. While diffusion coefficient numerical values vary with membrane constituents and, hence, from cell line to cell line, anomalous exponents are probably more transferable and indeed matches the exponent of the 2D fast fraction a_1 (figure 5.51) the exponent of glycerophospholipids.

The increase in sphingolipid content under 3D microenvironment conditions mentioned above seems to give an explanation for the lower anomalous exponent of the fast fraction in 3D.

It should be noted that FCS faces methodological limits [Baumann et al., 2010] in ergodicity-breaking anomalous diffusion scenarios [Weigel et al., 2011] whose analysis is subject of current research. Anomalous exponents in Mueller et al. [2011] vary with time scale; mentioned inequalities refer to shortest periods. One aspect of difficultes arising in ergodicity-breakings is that by design, membrane regions contained by obstacles such as membrane proteins are only probed by FCS if the excitation volume is located within the region. Secondly, as explained in the section on continuous-time random walks (section 2.5.5), temporary binding events may induce non-central limit mathematics rendering averaging useless. Consequently, FCS is unaware of a second fraction. Mueller et al. [2011] see the trapping of sphingomyelin as “cholesterol-assisted” and “cytoskeleton-dependent” but stress that “these interactions are different from those responsible for phase separation in model membranes”.

6.8 Impact of ionizing radiation on membrane organization of U2OS cells

No differences in relative fraction size α, coefficients K_a, and anomalous exponents a are observed irrespective of the cell culture condition even for a dose of 25 Gy, where radiation damage to the membrane is expected. This finding is in line with the model of anchored membrane proteins posing as obstacles with an obstacle density unaltered by irradiation. While the cytoskeleton is a dynamic structure with continuous formation and degradation of actin fibers, there is no evidence that ionizing radiation influences the distribution of obstacles for instance by hypothesized induction of actin fiber crosslinking and tighter compartmentalization. Ionizing radiation may affect the degree of crosslinking of the collagen hydrogel and thereby increase the ECM’s elastic modulus [Mohamed et al., 2007]. Although cells are known to respond to changes in matrix elasticity by mechanosensing, effects on the cellular adhesion receptor distribution as probed by the fluorescent lipid-mimetic tracer were not evident.

This suggests that the distribution of protein-rich lipid rafts is not affected by ionizing radiation. Note that cellular responsiveness to radiation-induced increases in matrix elastic moduli may be beyond the temporal scope of the measurements conducted.

On the other hand, ceramide production is expected to be induced. Ceramide content of bovine aortic endothelial cell lipid extracts increased after irradiation with 10 Gy by 30 % from 0.95 nmol/10^6 cells to 1.25 nmol/10^6 cells within 2 minutes independently of DNA damage [Haimovitz-Friedman et al., 1994] by ROS-mediated translocation of ASMase from the lysosome to the plasma membrane. Ceramide content in the plasma membrane of T47D human breast cancer cells is tripled 2 h post 20 Gy irradiation with x-rays due to increased activity of cell surface glycohydrolases [Aureli et al., 2012]. Generation of ceramide in the regime of hours post irradiation is due to *de novo* ceramide synthase pathway is dependent on DNA damage and involves ataxia telangiectasia mutated (ATM) [Vit and Rosselli, 2003, Corre et al., 2010]. DNA damage such as caused by ionizing radiation induces downregulation of uridine diphosphate-glucose ceramide glucosyltransferase which increases ceramide levels with subsequent apoptosis in p53 deficient cells [Haynes et al., 2012, DNA damage there induced by DNA crosslinker Mitomycin C]. Increase in ceramide levels as e.g. induced by tumor necrosis factor α leads to ceramide-mediated apoptosis in U2OS cells. However, U2OS cells with wildtype p53 are reported to not show an increase in ceramide levels post DNA damage induction by Mitomycin C [Haynes et al., 2008].

Ceramide increases membrane density and viscosity so that slower or more hindered diffusion would take place: Diffusion of 5.75 μm diameter poly(methyl methacrylate) (PMMA) particles on an egg-sphingomyelin monolayer was observed with a diffusion coefficient of 0.68 $\mu\text{m}^2/\text{s}$ in contrast to 0.15 $\mu\text{m}^2/\text{s}$ on a egg-ceramide monolayer [Catapano et al., 2011]. The same study showed that the ratio of shear modulus to frictional shear loss interpreted as degree of “solid character” increases with larger ceramide content of sphingomyelin/ceramide mixtures at room temperature.

6.9 Contrasting U2OS vs. endothelium radiation response

Thus, the findings of section 5.2 combined with the fact that U2OS do not go into apoptosis after x-ray irradiation [Allan and Fried, 1999] agree that DNA damage does neither trigger “conventional” p53-dependent apoptosis nor ceramide-mediated apoptosis via ceramide synthase. Furthermore, no increase in ceramide in the exoplasmic leaflet of the plasma membrane due to translocation of acid sphingomyelinase (ASMase) is suggested by the findings, in agreement with the observation that ceramide would lead to apoptosis [Haynes et al., 2008].

Based on investigations of radiosensitive and radioresistant human head and neck squamous carcinoma cells irradiated with 10 Gy of x-rays, it has been suggested that glutathion (GSH) scavenges intracellular reactive oxygen species (ROS) created in the radiolysis of water, preventing the activation of ASMase by oxidative stress [Bionda et al., 2007]. This is in line with the significant amount of base expression of TIGAR (TP53-induced glycolysis and apoptosis regulator) in U2OS cells, which results in an inhibition of glycolysis, an overall decrease in intracellular ROS levels and correlates to the ability to protect from ROS-associated apoptosis [Bensaad et al., 2006]. Although endothelial cells are suggested to exhibit significant GSH levels as well, subunits $\text{gp91}^{\text{phox}}$ and p47^{phox} of the nicotinamide adenine dinucleotide phosphate (NADPH) oxidase (NOX) are known to concentrate in ceramide-enriched domains of endothelial cells following ASMase activation. Endothelial NOX is an enzyme complex that is involved in the generation of superoxide radicals, $O_2^{\bullet -}$, and now considered as the primary enzymatic source of vascular ROS [Corre et al., 2013]. In consequence, there is a feed-forward amplification in endothelial cells with ROS produced by NOX within ceramide-rich domains furher promoting ASMase activation by oxidative stress in turn generating more ceramide. A similar feed-forward mechanism has been reported for ASMase activity induced by Fas ligands [Zhang et al., 2007, 2006].

6.10 Radiation damage to the plasma membrane

Thus, initial activation of ASMase is amplified in endothelial cells but countered or inhibited in U2OS cells. This initial activation may be due to radiation damage to the membrane. The impact of *direct* damage at a dose of 25 Gy can be roughly estimated by the mean number of excitations to typical membrane lipid POPC (1-palmitoyl-2-oleoylphosphatidylcholine, $C_{42}H_{82}NO_8P$) assuming a density of

1 g/cm^3, 1 lipid per 0.5 nm^2 in a membrane leaflet of 2 nm thickness and a mean excitation energy according to Bragg additivity

$$\ln\langle I\rangle = \frac{\sum_j w_j(Z_j/A_j)\ln I_j}{\sum_j w_j(Z_j/A_j)} \tag{6.1}$$

with fraction of weight w_j, atomic number Z_j, mass number A_j, and mean excitation energy I_j of the jth component, yielding with $\langle I\rangle = 63$ eV obtained by insertion of I-values from Hubbell and Seltzer [1996] finally

$$25\ \text{Gy}\ 1\frac{\text{g}}{\text{cm}^3}1\ \text{nm}^3/63\ \text{eV} = 2.510^{-6} \tag{6.2}$$

However, indirect damage by ROS outweights direct damage for x-rays.

The impact of ROS-mediated redox-signaling on mitochondria [Leach et al., 2001] or redox-related signaling via Ca^{2+} release which take part in ROS cascades potentially affecting the plasma membrane is subsumed under the idea of general oxidative stress response which his beyond the scope of this discussion. Focusing on radiation damage to the plasma membrane, possible effects are lipid fragmentation, i.e. lipid radiolysis, which leads to a denser packing, lipid crosslinking, and peroxidation. Lidid radiolysis and crosslinking are associated with an increase in membrane rigidity while peroxidation leads to membrane disordering, decrease in density, increase in membrane penetration of water molecules, and a higher fluidity. Interpretation of experimental findings is not straightforward since experiments on cells using clinical doses are rare and occasionally seemingly in contradiction with earlier, less sensitive methods or experiments on liposomes in the kGy range. It is believed that rigidity increasing effects dominate for high doses (>1 kGy [Marathe and Mishra, 2002]) until breakdown of the bilayer whereas at lower doses effects dominate which increase fluidity. Fluidity has been assessed in terms of fluorescence anisotropy using fluorescent probe DPH (1,6-diphenyl-1,3,5-hexatriene) in membranes of erythrocyte “ghosts” (i.e. lysed and resealed red blood cells) reporting an decrease in anisotropy [Kölling et al., 1994, Berroud et al., 1996, Yonei et al., 1979] which is interpreted as an increase in fluidity, detectable at 10 Gy [Benderitter et al., 2003]. This has been attributed to peroxidation (-OOH) of unsaturated fatty acid residues. Peroxide and hydroxyl groups but also penetrating water molecules increase polarity within the membrane which was detected using fluorescent probes Laurdan (6-lauroyl-2-(dimethylamino) naphthalene) and Prodan (6-propionyl-2-(dimethylamino) naphthalene) which are sensitive to the polarity of their molecular environment [Parasassi et al., 1994, 1991]. Also, oxidation of thiol groups (-SH) [Yonei et al., 1979] leading to conformational changes of membrane proteins was observed [Grzelińska et al., 1979]. Consequently, proteins have been made responsible for the differences between natural membranes and liposomes at equivalent lipids not only in terms of fluidity but also in generation of lipid peroxidation end-product malondialdehyde [Kölling et al., 1994]. In contrast, Leyko and Bartosz [1986] are critical of the impact of thiol groups on radiation response. Keep in mind for the interpretation that erythrocytes used in many of the cited studies lack lysosomes which moonlight as ASmase reservoirs. Furthermore, lipid peroxidation depends not only on the lipid species which vary from cell line to cell line but is in addition modulated by several agents including GSH [Konings et al., 1979] and cholesterol [Pandey and Mishra, 1999, Parasassi et al., 1995]. Intriguingly, not only cholesterol content is enhanced in cells growing under 3D conditions compared to 2D condition but also the cholesterol chemical activity as assessed by its susceptibility to cholesterol oxidase [Stefanova et al., 2009].

With regards to radiation-induced cytoskeleton reorganization, Gabryś et al. [2007] report that microvessel endothelial cells respond to irradiation with stress fiber formation whereas the endothelium of larger vessels such as from the umbilical vein does not [Jelonek et al., 2011]. This highlights once more the particularity of microvasculature endothelium with respect to ionizing irradiation which might explain the difference in U2OS and tumor microvessel radiation response.

6.11 Summary and Outlook

Even though U2OS may have turned out as an unlucky choice to investigate the connection between 3D culture conditions and radioresistance by assessing the dynamics of the plasma membrane, the results clearly show the capabilities of single molecule microscopy to contribute to the revelation of molecular dynamics and the potential to discover the onset of signaling pathways at the plasma membrane, the doorstep between the intra- and extracellular space under conditions much better reflecting the conditions present in native tissue as they are realized by traditional culture conditions on 2D glass or plastic substrates. An already tested modification of the technique involves astigmatic imaging by means of a cylindrical lens in the imaging light path which enables the encoding of the third spatial axis around the focal plane which is of particlular interest for the tracking of cytosolic fluorescently labeled proteins or might even address the curvature of the plasma membrane [Deserno, 2014]. More confined illumination using a light sheet formed by means of a cylindrical beam expander has been shown to improve contrast – essential in image quality degrading 3D matrices – in first tests. Better modeling of the noise in electron-multiplying cameras [Hirsch et al., 2013] will improve localization accuracy which translates into more reliable displacements at small time increments. Future experiments using probes that feature the RGD-sequence (arginine-glycine-aspartic acid, see also section 2.2.3.1), will perform *molecular imaging* on native integrin receptor levels as encountered in wild type cells. This has the clear benefit that changes in expression levels are captured as the system is genetically unmodified. Entire proteins diffuse more slowly than the light lipid analogue used here, which means smaller displacements at the same frame rate translating into even less dubious tracking at given fluorophore densities. Unfortunately, tracking of fluorescently labeled membrane proteins was not conducted in the present thesis as the development and establishment of the analysis procedure was taking more time than expected.

As a complement to fluorescent protein localizations, improvements in quantum dot coating technology may render quantum dots more suitable for sensitive single particle tracking experiments by reducing the passivating layer and employing targeting moiety monovalency [Howarth et al., 2008] which would allow for exploitation of the photostability in terms of increased signal to noise ratio and higher statistics due to longer particle tracks. Ultimately, track lengths corresponding to photobleaching resistant quantum dots may distinguish different types of anomalous diffusion [Ernst et al., 2014].

As discussed by Lauer et al. [2014], intravital single molecule microscopy of intact organs, e.g. of mice, is imminent. Intact organs pose a severe imaging challenge that calls for advanced analysis technologies such as presented in this thesis. A key step towards single molecule microscopy in living tissue – the development of analysis software capable of coping with swift, low SNR, low photon number fluorescence probes on moving, heterogeneous background – has thus been accomplished. This opens up new gates for science to hitherto inaccessible parts of life.

7 Conclusion

In this thesis, single molecule microscopy studies were carried out in order to investigate the impact of ionizing radiation on the plasma membrane architecture as regulated in presence and absence of an near-native 3D microenvironment extracellular matrix. To this end, a widefield microscope optical setup was developed into a single molecule detection setup. For the analysis of acquired data, routines were written. Routines were implemented with customizability in mind to tailor analysis procedures to the experiment at hand both by parameter adjustment and module extension. Each step in the analysis procedure was rigorously evaluated by simulations and performance was quantified: Background estimation, noise estimation, denoising, single fluorophore detection, and sub-pixel localization. Traces were obtained from the localization data using established tracking software whose accuracy was also evaluated using simulations.

Applying simultanously developed protocols for collagen I based hydrogels posing as 3D microenvironments that mimic tissuelike extracellular matrices in terms of elasticity, porosity, ligand density for cellular adhesion molecules and nutrient permeability etc. [Kämmerer, 2014], that provide samples compatible with microscopy, measurements of the motion of a fluorescent lipid analogue to probe the plasma membrane architecture were carried out in osteosarcoma cells cultured under these more tissuelike 3D and under conventional 2D conditions. The tracking data was described as composed of two modes of diffusion: a fast one, a slower one and their relative weight. The diffusion of both fractions was anomalous both in 2D and in 3D. Anomalous diffusion is well explained by impenetrable obstacles, i.e. membrane proteins, to lateral diffusion within a membrane or temporary trapping events by binding. It was shown that the membrane organization is different in 3D cell culture conditions in comparison to 2D: While the slow fraction and the relative size of the fractions remain the same in 3D as in the less involved 2D cell culture, coefficents and anomalous exponents of the faster fraction differ. Both coefficients and anomalous exponents are smaller in 3D, indicating a microenvironment-associated change of transmembrane protein distribution. This interpretation is in agreement with the known morphological changes that come with 3D microenvironments and that are mediated by differently organized cytoskeleton and adhesion molecule organization.

In combination with a different lipid composition of the plasma membrane, this links the cytoskeleton, cytoskeleton-anchored membrane proteins, mobile membrane proteins including ECM receptors, 3D adhesion sites, obstacle density, protein-rich membrane domain distribution, lipid content, cholesterol level, membrane order, and membrane viscosity to a non-oneway chain of effect which is subject to perturbations when exposed to ionizing radiation. Unexpectedly, membrane architecture of U2OS cells is stable even after application of 25 Gy. The U2OS line's ability to go into cell cycle arrest rather than apoptosis seems to circumvent membrane remodeling in the course of a ceramide-mediated radiation stress response, probably by inhibiting the translocation of acid sphingomyelinase from the lysosome to the membrane. Yet, as response and remodeling of the cytoskeleton which translate into altered plasma membrane organization have been observed to be tissue-specific [Gabryś et al., 2007, Jelonek et al., 2011] the results of this thesis – namely the ability to detect and track single fluorescent molecules in a depth of tens of micrometers within a 3D-extracellular matrix – underline the peculiarity of microvessel endothial cells and encourage investigations on cell lines different from the used human osteosarcoma cells regarding membrane organization and impact on receptor kinetics such as of adhesion molecules or death receptors. Continuing research in this direction is anticipated to yield results of high relevance to radiation oncology, where tumor microvessels are recognized as target of stereotactic body radiation therapy.

8 Appendix

List of Figures

List of Tables

Bibliography

Anish V Abraham, Sripad Ram, Jerry Chao, E S Ward, and Raimund J Ober. Quantitative study of single molecule location estimation techniques. *Optics express*, 17(26):23352–73, December 2009. ISSN 1094-4087. URL `http://www.pubmedcentral.nih.gov/articlerender.fcgi?artid=2813811&tool=pmcentrez&rendertype=abstract`.

Kazi Mokim Ahmed and Jian Jian Li. NF-kappa B-mediated adaptive resistance to ionizing radiation. *Free radical biology & medicine*, 44(1):1–13, January 2008. ISSN 0891-5849. doi: 10.1016/j.freeradbiomed.2007.09.022. URL `http://www.pubmedcentral.nih.gov/articlerender.fcgi?artid=2266095&tool=pmcentrez&rendertype=abstract`.

Hirotugu Akaike. Information theory and an extenson of the maximum likelihood principle. In B. N. Petrov and F. Csaki, editors, *2nd International Symponsium on Information Theory*, pages 267–281, Budapest, 1973. Akademiai Kiado.

Hirotugu Akaike. A New Look at the Statistical Model Identification. *IEEE Transactions On Automatic Control*, 19(6):716–723, 1974.

Alberts, Bray, Hopkin, Johnson, Lewis, Raff, Roberts, and Walter. *Lehrbuch der molekularen Zellbiologie*. Wiley, Weinheim, 4 edition, 2005.

Jordi Alcaraz, Lara Buscemi, Mireia Grabulosa, Xavier Trepat, Ben Fabry, Ramon Farré, and Daniel Navajas. Microrheology of human lung epithelial cells measured by atomic force microscopy. *Biophysical journal*, 84(3):2071–9, March 2003. ISSN 0006-3495. doi: 10.1016/S0006-3495(03)75014-0. URL `http://www.pubmedcentral.nih.gov/articlerender.fcgi?artid=1302775&tool=pmcentrez&rendertype=abstract`.

Lindsey A Allan and Mike Fried. p53-dependent apoptosis or growth arrest induced by different forms of radiation in U2OS cells: p21 WAF1 / CIP1 repression in UV induced apoptosis. *Oncogene*, 18(39): 5403–5412, 1999.

P F F Almeida and W L C Vaz. Lateral Diffusion in Membranes. In R. Lipowsky and E. Sackmann, editors, *Handbook of Biological Physics, Vol. 1*, volume 1, chapter 6, pages 305–357. Elsevier, Amsterdam, 1995.

Sean B Andersson. Localization of a fluorescent source without numerical fitting. *Optics express*, 16 (23):18714–24, November 2008. ISSN 1094-4087. URL `http://www.ncbi.nlm.nih.gov/pubmed/19581957`.

Andor Technology. iXon3 hardware guide, 2011.

F.J. Anscombe. The Transformation of Poisson, Binomial and Negative-Binomial Data. *Biometrika*, 35 (3):246–254, 1948.

J. E. Aubin. Autofluorescence of viable cultured mammalian cells. *Journal of Histochemistry & Cytochemistry*, 27(1):36–43, January 1979. ISSN 0022-1554. doi: 10.1177/27.1.220325. URL `http://jhc.sagepub.com/lookup/doi/10.1177/27.1.220325`.

Massimo Aureli, Rosaria Bassi, Alessandro Prinetti, Elena Chiricozzi, Brigida Pappalardi, Vanna Chigorno, Nadia Di Muzio, Nicoletta Loberto, and Sandro Sonnino. Ionizing radiations increase the activity of the cell surface glycohydrolases and the plasma membrane ceramide content. *Glycoconjugate journal*, 29(8-9):585–97, December 2012. ISSN 1573-4986. doi: 10.1007/s10719-012-9385-2. URL `http://www.ncbi.nlm.nih.gov/pubmed/22592846`.

D Axelrod. Cell-substrate contacts illuminated by total internal reflection fluorescence. *The Journal of cell biology*, 89(1):141–5, April 1981. ISSN 0021-9525. URL `http://www.pubmedcentral.nih.gov/articlerender.fcgi?artid=2111781&tool=pmcentrez&rendertype=abstract`.

Hazen Babcock, Yaron M Sigal, and Xiaowei Zhuang. A high-density 3D localization algorithm for stochastic optical reconstruction microscopy. *Optical Nanoscopy*, 1(1):6, 2012. ISSN 2192-2853. doi: 10.1186/2192-2853-1-6. URL `http://www.optnano.com/content/1/1/6`.

Hazen P Babcock, Jeffrey R Moffitt, Yunlong Cao, and Xiaowei Zhuang. Fast compressed sensing analysis for super- resolution imaging using L1-homotopy. *Optics Express*, 21(23):28583–28596, 2013. doi: 10.1364/OE.21.028583.

Martial Balland, Nicolas Desprat, Delphine Icard, Sophie Féréol, Atef Asnacios, Julien Browaeys, Sylvie Hénon, and François Gallet. Power laws in microrheology experiments on living cells: Comparative analysis and modeling. *Physical Review E*, 74(2):021911, August 2006. ISSN 1539-3755. doi: 10.1103/PhysRevE.74.021911. URL `http://link.aps.org/doi/10.1103/PhysRevE.74.021911`.

Gerd Baumann, Robert F Place, and Zeno Földes-papp. Meaningful Interpretation of Subdiffusive Measurements in Living Cells (Crowded Environment) by Fluorescence Fluctuation Microscopy. *Current Pharmaceutical Biotechnology*, 11:527–543, 2010.

Michael Baumann, Mechthild Krause, and Richard Hill. Exploring the role of cancer stem cells in radioresistance. *Nature reviews. Cancer*, 8(7):545–54, July 2008. ISSN 1474-1768. doi: 10.1038/nrc2419. URL `http://www.ncbi.nlm.nih.gov/pubmed/18511937`.

M. J. Bayarri and J. O. Berger. The Interplay of Bayesian and Frequentist Analysis. *Statistical Science*, 19(1):58–80, February 2004. ISSN 0883-4237. doi: 10.1214/088342304000000116. URL `http://projecteuclid.org/Dienst/getRecord?id=euclid.ss/1089808273/`.

Thomas Bayes. An Essay towards Solving a Problem in the Doctrine of Chances. *Philosophical Transactions of the Royal Society of London (1683-1775)*, 53:370–418, 1763. URL `http://www.jstor.org/stable/105741`.

M Benderitter, L Vincent-Genod, J P Pouget, and P Voisin. The Cell Membrane as a Biosensor of Oxidative Stress Induced by Radiation Exposure : A Multiparameter Investigation The Cell Membrane as a Biosensor of Oxidative Stress Induced by Radiation Exposure : A Multiparameter Investigation. *Radiation research*, 159(4):471–483, 2003.

Karim Bensaad, Atsushi Tsuruta, Mary a Selak, M Nieves Calvo Vidal, Katsunori Nakano, Ramon Bartrons, Eyal Gottlieb, and Karen H Vousden. TIGAR, a p53-inducible regulator of glycolysis and apoptosis. *Cell*, 126(1):107–20, July 2006. ISSN 0092-8674. doi: 10.1016/j.cell.2006.05.036. URL `http://www.ncbi.nlm.nih.gov/pubmed/16839880`.

R. C. Benson, R. a. Meyer, M. E. Zaruba, and G. M. McKhann. Cellular autofluorescence–is it due to flavins? *Journal of Histochemistry & Cytochemistry*, 27(1):44–48, January 1979. ISSN 0022-1554. doi: 10.1177/27.1.438504. URL `http://jhc.sagepub.com/lookup/doi/10.1177/27.1.438504`.

M.J. Berger, J.S. Coursey, M.A. Zucker, and J. Chang. ESTAR, PSTAR, and ASTAR: Computer Programs for Calculating Stopping-Power and Range Tables for Electrons, Protons, and Helium Ions (version 1.2.3)., 2005. URL `http://physics.nist.gov/Star`.

Michael J Berridge and Robin F Irvine. Inositol triphosphate, a novel second messenger in cellular signal transduction. *nature*, 312(5992):315–321, 1984.

Allison L Berrier and Kenneth M Yamada. Cell âĂŞ Matrix Adhesion. *Journal of Cellular Physiology*, 213 (June):565–573, 2007. doi: 10.1002/JCP.

A. Berroud, A. Le Roy, and P. Voisin. Membrane oxidative damage induced by ionizing radiation detected by fluorescence polarization. *Radiation and Environmental Biophysics*, 35(4):289, 1996. ISSN 0301634X. doi: 10.1007/s004110050042. URL `http://link.springer.com/10.1007/s004110050042`.

H Bethe. Zur Theorie des Durchgangs schneller Korpuskularstrahlen durch Materie. *Annalen der Physik*, 397(3):325–400, 1930.

Eric Betzig, George H Patterson, Rachid Sougrat, O Wolf Lindwasser, Scott Olenych, Juan S Bonifacino, Michael W Davidson, Jennifer Lippincott-Schwartz, and Harald F Hess. Imaging intracellular fluorescent proteins at nanometer resolution. *Science (New York, N.Y.)*, 313(5793):1642–5, September 2006. ISSN 1095-9203. doi: 10.1126/science.1127344. URL `http://www.ncbi.nlm.nih.gov/pubmed/16902090`.

B Biermann, S Sokoll, J Klueva, M Missler, J S Wiegert, J-B Sibarita, and M Heine. Imaging of molecular surface dynamics in brain slices using single-particle tracking. *Nature communications*, 5:3024, January 2014. ISSN 2041-1723. doi: 10.1038/ncomms4024. URL `http://www.pubmedcentral.nih.gov/articlerender.fcgi?artid=3905702&tool=pmcentrez&rendertype=abstract`.

Clara Bionda, Elie Hadchity, Gersende Alphonse, Olivier Chapet, Robert Rousson, Claire Rodriguez-Lafrasse, and Dominique Ardail. Radioresistance of human carcinoma cells is correlated to a defect in raft membrane clustering. *Free radical biology & medicine*, 43(5):681–94, September 2007. ISSN 0891-5849. doi: 10.1016/j.freeradbiomed.2007.04.031. URL `http://www.ncbi.nlm.nih.gov/pubmed/17664132`.

R Birch and M Marshall. Computation of bremsstrahlung X-ray spectra and comparison with spectra measured with a Ge(Li) detector. *Physics in Medicine and Biology*, 24(3):505–517, May 1979. ISSN 00319155. doi: 10.1088/0031-9155/24/3/002. URL `http://stacks.iop.org/0031-9155/24/i=3/a=002?key=crossref.337962dc63ffd04a2b561462d54670dc`.

Felix Bloch. Zur Bremsung rasch bewegter Teilchen beim Durchgang durch Materie. *Annalen der Physik*, 408(3):285–320, 1933.

Norman Bobroff. Position measurement with a resolution and noise-limited instrument. *Review of Scientific Instruments*, 57(6):1152, 1986. ISSN 00346748. doi: 10.1063/1.1138619. URL `http://scitation.aip.org/content/aip/journal/rsi/57/6/10.1063/1.1138619`.

Niels Bohr. On the Theory of the Decrease of Velocity of Moving Electrified Particles on passing through Matter. *The London, Edinburgh, and Dublin Philosophical Magazine and Journal of Science*, 25(145): 10–31, 1913.

George E.P. Box, J. Stuart Hunter, and William G. HUnter. *Statistics for Experimenters*. John Wiley & Sons, Hoboken, New Jersey, 2005.

Mark S Bretscher. Asymmetrical Lipid Bilayer Structure for Biological Membranes. *Nature Cell Biology*, 236(1):11–12, 1972.

Stephen P Brooks and Andrew Gelman. General Methods for Monitoring Convergence of Iterative Simulations. *Journal of Computational and Graphical Statistics*, 7(4):434–455, 1998. URL `http://dx.doi.org/10.1080/10618600.1998.10474787`.

D a Brown and E London. Structure and function of sphingolipid- and cholesterol-rich membrane rafts. *The Journal of biological chemistry*, 275(23):17221–4, June 2000. ISSN 0021-9258. doi: 10.1074/jbc.R000005200. URL `http://www.ncbi.nlm.nih.gov/pubmed/10770957`.

Robert Brown. A brief account of microscopical observations made in the months of June, July and August, 1827 on the particles contained in the pollen of plants; and on the general existence of active molecules in organic and inorganic bodies. *Phil. Mag*, 4(21):161–173, 1828.

A Buades, B Coll, and J M Morel. A REVIEW OF IMAGE DENOISING ALGORITHMS, WITH A NEW ONE. *SIAM Journal on Multiscale Modeling and Simulation*, 4(2):490–530, 2005a.

Antoni Buades, Bartomeu Coll, and Jean-michel Morel. A non-local algorithm for image denoising. In *IEEE Computer Society Conference on Computer Vision and Pattern Recognition*, volume 2, pages 60–65. IEEE, 2005b.

K.E. Burkard and E. Cela. Linear assignments problems and extensions. In D.Z. Du and P.M. Pardalos, editors, *Handbook of Combinatorial Optimization - Supplement Volume A*. Kluwer Academic Publishers, Dordrecht, NL, 1999.

K. P. Burnham and David R. Anderson. Multimodel Inference: Understanding AIC and BIC in Model Selection. *Sociological Methods & Research*, 33(2):261–304, November 2004. ISSN 0049-1241. doi: 10.1177/0049124104268644. URL `http://smr.sagepub.com/cgi/doi/10.1177/0049124104268644`.

Jack Capon. On the Asymptotic Efficiency of Locally Optimum Detectors. *IRE TRANSACTIONS ON INFORMATION THEORY*, 19(604):67–71, 1961.

Elisa R Catapano, Laura R Arriaga, Gabriel Espinosa, Francisco Monroy, Dominique Langevin, and Iván López-Montero. Solid character of membrane ceramides: a surface rheology study of their mixtures with sphingomyelin. *Biophysical journal*, 101(11):2721–30, December 2011. ISSN 1542-0086. doi: 10.1016/j.bpj.2011.10.049. URL `http://www.pubmedcentral.nih.gov/articlerender.fcgi?artid=3297809&tool=pmcentrez&rendertype=abstract`.

I. C. Chang. Noncollinear acousto-optic filter with large angular aperture. *Applied Physics Letters*, 25(7):370, 1974. ISSN 00036951. doi: 10.1063/1.1655512. URL `http://scitation.aip.org/content/aip/journal/apl/25/7/10.1063/1.1655512`.

M K Cheezum, W F Walker, and W H Guilford. Quantitative comparison of algorithms for tracking single fluorescent particles. *Biophysical journal*, 81(4):2378–88, October 2001. ISSN 0006-3495. doi: 10.1016/S0006-3495(01)75884-5. URL `http://www.pubmedcentral.nih.gov/articlerender.fcgi?artid=1301708&tool=pmcentrez&rendertype=abstract`.

Jingdong Chen, Jacob Benesty, Senior Member, Yiteng Arden Huang, and Simon Doclo. New Insights Into the Noise Reduction Wiener Filter. *IEEE TRANSACTIONS ON AUDIO, SPEECH, AND LANGUAGE PROCESSING*, 14(4):1218–1234, 2006.

Nicolas Chenouard, Ihor Smal, Fabrice de Chaumont, Martin Maška, Ivo F Sbalzarini, Yuanhao Gong, Janick Cardinale, Craig Carthel, Stefano Coraluppi, Mark Winter, Andrew R Cohen, William J Godinez, Karl Rohr, Yannis Kalaidzidis, Liang Liang, James Duncan, Hongying Shen, Yingke Xu, Klas E G Magnusson, Joakim Jaldén, Helen M Blau, Perrine Paul-Gilloteaux, Philippe Roudot, Charles Kervrann, François Waharte, Jean-Yves Tinevez, Spencer L Shorte, Joost Willemse, Katherine Celler, Gilles P van Wezel, Han-Wei Dan, Yuh-Show Tsai, Carlos Ortiz de Solórzano, Jean-Christophe Olivo-Marin, and Erik Meijering. Objective comparison of particle tracking methods. *Nature methods*, 11(3):281—-289, January 2014. ISSN 1548-7105. doi: 10.1038/nmeth.2808. URL `http://www.ncbi.nlm.nih.gov/pubmed/24441936`.

J Clover and M Gowen. Are MG-63 and HOS TE85 human osteosarcoma cell lines representative models of the osteoblastic phenotype? *Bone*, 15(6):585–91, 1994. ISSN 8756-3282. URL `http://www.ncbi.nlm.nih.gov/pubmed/7873286`.

R R Coifman and D L Donoho. Translation-Invariant De-Noising. In *Lecture Notes in Statistics: Wavelets and Statistics, vol. 103*, pages 125–150. Springer, New York, 1995.

Thomas F Coleman and Yuying Li. On the convergence of interior-reflective Newton methods for nonlinear minimization subject to bounds. *Mathematical Programming*, 67(2):189–224, 1994.

Thomas F Coleman and Yuying Li. An Interior Trust Region Approach for Nonlinear Minimization Subject to Bounds. *SIAM Journal on Optimization*, 6(2):418–445, 1996.

N Cordes and D van Beuningen. Cell adhesion to the extracellular matrix protein fibronectin modulates radiation-dependent G2 phase arrest involving integrin-linked kinase (ILK) and glycogen synthase kinase-3beta (GSK-3beta) in vitro. *British journal of cancer*, 88(9):1470–9, May 2003. ISSN 0007-0920. doi: 10.1038/sj.bjc.6600912. URL `http://www.pubmedcentral.nih.gov/articlerender.fcgi?artid=2741045&tool=pmcentrez&rendertype=abstract`.

N Cordes, F Rödel, and H-P Rodemann. Molecular signaling pathways. Mechanisms and clinical use. *Strahlentherapie und Onkologie*, 188 Suppl(August):308–11, November 2012. ISSN 1439-099X. doi: 10.1007/s00066-012-0205-1. URL `http://www.ncbi.nlm.nih.gov/pubmed/22907579`.

Isabelle Corre, Colin Niaudet, and Francois Paris. Plasma membrane signaling induced by ionizing radiation. *Mutation research*, 704(1-3):61–7, 2010. ISSN 0027-5107. doi: 10.1016/j.mrrev.2010.01.014. URL `http://www.ncbi.nlm.nih.gov/pubmed/20117234`.

Isabelle Corre, Maëva Guillonneau, and François Paris. Membrane signaling induced by high doses of ionizing radiation in the endothelial compartment. Relevance in radiation toxicity. *International journal of molecular sciences*, 14(11):22678–96, January 2013. ISSN 1422-0067. doi: 10.3390/ijms141122678. URL `http://www.pubmedcentral.nih.gov/articlerender.fcgi?artid=3856084&tool=pmcentrez&rendertype=abstract`.

Susan Cox, Edward Rosten, James Monypenny, Tijana Jovanovic-Talisman, Dylan T Burnette, Jennifer Lippincott-Schwartz, Gareth E Jones, and Rainer Heintzmann. Bayesian localization microscopy reveals nanoscale podosome dynamics. *Nature methods*, 9(2):195–200, January 2011. ISSN 1548-7105. doi: 10.1038/nmeth.1812. URL `http://www.pubmedcentral.nih.gov/articlerender.fcgi?artid=3272474&tool=pmcentrez&rendertype=abstract`.

Jonathan M Crane and a S Verkman. Long-range nonanomalous diffusion of quantum dot-labeled aquaporin-1 water channels in the cell plasma membrane. *Biophysical journal*, 94(2):702–13, January 2008. ISSN 1542-0086. doi: 10.1529/biophysj.107.115121. URL `http://www.pubmedcentral.nih.gov/articlerender.fcgi?artid=2157255&tool=pmcentrez&rendertype=abstract`.

Edna Cukierman, Roumen Pankov, Daron R Stevens, and Kenneth M Yamada. Taking Cell-Matrix Adhesions to the Third Dimension. *Science*, 294(November):1708–1712, 2001.

Edna Cukierman, Roumen Pankov, and Kenneth M Yamada. Cell interactions with three-dimensional matrices. *Current Opinion in Cell Biology*, 13:633–639, 2002.

David L Daleke. Regulation of transbilayer plasma membrane phospholipid asymmetry. *Journal of lipid research*, 44(2):233–42, February 2003. ISSN 0022-2275. doi: 10.1194/jlr.R200019-JLR200. URL `http://www.ncbi.nlm.nih.gov/pubmed/12576505`.

E M Danielsen and G H Hansen. Lipid raft organization and function in the small intestinal brush border. *Journal of physiology and biochemistry*, 64(4):377–82, December 2008. ISSN 1138-7548. URL http://www.ncbi.nlm.nih.gov/pubmed/19391463.

Gaudenz Danuser. Computer vision in cell biology. *Cell*, 147(5):973–8, November 2011. ISSN 1097-4172. doi: 10.1016/j.cell.2011.11.001. URL http://www.ncbi.nlm.nih.gov/pubmed/22118455.

J E de Ruijter, P J ter Brugge, S C Dieudonné, S J van Vliet, R Torensma, and J a Jansen. Analysis of integrin expression in U2OS cells cultured on various calcium phosphate ceramic substrates. *Tissue engineering*, 7(3):279–89, June 2001. ISSN 1076-3279. doi: 10.1089/10763270152044143. URL http://www.ncbi.nlm.nih.gov/pubmed/11429148.

Charles-Alban Deledalle and Florence Tupin. POISSON NL MEANS: UNSUPERVISED NON LOCAL MEANS FOR POISSON NOISE. In *Proceedings of 2010 IEEE 17th International Conference on Image Processing*, pages 801–804, 2010. ISBN 9781424479931.

GT Dempsey, JC Vaughan, KH Chen, Mark Bates, and Xiaowei Zhuang. Evaluation of fluorophores for optimal performance in localization-based super-resolution imaging. *Nature Methods*, 8(12):1027–1036, 2011. doi: 10.1038/NMETH.1768. URL http://www.nature.com/nmeth/journal/vaop/ncurrent/full/nmeth.1768.html.

Wolfgang Demtröder. *Experimentalphysik 1*. Springer, Berlin Heidelberg New York, 4 edition, 2006. ISBN 3-540-26034-X.

Markus Deserno. Fluid lipid membranes: From differential geometry to curvature stresses. *Chemistry and physics of lipids*, 2:1–35, May 2014. ISSN 1873-2941. doi: 10.1016/j.chemphyslip.2014.05.001. URL http://www.ncbi.nlm.nih.gov/pubmed/24835737.

Nicolas Desprat, Alain Richert, Jacqueline Simeon, and Atef Asnacios. Creep function of a single living cell. *Biophysical journal*, 88(3):2224–33, March 2005. ISSN 0006-3495. doi: 10.1529/biophysj.104.050278. URL http://www.pubmedcentral.nih.gov/articlerender.fcgi?artid=1305272&tool=pmcentrez&rendertype=abstract.

Arthur Edelstein, Nenad Amodaj, Karl Hoover, Ron Vale, and Nico Stuurman. *Computer Control of Microscopes Using ÃĆÂţManager*, chapter 14.20., pages 1–17. John Wiley & Sons, Inc., 2010. ISBN 9780471142720. doi: 10.1002/0471142727.mb1420s92. URL http://dx.doi.org/10.1002/0471142727.mb1420s92.

Christian Eggeling, Christian Ringemann, Rebecca Medda, Günter Schwarzmann, Konrad Sandhoff, Svetlana Polyakova, Vladimir N Belov, Birka Hein, Claas von Middendorff, Andreas Schönle, and Stefan W Hell. Direct observation of the nanoscale dynamics of membrane lipids in a living cell. *Nature*, 457(7233):1159–62, February 2009. ISSN 1476-4687. doi: 10.1038/nature07596. URL http://www.ncbi.nlm.nih.gov/pubmed/19098897.

Albert Einstein. Zur Theorie der Brownschen Bewegung. *Annalen der Physik*, 324:371–381, 1906.

Iris Eke and Nils Cordes. Radiobiology goes 3D: How ECM and cell morphology impact on cell survival after irradiation. *Radiotherapy and oncology : journal of the European Society for Therapeutic Radiology and Oncology*, 99(3):271–8, June 2011. ISSN 1879-0887. doi: 10.1016/j.radonc.2011.06.007. URL http://www.ncbi.nlm.nih.gov/pubmed/21704412.

Joerg Enderlein, Erdal Toprak, and Paul R Selvin. Polarization effect on position accuracy of fluorophore localization. *Optics express*, 14(18):8111–20, September 2006. ISSN 1094-4087. URL http://www.ncbi.nlm.nih.gov/pubmed/19529183.

Dominique Ernst and Jürgen Köhler. Measuring a diffusion coefficient by single-particle tracking: statistical analysis of experimental mean squared displacement curves. *Physical chemistry chemical physics : PCCP*, 15(3):845–9, January 2013. ISSN 1463-9084. doi: 10.1039/c2cp43433d. URL `http://www.ncbi.nlm.nih.gov/pubmed/23202416`.

Dominique Ernst, Jürgen Köhler, and Matthias Weiss. Probing the type of anomalous diffusion with single-particle tracking. *Physical chemistry chemical physics : PCCP*, 16(17):7686–91, May 2014. ISSN 1463-9084. doi: 10.1039/c4cp00292j. URL `http://www.ncbi.nlm.nih.gov/pubmed/24651929`.

Ben Fabry, Geoffrey Maksym, James Butler, Michael Glogauer, Daniel Navajas, and Jeffrey Fredberg. Scaling the Microrheology of Living Cells. *Physical Review Letters*, 87(14):148102, September 2001. ISSN 0031-9007. doi: 10.1103/PhysRevLett.87.148102. URL `http://link.aps.org/doi/10.1103/PhysRevLett.87.148102`.

Eoin Fahy, Shankar Subramaniam, Robert C Murphy, Masahiro Nishijima, Christian R H Raetz, Takao Shimizu, Friedrich Spener, Gerrit van Meer, Michael J O Wakelam, and Edward a Dennis. Update of the LIPID MAPS comprehensive classification system for lipids. *Journal of lipid research*, 50 Suppl:S9–14, April 2009. ISSN 0022-2275. doi: 10.1194/jlr.R800095-JLR200. URL `http://www.pubmedcentral.nih.gov/articlerender.fcgi?artid=2674711&tool=pmcentrez&rendertype=abstract`.

T J Feder, I Brust-Mascher, J P Slattery, B Baird, and W W Webb. Constrained diffusion or immobile fraction on cell surfaces: a new interpretation. *Biophysical journal*, 70(6):2767–73, June 1996. ISSN 0006-3495. doi: 10.1016/S0006-3495(96)79846-6. URL `http://www.pubmedcentral.nih.gov/articlerender.fcgi?artid=1225256&tool=pmcentrez&rendertype=abstract`.

Stephanie I Fraley, Yunfeng Feng, Ranjini Krishnamurthy, Dong-hwee Kim, Alfredo Celedon, Gregory D Longmore, and Denis Wirtz. A distinctive role for focal adhesion proteins in three-dimensional cell motility. *Nature cell biology*, 12(6):598–604, June 2010. ISSN 1476-4679. doi: 10.1038/ncb2062. URL `http://www.pubmedcentral.nih.gov/articlerender.fcgi?artid=3116660&tool=pmcentrez&rendertype=abstracthttp://dx.doi.org/10.1038/ncb2062`.

Stephanie I Fraley, Yunfeng Feng, Denis Wirtz, Gregory D Longmore, Kristopher E Kubow, and Alan Rick Horwitz. Reply: Reducing background fluorescence reveals adhesions in 3D matrices. *Nature cell biology*, 13(1):3–5; author reply 5–7, January 2011. ISSN 1476-4679. doi: 10.1038/ncb0111-3. URL `http://www.pubmedcentral.nih.gov/articlerender.fcgi?artid=3083631&tool=pmcentrez&rendertype=abstract`.

Christian Frantz, Kathleen M Stewart, and Valerie M Weaver. The extracellular matrix at a glance. *Journal of cell science*, 123(Pt 24):4195–200, December 2010. ISSN 1477-9137. doi: 10.1242/jcs.023820. URL `http://www.pubmedcentral.nih.gov/articlerender.fcgi?artid=2995612&tool=pmcentrez&rendertype=abstract`.

Takahiro Fujiwara, Ken Ritchie, Hideji Murakoshi, Ken Jacobson, and Akihiro Kusumi. Phospholipids undergo hop diffusion in compartmentalized cell membrane. *The Journal of cell biology*, 157(6):1071–81, June 2002. ISSN 0021-9525. doi: 10.1083/jcb.200202050. URL `http://www.pubmedcentral.nih.gov/articlerender.fcgi?artid=2174039&tool=pmcentrez&rendertype=abstract`.

Zvi Fuks, Israel Vlodavsky, Michael Andreeff, Maureen Mclaughlin, and Adriana Naimovitz-friedman. Effects of Extracellular Matrix on the Response of Endothelial Cells to Radiation in vitro. *Eur J Cancer*, 28A(4/5):725–731, 1992.

Dorota Gabryś, Olga Greco, Gaurang Patel, Kevin M. Prise, Gillian M. Tozer, and Chryso Kanthou. Radiation effects on the cytoskeleton of endothelial cells and endothelial monolayer permeability.

*International Journal of Radiation Oncology*Biology*Physics*, 69(5):1553 – 1562, 2007. ISSN 0360-3016. doi: http://dx.doi.org/10.1016/j.ijrobp.2007.08.039. URL `http://www.sciencedirect.com/science/article/pii/S0360301607039892`.

Monica Garcia-Barros, Francois Paris, Carlos Cordon-Cardo, David Lyden, Shahin Rafii, Adriana Haimovitz-Friedman, Zvi Fuks, and Richard Kolesnick. Tumor response to radiotherapy regulated by endothelial cell apoptosis. *Science*, 300(5622):1155–9, May 2003. ISSN 1095-9203. doi: 10.1126/science.1082504. URL `http://www.ncbi.nlm.nih.gov/pubmed/12750523`.

Benjamin Geiger, Joachim P Spatz, and Alexander D Bershadsky. Environmental sensing through focal adhesions. *Nature reviews. Molecular cell biology*, 10(1):21–33, January 2009. ISSN 1471-0080. doi: 10.1038/nrm2593. URL `http://www.ncbi.nlm.nih.gov/pubmed/19197329`.

Tamar Geiger and Ronen Zaidel-Bar. Opening the floodgates: proteomics and the integrin adhesome. *Current opinion in cell biology*, 24(5):562–8, October 2012. ISSN 1879-0410. doi: 10.1016/j.ceb.2012.05.004. URL `http://www.ncbi.nlm.nih.gov/pubmed/22728062`.

Jeff Gelles, Bruce J. Schnapp, and Michael P. Sheetz. Tracking kinesin-driven movements with nanometre-scale precision. *Nature*, 331(4):450–453, 1988.

Andrew Gelman and Donald B. Rubin. Inference from Iterative Simulation Using Multiple Sequences. *Statistical Science*, 7(4):457–511, 1992.

Andrew Gelman, John B. Carlin, and Hal S. Stern. *Bayesian Data Analysis*. Chapman & Hall, 3rd edition, 2013.

Charles J Geyer. Practical Markov Chain Monte Carlo. *Statistical Science*, 7(4):473–483, 1992.

F. G. Giancotti. Integrin Signaling. *Science*, 285(5430):1028–1033, August 1999. ISSN 00368075. doi: 10.1126/science.285.5430.1028. URL `http://www.sciencemag.org/cgi/doi/10.1126/science.285.5430.1028`.

W. R. Gilks, S. Richardson, and D. J. Spiegelhalter, editors. *Markov Chain Monte Carlo In Practice*. Chapman & Hall, London, 1 edition, 1996. ISBN 0412055511. URL `http://www.leg.ufpr.br/~eder/Markov/MarkovChainMonteCarloInPractice.pdf`.

Hira Lal Goel, Aejaz Sayeed, Michael Breen, Matthew J Zarif, David S Garlick, Irwin Leav, Roger J Davis, Thomas J Fitzgerald, Andrea Morrione, Chung-Cheng Hsieh, Qin Liu, Adam P Dicker, Dario C Altieri, and Lucia R Languino. β1 integrins mediate resistance to ionizing radiation in vivo by inhibiting c-Jun amino terminal kinase 1. *Journal of cellular physiology*, 228(7):1601–9, July 2013. ISSN 1097-4652. doi: 10.1002/jcp.24323. URL `http://www.ncbi.nlm.nih.gov/pubmed/23359252`.

Mark a Gregory, Ying Qi, and Stephen R Hann. Phosphorylation by glycogen synthase kinase-3 controls c-myc proteolysis and subnuclear localization. *The Journal of biological chemistry*, 278(51):51606–12, December 2003. ISSN 0021-9258. doi: 10.1074/jbc.M310722200. URL `http://www.ncbi.nlm.nih.gov/pubmed/14563837`.

E. Grzelińska, G. Bartosz, K. Gwoździński, and W. Leyko. A Spin-label Study of the Effect of Gamma Radiation on Erythrocyte Membrane. Influence of Lipid Peroxidation on Membrane Structure. *International Journal of Radiation Biology*, 36(4):325–334, January 1979. ISSN 0955-3002. doi: 10.1080/09553007914551111. URL `http://informahealthcare.com/doi/abs/10.1080/09553007914551111`.

Adriana Haimovitz-Friedman, Chu-Cheng Kan, Desiree Ehleiter, Roger S Persaud, Maureen Mcloughlin, Zvi Fuks, and Richard N Kolesnick. Ionizing Radiation Acts on Cellular Membranes to Generate Ceramide and Initiate Apoptosis. *J. Exp. Med.*, 180(August):525–535, 1994.

Gregory Hannigan, Armelle a Troussard, and Shoukat Dedhar. Integrin-linked kinase: a cancer therapeutic target unique among its ILK. *Nature reviews. Cancer*, 5(1):51–63, January 2005. ISSN 1474-175X. doi: 10.1038/nrc1524. URL `http://www.ncbi.nlm.nih.gov/pubmed/15630415`.

Yusuf A. Hannun. Functions of ceramide in coordinating cellular responses to stress. *Science*, 274(5294): 1855–9, December 1996. ISSN 0036-8075. URL `http://www.ncbi.nlm.nih.gov/pubmed/8943189`.

Yusuf A Hannun and Lina M Obeid. Principles of bioactive lipid signalling: lessons from sphingolipids. *Nature reviews. Molecular cell biology*, 9(2):139–50, February 2008. ISSN 1471-0080. doi: 10.1038/nrm2329. URL `http://www.ncbi.nlm.nih.gov/pubmed/18216770`.

Jill S Harunaga and Kenneth M Yamada. Cell-matrix adhesions in 3D. *Matrix biology : journal of the International Society for Matrix Biology*, 30(7-8):363–8, September 2011. ISSN 1569-1802. doi: 10.1016/j.matbio.2011.06.001. URL `http://www.pubmedcentral.nih.gov/articlerender.fcgi?artid=3191245&tool=pmcentrez&rendertype=abstract`.

W K Hastings. Monte Carlo Sampling Methods Using Markov Chains and Their Applications. *Biometrika*, 57(1):97–109, 1970.

Teka-Ann S Haynes, Penelope J Duerksen-Hughes, Maria Filippova, Valery Filippov, and Kangling Zhang. C18 ceramide analysis in mammalian cells employing reversed-phase high-performance liquid chromatography tandem mass spectrometry. *Analytical biochemistry*, 378(1):80–6, July 2008. ISSN 1096-0309. doi: 10.1016/j.ab.2008.03.045. URL `http://www.ncbi.nlm.nih.gov/pubmed/18423390`.

Teka-Ann S Haynes, Valery Filippov, Maria Filippova, Jun Yang, Kangling Zhang, and Penelope J Duerksen-Hughes. DNA damage induces down-regulation of UDP-glucose ceramide glucosyltransferase, increases ceramide levels and triggers apoptosis in p53-deficient cancer cells. *Biochimica et biophysica acta*, 1821(7):943–53, July 2012. ISSN 0006-3002. doi: 10.1016/j.bbalip.2012.02.002. URL `http://www.pubmedcentral.nih.gov/articlerender.fcgi?artid=3614347&tool=pmcentrez&rendertype=abstract`.

Eugene Hecht. *Optics*. Addison-Wesley, Reading, 4 edition, 2001.

Mike Heilemann, Sebastian van de Linde, Mark Schüttpelz, Robert Kasper, Britta Seefeldt, Anindita Mukherjee, Philip Tinnefeld, and Markus Sauer. Subdiffraction-resolution fluorescence imaging with conventional fluorescent probes. *Angewandte Chemie (International ed. in English)*, 47(33):6172–6, January 2008. ISSN 1521-3773. doi: 10.1002/anie.200802376. URL `http://www.ncbi.nlm.nih.gov/pubmed/18646237`.

Mike Heilemann, Sebastian van de Linde, Anindita Mukherjee, and Markus Sauer. Super-resolution imaging with small organic fluorophores. *Angewandte Chemie (International ed. in English)*, 48(37): 6903–8, January 2009. ISSN 1521-3773. doi: 10.1002/anie.200902073. URL `http://www.ncbi.nlm.nih.gov/pubmed/19670280`.

Turid Hellevik and Iñigo Martinez-Zubiaurre. Radiotherapy and the Tumor Stroma: The Importance of Dose and Fractionation. *Frontiers in oncology*, 4(January):1, January 2014. ISSN 2234-943X. doi: 10.3389/fonc.2014.00001. URL `http://www.pubmedcentral.nih.gov/articlerender.fcgi?artid=3896881&tool=pmcentrez&rendertype=abstract`.

Ricardo Henriques, Caron Griffiths, E Hesper Rego, and Musa M Mhlanga. PALM and STORM: unlocking live-cell super-resolution. *Biopolymers*, 95(5):322–31, May 2011. ISSN 0006-3525. doi: 10.1002/bip.21586. URL `http://www.ncbi.nlm.nih.gov/pubmed/21254001`.

Franziska C. Heß. *Die Rolle von Zell-Matrix Interaktionen für die strahleninduzierte Apoptose von humanen promyelozytischen HL60-Zellen*. PhD thesis, Technische Universität Dresden, 2006.

Samuel T Hess, Thanu P K Girirajan, and Michael D Mason. Ultra-high resolution imaging by fluorescence photoactivation localization microscopy. *Biophysical journal*, 91(11):4258–72, December 2006. ISSN 0006-3495. doi: 10.1529/biophysj.106.091116. URL `http://www.pubmedcentral.nih.gov/articlerender.fcgi?artid=1635685&tool=pmcentrez&rendertype=abstract`.

Keigo Hirakawa, Patrick J Wolfe, and Senior Member. Skellam Shrinkage : Wavelet-Based Intensity Estimation for Inhomogeneous Poisson Data. *IEEE TRANSACTIONS ON INFORMATION THEORY*, 58 (2):1080–1093, 2012.

Michael Hirsch, Richard J Wareham, Marisa L Martin-Fernandez, Michael P Hobson, and Daniel J Rolfe. A stochastic model for electron multiplication charge-coupled devices–from theory to practice. *PloS one*, 8(1):e53671, January 2013. ISSN 1932-6203. doi: 10.1371/journal.pone.0053671. URL `http://www.pubmedcentral.nih.gov/articlerender.fcgi?artid=3561409&tool=pmcentrez&rendertype=abstract`.

Felix Höfling and Thomas Franosch. Anomalous transport in the crowded world of biological cells. *Reports on progress in physics. Physical Society (Great Britain)*, 76(4):046602, April 2013. ISSN 1361-6633. doi: 10.1088/0034-4885/76/4/046602. URL `http://www.ncbi.nlm.nih.gov/pubmed/23481518`.

Seamus J Holden, Stephan Uphoff, and Achilles N Kapanidis. DAOSTORM: an algorithm for high-density super-resolution microscopy Supplement. *nature methods*, 8(4):279–280, 2011. URL `http://www.nature.com/nmeth/journal/v8/n4/abs/nmeth0411-279.html`.

Laurent Holtzer, Tobias Meckel, and Thomas Schmidt. Nanometric three-dimensional tracking of individual quantum dots in cells. *Applied Physics Letters*, 90(5):053902, 2007. ISSN 00036951. doi: 10.1063/1.2437066. URL `http://link.aip.org/link/APPLAB/v90/i5/p053902/s1&Agg=doi`.

Mark Howarth, Wenhao Liu, Sujiet Puthenveetil, Yi Zheng, Lisa F Marshall, Michael M Schmidt, K Dane Wittrup, Moungi G Bawendi, and Alice Y Ting. Monovalent, reduced-size quantum dots for imaging receptors on living cells. *Nature methods*, 5(5):397–9, May 2008. ISSN 1548-7105. doi: 10.1038/nmeth.1206. URL `http://www.pubmedcentral.nih.gov/articlerender.fcgi?artid=2637151&tool=pmcentrez&rendertype=abstract`.

Fang Huang, Samantha L Schwartz, Jason M Byars, and Keith a Lidke. Simultaneous multiple-emitter fitting for single molecule super-resolution imaging. *Biomedical optics express*, 2(5):1377–93, January 2011a. ISSN 2156-7085. doi: 10.1364/BOE.2.001377. URL `http://www.pubmedcentral.nih.gov/articlerender.fcgi?artid=3087594&tool=pmcentrez&rendertype=abstract`.

Rongxin Huang, Isaac Chavez, Katja M. Taute, Branimir Lukić, Sylvia Jeney, Mark G. Raizen, and Ernst-Ludwig Florin. Direct observation of the full transition from ballistic to diffusive Brownian motion in a liquid. *Nature Physics*, 7(7):576–580, March 2011b. ISSN 1745-2473. doi: 10.1038/nphys1953. URL `http://www.nature.com/doifinder/10.1038/nphys1953`.

John H. Hubbell and Stephen M. Seltzer. Tables of x-ray mass attenuation coefficients and mass energy-absorption coefficients., 1996. URL `http://www.nist.gov/pml/data/xraycoef/index.cfm`.

A Huertas and G Medioni. Detection of intensity changes with subpixel accuracy using laplacian-gaussian masks. *IEEE transactions on pattern analysis and machine intelligence*, 8(5):651–64, May 1986. ISSN 0162-8828. URL `http://www.ncbi.nlm.nih.gov/pubmed/21869362`.

Richard O. Hynes. Integrins: Versatility, Modulation, and Signaling in Cell Adhesion. *Cell*, 69(April): 11–25, 1992.

Richard O Hynes. Integrins : Bidirectional , Allosteric Signaling Machines In their roles as major adhesion receptors , integrins. *Cell*, 110(September):673–687, 2002.

Richard O Hynes and Alexandra Naba. Overview of the matrisome–an inventory of extracellular matrix constituents and functions. *Cold Spring Harbor perspectives in biology*, 4(1):a004903, January 2012. ISSN 1943-0264. doi: 10.1101/cshperspect.a004903. URL `http://www.pubmedcentral.nih.gov/articlerender.fcgi?artid=3249625&tool=pmcentrez&rendertype=abstract`.

ICRU. ICRU Technical Report 49: Stopping Powers and Ranges for Protons and Alpha Particles. Technical report, International Commission on Radiation Units and Measurement, Bethesda, Maryland, USA, 1993.

ICRU. ICRU Technical Report 60: Fundamental Quantities and Units for Ionizing Radiation. Technical report, International Commission on Radiation Units and Measurements, Bethesda, Maryland, USA, 1998.

Johanna Ivaska. Unanchoring integrins in focal adhesions. *Nature cell biology*, 14(10):981–3, October 2012. ISSN 1476-4679. doi: 10.1038/ncb2592. URL `http://www.ncbi.nlm.nih.gov/pubmed/23033047`.

Ignacio Izeddin, Mohamed El Beheiry, Jordi Andilla, Daniel Ciepielewski, Xavier Darzacq, and Maxime Dahan. PSF shaping using adaptive optics for three-dimensional single-molecule super-resolution imaging and tracking. *Optics express*, 20(5):4957–67, February 2012. ISSN 1094-4087. URL `http://www.ncbi.nlm.nih.gov/pubmed/22418300`.

Khuloud Jaqaman, Dinah Loerke, Marcel Mettlen, Hirotaka Kuwata, Sandra L Schmid, and Gaudenz Danuser. Robust single particle tracking in live cell time-lapse sequences. *Nature Methods*, 5(8): 695–702, 2008. doi: 10.1038/nmeth.1237.Robust.

Karol Jelonek, Anna Walaszczyk, Dorota Gabryś, Monika Pietrowska, Chryso Kanthou, and Piotr WidÅĆak. Cardiac endothelial cells isolated from mouse heart âĂŤ a novel model for radiobiology. *Acta biochimica Polonica*, 58(3):397–404, 2011.

F . Jin, P . Fieguth, L . Winger, and E . Jernigan. ADAPTIVE WIENER FILTERING OF NOISY IMAGES AND IMAGE SEQUENCES. *IEEE International Conference on Image Processiong*, 3(2):349–352, 2003.

R. Jonker and A. Volgenant. A Shortest Augmenting Path Algorithm for Dense and Sparse Linear Assignment Problems. *Computing*, 38:325–340, 1987.

Albena Jordanova, Nadezhda Stefanova, Galya Staneva, Roumen Pankov, Albena Momchilova, and Zdravko Lalchev. Surface properties and behavior of lipid extracts from plasma membranes of cells cultured as monolayer and in tissue-like conditions. *Cell biochemistry and biophysics*, 54(1-3):47–55, January 2009. ISSN 1559-0283. doi: 10.1007/s12013-009-9050-y. URL `http://www.ncbi.nlm.nih.gov/pubmed/19484199`.

MF Juette, TJ Gould, and MD Lessard. Three-dimensional sub-100 nm resolution fluorescence microscopy of thick samples. *Nature Methods*, 5(6), 2008. doi: 10.1038/NMETH.1211. URL `http://www.nature.com/nmeth/journal/v5/n6/abs/nmeth.1211.html`.

Elke Kaemmerer, Ferry P W Melchels, Boris M Holzapfel, Tobias Meckel, Dietmar W Hutmacher, and Daniela Loessner. Gelatine methacrylamide-based hydrogels: An alternative three-dimensional cancer cell culture system. *Acta biomaterialia*, February 2014. ISSN 1878-7568. doi: 10.1016/j.actbio.2014.02.035. URL `http://www.ncbi.nlm.nih.gov/pubmed/24590158`.

Efstathios Kamaratos. The Mean Excitation Energy for Stopping Power I, the Bragg Rule, and Chemical and Phase Effects. Application of a Statistical Treatment to the Determination of I for Chemically Bound Particles. *Chem. Rev.*, 84:561–576, 1984.

Elke Kämmerer. *Influence of the extracellular matrix on cellular behaviour – Development and application of a bioengineered 3D cell culture system for cancer research and high resolution microscopy*. PhD thesis, Technische Universität Darmstadt, 2014.

Pakorn Kanchanawong, Gleb Shtengel, Ana M Pasapera, Ericka B Ramko, Michael W Davidson, Harald F Hess, and Clare M Waterman. Nanoscale architecture of integrin-based cell adhesions. *Nature*, 468(7323):580–4, November 2010. ISSN 1476-4687. doi: 10.1038/nature09621. URL `http://www.pubmedcentral.nih.gov/articlerender.fcgi?artid=3046339&tool=pmcentrez&rendertype=abstract`.

H P Kao and a S Verkman. Tracking of single fluorescent particles in three dimensions: use of cylindrical optics to encode particle position. *Biophysical journal*, 67(3):1291–300, September 1994. ISSN 0006-3495. doi: 10.1016/S0006-3495(94)80601-0. URL `http://www.pubmedcentral.nih.gov/articlerender.fcgi?artid=1225486&tool=pmcentrez&rendertype=abstract`.

Tadashi Kasahara, Emiko Koguchi, Megumi Funakoshi, Eriko Aizu-Yokota, and Yoshiko Sonoda. Anti-apoptotic Action of Focal Adhesion Kinase (FAK) Against Ionizing Radiation. *Antioxidants & Redox Signaling*, 4(3):491–499, 2002.

Adel Kechkar, Deepak Nair, Mike Heilemann, Daniel Choquet, and Jean-Baptiste Sibarita. Real-time analysis and visualization for single-molecule based super-resolution microscopy. *PloS one*, 8(4):e62918, January 2013. ISSN 1932-6203. doi: 10.1371/journal.pone.0062918. URL `http://www.pubmedcentral.nih.gov/articlerender.fcgi?artid=3639901&tool=pmcentrez&rendertype=abstract`.

Peter Kegel, Enriqueta Riballo, Martin Kühne, Penny a Jeggo, and Markus Löbrich. X-irradiation of cells on glass slides has a dose doubling impact. *DNA repair*, 6(11):1692–7, November 2007. ISSN 1568-7864. doi: 10.1016/j.dnarep.2007.05.013. URL `http://www.ncbi.nlm.nih.gov/pubmed/17644493`.

Kyungsang Kim, Junhong Min, Lina Carlini, Michael Unser, Suliana Manley, Daejong Jeon, Jong Chul Ye, and A Problem Formulation. Fast Maximum Likelihood High-density Low-SNR Super-resolution Localization Microscopy. In *Proceedings of the 10th International Conference on Sampling Theory and Applications*, pages 285–288, 2013.

Soo-Hyun Kim, Jeremy Turnbull, and Scott Guimond. Extracellular matrix and cell signalling: the dynamic cooperation of integrin, proteoglycan and growth factor receptor. *The Journal of endocrinology*, 209(2):139–51, May 2011. ISSN 1479-6805. doi: 10.1530/JOE-10-0377. URL `http://www.ncbi.nlm.nih.gov/pubmed/21307119`.

Lauren C Kimlin, Giovanna Casagrande, and Victoria M Virador. In vitro three-dimensional (3D) models in cancer research: an update. *Molecular carcinogenesis*, 52(3):167–82, March 2013. ISSN 1098-2744. doi: 10.1002/mc.21844. URL `http://www.ncbi.nlm.nih.gov/pubmed/22162252`.

Richard Kolesnick and Zvi Fuks. Radiation and ceramide-induced apoptosis. *Oncogene*, 22(37):5897–906, September 2003. ISSN 0950-9232. doi: 10.1038/sj.onc.1206702. URL `http://www.ncbi.nlm.nih.gov/pubmed/12947396`.

Axel Kölling, Carmen Maldonado, Flavio Ojeda, and Horst A Diehl. Membrane fluidity of microsomal and thymocyte membranes after X-ray and UV irradiation. *Radiation and environmental biophysics*, 33: 303–313, 1994.

A.W.T. Konings, J. Damen, and W.B. Trieling. Protection of Liposomal Lipids against Radiation Induced Oxidative Damage. *International Journal of Radiation Biology*, 35(4):343–350, January 1979. ISSN 0955-3002. doi: 10.1080/09553007914550411. URL `http://informahealthcare.com/doi/abs/10.1080/09553007914550411`.

D T Kuan, a a Sawchuk, T C Strand, and P Chavel. Adaptive noise smoothing filter for images with signal-dependent noise. *IEEE transactions on pattern analysis and machine intelligence*, 7(2):165–77, February 1985. ISSN 0162-8828. URL `http://www.ncbi.nlm.nih.gov/pubmed/21508198`.

U Kubitscheck, O Kückmann, T Kues, and R Peters. Imaging and tracking of single GFP molecules in solution. *Biophysical journal*, 78(4):2170–9, April 2000. ISSN 0006-3495. doi: 10.1016/S0006-3495(00)76764-6. URL `http://www.pubmedcentral.nih.gov/articlerender.fcgi?artid=1300809&tool=pmcentrez&rendertype=abstract`.

Kristopher E. Kubow and Alan Rick Horwitz. Reducing background fluorescence reveals adhesion in 3D matrices. *Nat Cell Biol*, 13(1):3–7, 2011. doi: 10.1038/ncb0111-3.Reducing.

J. Kuha. AIC and BIC: Comparisons of Assumptions and Performance. *Sociological Methods & Research*, 33(2):188–229, November 2004. ISSN 0049-1241. doi: 10.1177/0049124103262065. URL `http://smr.sagepub.com/cgi/doi/10.1177/0049124103262065`.

S. Kullback and R. A. Leibler. On Information and Sufficiency. *The Annals of Mathematical Statistics*, 22(1):79–86, 1951. doi: 10.1214/aoms/1177729694. URL `http://projecteuclid.org/euclid.aoms/1177729694`.

Suresh Kumar, Papendra Kumar, Manoj Gupta, and Ashok Kumar Nagawat. Performance Comparison of Median and Wiener Filter in Image De-noising. *International Journal of Computer Applications*, 12(4):27–31, 2010.

a Kusumi, Y Sako, and M Yamamoto. Confined lateral diffusion of membrane receptors as studied by single particle tracking (nanovid microscopy). Effects of calcium-induced differentiation in cultured epithelial cells. *Biophysical journal*, 65(5):2021–40, November 1993. ISSN 0006-3495. doi: 10.1016/S0006-3495(93)81253-0. URL `http://www.pubmedcentral.nih.gov/articlerender.fcgi?artid=1225938&tool=pmcentrez&rendertype=abstract`.

Akihiro Kusumi, Yuki M Shirai, Ikuko Koyama-Honda, Kenichi G N Suzuki, and Takahiro K Fujiwara. Hierarchical organization of the plasma membrane: investigations by single-molecule tracking vs. fluorescence correlation spectroscopy. *FEBS letters*, 584(9):1814–23, May 2010. ISSN 1873-3468. doi: 10.1016/j.febslet.2010.02.047. URL `http://www.ncbi.nlm.nih.gov/pubmed/20178787`.

Akihiro Kusumi, Takahiro K Fujiwara, Rahul Chadda, Min Xie, Taka a Tsunoyama, Ziya Kalay, Rinshi S Kasai, and Kenichi G N Suzuki. Dynamic organizing principles of the plasma membrane that regulate signal transduction: commemorating the fortieth anniversary of Singer and Nicolson's fluid-mosaic model. *Annual review of cell and developmental biology*, 28:215–50, January 2012. ISSN 1530-8995. doi: 10.1146/annurev-cellbio-100809-151736. URL `http://www.ncbi.nlm.nih.gov/pubmed/22905956`.

Paul Langevin. Sur la théorie du mouvement brownien. *C. R. Acad. Sci. (Paris)*, 146:530–533, 1908.

Joshua D Larkin and Peter R Cook. Maximum precision closed-form solution for localizing diffraction-limited spots in noisy images. *Opt Express*, 20(16):18478–18493, 2012.

Florian Lauer, Elke Kaemmerer, and Tobias Meckel. Single molecule microscopy in 3D cell cultures and tissues. *Advanced drug delivery reviews*, 79-80:79–94, 2014.

S. L. Lauritzen, A. P. Dawid, B. N. Larsen, and H.-G. Leimer. Independence properties of directed markov fields. *Networks*, 20(5):491–505, August 1990. ISSN 00283045. doi: 10.1002/net.3230200503. URL http://doi.wiley.com/10.1002/net.3230200503.

J Kevin Leach, Glenn Van Tuyle, Peck-sun Lin, J Kevin Leach, Glenn Van Tuyle, Peck-sun Lin, Rupert Schmidt-ullrich, and Ross B Mikkelsen. Generation of Reactive Oxygen / Nitrogen Ionizing Radiation-induced, Mitochondria-dependent Generation of Reactive. *Cancer research*, 61:3894–3901, 2001.

Jong-sen Lee. Digital Image Enhancement and Noise Filtering by Use of Local Statistics. *IEEE TRANSACTIONS ON PATTERN ANALYSIS AND MACHINE INTELLIGENCE*, PAMI-2(2):165–168, 1980.

Steven F Lee, Michael a Thompson, Monica a Schwartz, Lucy Shapiro, and W E Moerner. Super-resolution imaging of the nucleoid-associated protein HU in Caulobacter crescentus. *Biophysical journal*, 100(7):L31–3, April 2011. ISSN 1542-0086. doi: 10.1016/j.bpj.2011.02.022. URL http://www.pubmedcentral.nih.gov/articlerender.fcgi?artid=3072666&tool=pmcentrez&rendertype=abstract.

Kyle R Legate, Eloi Montañez, Oliver Kudlacek, and Reinhard Fässler. ILK, PINCH and parvin: the tIPP of integrin signalling. *Nature reviews. Molecular cell biology*, 7(1):20–31, January 2006. ISSN 1471-0072. doi: 10.1038/nrm1789. URL http://www.ncbi.nlm.nih.gov/pubmed/16493410.

Don S. Lemons and Anthony Gythiel. Paul LangevinâĂŹs 1908 paper âĂIJOn the Theory of Brownian MotionâĂ? [âĂIJSur la theÌ?orie du mouvement brownien,âĂ? C. R. Acad. Sci. (Paris) 146, 530âĂŞ533 (1908)]. *American Journal of Physics*, 65(11):1079, 1997. ISSN 00029505. doi: 10.1119/1.18725. URL http://link.aip.org/link/?AJP/65/1079/1&Agg=doi.

Kenneth Levenberg. A method for the solution of certain problems in least squares. *Quarterly of Applied Mathematics*, 2:164–168, 1944.

Arnold J Levine, Jamil Momand, and Cathy A Finaly. The p53 tumor suppressor gene. *nature*, 351(June): 453–6, 1991.

W Leyko and G Bartosz. Review Membrane effects of ionizing radiation and hyperthermia. *Int J Radiat Biol*, 49(5):743–770, 1986.

life Technologies. CellMask âĎć Plasma Membrane Stains, 2014. URL http://tools.lifetechnologies.com/content/sfs/manuals/CellMask_Plasma_Membrane_Stains_PI.pdf.

Daniel Lingwood and Kai Simons. Lipid rafts as a membrane-organizing principle. *Science*, 327(5961): 46–50, January 2010. ISSN 1095-9203. doi: 10.1126/science.1174621. URL http://www.ncbi.nlm.nih.gov/pubmed/20044567.

Jing Liu and Anning Lin. Role of JNK activation in apoptosis: a double-edged sword. *Cell research*, 15 (1):36–42, January 2005. ISSN 1001-0602. doi: 10.1038/sj.cr.7290262. URL http://www.ncbi.nlm.nih.gov/pubmed/15686625.

John G Lock, Bernhard Wehrle-haller, Staffan Strömblad, and Staffan Str. Cell-matrix adhesion complexes: master control machinery of cell migration. *Seminars in cancer biology*, 18(1):65–76, February 2008. ISSN 1044-579X. doi: 10.1016/j.semcancer.2007.10.001. URL http://www.ncbi.nlm.nih.gov/pubmed/18023204.

Piet H M Lommerse, B Ewa Snaar-Jagalska, Herman P Spaink, and Thomas Schmidt. Single-molecule diffusion measurements of H-Ras at the plasma membrane of live cells reveal microdomain localization upon activation. *Journal of cell science*, 118(Pt 9):1799–809, May 2005. ISSN 0021-9533. doi: 10.1242/jcs.02300. URL http://www.ncbi.nlm.nih.gov/pubmed/15860728.

Anna Löschberger, Sebastian van de Linde, Marie-Christine Dabauvalle, Bernd Rieger, Mike Heilemann, Georg Krohne, and Markus Sauer. Super-resolution imaging visualizes the eightfold symmetry of gp210 proteins around the nuclear pore complex and resolves the central channel with nanometer resolution. *Journal of cell science*, 125(Pt 3):570–5, February 2012. ISSN 1477-9137. doi: 10.1242/jcs.098822. URL `http://www.ncbi.nlm.nih.gov/pubmed/22389396`.

Florian Luisier, Cédric Vonesch, Thierry Blu, and Michael Unser. Fast interscale wavelet denoising of Poisson-corrupted images. *Signal Processing*, 90(2):415–427, February 2010. ISSN 01651684. doi: 10.1016/j.sigpro.2009.07.009. URL `http://linkinghub.elsevier.com/retrieve/pii/S0165168409003016`.

David Lunn, David Spiegelhalter, Andrew Thomas, and Nicky Best. The BUGS project : Evolution , critique and future directions. *STATISTICS IN MEDICINE*, 28(June):3049–3067, 2009. doi: 10.1002/sim.

David J Lunn, Andrew Thomas, Nicky Best, and David Spiegelhalter. WinBUGS âĂŞ A Bayesian modelling framework: Concepts, structure, and extensibility. *Statistics and Computing*, 10(4):325–337, 2000.

Carlo Manzo, Thomas S van Zanten, Suvrajit Saha, Juan a Torreno-Pina, Satyajit Mayor, and Maria F Garcia-Parajo. PSF decomposition of nanoscopy images via Bayesian analysis unravels distinct molecular organization of the cell membrane. *Scientific reports*, 4:4354, January 2014. ISSN 2045-2322. doi: 10.1038/srep04354. URL `http://www.pubmedcentral.nih.gov/articlerender.fcgi?artid=3950809&tool=pmcentrez&rendertype=abstract`.

Dipti Marathe and K P Mishra. Radiation-Induced Changes in Permeability in Unilamellar Phospholipid Liposomes Radiation-Induced Changes in Permeability in Unilamellar Phospholipid Liposomes. *Radiation Research*, 157(6):685–692, 2002.

Loredana G Marcu. Altered fractionation in radiotherapy: from radiobiological rationale to therapeutic gain. *Cancer treatment reviews*, 36(8):606–14, December 2010. ISSN 1532-1967. doi: 10.1016/j.ctrv.2010.04.004. URL `http://www.ncbi.nlm.nih.gov/pubmed/20494524`.

Donald W . Marquardt. An Algorithm for Least-Squares Estimation of Nonlinear Parameters. *Journal of the Society for Industrial and Applied Mathematics*, 11(2):431–441, 1963.

Derek Marsh. Thermodynamics of phospholipid self-assembly. *Biophysical journal*, 102(5):1079–87, March 2012. ISSN 1542-0086. doi: 10.1016/j.bpj.2012.01.049. URL `http://www.pubmedcentral.nih.gov/articlerender.fcgi?artid=3296042&tool=pmcentrez&rendertype=abstract`.

Marisa L Martin-Fernandez and David T Clarke. Single Molecule Fluorescence Detection and Tracking in Mammalian Cells: The State-of-the-Art and Future Perspectives. *International journal of molecular sciences*, 13(11):14742–65, January 2012. ISSN 1422-0067. doi: 10.3390/ijms131114742. URL `http://www.pubmedcentral.nih.gov/articlerender.fcgi?artid=3509608&tool=pmcentrez&rendertype=abstract`.

A. D. McNaught and A. Wilkinson, editors. *IUPAC. Compendium of Chemical Terminology*. Blackwell Scientific Publications, Oxford, 2 edition, 1997. ISBN 0-9678550-9-8.

Tobias Meckel, Stefan Semrau, Marcel J M Schaaf, and Thomas Schmidt. Robust assessment of protein complex formation in vivo via single-molecule intensity distributions of autofluorescent proteins. *Journal of Biomedical Optics*, 16(7):076016, July 2011. ISSN 1560-2281. doi: 10.1117/1.3600002. URL `http://www.ncbi.nlm.nih.gov/pubmed/21806277`.

Doris Meder, Maria Joao Moreno, Paul Verkade, Winchil L C Vaz, and Kai Simons. Phase coexistence and connectivity in the apical membrane of polarized epithelial cells. *Proceedings of the National Academy of Sciences of the United States of America*, 103(2):329–34, January 2006. ISSN 0027-8424. doi: 10.1073/pnas.0509885103. URL `http://www.pubmedcentral.nih.gov/articlerender.fcgi?artid=1324955&tool=pmcentrez&rendertype=abstract`.

Erik Meijering, Oleh Dzyubachyk, and Ihor Smal. Methods for Cell and Particle Tracking. *Methods in enzymology*, 504(February):183–200, January 2012. ISSN 1557-7988. doi: 10.1016/B978-0-12-391857-4.00009-4. URL `http://www.ncbi.nlm.nih.gov/pubmed/22264535`.

J E Meredith, B Fazeli, and M a Schwartz. The extracellular matrix as a cell survival factor. *Molecular biology of the cell*, 4(9):953–61, September 1993. ISSN 1059-1524. URL `http://www.pubmedcentral.nih.gov/articlerender.fcgi?artid=275725&tool=pmcentrez&rendertype=abstract`.

Nicholas Metropolis and S. Ulam. The Monte Carlo Method. *Journal of the American Statistical Association*, 44(247):335–341, 1949.

Nicholas Metropolis, Arianna W. Rosenbluth, Marshall N. Rosenbluth, Augusta H. Teller, and Edward Teller. Equation of State Calculations by Fast Computing Machines. *The Journal of Chemical Physics*, 21(6):1087, 1953. ISSN 00219606. doi: 10.1063/1.1699114. URL `http://scitation.aip.org/content/aip/journal/jcp/21/6/10.1063/1.1699114`.

Ralf Metzler and Joseph Klafter. The random walk's guide to anomalous diffusion: a fractional dynamics approach. *Physics Reports (Review Section of Physics Letters)*, 339:1–77, 2000.

X Michalet, O H W Siegmund, J V Vallerga, P Jelinsky, J E Millaud, and S Weiss. Detectors for single-molecule fluorescence imaging and spectroscopy. *Journal of modern optics*, 54(2-3):239, January 2007. ISSN 0950-0340. doi: 10.1080/09500340600769067. URL `http://www.pubmedcentral.nih.gov/articlerender.fcgi?artid=2821066&tool=pmcentrez&rendertype=abstract`.

Xavier Michalet. Mean square displacement analysis of single-particle trajectories with localization error: Brownian motion in an isotropic medium. *Physical Review E*, 82(4):041914, October 2010. ISSN 1539-3755. doi: 10.1103/PhysRevE.82.041914. URL `http://link.aps.org/doi/10.1103/PhysRevE.82.041914`.

René Michel, Ralf Steinmeyer, Michael Falk, and Gregory S Harms. A New Detection Algorithm for Image Analysis of Single , Fluorescence-labeled Proteins in Living Cells. *Microscopy Research and Technique*, 770(December 2006):763–770, 2007. doi: 10.1002/jemt.

Junhong Min, Cédric Vonesch, Hagai Kirshner, Lina Carlini, Nicolas Olivier, Seamus Holden, Suliana Manley, Jong Chul Ye, and Michael Unser. FALCON: fast and unbiased reconstruction of high-density super-resolution microscopy data. *Scientific reports*, 4:4577, January 2014. ISSN 2045-2322. doi: 10.1038/srep04577. URL `http://www.pubmedcentral.nih.gov/articlerender.fcgi?artid=3974135&tool=pmcentrez&rendertype=abstract`.

Satyajit K Mitra and David D Schlaepfer. Integrin-regulated FAK-Src signaling in normal and cancer cells. *Current opinion in cell biology*, 18(5):516–23, October 2006. ISSN 0955-0674. doi: 10.1016/j.ceb.2006.08.011. URL `http://www.ncbi.nlm.nih.gov/pubmed/16919435`.

Michael J Mlodzianoski, Manuel F Juette, Glen L Beane, and Joerg Bewersdorf. Experimental characterization of 3D localization techniques for particle-tracking and super-resolution microscopy. *Optics express*, 17(10):8264–77, May 2009. ISSN 1094-4087. URL `http://www.ncbi.nlm.nih.gov/pubmed/19434159`.

F. Mohamed, D.a. Bradley, and C.P. Winlove. Effects of ionizing radiation on extracellular matrix. *Nuclear Instruments and Methods in Physics Research Section A: Accelerators, Spectrometers, Detectors and Associated Equipment*, 580(1):566–569, September 2007. ISSN 01689002. doi: 10.1016/j.nima.2007.05.236. URL `http://linkinghub.elsevier.com/retrieve/pii/S0168900207011242`.

Alexander B Mohseny, Isidro Machado, Yongping Cai, Karl-Ludwig Schaefer, Massimo Serra, Pancras C W Hogendoorn, Antonio Llombart-Bosch, and Anne-Marie Cleton-Jansen. Functional characterization of osteosarcoma cell lines provides representative models to study the human disease. *Laboratory investigation; a journal of technical methods and pathology*, 91(8):1195–205, August 2011. ISSN 1530-0307. doi: 10.1038/labinvest.2011.72. URL `http://www.ncbi.nlm.nih.gov/pubmed/21519327`.

Monica Monici. Cell and tissue autofluorescence research and diagnostic applications. *Biotechnology annual review*, 11:227–56, January 2005. ISSN 1387-2656. URL `http://www.ncbi.nlm.nih.gov/pubmed/16216779`.

Kim I Mortensen, L Stirling Churchman, James a Spudich, and Henrik Flyvbjerg. Optimized localization analysis for single-molecule tracking and super-resolution microscopy. *Nature methods*, 7(5):377–81, May 2010. ISSN 1548-7105. doi: 10.1038/nmeth.1447. URL `http://www.pubmedcentral.nih.gov/articlerender.fcgi?artid=3127582&tool=pmcentrez&rendertype=abstract`.

V Mueller, C Ringemann, A Honigmann, G Schwarzmann, R Medda, M Leutenegger, S Polyakova, V N Belov, S W Hell, and C Eggeling. STED nanoscopy reveals molecular details of cholesterol- and cytoskeleton-modulated lipid interactions in living cells. *Biophysical journal*, 101(7):1651–60, October 2011. ISSN 1542-0086. doi: 10.1016/j.bpj.2011.09.006. URL `http://www.pubmedcentral.nih.gov/articlerender.fcgi?artid=3183802&tool=pmcentrez&rendertype=abstract`.

Andrew Mugler, Aimee Gotway Bailey, Koichi Takahashi, and Pieter Rein ten Wolde. Membrane clustering and the role of rebinding in biochemical signaling. *Biophysical journal*, 102(5):1069–78, March 2012. ISSN 1542-0086. doi: 10.1016/j.bpj.2012.02.005. URL `http://www.pubmedcentral.nih.gov/articlerender.fcgi?artid=3296021&tool=pmcentrez&rendertype=abstract`.

Eran A Mukamel, Hazen Babcock, and Xiaowei Zhuang. Statistical deconvolution for superresolution fluorescence microscopy. *Biophysical journal*, 102(10):2391–400, May 2012. ISSN 1542-0086. doi: 10.1016/j.bpj.2012.03.070. URL `http://www.ncbi.nlm.nih.gov/pubmed/22677393http://www.pubmedcentral.nih.gov/articlerender.fcgi?artid=3353000&tool=pmcentrez&rendertype=abstract`.

Sean Munro. Lipid Rafts: Elusive or Illusive ? *Cell*, 115(4):377–388, 2003.

Kotono Murase, Takahiro Fujiwara, Yasuhiro Umemura, Kenichi Suzuki, Ryota Iino, Hidetoshi Yamashita, Mihoko Saito, Hideji Murakoshi, Ken Ritchie, and Akihiro Kusumi. Ultrafine membrane compartments for molecular diffusion as revealed by single molecule techniques. *Biophysical journal*, 86(6):4075–93, June 2004. ISSN 0006-3495. doi: 10.1529/biophysj.103.035717. URL `http://www.pubmedcentral.nih.gov/articlerender.fcgi?artid=1304307&tool=pmcentrez&rendertype=abstract`.

Alexandra C Newton. Protein kinase C : poised to signal. *Am J Physiol Endocrinol Metab*, 298(35): E395–E402, 2010. doi: 10.1152/ajpendo.00477.2009.

Jason W Nichol, Sandeep T Koshy, Hojae Bae, Chang M Hwang, Seda Yamanlar, and Ali Khademhosseini. Cell-laden microengineered gelatin methacrylate hydrogels. *Biomaterials*, 31(21):5536–44, July 2010. ISSN 1878-5905. doi: 10.1016/j.biomaterials.2010.03.064. URL `http://www.pubmedcentral.nih.gov/articlerender.fcgi?artid=2878615&tool=pmcentrez&rendertype=abstract`.

Katerina M Niforou, Athanasios K Anagnostopoulos, Konstantinos Vougas, Christos Kittas, Vassilis G Gorgoulis, and George T Tsangaris. The proteome profile of the human osteosarcoma U2OS cell line. *Cancer genomics & proteomics*, 5(1):63–78, 2008. ISSN 1109-6535. URL http://www.ncbi.nlm.nih.gov/pubmed/18359981.

Stefanie Y Nishimura, Samuel J Lord, Lawrence O Klein, Katherine a Willets, Meng He, Zhikuan Lu, Robert J Twieg, and W E Moerner. Diffusion of lipid-like single-molecule fluorophores in the cell membrane. *The journal of physical chemistry. B*, 110(15):8151–7, April 2006. ISSN 1520-6106. doi: 10.1021/jp0574145. URL http://www.pubmedcentral.nih.gov/articlerender.fcgi?artid=1702323&tool=pmcentrez&rendertype=abstract.

Yasutomi Nishizuka. The role of protein kinase C in cell surface signal transduction and tumour promotion. *Nature*, 308:693–698, 1984.

Yasutomi Nishizuka. Intracellular Signaling by Hydrolysis of Phospholipids and Activation of Protein Kinase C. *Science*, 258(5082):607–614, March 1992. ISSN 0036-8075. URL http://www.pubmedcentral.nih.gov/articlerender.fcgi?artid=321207&tool=pmcentrez&rendertype=abstract.

Yasutomi Nishizuka. Protein kinase C and lipid signaling for sustained cellular responses. *The FASEB Journal*, 9(7):484–496, 1995.

NSA, 1999. URL http://www.nsa.gov/about/cryptologic_heritage/hall_of_honor/1999/kullback.shtml.

NSA, 2002. URL http://www.nsa.gov/about/cryptologic_heritage/hall_of_honor/2002/leibler.shtml.

Lina M. Obeid, Corinne M. Linardic, Linda A. Karolak, and Yusuf A. Hannun. Programmed Cell Death Induced by Ceramide. *Science*, 259(5102):1769–1771, December 1993. ISSN 0036-8075.

Raimund J Ober, Sripad Ram, and E Sally Ward. Localization accuracy in single-molecule microscopy. *Biophysical journal*, 86(2):1185–200, February 2004. ISSN 0006-3495. doi: 10.1016/S0006-3495(04)74193-4. URL http://www.pubmedcentral.nih.gov/articlerender.fcgi?artid=1303911&tool=pmcentrez&rendertype=abstract.

Yu Ohsugi, Kenta Saito, Mamoru Tamura, and Masataka Kinjo. Lateral mobility of membrane-binding proteins in living cells measured by total internal reflection fluorescence correlation spectroscopy. *Biophysical journal*, 91(9):3456–64, November 2006. ISSN 0006-3495. doi: 10.1529/biophysj.105.074625. URL http://www.pubmedcentral.nih.gov/articlerender.fcgi?artid=1614500&tool=pmcentrez&rendertype=abstract.

Bernt Øksendal. *Stochastic differential equations*. Springer Berlin Heidelberg New York, 6th edition, 2003. ISBN 3-540-04758-1.

Jean-Christophe Olivo-Marin. Extraction of spots in biological images using multiscale products. *Pattern Recognition*, 35(9):1989–1996, September 2002. ISSN 00313203. doi: 10.1016/S0031-3203(01)00127-3. URL http://linkinghub.elsevier.com/retrieve/pii/S0031320301001273.

Martin Ovesny, Pavel KÅŹižek, Josef Borkovec, Zdeněk Svindrych, and Guy M Hagen. ThunderSTORM: a comprehensive ImageJ plugin for PALM and STORM data analysis and super-resolution imaging. *Bioinformatics (Oxford, England)*, pages 1–2, April 2014. ISSN 1367-4811. doi: 10.1093/bioinformatics/btu202. URL http://www.ncbi.nlm.nih.gov/pubmed/24771516.

Francesco Pampaloni, Emmanuel G Reynaud, and Ernst H K Stelzer. The third dimension bridges the gap between cell culture and live tissue. *Nature Reviews Molecular Cell Biology*, 8:839–845, 2007.

B N Pandey and K P Mishra. Radiation induced oxidative damage modification by cholesterol in liposomal membrane. *Radiation physics and chemistry*, 54:481–489, 1999.

T Parasassi, O Sapora, A M Giustit, G De Stasio, and G Ravagnan. Alterations in erythrocyte membrane lipids induced by low doses of ionizing radiation as revealed by 1,6-diphenyl-1,3,5-hexatriene fluorescence lifetime. *Int J Radiat Biol*, 59(1):59–69, 1991.

T Parasassi, A M Giusti, E Gratton, M Raimondi, G Ravagnan, and O Sapora. Evidence for an increase in water concentration in bilayers after oxidative damage of phospholipids induced by ionizing radiation. *Int J Radiat Biol*, 65(3):329–334, 1994.

Tiziana Parasassi, Anna Maria Giusti, Margherita Raimondi, Giampietro Ravangnan, Orazio Sapora, and Enrico Gratton. Cholesterol protects the phospholipid bilayer from oxidative damage. *Free Radical Biology & Medicine*, 19(4):511–516, 1995.

Heon Joo Park, Robert J Griffin, Susanta Hui, H Levitt, and Chang W Song. Radiation-Induced Vascular Damage in Tumors: Implications of Vascular Damage in Ablative Hypofractionated Radiotherapy (SBRT and SRS). *Radiation Research*, 327:311–327, 2012. doi: 10.1667/RR2773.1.

Raghuveer Parthasarathy. Rapid, accurate particle tracking by calculation of radial symmetry centers. *Nature methods*, 9(7):724–6, July 2012. ISSN 1548-7105. doi: 10.1038/nmeth.2071. URL `http://www.ncbi.nlm.nih.gov/pubmed/22688415`.

Robert G Parton and Kai Simons. The multiple faces of caveolae. *Nature reviews. Molecular cell biology*, 8(3):185–94, March 2007. ISSN 1471-0072. doi: 10.1038/nrm2122. URL `http://www.ncbi.nlm.nih.gov/pubmed/17318224`.

Wolfgang Paul and Jörg Baschnagel. *Stochastic Processes: From Physics to Finance*. Springer, Heidelberg, New York, Dordrecht, London, 2 edition, 2013. ISBN 3319003275.

Sri Rama Prasanna Pavani, Michael A Thompson, Julie S Biteen, Samuel J Lord, Na Liu, Robert J Twieg, Rafael Piestun, and W E Moerner. Three-dimensional, single-molecule fluorescence imaging beyond the diffraction limit by using a double-helix point spread function. *Proc. Natl. Acad. Sci. USA*, 106(9), 2009.

Stéphanie Pellegrin and Harry Mellor. Actin stress fibres. *Journal of cell science*, 120(Pt 20):3491–9, October 2007. ISSN 0021-9533. doi: 10.1242/jcs.018473. URL `http://www.ncbi.nlm.nih.gov/pubmed/17928305`.

Linda J Pike. Lipid rafts: bringing order to chaos. *Journal of lipid research*, 44(4):655–67, April 2003. ISSN 0022-2275. doi: 10.1194/jlr.R200021-JLR200. URL `http://www.ncbi.nlm.nih.gov/pubmed/12562849`.

T Pomorski and A K Menon. Lipid flippases and their biological functions. *Cell. Mol. Life Sci.*, 63: 2908–2921, January 2006. ISSN 0923-6082.

William Press, Saul Teukolsky, William Vetterling, and Brian Flannery. *Numerical Recipes in C: The Art of Scientific Computing*. Cambridge University Press, Cambridge, 2 edition, 1997. ISBN 0521431085. doi: 10.2307/1269484. URL `http://www.jstor.org/stable/1269484?origin=crossref`.

Sarah T Pruett, Anatoliy Bushnev, Kerri Hagedorn, Madhura Adiga, Christopher a Haynes, M Cameron Sullards, Dennis C Liotta, and Alfred H Merrill. Biodiversity of sphingoid bases („sphingosines“) and related amino alcohols. *Journal of lipid research*, 49(8):1621–39, August 2008. ISSN 0022-2275. doi: 10.1194/jlr.R800012-JLR200. URL `http://www.pubmedcentral.nih.gov/articlerender.fcgi?artid=2444003&tool=pmcentrez&rendertype=abstract`.

H Qian, M P Sheetz, and E L Elson. Single particle tracking. Analysis of diffusion and flow in two-dimensional systems. *Biophysical journal*, 60(4):910–21, October 1991. ISSN 0006-3495. doi: 10.1016/S0006-3495(91)82125-7. URL `http://www.pubmedcentral.nih.gov/articlerender.fcgi?artid=1260142&tool=pmcentrez&rendertype=abstract`.

Tingwei Quan, Hongyu Zhu, Xiaomao Liu, Yongfeng Liu, Jiuping Ding, Shaoqun Zeng, and Zhen-Li Huang. High-density localization of active molecules using Structured Sparse Model and Bayesian Information Criterion. *Optics express*, 19(18):16963–74, August 2011. ISSN 1094-4087. URL `http://www.ncbi.nlm.nih.gov/pubmed/21935056`.

J Quintanilla, S Torquato, and RM Ziff. Efficient measurement of the percolation threshold for fully penetrable discs. *J. Phys. A: Math. Gen.*, 33(42):L399–L407, 2000.

Sripad Ram, E. Sally Ward, and Raimund J. Ober. A Stochastic Analysis of Performance Limits for Optical Microscopes. *Multidimensional Systems and Signal Processing*, 17(1):27–57, January 2006. ISSN 0923-6082. doi: 10.1007/s11045-005-6237-2. URL `http://link.springer.com/10.1007/s11045-005-6237-2`.

Sripad Ram, E Sally Ward, and Raimund J Ober. How accurately can a single molecule be localized in three dimensions using a fluorescence microscope? In *Proc SPIE*, pages 426–435, 2010. doi: 10.1117/12.587878.How.

R Rathinam and Suresh K Alahari. Important role of integrins in the cancer biology. *Cancer*, pages 223–237, 2010. doi: 10.1007/s10555-010-9211-x.

D. Reid. An algorithm for tracking multiple targets. *IEEE Transactions on Automatic Control*, 24(6):843–854, December 1979. ISSN 0018-9286. doi: 10.1109/TAC.1979.1102177. URL `http://ieeexplore.ieee.org/lpdocs/epic03/wrapper.htm?arnumber=1102177`.

Julie a Reisz, Nidhi Bansal, Jiang Qian, Weiling Zhao, and Cristina M Furdui. Effects of Ionizing Radiation on Biological Molecules-Mechanisms of Damage and Emerging Methods of Detection. *Antioxidants & redox signaling*, 00(00):1–33, February 2014. ISSN 1557-7716. doi: 10.1089/ars.2013.5489. URL `http://www.ncbi.nlm.nih.gov/pubmed/24382094`.

Anne J. Ridley and Alan Hall. The Small GTP-Binding Protein rho Regulates the Assembly of Focal Adhesions and Actin Stress Fibers in Response to Growth Factors. *Cell*, 70(August):389–399, November 1992. ISSN 0006-3002. doi: 10.1016/j.bbamem.2004.05.012. URL `http://www.ncbi.nlm.nih.gov/pubmed/15519309`.

Bernd Rieger and Sjoerd Stallinga. The lateral and axial localization uncertainty in super-resolution light microscopy. *Chemphyschem : a European journal of chemical physics and physical chemistry*, 15(4):664–70, March 2014. ISSN 1439-7641. doi: 10.1002/cphc.201300711. URL `http://www.ncbi.nlm.nih.gov/pubmed/24302478`.

Ken Ritchie, Xiao-Yuan Shan, Junko Kondo, Kokoro Iwasawa, Takahiro Fujiwara, and Akihiro Kusumi. Detection of non-Brownian diffusion in the cell membrane in single molecule tracking. *Biophysical journal*, 88(3):2266–77, March 2005. ISSN 0006-3495. doi: 10.1529/biophysj.104.054106. URL `http://www.pubmedcentral.nih.gov/articlerender.fcgi?artid=1305276&tool=pmcentrez&rendertype=abstract`.

Jörg G Ritter, Jan-Hendrik Spille, Tim Kaminski, and Ulrich Kubitscheck. A cylindrical zoom lens unit for adjustable optical sectioning in light sheet microscopy. *Biomedical optics express*, 2(1):185–93, January 2010a. ISSN 2156-7085. doi: 10.1364/BOE.2.000185. URL `http://www.pubmedcentral.nih.gov/articlerender.fcgi?artid=3028493&tool=pmcentrez&rendertype=abstract`.

Jörg Gerhard Ritter, Roman Veith, Andreas Veenendaal, Jan Peter Siebrasse, and Ulrich Kubitscheck. Light sheet microscopy for single molecule tracking in living tissue. *PloS one*, 5(7):e11639, January 2010b. ISSN 1932-6203. doi: 10.1371/journal.pone.0011639. URL `http://www.pubmedcentral.nih.gov/articlerender.fcgi?artid=2909143&tool=pmcentrez&rendertype=abstract`.

Mark Stanford Robbins, Senior Member, and Benjamin James Hadwen. The Noise Performance of Electron Multiplying Charge-Coupled Devices. *IEEE TRANSACTIONS ON ELECTRON DEVICES*, 50 (5):1227–1232, 2003. URL `http://www.bioee.ee.columbia.edu/courses/upload/Bibliography/robbins2003.pdf`.

François B Robin, William M McFadden, Baixue Yao, and Edwin M Munro. Single-molecule analysis of cell surface dynamics in Caenorhabditis elegans embryos. *Nature methods*, 11(6):677–682, April 2014. ISSN 1548-7105. doi: 10.1038/nmeth.2928. URL `http://www.ncbi.nlm.nih.gov/pubmed/24727651`.

Daniel J Rolfe, Charles I McLachlan, Michael Hirsch, Sarah R Needham, Christopher J Tynan, Stephen E D Webb, Marisa L Martin-Fernandez, and Michael P Hobson. Automated multidimensional single molecule fluorescence microscopy feature detection and tracking. *European biophysics journal : EBJ*, 40(10):1167–86, October 2011. ISSN 1432-1017. doi: 10.1007/s00249-011-0747-7. URL `http://www.ncbi.nlm.nih.gov/pubmed/21928120`.

Harald H. Rossi and M Zaider. *Microdosimetry and Its Applications*. Springer, Berlin Heidelberg, 1996. ISBN 978-3540585411.

Olivier Rossier, Vivien Octeau, Jean-Baptiste Sibarita, Cécile Leduc, Béatrice Tessier, Deepak Nair, Volker Gatterdam, Olivier Destaing, Corinne Albigès-Rizo, Robert Tampé, Laurent Cognet, Daniel Choquet, Brahim Lounis, and Grégory Giannone. Integrins $\beta 1$ and $\beta 3$ exhibit distinct dynamic nanoscale organizations inside focal adhesions. *Nature cell biology*, 14(10):1057–67, October 2012. ISSN 1476-4679. doi: 10.1038/ncb2588. URL `http://www.ncbi.nlm.nih.gov/pubmed/23023225`.

E Ruoslahti. RGD and other recognition sequences for integrins. *Annual review of cell and developmental biology*, 12:697–715, January 1996. ISSN 1081-0706. doi: 10.1146/annurev.cellbio.12.1.697. URL `http://www.ncbi.nlm.nih.gov/pubmed/8970741`.

Michael J Rust, Mark Bates, and Xiaowei Zhuang. Sub-diffraction-limit imaging by stochastic optical reconstruction microscopy (STORM). *Nature methods*, 3(10):793–795, 2006. doi: 10.1038/NMETH929.

PG Saffman and M Delbrück. Brownian motion in biological membranes. *Proceedings of the National Academy of Sciences*, 72(8):3111–3113, 1975. URL `http://www.pnas.org/content/72/8/3111.short`.

Bahaa E. A. Saleh and Malvin Carl Teich. *Grundlagen der Photonik*. Wiley-VCH, Weinheim, 2008.

V Sandfort, U Koch, and N Cordes. Cell adhesion-mediated radioresistance revisited. *International journal of radiation biology*, 83(11-12):727–32, 2007. ISSN 0955-3002. doi: 10.1080/09553000701694335. URL `http://www.ncbi.nlm.nih.gov/pubmed/17952769`.

P Santana, L a Peña, a Haimovitz-Friedman, S Martin, D Green, M McLoughlin, C Cordon-Cardo, E H Schuchman, Z Fuks, and R Kolesnick. Acid sphingomyelinase-deficient human lymphoblasts and mice are defective in radiation-induced apoptosis. *Cell*, 86(2):189–99, July 1996. ISSN 0092-8674. URL `http://www.ncbi.nlm.nih.gov/pubmed/8706124`.

Thierry Savin and Patrick S Doyle. Static and dynamic errors in particle tracking microrheology. *Biophysical journal*, 88(1):623–38, January 2005. ISSN 0006-3495. doi: 10.1529/biophysj.104.042457. URL `http://www.pubmedcentral.nih.gov/articlerender.fcgi?artid=1305040&tool=pmcentrez&rendertype=abstract`.

M J Saxton. Lateral diffusion in an archipelago. Single-particle diffusion. *Biophysical journal*, 64(6):1766–80, June 1993. ISSN 0006-3495. doi: 10.1016/S0006-3495(93)81548-0. URL `http://www.pubmedcentral.nih.gov/articlerender.fcgi?artid=1262511&tool=pmcentrez&rendertype=abstract`.

M J Saxton. Single-particle tracking: the distribution of diffusion coefficients. *Biophysical journal*, 72(4):1744–53, April 1997. ISSN 0006-3495. doi: 10.1016/S0006-3495(97)78820-9. URL `http://www.pubmedcentral.nih.gov/articlerender.fcgi?artid=1184368&tool=pmcentrez&rendertype=abstract`.

Marcel J M Schaaf, Wiepke J A Koopmans, Tobias Meckel, John van Noort, B Ewa Snaar-Jagalska, Thomas S Schmidt, and Herman P Spaink. Single-molecule microscopy reveals membrane microdomain organization of cells in a living vertebrate. *Biophysical journal*, 97(4):1206–14, August 2009. ISSN 1542-0086. doi: 10.1016/j.bpj.2009.05.044. URL `http://www.pubmedcentral.nih.gov/articlerender.fcgi?artid=2726327&tool=pmcentrez&rendertype=abstract`.

Carolin Schild, Matthias Wirth, Maximilian Reichert, Roland M Schmid, Dieter Saur, and Günter Schneider. PI3K signaling maintains c-myc expression to regulate transcription of E2F1 in pancreatic cancer cells. *Molecular carcinogenesis*, 48(12):1149–58, December 2009. ISSN 1098-2744. doi: 10.1002/mc.20569. URL `http://www.ncbi.nlm.nih.gov/pubmed/19603422`.

Th. Schmidt, G. J. Schütz, W. Baumgartner, H. J. Gruber, and H. Schindler. Imaging of single molecule diffusion. *Proc. Natl. Acad. Sci. USA*, 93(April):2926–2929, 1996.

G J Schütz, H Schindler, and T Schmidt. Single-molecule microscopy on model membranes reveals anomalous diffusion. *Biophysical journal*, 73(2):1073–80, August 1997. ISSN 0006-3495. doi: 10.1016/S0006-3495(97)78139-6. URL `http://www.pubmedcentral.nih.gov/articlerender.fcgi?artid=1181003&tool=pmcentrez&rendertype=abstract`.

Gideon Schwarz. Estimating The Dimension Of A Model. *The Annals of Statistics*, 6(2):61–464, 1978.

S Semrau and T Schmidt. Particle image correlation spectroscopy (PICS): retrieving nanometer-scale correlations from high-density single-molecule position data. *Biophysical journal*, 92(2):613–21, January 2007. ISSN 0006-3495. doi: 10.1529/biophysj.106.092577. URL `http://www.pubmedcentral.nih.gov/articlerender.fcgi?artid=1751376&tool=pmcentrez&rendertype=abstract`.

Arnauld Sergé, Nicolas Bertaux, Hervé Rigneault, and Didier Marguet. Dynamic multiple-target tracing to probe spatiotemporal cartography of cell membranes. *Nature methods*, 5(8):687–94, August 2008. ISSN 1548-7105. doi: 10.1038/nmeth.1233. URL `http://dx.doi.org/10.1038/nmeth.1233`.

Sanford J Shattil, Chungho Kim, and Mark H Ginsberg. The final steps of integrin activation : the end game. *EMBO Journal*, 11(April):288–300, 2010. doi: 10.1038/nrm2871.

Akihiro C E Shibata, Takahiro K Fujiwara, Limin Chen, Kenichi G N Suzuki, Yoshiro Ishikawa, Yuri L Nemoto, Yoshihiro Miwa, Ziya Kalay, Rahul Chadda, Keiji Naruse, and Akihiro Kusumi. Archipelago architecture of the focal adhesion: membrane molecules freely enter and exit from the focal adhesion zone. *Cytoskeleton (Hoboken, N.J.)*, 69(6):380–92, April 2012. ISSN 1949-3592. doi: 10.1002/cm.21032. URL `http://www.ncbi.nlm.nih.gov/pubmed/22488960`.

Akihiro C E Shibata, Limin H Chen, Rie Nagai, Fumiyoshi Ishidate, Rahul Chadda, Yoshihiro Miwa, Keiji Naruse, Yuki M Shirai, Takahiro K Fujiwara, and Akihiro Kusumi. Rac1 recruitment to the archipelago structure of the focal adhesion through the fluid membrane as revealed by single-molecule analysis. *Cytoskeleton (Hoboken, N.J.)*, 70(3):161–77, March 2013. ISSN 1949-3592. doi: 10.1002/cm.21097. URL `http://www.pubmedcentral.nih.gov/articlerender.fcgi?artid=3627312&tool=pmcentrez&rendertype=abstract`.

Bo Shuang, Jixin Chen, Lydia Kisley, and Christy F Landes. Troika of single particle tracking programing: SNR enhancement, particle identification, and mapping. *Physical chemistry chemical physics : PCCP*, 16(2):624–34, January 2014. ISSN 1463-9084. doi: 10.1039/c3cp53968g. URL `http://www.ncbi.nlm.nih.gov/pubmed/24263676`.

Jean-Baptiste Sibarita. High-density single-particle tracking: quantifying molecule organization and dynamics at the nanoscale. *Histochemistry and cell biology*, March 2014. ISSN 1432-119X. doi: 10.1007/s00418-014-1214-1. URL `http://www.ncbi.nlm.nih.gov/pubmed/24671496`.

K Simons and E Ikonen. Functional rafts in cell membranes. *Nature*, 387(6633):569–72, June 1997. ISSN 0028-0836. doi: 10.1038/42408. URL `http://www.ncbi.nlm.nih.gov/pubmed/9177342`.

K Simons and D Toomre. Lipid rafts and signal transduction. *Nature reviews. Molecular cell biology*, 1(1): 31–9, October 2000. ISSN 1471-0072. doi: 10.1038/35036052. URL `http://www.ncbi.nlm.nih.gov/pubmed/11413487`.

S J Singer and G L Nicolson. The structure and chemistry of mammalian cell membranes. *The American journal of pathology*, 65(2):427–37, November 1971. ISSN 0002-9440. URL `http://www.pubmedcentral.nih.gov/articlerender.fcgi?artid=2047445&tool=pmcentrez&rendertype=abstract`.

S J Singer and G L Nicolson. The fluid mosaic model of the structure of cell membranes. *Science (New York, N.Y.)*, 175(4023):720–31, February 1972. ISSN 0036-8075. URL `http://www.ncbi.nlm.nih.gov/pubmed/4333397`.

D. S. Sivia and J. Skilling. *Data Analysis. A Bayesian Tutorial*. Oxford University Press, Oxford, reprint of 2nd edition, 2012. ISBN 978-0-19-856832-2.

Ihor Smal, Marco Loog, Wiro Niessen, and Erik Meijering. Quantitative comparison of spot detection methods in fluorescence microscopy. *Medical Imaging, IEEE Transactions on*, 29(2):282–301, June 2010. doi: 10.1109/ISBI.2009.5193268. URL `http://ieeexplore.ieee.org/lpdocs/epic03/wrapper.htm?arnumber=5193268`.

Alex Small and Shane Stahlheber. Fluorophore localization algorithms for super-resolution microscopy. *Nature methods*, 11(3):267–79, March 2014. ISSN 1548-7105. doi: 10.1038/nmeth.2844. URL `http://www.ncbi.nlm.nih.gov/pubmed/24577277`.

A. F. M. Smith and G. O. Roberts. Bayesian Computation Via the Gibbs Sampler and Related Markov Chain Monte Carlo Methods. *Journal of the Royal Statistical Society. Series B (Methodological)*, 55(1): 3–23, 1993.

Carlas S Smith, Nikolai Joseph, Bernd Rieger, and Keith a Lidke. Fast, single-molecule localization that achieves theoretically minimum uncertainty. *Nature methods*, 7(5):373–5, May 2010. ISSN 1548-7105. doi: 10.1038/nmeth.1449. URL `http://www.pubmedcentral.nih.gov/articlerender.fcgi?artid=2862147&tool=pmcentrez&rendertype=abstract`.

Eric L Smith and Edward H Schuchman. The unexpected role of acid sphingomyelinase in cell death and the pathophysiology of common diseases. *FASEB journal : official publication of the Federation of American Societies for Experimental Biology*, 22(10):3419–31, October 2008. ISSN 1530-6860. doi: 10.1096/fj.08-108043. URL `http://www.pubmedcentral.nih.gov/articlerender.fcgi?artid=2537423&tool=pmcentrez&rendertype=abstract`.

Niall Smith, Colin Coates, Alan Giltinan, John Howard, Aidan O'Connor, Stephen O'Driscoll, Marcus Hauser, and Stephan Wagner. EMCCD technology and its impact on rapid low-light photometry. *Proc. SPIE*, 5499(Optical and Infrared Detectors for Astronomy):162–172, September 2004.

doi: 10.1117/12.549789. URL `http://proceedings.spiedigitallibrary.org/proceeding.aspx?articleid=848392`.

Steven W. Smith. Properties of Convolution. In *The Scientist and Engineer's Guide to Digital Signal Processing*, chapter 7, pages 123–140. California Technical Pub, 1997a. URL `http://www.dspguide.com/ch7.htm`.

Steven W. Smith. Custom Filters. In *The Scientist and Engineer's Guide to Digital Signal Processing*, chapter 17, pages 297–310. California Technical Pub, 1997b. ISBN 9780750674447. doi: 10.1016/B978-0-7506-7444-7/50054-6. URL `http://www.dspguide.com/ch17.htm`.

D. Spiegelhalter, A. Thomas, N. Best, and W Gilks. *BUGS 0.5: Bayesian inference Using Gibbs SamplingŰ-Manual (version ii)*. Medical Research Council Biostatistics Unit, Cambridge, 1996.

Jan-Hendrik Spille. *Three-dimensional single particle tracking in a light sheet microscope*. PhD thesis, Universität Bonn, 2014.

Jan-Hendrik Spille, Tim Kaminski, Heinz-Peter Königshoven, and Ulrich Kubitscheck. Dynamic three-dimensional tracking of single fluorescent nanoparticles deep inside living tissue. *Optics Express*, 20(18):19697, August 2012. ISSN 1094-4087. doi: 10.1364/OE.20.019697. URL `http://www.opticsexpress.org/abstract.cfm?URI=oe-20-18-19697`.

J.W.T. Spinks and R.J. Woods. Water and Inorganic Aqueous Systems. In *An introduction to radiation chemistry*, pages 243–313. John-Wiley and Sons, Inc., New York, Toronto, 3 edition, 1990. ISBN 0-471-61403-3.

Mélanie Spotheim-Maurizot, Mehran Mostafavi, Thierry Douki, and Jacqueline Belloni, editors. *Radiation Chemistry. From Basics to Applications in Material and Life Sciences.* EDP Sciences, 2008. ISBN 9782759800247.

Sjoerd Stallinga and Bernd Rieger. Accuracy of the gaussian point spread function model in 2D localization microscopy. *Optics express*, 18(24):24461–76, November 2010. ISSN 1094-4087. URL `http://www.ncbi.nlm.nih.gov/pubmed/21164793`.

Sjoerd Stallinga and Bernd Rieger. THE EFFECT OF BACKGROUND ON LOCALIZATION UNCERTAINTY IN SINGLE EMITTER IMAGING. In *Biomedical Imaging (ISBI), 2012 9th IEEE International Symposium on*, pages 988–991, 2012. ISBN 9781457718588.

D Stauffer. Scaling theory of percolation clusters. *Physics Reports (Review Section of Physics Letters)*, 54 (1):1–74, 1979.

Nadezhda Stefanova, Galya Staneva, Diana Petkova, Teodora Lupanova, Roumen Pankov, and Albena Momchilova. Cell culturing in a three-dimensional matrix affects the localization and properties of plasma membrane cholesterol. *Cell biology international*, 33(10):1079–86, October 2009. ISSN 1095-8355. doi: 10.1016/j.cellbi.2009.06.024. URL `http://www.ncbi.nlm.nih.gov/pubmed/19589391`.

Charles M. Stein. Estimation of the mean of a multivariate normal distribution. *The Annals of Statistics*, 9(6):1135–1151, 1981.

Katja Storch and Nils Cordes. Focal adhesion-chromatin linkage controls tumor cell resistance to radio- and chemotherapy. *Chemotherapy research and practice*, 2012:319287, January 2012. ISSN 2090-2115. doi: 10.1155/2012/319287. URL `http://www.pubmedcentral.nih.gov/articlerender.fcgi?artid=3385588&tool=pmcentrez&rendertype=abstract`.

Katja Storch, Iris Eke, Kerstin Borgmann, Mechthild Krause, Christian Richter, Kerstin Becker, Evelin Schröck, and Nils Cordes. Three-dimensional cell growth confers radioresistance by chromatin density modification. *Cancer research*, 70(10):3925–34, May 2010. ISSN 1538-7445. doi: 10.1158/0008-5472.CAN-09-3848. URL `http://www.ncbi.nlm.nih.gov/pubmed/20442295`.

Yi Sun. p53 and Its Downstream Proteins as Molecular Targets of Cancer. *MOLECULAR CARCINOGENESIS*, 415(May):409–415, 2006. doi: 10.1002/mc.

Christopher S. Szot, Cara F. Buchanan, Joseph W. Freeman, and Marissa N. Rylander. 3D inÂăvitro bioengineered tumors based on collagen I hydrogels. *Biomaterials*, 32(31):7905–7912, 2011. URL `http://www.sciencedirect.com/science/article/pii/S0142961211007721`.

Sylvain Tchani. *Kamera-synchronisierte Steuerung der Laser-Beleuchtung eines Einzelmolekül-Fluoreszenz-Mikroskops mit LabVIEW Bachelorarbeit Eidesstattliche Erklärung Kamera-synchronisierte Steuerung der Laser-Beleuchtung eines Einzelmolekül-Fluoreszenz-Mikroskops mit La*. Bachelor thesis, Technische Universität Darmstadt, 2013.

Michael a Thompson, Jason M Casolari, Majid Badieirostami, Patrick O Brown, and W E Moerner. Three-dimensional tracking of single mRNA particles in Saccharomyces cerevisiae using a double-helix point spread function. *Proceedings of the National Academy of Sciences of the United States of America*, 107(42):17864–71, October 2010. ISSN 1091-6490. doi: 10.1073/pnas.1012868107. URL `http://www.pubmedcentral.nih.gov/articlerender.fcgi?artid=2964242&tool=pmcentrez&rendertype=abstract`.

Russell E Thompson, Daniel R Larson, and Watt W Webb. Precise nanometer localization analysis for individual fluorescent probes. *Biophysical journal*, 82(5):2775–83, May 2002. ISSN 0006-3495. doi: 10.1016/S0006-3495(02)75618-X. URL `http://www.pubmedcentral.nih.gov/articlerender.fcgi?artid=1302065&tool=pmcentrez&rendertype=abstract`.

Silvanus P. Thompson. On Obliquely-crossed Cylindrical Lenses. *The London, Edinburgh, and Dublin Philosophical Magazine and Journal of Science*, 49(298):316–324, 1900.

Luke Tierney. Markov Chains for exploring posterior distributions. *The Annals of Statistics*, 22(4):1701–1728, 1994.

Makio Tokunaga, Naoko Imamoto, and Kumiko Sakata-sogawa. Highly inclined thin illumination enables clear single-molecule imaging in cells. *Nature Methods*, 5(2):159–161, 2008. doi: 10.1038/NMETH.1171.

Hermann Träuble, Max Teubner, Paul Woolley, and Hansjörg Eibl. Electrostatic interactions at charged lipid membranes. I. Effects of pH and univalent cations on membrane structure. *Biophysical Chemistry*, 4(4):319–342, September 1976. ISSN 13504487.

Stephanie Tristram-Nagle and John F. Nagle. Lipid bilayers: thermodynamics, structure, fluctuations, and interactions. *Chemistry and Physics of Lipids*, 127(1):3–14, January 2004. ISSN 00093084. doi: 10.1016/j.chemphyslip.2003.09.002. URL `http://linkinghub.elsevier.com/retrieve/pii/S0009308403001294`.

A Tsuji, K Kawasaki, S Ohnishi, H Merkle, and A Kusumi. Regulation of band 3 mobilities in erythrocyte ghost membranes by protein association and cytoskeletal meshwork. *Biochemistry*, 27(19):7447–52, September 1988. ISSN 0006-2960. URL `http://www.ncbi.nlm.nih.gov/pubmed/2462903`.

George L. Turin. An Introduction to Matched Filters. *IRE Transactions on Information Theory*, 6(3):311–329, 1960.

Yasuhiro M Umemura, Marija Vrljic, Stefanie Y Nishimura, Takahiro K Fujiwara, Kenichi G N Suzuki, and Akihiro Kusumi. Both MHC class II and its GPI-anchored form undergo hop diffusion as observed by single-molecule tracking. *Biophysical journal*, 95(1):435–50, July 2008. ISSN 1542-0086. doi: 10.1529/biophysj.107.123018. URL `http://www.pubmedcentral.nih.gov/articlerender.fcgi?artid=2426619&tool=pmcentrez&rendertype=abstract`.

Sebastian van de Linde, Anna Löschberger, Teresa Klein, Meike Heidbreder, Steve Wolter, Mike Heilemann, and Markus Sauer. Direct stochastic optical reconstruction microscopy with standard fluorescent probes. *Nature protocols*, 6(7):991–1009, July 2011. ISSN 1750-2799. doi: 10.1038/nprot.2011.336. URL `http://www.ncbi.nlm.nih.gov/pubmed/21720313`.

Gerrit van Meer and Anton I P M de Kroon. Lipid map of the mammalian cell. *Journal of cell science*, 124 (Pt 1):5–8, January 2011. ISSN 1477-9137. doi: 10.1242/jcs.071233. URL `http://www.ncbi.nlm.nih.gov/pubmed/21172818`.

Marcel Verheij, Ron Bose, Xin Hua Lin, Bei Yao, W. David Jarvis, Steven Grant, Michael J. Birrer, Eva Szabo, Leonard I. Zon, John M. Kyriakis, Adriana Haimovitz-Friedman, Zvi Fuks, and Richard N. Kolesnick. Requirement for ceramide-initiated SAPK/JNK signalling in stress-induced apoptosis. *Nature*, 380:75–79, 1996.

Jean-Philippe Vit and Filippo Rosselli. Role of the ceramide-signaling pathways in ionizing radiation-induced apoptosis. *Oncogene*, 22(54):8645–52, November 2003. ISSN 0950-9232. doi: 10.1038/sj.onc.1207087. URL `http://www.ncbi.nlm.nih.gov/pubmed/14647458`.

Ning Wang, Jessica D Tytell, and Donald E Ingber. Mechanotransduction at a distance: mechanically coupling the extracellular matrix with the nucleus. *Nature reviews. Molecular cell biology*, 10(1):75–82, January 2009. ISSN 1471-0080. doi: 10.1038/nrm2594. URL `http://www.ncbi.nlm.nih.gov/pubmed/19197334`.

Yi Wang, Joana F da Silva Domingues, Guruprakash Subbiahdoss, Henny C van der Mei, Henk J Busscher, and Matthew Libera. Conditions of lateral surface confinement that promote tissue-cell integration and inhibit biofilm growth. *Biomaterials*, 35(21):5446–52, July 2014. ISSN 1878-5905. doi: 10.1016/j.biomaterials.2014.03.057. URL `http://www.ncbi.nlm.nih.gov/pubmed/24726539`.

Yina Wang, Tingwei Quan, Shaoqun Zeng, and Zhen-li Huang. PALMER : a method capable of parallel localization of multiple emitters for high-density localization microscopy. *Optics Express*, 20(14): 16039–16049, 2012. doi: 10.1038/nmeth.1978.S.

Aubrey V Weigel, Blair Simon, Michael M Tamkun, and Diego Krapf. Ergodic and nonergodic processes coexist in the plasma membrane as observed by single-molecule tracking. *PNAS*, 108(16): 6438–6443, 2011. doi: 10.1073/pnas.1016325108/-/DCSupplemental.www.pnas.org/cgi/doi/10.1073/pnas.1016325108.

Aubrey V. Weigel, Shankarachary Ragi, Michael L. Reid, Edwin K. P. Chong, Michael M. Tamkun, and Diego Krapf. Obstructed diffusion propagator analysis for single-particle tracking. *Physical Review E*, 85(4):041924, April 2012. ISSN 1539-3755. doi: 10.1103/PhysRevE.85.041924. URL `http://link.aps.org/doi/10.1103/PhysRevE.85.041924`.

Stefan Wieser and Gerhard J Schütz. Tracking single molecules in the live cell plasma membrane-Do's and Don't's. *Methods (San Diego, Calif.)*, 46(2):131–40, October 2008. ISSN 1095-9130. doi: 10.1016/j.ymeth.2008.06.010. URL `http://www.ncbi.nlm.nih.gov/pubmed/18634880`.

Stefan Wieser, Manuel Moertelmaier, Elke Fuertbauer, Hannes Stockinger, and Gerhard J Schütz. (Un)confined diffusion of CD59 in the plasma membrane determined by high-resolution single molecule microscopy. *Biophysical journal*, 92(10):3719–28, May 2007. ISSN 0006-3495. doi: 10.1529/biophysj.106.095398. URL `http://www.pubmedcentral.nih.gov/articlerender.fcgi?artid=1853144&tool=pmcentrez&rendertype=abstract`.

Claire Wilhelm. Out-of-Equilibrium Microrheology inside Living Cells. *Physical Review Letters*, 101(2): 028101, July 2008. ISSN 0031-9007. doi: 10.1103/PhysRevLett.101.028101. URL `http://link.aps.org/doi/10.1103/PhysRevLett.101.028101`.

Kim A Winick. Cramer-Rao lower bounds on the performance of charge-coupled-device optical position estimators. *J. Opt. Soc. Am. A*, 3(11):1809–1815, 1986.

Dominik Wöll, Christoph Kölbl, Beate Stempfle, and Andreas Karrenbauer. A novel method for automatic single molecule tracking of blinking molecules at low intensities. *Physical chemistry chemical physics : PCCP*, 15(17):6196–205, May 2013. ISSN 1463-9084. doi: 10.1039/c3cp44693j. URL `http://www.ncbi.nlm.nih.gov/pubmed/23429424`.

Nailong Wu. Using a Matched Filter to Improve SNR of Radio Maps. In Diana M. Worrall, Chris Biemesderfer, and Jeannette Barnes, editors, *Astronomical Data Analysis Software and Systems I, A.S.P. Conference Series, Vol. 25*, pages 291–295, 1992.

Ke Xu, Hazen P Babcock, and Xiaowei Zhuang. Dual-objective STORM reveals three-dimensional filament organization in the actin cytoskeleton. *Nature Methods*, 9(2):185–190, 2012. doi: 10.1038/NMETH.1841.

Kenneth M Yamada and Edna Cukierman. Modeling Tissue Morphogenesis and Cancer in 3D. *Cell*, 130 (4):601–10, August 2007. ISSN 0092-8674. doi: 10.1016/j.cell.2007.08.006. URL `http://www.ncbi.nlm.nih.gov/pubmed/17719539`.

Yoshiya Yamada, Mark H Bilsky, D Michael Lovelock, Ennapadam S Venkatraman, Sean Toner, Jared Johnson, Joan Zatcky, Michael J Zelefsky, and Zvi Fuks. High-Dose, Single-Fraction Image-Guided Intensity-Modulated Radiotherapy for Metastatic Spinal Lesions. *International Journal of Radiation Oncology*Biology*Physics*, 71(2):484–490, 2008. ISSN 0360-3016. doi: http://dx.doi.org/10.1016/j.ijrobp.2007.11.046. URL `http://www.sciencedirect.com/science/article/pii/S0360301607046585`.

M Yanai, J P Butler, T Suzuki, H Sasaki, and H Higuchi. Regional rheological differences in locomoting neutrophils. *American journal of physiology. Cell physiology*, 287(3):C603–11, September 2004. ISSN 0363-6143. doi: 10.1152/ajpcell.00347.2003. URL `http://www.ncbi.nlm.nih.gov/pubmed/15163623`.

Tony Yeung and Sergio Grinstein. Lipid signaling and the modulation of surface charge during phagocytosis. *Immunological reviews*, 219:17–36, October 2007. ISSN 0105-2896. doi: 10.1111/j.1600-065X.2007.00546.x. URL `http://www.ncbi.nlm.nih.gov/pubmed/17850479`.

S. Yonei, T. Todo, and M. Kato. Radiation effects on erythrocyte membrane structure studied by the intrinsic fluorescence. *Int J Radiat Biol*, 35(2):161–170, 1979.

Ji Won Yoon, Andreas Bruckbauer, William J Fitzgerald, and David Klenerman. Bayesian inference for improved single molecule fluorescence tracking. *Biophysical journal*, 94(12):4932–47, June 2008. ISSN 1542-0086. doi: 10.1529/biophysj.107.116285. URL `http://www.pubmedcentral.nih.gov/articlerender.fcgi?artid=2397372&tool=pmcentrez&rendertype=abstract`.

Ronen Zaidel-Bar. Evolution of complexity in the integrin adhesome. *The Journal of cell biology*, 186(3):317–21, August 2009. ISSN 1540-8140. doi: 10.1083/jcb.200811067. URL `http://www.pubmedcentral.nih.gov/articlerender.fcgi?artid=2728394&tool=pmcentrez&rendertype=abstract`.

Ronen Zaidel-Bar and Benjamin Geiger. The switchable integrin adhesome. *Journal of cell science*, 123(Pt 9):1385–8, May 2010. ISSN 1477-9137. doi: 10.1242/jcs.066183. URL `http://www.pubmedcentral.nih.gov/articlerender.fcgi?artid=2858016&tool=pmcentrez&rendertype=abstract`.

Ronen Zaidel-Bar, Shalev Itzkovitz, Avi Ma'ayan, Ravi Iyengar, and Benjamin Geiger. Functional atlas of the integrin adhesome. *Nature cell biology*, 9(8):858–67, August 2007. ISSN 1465-7392. doi: 10.1038/ncb0807-858. URL `http://www.pubmedcentral.nih.gov/articlerender.fcgi?artid=2735470&tool=pmcentrez&rendertype=abstract`.

E Zamir and B Geiger. Molecular complexity and dynamics of cell-matrix adhesions. *Journal of cell science*, 114(Pt 20):3583–90, October 2001. ISSN 0021-9533. URL `http://www.ncbi.nlm.nih.gov/pubmed/11707510`.

Andrew Y Zhang, Fan Yi, Guo Zhang, Erich Gulbins, and Pin-Lan Li. Lipid raft clustering and redox signaling platform formation in coronary arterial endothelial cells. *Hypertension*, 47(1):74–80, January 2006. ISSN 1524-4563. doi: 10.1161/10.1161/01.HYP.0000196727.53300.62. URL `http://www.ncbi.nlm.nih.gov/pubmed/16344372`.

Andrew Y Zhang, Fan Yi, Si Jin, Min Xia, Qi-Zheng Chen, Erich Gulbins, and Pin-Lan Li. Acid sphingomyelinase and its redox amplification in formation of lipid raft redox signaling platforms in endothelial cells. *Antioxidants & redox signaling*, 9(7):817–28, July 2007. ISSN 1523-0864. doi: 10.1089/ars.2007.1509. URL `http://www.ncbi.nlm.nih.gov/pubmed/17508908`.

Lei Zhu, Wei Zhang, and Daniel Elnatan. Faster STORM using compressed sensing. *Nature Methods*, 9(April), 2012. doi: 10.1038/NMETH.1978. URL `http://www.nature.com/nmeth/journal/vaop/ncurrent/full/nmeth.1978.html`.

A Acknowledgements

First of all, I would like to thank Tobias for his supervision and the possibility to work in an environment unique in its transgression of discipline boundaries. I am grateful for the trust in me, the freedoms granted and his encouraging confidence in my skills.

I also thank Gerd for the inclusion into his lab and the support I enjoyed. Especially his openness to ideas of mine like the mathematics-only labcourse experiment and the discussions on general topics are highly appreciated.

Furthermore, I am happy about this opportunity to thank Prof. Durante for his kind willingness to sign responsible to the faculty of physics for my doing a doctorate. I am grateful for the insightful comments I received that highlighted scientific developments I was not aware of previously and thereby lead the route of investigation to areas I would have missed otherwise.

I want to thank Prof. Drossel and Prof. Walther for kindly agreeing to take part in my examining committee.

Special thanks deserve Elke and Miriam who taught me cell culture and made the transition to biology less rough. I especially liked the office company of Miriam and the discussions over a cup of coffee. The 2011/12 staff of the Kinderzimmer plus Vera is acknowledged for the fun at the table soccer.

The GRK 1657 deserves credit for providing me the opportunity to conduct research in an exciting environment and is also acknowledged for being a platform for interesting dialogues, especially – as one DFG assessor put it – “at the bar”.

Finally, I want to thank my parents for their unlimited confidence in me and my grandma Anny who is excited about my PhD more than everyone else and who I dedicate this thesis.

B Curriculum Vitae

Name:	Florian Lauer
Birth:	November 26th 1984 in Freudenstadt, Germany
February 28th, 2011	Diplom-Physiker with the diploma thesis “Investigations of a fluorescent nuclear track detector for use in therapeutic ion beams”. Minor in philosophy and specialization in medical physics, grade “sehr gut”
September 10th, 2007	Vordiplom, grade “sehr gut”, with minor subject chemistry
2005–2011	study of physics (Diplom) at University of Heidelberg
2004–2005	Zivildienst (civil service)
2004	Abitur, grade 1.6
1994–2004	Schickhardt Gymnasium Herrenberg
1991–1994	Grundschule Gültstein (elementary school)
Publications:	– S Greilich, J-M Osinga, M Niklas, *FM Lauer*, G Klimpki, F Bestvater, JA Bartz, MS Akselrod, and O Jäkel. Fluorescent Nuclear Track Detectors as a Tool for Ion-Beam Therapy Research. *Radiation Measurements*. 56 (2013):267–272 – *FM Lauer*, E Kämmerer, and T Meckel. Single molecule microscopy in 3D cell cultures and tissues. *Advanced Drug Delivery Reviews*. 79–80 (2014):79–94
Conference contributions:	– *FM Lauer*, S Greilich, MS Akselrod, and O Jäkel. Fluorescent Nuclear Track Detectors for Particle Therapy. *41. Jahrestagung der Deutschen Gesellschaft für Medizinische Physik in Freiburg* (2010). Poster contribution. – *FM Lauer*, S Greilich, MS Akselrod, and O Jäkel. Fluorescent Nuclear Track Detectors in Ion Therapy. *Jahrestagung der Gesellschaft für Biologische Strahlenforschung* (2011) in Cologne. Poster contribution. – *FM Lauer*, E Kämmerer, and T Meckel. Influence of the extracellular environment and ionizing radiation on the spatio-temporal dynamics of the plasma membrane. *Seeing is believing 2013*. Poster contribution. – M Grunewald, *FM Lauer*, G Thiel, and T Meckel. Dynamics and stoichiometry of low-abundant integral plasma membrane proteins imaged in supported native membranes. *Seeing is believing 2013*. Poster contribution. – M Grunewald, *FM Lauer*, A Bertold, G Thiel, and T Meckel. Single molecule counting and stoichiometry of low-abundant plasma membrane proteins, *Focus on Micoscopy 2014*. Talk contribution. – L Babel, *FM Lauer*, E Kämmerer, S Bump, and T Meckel. Effects of ionizing radiation on plasma membrane dynamics measured in a 3D cell culture system. *Jahrestagung der Gesellschaft für Biologische Strahlenforschung* (2014) in Tübingen. Poster contribution.

Erklärung zur Dissertation

Hiermit versichere ich, die vorliegende Dissertation ohne Hilfe Dritter nur mit den angegebenen Quellen und Hilfsmitteln angefertigt zu haben. Alle Stellen, die aus Quellen entnommen wurden, sind als solche kenntlich gemacht. Diese Arbeit hat in gleicher oder ähnlicher Form noch keiner Prüfungsbehörde vorgelegen.

Darmstadt, den 23rd April 2015

(F. Lauer)